

2011-01-01

# Fundamental Studies Of Co-Base Superalloy Biomedical Prototypes Fabricated By Electron Beam Melting: Microstructures And Microstructural Architecture

Sara M. Gaytan

*University of Texas at El Paso*, [smgaytan@miners.utep.edu](mailto:smgaytan@miners.utep.edu)

Follow this and additional works at: [https://digitalcommons.utep.edu/open\\_etd](https://digitalcommons.utep.edu/open_etd)



Part of the [Materials Science and Engineering Commons](#), and the [Mechanics of Materials Commons](#)

---

## Recommended Citation

Gaytan, Sara M., "Fundamental Studies Of Co-Base Superalloy Biomedical Prototypes Fabricated By Electron Beam Melting: Microstructures And Microstructural Architecture" (2011). *Open Access Theses & Dissertations*. 2290.  
[https://digitalcommons.utep.edu/open\\_etd/2290](https://digitalcommons.utep.edu/open_etd/2290)

This is brought to you for free and open access by DigitalCommons@UTEP. It has been accepted for inclusion in Open Access Theses & Dissertations by an authorized administrator of DigitalCommons@UTEP. For more information, please contact [lweber@utep.edu](mailto:lweber@utep.edu).

FUNDAMENTAL STUDIES OF CO-BASE SUPERALLOY BIOMEDICAL  
PROTOTYPES FABRICATED BY ELECTRON BEAM MELTING:  
MICROSTRUCTURES AND MICROSTRUCTURAL ARCHITECTURE

SARA MARISELA GAYTAN GUILLEN

Materials Science and Engineering

APPROVED:

---

Lawrence E. Murr, Ph.D., Chair

---

Stephen W. Stafford, Ph.D.

---

Jorge A. Lopez, Ph.D.

---

Juan C. Noveron, Ph.D.

---

Benjamin C. Flores, Ph.D.  
Acting Dean of the Graduate School

Copyright ©

by

Sara M. Gaytan

2011

## **DEDICATION**

Thank you to everyone that has been part of my life, especially to my family and Alejandro. Without them this would have been harder to accomplish. I can tell you that the two phrases that kept me motivated and kept my stress level low were: “Dios dira” (“God knows better”) and “Un dia a la vez” (“One day at a time”), so feel free to use them as convenient ☺.



FUNDAMENTAL STUDIES OF CO-BASE SUPERALLOY BIOMEDICAL  
PROTOTYPES FABRICATED BY ELECTRON BEAM MELTING:  
MICROSTRUCTURES AND MICROSTRUCTURAL ARCHITECTURE

by

SARA MARISELA GAYTAN GUILLEN, M.S.

DISSERTATION

Presented to the Faculty of the Graduate School of  
The University of Texas at El Paso  
in Partial Fulfillment  
of the Requirements  
for the Degree of

DOCTOR OF PHILOSOPHY

Materials Science and Engineering  
THE UNIVERSITY OF TEXAS AT EL PASO  
December 2011

## **ACKNOWLEDGEMENTS**

First I want to thank Dr. L. E. Murr for all his support and advice, without him I would not have stayed for this degree. Thank you to my research group, especially Frank Medina, Edwin Martinez and Brenda Machado. This project could not have been accomplished without the help of David K. Brown. To all of you, thank you very much.

## **ABSTRACT**

Rapid prototyping, especially electron beam melting (EBM) technology by ARCAM have proven to provide outstanding microstructural and mechanical properties on different alloys fabricated by this technology. Being a computer designed driven technology, complex components, that are hard or even impossible to fabricate by traditional manufacturing techniques, can be fabricated by layer-by-layer EBM technology.

Microstructural and mechanical properties are compared for an EBM femoral knee component prototype with a traditionally-fabricated and body-removed femoral knee implant. Block and cylindrical shape components fabricated by EBM were also analyzed for this project. The alloy utilized for these components is Co-26Cr-6Mo-0.2C characterized by the standards of ASTM F75 cobalt alloy. Microstructural characterization was performed by optical metallography as well as SEM, TEM, EDS and XRD. Mechanical properties consist of Vickers and Rockwell-C scale hardness, as well as tensile testing. Tensile testing for the EBM as-fabricated components and annealed components was performed in two different directions. Only hardness testing was possible on the patient-extracted, traditional knee component.

# TABLE OF CONTENTS

DEDICATION .....	III
ACKNOWLEDGEMENTS .....	V
ABSTRACT .....	VI
TABLE OF CONTENTS .....	VII
LIST OF TABLES .....	IX
LIST OF FIGURES .....	X
STATEMENT OF THE PROBLEM.....	1
JUSTIFICATION.....	1
PROPOSAL .....	2
CHAPTER 1.....	4
INTRODUCTION.....	4
CHAPTER 2.....	6
BACKGROUND.....	6
2.1 RAPID PROTOTYPING.....	6
2.2 GAS ATOMIZATION PROCESS .....	7
2.3 ELECTRON BEAM MELTING (EBM).....	7
2.3.1 EBM ADVANTAGES.....	8
2.3.1.1 DIRECTIONAL SOLIDIFICATION.....	8
2.4 CO-BASE ALLOYS.....	9
2.4.1 Co-Cr-Mo .....	10
2.4.1.1 METALLIC IMPLANTS AND AEROSPACE APPLICATIONS.....	12
2.4.1.2 SAMPLE ACQUISITION .....	13
CHAPTER 3.....	14
METHODOLOGY .....	14
3.1 EBM.....	14
3.2 OPTICAL METALLOGRAPHY .....	16

3.3	HARDNESS AND TENSILE TESTING .....	17
3.4	SCANNING ELECTRON AND TRANSMISSION ELECTRON MICROSCOPY .....	17
3.5	X-RAY DIFFRACTION .....	18
CHAPTER 4.....		19
RESULTS .....		19
4.1	POWDER .....	19
4.2	AS-FABRICATED COMPONENTS.....	24
4.2.1	SOLID COMPONENTS.....	26
4.2.2	MESH COMPONENT .....	44
4.3	HIPED AND ANNEALED COMPONENTS .....	46
4.4	TRADITIONAL IMPLANT CHARACTERIZATION .....	63
CHAPTER 5.....		74
DISCUSSION .....		74
5.1	OPTICAL MICROSCOPY.....	74
5.2	TRANSMISSION ELECTRON MICROSCOPY .....	80
5.3	HARDNESS TESTING.....	84
5.4	TENSILE TESTING.....	87
5.5	X-RAY DIFFRACTION .....	88
CHAPTER 6.....		90
CONCLUSIONS .....		90
REFERENCES .....		93
APPENDIX .....		96
VITA .....		120

**LIST OF TABLES**

TABLE 1. NOMINAL COMPOSITIONS ..... 12

TABLE 2. TENSILE TESTING RESULTS..... 87

## LIST OF FIGURES

FIGURE 1.1: CHRONOLOGICAL REPRESENTATION OF ANALOG AND DIGITAL MANUFACTURING THROUGH THE YEARS (YOGNIAN, ET AL. 2009) ...PP: 4	4
FIGURE 1.2: FABRICATION METHODS FOR CLOSED AND OPEN CELL COMPONENTS (RYAND, ET AL. 2006) ...PP:5	5
FIGURE 3.1: SCHEMATIC OF ELECTRON BEAM MELTING (A) AND CO-CR-MO POWDER PARTICLES (B) ...PP:15	15
FIGURE 4.1.1: LOW MAGNIFICATION SEM IMAGE OF CO-CR-MO POWDER PARTICLES ...PP:20	20
FIGURE 4.1.2: POWDER PARTICLES HISTOGRAM ...PP:20	20
FIGURE 4.1.3: HIGHER MAGNIFICATION SEM IMAGE OF SMALLER POWDER PARTICLES ATTACHED TO BIG PARTICLES ...PP:21	21
FIGURE 4.1.4: DEFECT IN POWDER PARTICLE OBTAINED FROM THE GAS ATOMIZATION PROCESS ...PP:21	21
FIGURE 4.1.5: HIGH MAGNIFICATION OF SEM MICROGRAPH SHOWING POWDER PARTICLE TOMOGRAPHY FEATURES ...PP:22	22
FIGURE 4.1.6: MICROSTRUCTURAL FEATURES OF POWDER PARTICLES CROSS SECTION ...PP:22	22
FIGURE 4.1.7: X-RAY DIFFRACTION OF POWDER PARTICLES ...PP:23	23
FIGURE 4.2.1: CO-CR-MO AS-FABRICATED SOLID COMPONENTS ...PP:25	25
FIGURE 4.2.2: MESH COMPONENT ...PP:25	25
FIGURE 4.2.1.1: COLUMNAR ARCHITECTURE FROM BLOCK COMPONENT ...PP:26	26
FIGURE 4.2.1.2 A) TEM IMAGE OF BLOCK COMPONENT ...PP:27	27
FIGURE 4.2.1.2 B) TEM IMAGE OF BLOCK COMPONENT ...PP:28	28
FIGURE 4.2.1.3: CR23C6 PRECIPITATES OBSERVED IN BLOCK COMPONENT ...PP:29	29
FIGURE 4.2.1.4: STACKING FAULTS IN BLOCK COMPONENT AT 10KX ...PP:30	30
FIGURE 4.2.1.5: PRECIPITATES AND DISLOCATIONS INTERACTION IN AS-FABRICATED EBM COMPONENT ...PP:31	31
FIGURE 4.2.1.6: INTERSECTING INTRINSIC STACKING FAULTS ...PP:32	32
FIGURE 4.2.1.7: MICROSTRUCTURE OBTAINED FROM CYLINDRICAL COMPONENT ...PP:33	33
FIGURE 4.2.1.8: TEM IMAGE OF CYLINDRICAL COMPONENT AT 4000X ...PP:34	34
FIGURE 4.2.1.9: TEM IMAGE OF AS-FABRICATED CYLINDER SHOWING A DISLOCATION DENSITY OF $3.6 \times 10^9/\text{CM}^2$ ...PP:35	35
FIGURE 4.2.1.10: TEM IMAGES OBTAINED FROM CYLINDRICAL COMPONENT. A) AND B) SHOW SAME AREA WITH DIFFERENT TILT ANGLE ...PP:37	37
FIGURE 4.2.1.11: SEM IMAGES OBTAINED FROM FRACTURED END OF TENSILE SPECIMEN FAILED AT 5% ELONGATION ...PP:39	39
FIGURE 4.2.1.12: INTERGRANULAR FRACTURE FROM SAMPLE ELONGATED 5% ...PP:40	40
FIGURE 4.2.1.13: MICROSTRUCTURE FROM AS-FABRICATED FEMORAL KNEE COMPONENT ...PP:41	41
FIGURE 4.2.1.14: MICROSTRUCTURE OF FEMORAL KNEE COMPONENT ...PP:41	41
FIGURE 4.2.1.15: XRD SPECTRA OF AS-FABRICATED COMPONENTS ...PP:43	43
FIGURE 4.2.2.1: SEM IMAGE OF MESH COMPONENT SURFACE ...PP:44	44
FIGURE 4.2.2.2: MICROSTRUCTURE OBTAINED FROM CO-CR-MO MESH COMPONENT ...PP:45	45
FIGURE 4.3.1: POST-TREATED FEMORAL KNEE COMPONENT WITH MESH INCLUSION FABRICATED BY EBM ...PP:47	47
FIGURE 4.3.2: SECTION USED FOR ANALYSIS OBTAINED FROM FEMORAL KNEE COMPONENT ...PP:48	48
FIGURE 4.3.3: HORIZONTAL PLANE OF BLOCK COMPONENT ...PP:50	50
FIGURE 4.3.4: VERTICAL PLANE OF BLOCK COMPONENT ...PP:50	50
FIGURE 4.3.5: HORIZONTAL PLANE OF CYLINDRICAL COMPONENT ...PP:51	51
FIGURE 4.3.6: VERTICAL PLANE OF CYLINDRICAL COMPONENT ...PP:51	51
FIGURE 4.3.7: VERTICAL PLANE OF FEMORAL KNEE COMPONENT ...PP:52	52
FIGURE 4.3.8: VERTICAL PLANE OF FEMORAL KNEE COMPONENT ...PP:52	52
FIGURE 4.3.9: BLOCK HORIZONTAL, NO PRECIPITATES IN DIFFRACTION ...PP:53	53
FIGURE 4.3.10: HORIZONTAL PLANE OF ANNEALED AND HIPED CYLINDRICAL COMPONENT FABRICATED BY EBM ...PP:54	54
FIGURE 4.3.11: VERTICAL PLANE OF ANNEALED FEMORAL KNEE COMPONENT ...PP:55	55
FIGURE 4.3.12: HIGH DENSITY OF STACKING FAULTS IN ANNEALED EBM FABRICATED FEMORAL KNEE COMPONENT ...PP:56	56
FIGURE 4.3.13: VERTICAL PLANE FROM ANNEALED FEMORAL KNEE COMPONENT ...PP:57	57
FIGURE 4.3.14: VERTICAL PLANE IN ANNEALED KNEE COMPONENT ...PP:58	58

FIGURE 4.3.15: FRACTURE SURFACE FROM TENSILE TESTING ...PP:60

FIGURE 4.3.16: FRACTURED SURFACE SHOWING AN UNMELTED POWDER PARTICLE ...PP:61

FIGURE 4.3.17: XRD OF ANNEALED AND HIPED COMPONENTS ...PP:62

FIGURE 4.4.1: TRADITIONALLY MANUFACTURED FEMORAL KNEE COMPONENT IMPLANT ...PP:63

FIGURE 4.4.2: CO-CR-MO LOW MAGNIFICATION IMAGE SHOWING MICROSTRUCTURE ...PP:64

FIGURE 4.4.3: LOW MAGNIFICATION IMAGE FROM IMAGE FROM TRADITIONALLY MANUFACTURED FEMORAL KNEE COMPONENT ...PP:65

FIGURE 4.4.4: LOW MAGNIFICATION IMAGE FROM TRADITIONALLY MANUFACTURED FEMORAL KNEE COMPONENT ...PP:65

FIGURE 4.4.5: TRADITIONALLY MANUFACTURED KNEE IMPLANT ...PP:66

FIGURE 4.4.6: TEM IMAGE OF TRADITIONALLY MANUFACTURED CO-CR-MO IMPLANT COMPONENT ...PP:67

FIGURE 4.4.7: LOWER MAGNIFICATION TEM IMAGE OF CO-CR-MO TRADITIONALLY MANUFACTURED IMPLANT ...PP:68

FIGURE 4.4.8: XRD OF BODY REMOVED CO-CR-MO IMPLANT ...PP:69

FIGURE 4.4.9: LOW MAGNIFICATION IMAGE OF TI-6AL-4V ROD COMPONENT ...PP:70

FIGURE 4.4.10: HIGH MAGNIFICATION IMAGE OF TI-6AL-4V ROD COMPONENT ...PP:70

FIGURE 4.4.11: TEM IMAGE OF TI-6AL-4V ROD COMPONENT ...PP:71

FIGURE 4.4.12: TI-6AL-4V ROD COMPONENT FROM BODY-REMOVED IMPLANT ...PP:72

FIGURE 4.4.13: XRD OF BODY REMOVED TI-6AL-4V IMPLANT ...PP:73

FIGURE 5.1.1: CARBIDE PRECIPITATES PATTERN FORMATION ...PP:74

FIGURE 5.1.2: VERTICAL PLANE FROM THE BOTTOM PART OF AS-FABRICATED CYLINDRICAL COMPONENT ...PP:76

FIGURE 5.1.3: VERTICAL PLANE FROM THE TOP PART OF AS-FABRICATED CYLINDRICAL COMPONENT ...PP:76

FIGURE 5.1.4: HORIZONTAL PLANE FROM THE BOTTOM PART OF AS-FABRICATED CYLINDRICAL COMPONENT ...PP:77

FIGURE 5.1.5: HORIZONTAL PLANE FROM THE TOP PART OF AS-FABRICATED CYLINDRICAL COMPONENT ...PP:77

FIGURE 5.1.6: HORIZONTAL PLANE FROM THE TOP PART OF AS-FABRICATED CYLINDRICAL COMPONENT ...PP:78

FIGURE 5.1.7: HORIZONTAL PLANE FROM EBM FABRICATED ANNEALED CYLINDRICAL COMPONENT ...PP:78

FIGURE 5.1.8: MICROSTRUCTURE OBTAINED FROM BODY-REMOVED CO-CR-MO IMPLANT ...PP:79

FIGURE 5.2.1: A) AS-FABRICATED COMPONENT SHOWING CR<sub>23</sub>C<sub>6</sub> PRECIPITATES ...PP:81

FIGURE 5.2.1: B) AS-FABRICATED COMPONENT SHOWING CR<sub>23</sub>C<sub>6</sub> PRECIPITATES MAGNIFIED ...PP:82

FIGURE 5.2.2: EBM FABRICATED COMPONENT AFTER ANNEALING ...PP:83

FIGURE 5.2.3: BODY-REMOVED CO-CR-MO IMPLANT ...PP:84

FIGURE 5.3.1: HV IN GPA COMPARISON ...PP:86

FIGURE 5.3.2: HRC COMPARISON ...PP:86

FIGURE 5.5.1: XRD COMPARISON ...PP:89

FIGURE 1. OPTICAL MICROGRAPH SHOWING ACICULAR A -PHASE MICROSTRUCTURE FOR A SOLID EBM CYLINDRICAL COMPONENT. HARDNESS WAS 3.5 GPA (MURR, 2010) ...PP:96

FIGURE 2. 1.1MM THICK STRIP IN A TEST ELEMENT , SHOWING REFINED A' AND B' PHASE (DARK DOTS), WHERE THE HARDNESS WAS 4.8 GPA. SAME MAGNIFICATION AS FIGURE 1 (MURR, 2010) ..PP:96

FIGURE 3. TEM BRIGHT-FIELD IMAGES CORRESPONDING TO FIGURES 1 AND 2. (A) SOLID MONOLITH EXHIBITING 2 $\mu$ M WIDE A-PLATELETS WITH B-PHASE BOUNDARIES. ARROW DENOTES AN A/A GRAIN BOUNDARY. (B) 1.1MM TEST PLATE TEM IMAGE ILLUSTRATING REFINED B (DARK). THE SELECTED AREA ELECTRON DIFFRACTION (SAED) PATTERN INSERT IN (A) SHOWS THE A-PHASE (HCP) (0 0 1) PLANE WHILE THE SAED PATTERN INSERT IN (B) SHOWS ADDITIONAL, MULTIPLE DIFFRACTION SPOTS FROM THE REFINED B-PHASE (MURR, 2010) ...PP:97



## **STATEMENT OF THE PROBLEM**

The evolution of manufacturing technologies implies the need for characterizing different materials available in order to obtain the best properties intended for specific applications. Rapid manufacturing by electron beam melting is becoming an ideal technology to create complex shapes through computer-controlled self-assembly by sintering or melting of powder layers (Murr, et al. 2009a). The EBM system, more specifically the ARCAM system, has been created “to revolutionize the art of manufacturing”. The idea for this dissertation is to characterize Co-Cr-Mo components fabricated by electron beam melting (EBM) and compare microstructures with the properties obtained. Equally important is the urge to compare properties of as-fabricated components and fabricated components after annealing to obtain a better understanding on how to benefit the EBM manufactured components. The Co-Cr-Mo alloy is a Co-base superalloy and has had both aerospace and biomedical (implant component) applications.

## **JUSTIFICATION**

As stated in the 2010 Annual Worldwide Progress Report, and according to the president of Arcam, Magnus Rene, six EBM machines are being used by a client to manufacture more than 25,000 medical implants per year at one location, in Italy; these implants have already received CE-certification and therefore Europe’s acceptance of these implants is increasing (Wohlers, 2010).

It is already a fact that customized porous titanium-based alloy implants are being implanted in reconstructive surgery for motor vehicle accidents, tumors and combat injuries, i.e. “Christensen’s work (president and chief technical officer at Medical Modeling Inc.) with the Walter Reed Army Medical Center has enabled it to build and successfully

implant more than 30 custom porous titanium implants into wounded soldiers”; he was recognized in 2009 for introducing EBM technology into the fabrication of Ti-base alloy implants (Society of Manufacturing Engineers, 2009).

Rapid prototyping (RP) technology is available at UTEP, more specifically in the W. M. Keck Center for 3D Innovation. A variety of technologies are available for research at the Keck Center, but this dissertation research utilized the EBM system for implant fabrication. Being rapid prototyping an innovative technology, the reason for this project is to analyze Co-Cr-Mo alloys fabricated by electron beam melting, since the applications can be very varied. Being an alloy that can withstand high temperatures, and has a high wear resistance, it can be used in gas turbines; valve seats, nuclear power plants, automobile engines, aerospace fuel nozzles and engine vanes and components, as well as in a variety of orthopedic and dental implants (Anthony, 1983; Alamert and Bhadeshia, 1989; Shin, et al. 2003; ARCAM 2011a). Furthermore, while Co-base alloy microstructure-property relationships have been examined for cast and wrought products, there are no comparable studies for EBM fabricated products. Moreover, by combining 3D implant models and rapid prototyping technologies, the capability of fabricating custom anatomical implants can be realized (Vail, et al. 1999).

## **PROPOSAL**

Microstructural analyses and measurements of mechanical properties of different geometrical components as well as femoral-knee implant shape components fabricated by electron beam melting will be conducted and compared in this research effort. Equally important will be the comparison of these EBM fabricated components with a traditional manufactured and body-removed implant. This will provide a database for Co-Cr-Mo that could lead to a new era of customized Co-Cr-Mo implants and other applications fabricated by electron beam melting, as well as a microstructural understanding/comparison between

implants traditionally fabricated and EBM fabricated, specially a femoral-knee Co-Cr-Mo component. Of particular interest will be the correlation of optical microscope imaging with transmission electron microscope imaging for variously fabricated and heat treated components fabricated by EBM.

# CHAPTER 1

## INTRODUCTION

Rapid prototyping and manufacturing (RPM) technologies can be considered as new technologies if we compare them to other manufacturing technologies that have been around for a much longer time such as machine analog manufacturing. RPM technologies started in 1986 with the creation of stereolithography (SL) technology, and that led to the creation of more innovative technologies. In the period of 1986 to 1998 two hundred and seventy four patents were registered in the US related to RPM techniques, mainly related to the stereolithography process (Yognian, et al. 2009). Figure 1.1 shows a chronological representation on how analog and digital manufacturing appeared through the years. It can be observed how digital manufacturing by rapid prototyping started in mid 1980s.

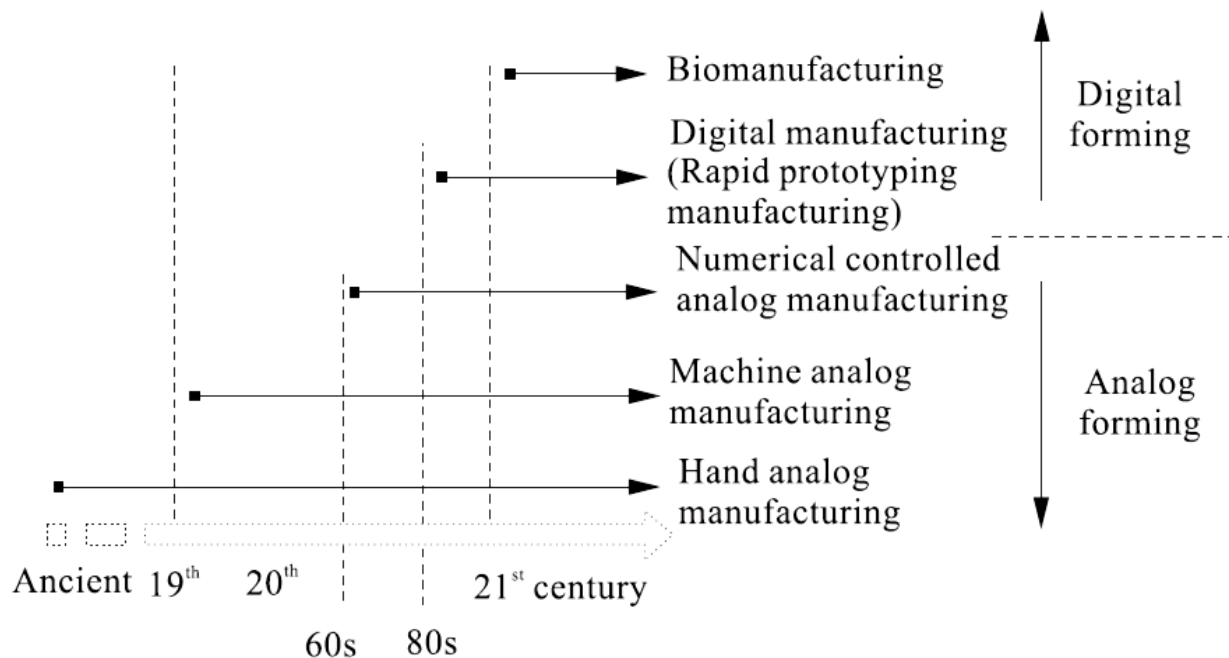


**Figure 12.3.1.1 Chronological representation of analog and digital manufacturing through the years (Yognian, et al. 2009).**

According to Ryan et al., porous metals or metal foams can be divided in two different categories: closed and open cell. In the first one the pores are completely surrounded by metal while in the open cell category the pores are only interconnected with each other allowing tissue ingrowth in the case of potential implants as well as gas or fluid flow which could allow heat exchange applications and the like (Ryan, et al. 2006). Figure 1.2 shows how porous metals have been categorized according to the resulting pore distribution providing the fabrication methods. Rapid prototyping only appears in the open-cell division to create homogeneous and functionally graded when in reality rapid prototyping is ideally able to create any component designed in CAD. It has already been proven that anything that can be designed by CAD can be built by EBM as long as the minimum specifications of the system are met (Murr, et al. 2009a).

Fabrication methods				
Closed-cell		Open-cell		
Random pore distribution	Graded pore distribution	Non-homogeneous	Homogeneous	Functionally graded
Gas injection into the metal melt [52]	Plasma spraying [15]	Sintered metal powders [62] Sintered metal fibres [69]	Orderly oriented wire mesh [83] Vapour deposition [92]	Rapid prototyping [55] Electro discharge compaction [103–105]
Decomposition of foaming agents [53]		Space holder method [70] Replication [74] Combustion synthesis [81] Plasma spraying [15]	Ferromagnetic fibre array [85] Rapid prototyping [55]	

**Figure 12.3.1.2 Fabrication methods for closed and open cell components (Ryan, et al. 2006).**

## **CHAPTER 2**

### **BACKGROUND**

#### **2.1 RAPID PROTOTYPING**

RP (rapid prototyping) refers to a process that takes information from a 3D computer-aided design (CAD) database to produce solid models which can have several benefits. Among these benefits can be the improved ability to visualize the part geometry and fit, and this way design errors can easily be detected and prevented due to the physical existence of the part, as well as the reduction/elimination of waste and costly late design changes (Noorani, 2006). Some of the available RP technologies for plastic components are stereolithography (SL), selective laser sintering (SLS), fused deposition modeling (FDM) and 3D printing (Noorani, 2006).

Rapid prototyping applications consist in different popular areas such as functional prototypes, casting patterns, medical models, artwork and engineering analysis models (Pham, et al. 2002). By prototypes it is understood that they play a role in the product development process and as such they can be used for different purposes. For experimentation, learning, testing and proofing, as well as interaction and integration (Chua, et al. 2003).

Nowadays some manufacturing enterprises have started to use rapid prototyping methods (or additive manufacturing, AM) for complex pattern making and component prototyping to shorten the time for pattern, molds and prototype development as well as the verification of form, fit and function (Yan and Gu, 1996; Noorani, 2006).

Three-dimensional printing (3DP), a rapid prototyping technology, has been used by Ryan et al. to create porous implants with controlled size, shape and distribution of the porosity from CoCr alloys in Galway, Ireland (Ryan, et al. 2006). Laser Engineered Net Shaping (LENS) is being used to fabricate Co-Cr-Mo porous load bearing implants in

Pullman WA (Espana, et al. 2010). However, as noted above, there are no systematic materials science and engineering analyses of Co-Cr-Mo components fabricated by EBM.

## **2.2 GAS ATOMIZATION PROCESS**

EBM consists in the melting or sintering of powder particles by an electron beam following instructions from a CAD design. Co-Cr-Mo powder utilized for this project is created by a gas atomization process. This process consists in the disintegration of molten metal into powder by using high pressure gas in a closed, inert gas-filled chamber to prevent contamination. Spherical particles are obtained by the expanding gas breaking the melt stream into molten droplets that spheroidize before reaching solidification, the process is performed in an inert atmosphere or in vacuum. Higher melt temperatures and gas pressures are used to obtain smaller particles (Oshida, 2007; German, 2005; Bradley, 1988).

## **2.3 ELECTRON BEAM MELTING (EBM)**

The company responsible for making available a rapid prototyping system that creates metal components with outstanding microstructural and mechanical properties is ARCAM AB from Sweden founded in 1997 and commercialized in 2001. The fundamental idea of ARCAM started in 1995 with the collaboration of Chalmers University of Technology in Gothenburg, Sweden (Chua, et al. 2003). ARCAM of Sweden offers a process called electron beam melting that basically utilizes an electron optical system to melt metal powder in vacuum. In 2009 a new system was launched: ARCAM A1 which is aiming at the orthopedic market. This technology used the patented MultiBeam technology that allows for simultaneous melting at multiple locations which is said to improve both productivity and surface finish (Wohlers, 2010).

### **2.3.1 EBM ADVANTAGES**

High precision and quality can be obtained in the ARCAM A2 machine used for this study. EBM rapid prototyping makes possible the creation of metal complex components out of a computer design model by melting powder particles. This process is ideal for high strength or high temperature applications, since the powder material used is Co-Cr-Mo, besides the advantage of being an alloy that can create light weight porous components, near-net shapes with reduced material input and less machining to produce a finished part (Bradley, 1988; Ramsdale, 2004-2006). If we compare AM technologies with injection molding, AM can lead to the elimination of tooling costs and lead times. When compared to computer numerical control (CNC) machining for part production, AM will have a minimum in waste material (Wohlers, 2010).

#### **2.3.1.1 DIRECTIONAL SOLIDIFICATION**

It can be assumed that the stronger a material becomes, it also becomes more susceptible to brittle fracture (Murr and Stein, 1976). Directionally solidified (DS) columnar grained superalloys are used for high temperature applications, such as turbine airfoils. Since it was found that grain boundaries represent weak points, columnar structures by directional solidification, with the grains aligned parallel to the blade axis can significantly improve the performance of the same, as stated by Durand-Charre (Durand-Charre, 1997). It is also stated that alignment of the grain boundaries normal to the stress axis improves ductility at elevated temperatures since failure is not initiated at the grain boundary, besides the fact that directionally solidified processes provide a preferred orientation parallel to the solidification direction that provides a preferred low modulus (<001> texture) (Sims, et al. 1987).



## 2.4 CO-BASE ALLOYS

Pure cobalt has very few applications but this metal is important for scientific study. It has a hexagonal closed packed crystal structure at lower temperatures and it transforms to face centered crystal structure at temperatures above 417°C up to its melting point (~1495°C). This temperature (417°C) depends on purity and rate of temperature change and controversy regarding fcc stability exists (Battelle Memorial Institute, 1960); in addition, fcc cobalt is a low-stacking fault energy element. Chromium, tungsten and molybdenum stabilize the fcc structure but most of the times the alloys will have the metastable fcc structure due to the slow fcc to hcp transformation process due to the very low free-energy change associated with the fcc to hcp transformation of cobalt (Battelle Memorial Institute, 1960). These alloying elements, besides acting as stabilizers, provide solid solution hardening and form hard, abrasion-resistant carbides. Chromium also provides a higher corrosion resistance to the alloy. Cobalt-base superalloys are mainly formed by a significant amount of nickel, chromium and tungsten, and lesser amounts of molybdenum, niobium, tantalum, titanium, lanthanum and iron in some instances, where cobalt is the major constituent. These alloys are strengthened by solid solution and carbide phases from the addition of 0.4 to 0.85% carbon. Commonly, high temperature applications use softer and tougher compositions while wear resistance applications use harder grades (Betteridge, 1982; Askeland and Phule, 2006; Campbell, 2008; Bradley, 1988).

Cobalt-base alloys can be considered high temperature materials, and the most important characteristics of these materials can be summarized in three categories. First, is the *ability to withstand loading at an operating temperature close to its melting point*, and this happens when the homologous temperature is more than 0.6 ( $T = [T_{oper}/T_m] > 0.6$ ). Another important characteristic of this alloys is a *substantial resistance to mechanical degradation over extended periods of time*, this means that creep must be considered as well

as the static properties of yield stress, ultimate tensile strength and fracture toughness. Finally, *tolerance of severe operating environments*. This could mean the corrosive environment due to high sulphur levels, potassium salts and the possibility of oxidation due to high operating temperatures, reminding that any surface degradation can diminish the life of the component (Reed, 2006).

Commercial cobalt-base superalloys always contain alloying elements that provide strength, creep resistance, or resistance to surface degradation to the alloy. It has been stated by Stoloff and others that cobalt-base alloy are hardened by precipitation of either carbides or intermetallic compounds (Sims, et al. 1987). Cobalt is used in corrosion and wear resistant alloys, high speed tool steels, cemented carbide tools, magnetic materials and low expansion alloys.

#### **2.4.1 CO-CR-MO**

Co-Cr-Mo has a high corrosion resistance due to the high chromium content that forms a thin passive oxide layer, which makes it an ideal candidate for metal-on-metal bearing surfaces in orthopedic implants. In addition to the excellent corrosion resistance this alloy also provides a high cycle fatigue resistance as well as strength and ductility, in addition, a high wear resistance depending on the size, shape and distribution of carbide precipitates is achieved. Another microstructural aspect to take into consideration is the prospect of a fine grain size for superior tensile and fatigue properties (Janaki, 2008; Campbell, 2008).

Co-Cr alloy's Young's modulus ranges between 100 to 200 GPa, 248 GPa for CoCrMo alloy, and by fabricating an implant with fully dense outer surface and interconnected porosity in the inside can reduce the stiffness of the material without sacrificing its wear resistance (España, 2010). Fully dense Co-Cr alloy stiffness is more than 10 times that for hard (cortical) bone. Co-Cr-Mo alloys are available for different purposes depending on

their compositions, manufacturing conditions and thermal treatments, which are dependent on temperature and time. Any variation of these factors alters the materials microstructure as well as the mechanical properties (Cawley, et al. 2003; Escobedo, et al. 1996).

Heat treatments alter the microstructure of materials, which can be the grain size and distribution of the carbide phases and/or the type of carbides obtained:  $M_{23}C_6$ ,  $M_7C_3$ ,  $M_6C$  where M can be chromium or a combination of chromium or molybdenum. A study conducted by Cawley et al., basically consisted in comparing the microstructures of the same Co-Cr-Mo alloy as cast, wrought and with different heat treatments, finding that the carbides obtained from all the thermally processed samples were richer in chromium than molybdenum and no difference in hardness was obtained from the as-cast and the thermally treated materials (Cawley, et al. 2003). None of these issues have been studied in any detail for Co-base alloys fabricated by additive manufacturing.

The cobalt alloy utilized for this project consisted in ASTM F75 and F799 Co-base powder consisting of 29%Cr, 6%Mo, 0.22%C, 0.25%Ni, 0.7%Si, and the balance Co in weight percent. Table 1 depicts nominal compositions of cobalt-base alloys for medical implant applications obtained from the ASM Handbook (ASM International, 2004). The average powder size was  $\sim 40\text{ }\mu\text{m}$ , while the powder melting point was  $\sim 1430^\circ\text{C}$ . Having a Young's modulus  $E=210\text{GPa}$ , and a density  $\rho=8.44\text{g/cm}^3$  (Gaytan, et al. 2010).

**Table 1. Nominal compositions**

ASTM	Trade name	Condition	Composition, wt%											
			Co	Cr	Mo	W	C	Ni	Fe	Si	Mn	N	S	P
F75	Haynes Stellite 21	Co/Cr/Mo castings	bal	27-30	5.0-7.0	0.20 max	0.35 max	1.00 max	0.75 max	1.00 max	1.00 max	0.25 max	0.01 max	0.02 max
F799	Haynes Stellite 21	Co/Cr/Mo forgings	bal	26-30	5.0-7.0	...	0.35 max	1.00 max	0.75 max	1.00 max	1.00 max	0.25 max	...	...

#### 2.4.1.1 METALLIC IMPLANTS AND AEROSPACE APPLICATIONS

Cobalt-base alloy use is limited due to the difficulty in fabrication, but continuous development in casting methods have been the result of continuous work. The first medical use of cobalt-base alloys was in the casting of dental implants due to its excellent resistance to degradation in the oral environment. Nowadays, the use of cobalt-base alloys for surgical applications is widely related to orthopedic prostheses for the knee, shoulder and hip (socket ball and stem) as well as fracture fixation devices (Marti, 2000; Shetty, 1995; Higuchi, et al. 1997).

Determination of the material, design and manufacturing process depends on the intended application. Customized maxillofacial implants start with the physical model of the patient's CT scans and the use of current RP techniques (Bertol, et al. 2010). A successful total knee replacement can last more than 10 years while an implant replacement with a critical outcome can have a high failure rate: reported failure rates range between 3% at 10 years and 39% at 4 years (Cristofolini, et al. 2009). Similarly, these alloys find numerous applications in hard-facing aerospace/aeronautics components. Cobalt-base alloys, also known as Stellite ® alloys are also used for applications that require high resistance to wear, particularly at elevated temperatures and corrosive environments, for example in nuclear, aerospace and gas turbine industries (Radu, et al. 2004; Ning, et al. 2005).

#### **2.4.1.2 SAMPLE ACQUISITION**

Build components fabricated by EBM have been obtained from different places and people, thanks to Francisco Medina at the W. M. Keck Center. It can be stated that solid and as-fabricated components in the shape of blocks and cylinders were obtained from Andy Christiansen at Medical Modeling located in Golden Colorado. The as-fabricated component in the shape of a knee implant was obtained from Mylin Cumberland at De Puy Orthopaedics in the Johnson and Johnson Medical Devices section, located in Fort Wayne, Indiana. On the other hand, the as-fabricated mesh and the annealed and polished knee implant component were obtained from Shane Collins at ARCAM located in Sweden, while the annealed and HIPped blocks and cylinders were sent from Ulf Ackelid from ARCAM at Sweden. The body-removed implant utilized for this project was provided by Dr. S. W. Stafford from The University of Texas at El Paso.

## **CHAPTER 3**

### **METHODOLOGY**

#### **3.1 EBM**

The EBM system schematic is shown in Figure 3.1 corresponds to an ARCAM A2. There are two different and available EBM systems as provided by ARCAM. ARCAM A1 system has been designed by specialists for implant manufacturing while the ARCAM A2 system has been designed for the aerospace and defense industries since the building chamber can be interchanged to choose between wide and tall. Another system mentioned and utilized for this project is the S12 system which basically is the first version of the A1 system, and the same material quality is expected from both systems.

In general, the EBM machine has an operation system similar to an optical or electron beam welding system. It utilizes a current of  $\sim 10\text{A}$  (DC) that drives a tungsten filament in the electron gun operating at an anode potential of 60 kV, shown by number 1. A set of electromagnetic lenses are used to focus the electron beam along with the aid of scanning coils, appreciated in number 2 and 3. Number 4 shows two powder cassettes located at each side of the system that gravity-feed the building table of Co-Cr-Mo powder that is being raked (5) providing a uniform layer of approximately  $100\mu\text{m}$  in thickness to create the designed component into a solid form in the building chamber at number 6. Number 7 shows the building table that goes down 1mm at a time to provide the sequential layer requirement to finish the build component originally designed. The build chamber works under a vacuum of  $\sim 10^{-4}$  Torr and normal building utilizes a helium gas bleed at  $\sim 10^{-2}$  Torr to facilitate build cooling and thermal stability. The melt scan is driven by a three dimensional (3D) computer aided design (CAD) program melting only the desired portions in the powder layer (Murr, et al. 2009b; Murr, et al. 2009c). The maximum built

size is 200x200x330 mm, meaning that it can accommodate building components up to  $\sim 0.2 \text{ m}^3$  (Arcam A2, 2011).

Along with the EBM system there is a powder recovery system that enables 95% powder recovery from build components that can be reused for subsequent building after sifting the powder obtained to utilize powders only in the proper range size. Pressured air is blown to recently fabricated components in a closed chamber in order to obtain loose and unmelted powder attached to the build component. The air used for this system is compressed at a pressure of 500 kPa and it is filtered to remove moisture and oil traces (Ulf, 2011).

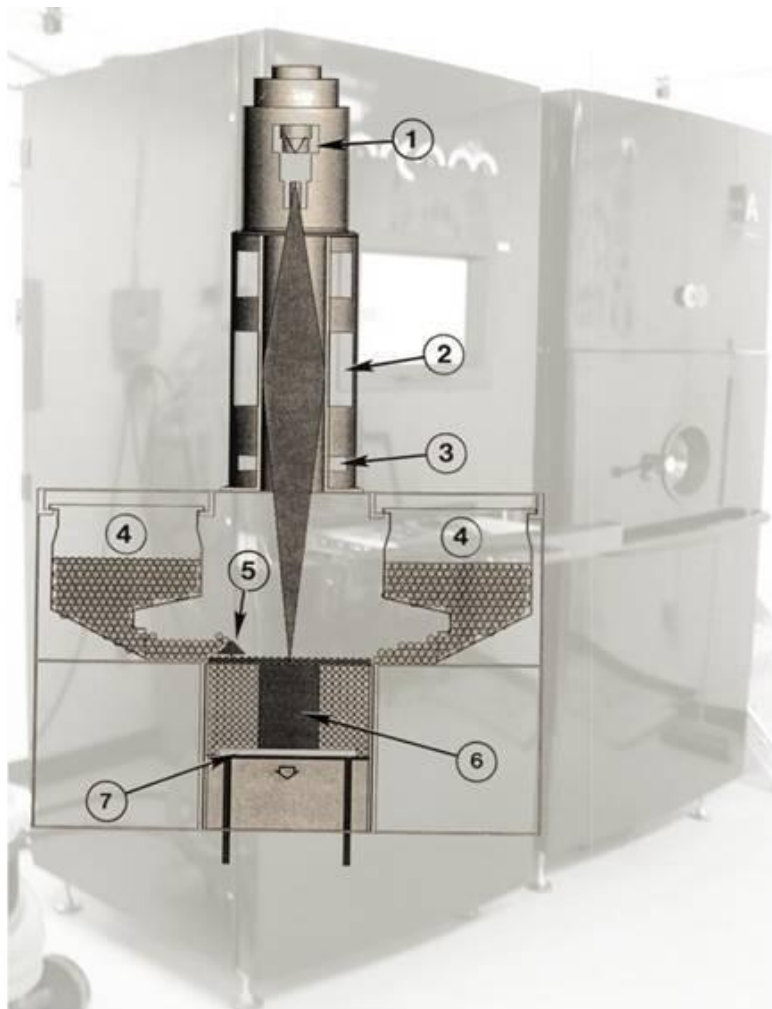


**Figure 2.4.1.1 Schematic of Electron Beam Melting (a) and Co-Cr-Mo powder particles (b).**

## 3.2 OPTICAL METALLOGRAPHY

Optical metallography was performed on the horizontal and vertical planes layer-built samples by EBM. The horizontal plane is perpendicular to the EBM build direction while the vertical plane is parallel to the same. Sample preparation consisted in cutting the component and mounting the cut sample with the area to be examined facing down the mount, a mixture of powder and liquid Koldmount® was poured into a 3cm diameter mount and it solidified in 30 minutes. Proper grinding consists in placing the plane-to-be-examined in the standard 8-inch rotating wheels with a consecutive sequence of grinding paper, from coarsest to finest (80, 220, 320, 500, 800, 1000 and 1200), with a 90° rotation after each paper used; water running is used to avoid sample heating. After grinding, the sample was rinsed in water and then polished in a soft cloth with 1µm, 0.3µm and 0.03µm alumina and then rinsed in ethyl alcohol. Once the surfaces were mirror-like, with no visible scratches, they were ready to be etched.

Etchant solutions used were three different ones. For the as-fabricated samples a solution consisting of 12 parts of hydrofluoric acid (HF) and one part of hydrogen peroxide (H<sub>2</sub>O<sub>2</sub>) was used, the interesting part on this is that a 16 hour exposure was necessary to obtain a decent microstructure, when usually takes about 30 seconds. The annealed and polished-finish samples were attacked with two different etchant solution consisting of 100mL water, 10mL hydrochloric acid (HCl), 10mL nitric acid (HNO<sub>3</sub>) and 3 gr. of iron (III) chloride (FeCl<sub>3</sub>) with an exposure of approximately 5 minutes to obtain a grain boundary contrast. A different variation of an etchant used for electrolytic etching consists of 100ml H<sub>2</sub>O, 5ml HCl and 10g of FeCl<sub>3</sub> for 20 seconds at 8V, the other solution used for these components consists of 6 parts of HCL and 1 part of H<sub>2</sub>O<sub>2</sub> for a period of time of about 5 minutes. Samples were analyzed in a Reichert MEF4 A/M metallograph microscope and photographs were recorded using an AmScope Microscope MD600 digital camera.



### **3.3 HARDNESS AND TENSILE TESTING**

Vickers microindentation hardness testing was performed on samples analyzed by optical microscopy using a Shimadzu HMV-2000 microindentation tester. Rockwell C-scale hardness (HRC) with a load of 150kgf (1.5kN) was also performed on the horizontal and vertical planes of all the samples with the exception of the mesh component. Tensile testing was performed in an Instron 500R tensile machine at room temperature (20°C) to pull as-fabricated cylindrical components that were machined by David Brown to create tensile specimens, this components were pulled in the direction parallel to the building direction. As-fabricated tensile specimens pulled in the direction perpendicular to the building direction as well as components that had been under annealing and HIPing pulled in both directions were sent to Metals Technology, Inc., located in Northridge California for tensile testing. Scanning electron microscopy was used to analyze the fractured surfaces. From tensile testing, yield strength, ultimate tensile strength and percent elongation were obtained.

### **3.4 SCANNING ELECTRON AND TRANSMISSION ELECTRON MICROSCOPY**

A Hitachi S4800 field-emission SEM utilizing secondary electron imaging at a voltage of 20kV was used to analyze the fractured surfaces from the tensile testing, as well as the Co-Cr-Mo powder utilized for the electron beam melting system. Energy Dispersive X-ray Spectroscopy (EDAX) in the SEM was used to perform chemical analysis of the components. Samples in the vertical and the horizontal direction were prepared for TEM analysis. Sample preparation consisted in thinning the area of interest to a thickness less than 0.2mm and then punched into 3mm disks followed by electro-polishing of each sample. Electrojet polishing was performed using a Struers Tenupol-5 dual-jet unit using a solution consisting of 15% perchloric acid ( $\text{HClO}_4$ ) and 85% acetic acid at a temperature of

-10°C and using a voltage of 20V. Once successful samples were obtained, they were analyzed in a Hitachi H-9500 TEM at 300kV.

### **3.5 X-RAY DIFFRACTION**

Specimens from this project were analyzed in a D8 Discover XRD system by Bruker. Powder was deposited in a powder holder container consisting in an indented cylinder of ~2 cm in diameter and approximately 0.5 cm in height. Solid EBM manufactured components were also analyzed to find the chemical composition of the carbides obtained from the optical micrographs as well as the crystal structure and preferred orientation of the cobalt alloy. Solid specimens that were analyzed were accommodated so that the polished sides faced the beam path (obtained from metallography specimen preparation). Annealed samples and samples obtained from the body-removed implant were analyzed as well by XRD.

## CHAPTER 4

### RESULTS

#### 4.1 POWDER

Powder particles utilized for the ARCAM system were analyzed by SEM; Figure 4.1.1 is a low magnification image of the powder particles. A histogram was obtained finding an average powder size of  $\sim 40\text{ }\mu\text{m}$  and a bimodal distribution of the particles was obtained as can be observed from Figure 4.1.2. Consider the fact that both small and attached particles to larger particles and large particles were considered for the analysis, therefore obtaining a bimodal distribution. Figure 4.1.3 and 4.1.4 show defective powder particles due to the gas atomization process. From Figure 4.1.3 it can also be observed how small particles are attached to bigger particles. Figure 4.1.5 illustrates a magnified SEM view of the Co-Cr-Mo atomized precursor powder; powder particle morphology can be appreciated. In the same way, Figure 4.1.6 shows the cross section of a powder particle which was mounted in a resin solution material and then proper sample preparation was performed, grinding up to 1000 grid paper, polished with 1.0, 0.05, and  $0.03\text{ }\mu\text{m}$  alumina powder, and etched to reveal a unique solidification microstructure.

Figure 4.1.7 illustrates the characteristic XRD spectrum for the Co-Cr-Mo powder in Figure 4.1.1 to represent  $\text{Co}_{0.8}\text{Cr}_{0.2}$  hcp/hexagonal crystal structure with a P63/mmc space group, and lattice parameters  $a = 2.52\text{ }\text{\AA}$ ;  $c = 4.06\text{ }\text{\AA}$ . As it was expected, the powder particles had no evidence of carbides or intermetallic ordered compounds such as  $\text{Co}_3\text{Mo}$  (hcp) for incipient melting or slower solidification processes (Kilner, et al. 1982).

Only microindentation hardness was performed on the precursor Co-Cr-Mo powder. Vickers hardness was measured on powder's cross section that had previously polished and etched, as shown in Figure 4.1.6. The average obtained was 630 HV which corresponds to a value of 6.3GPa.

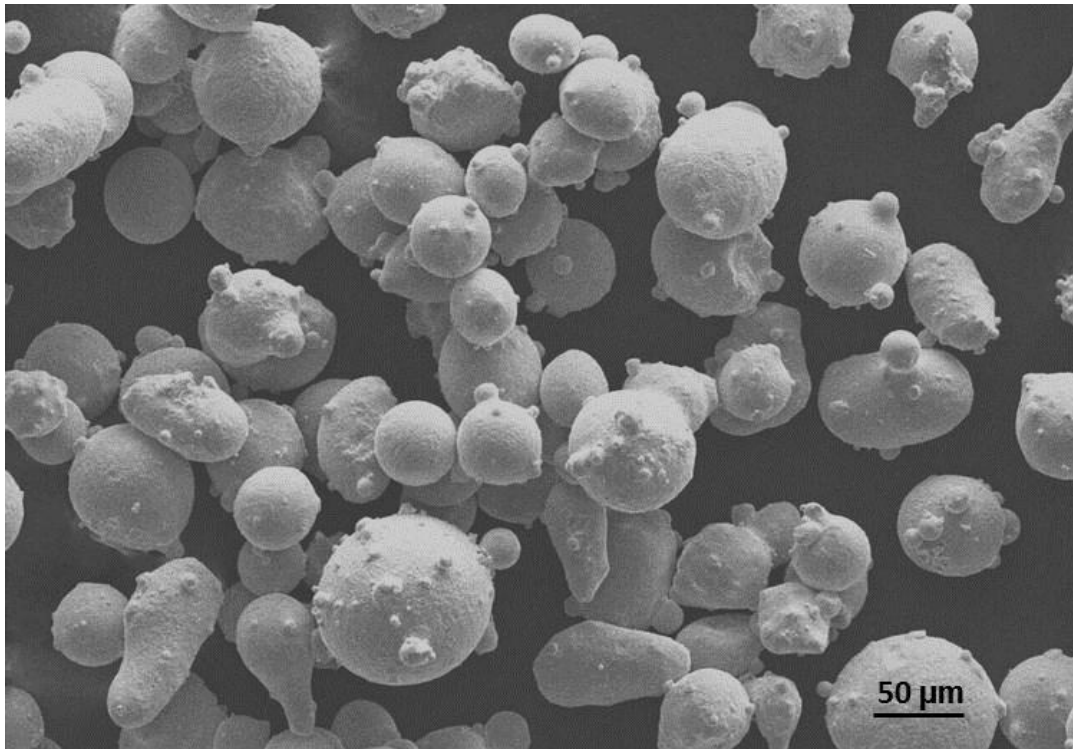


Figure 2.4.1.1 Low magnification SEM image of Co-Cr-Mo powder particles

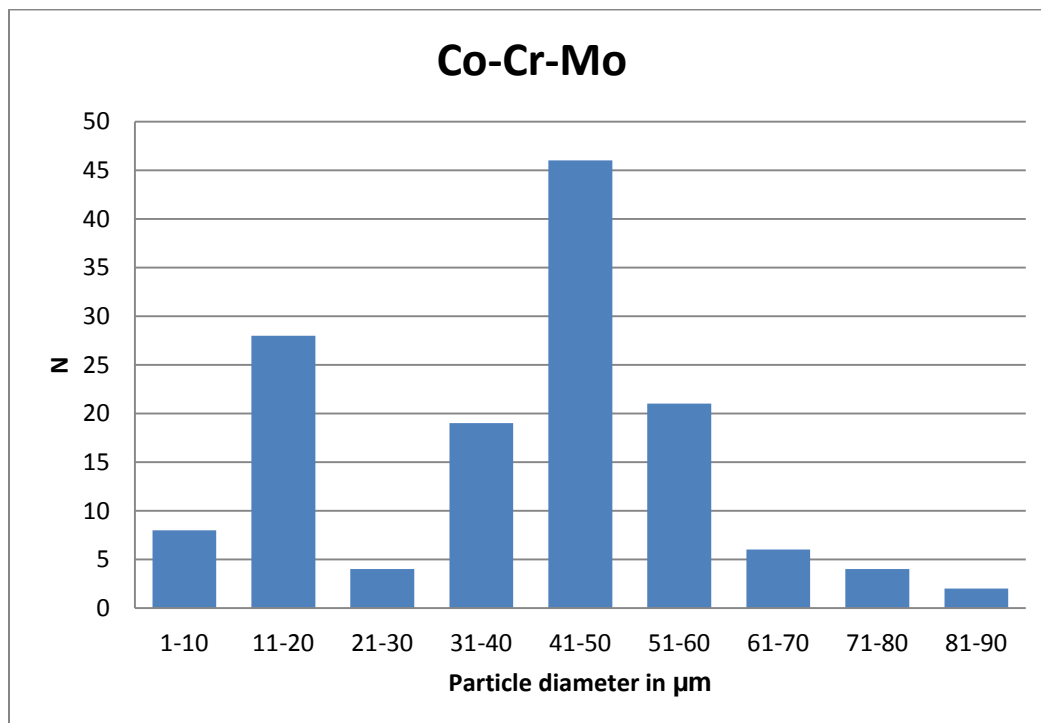
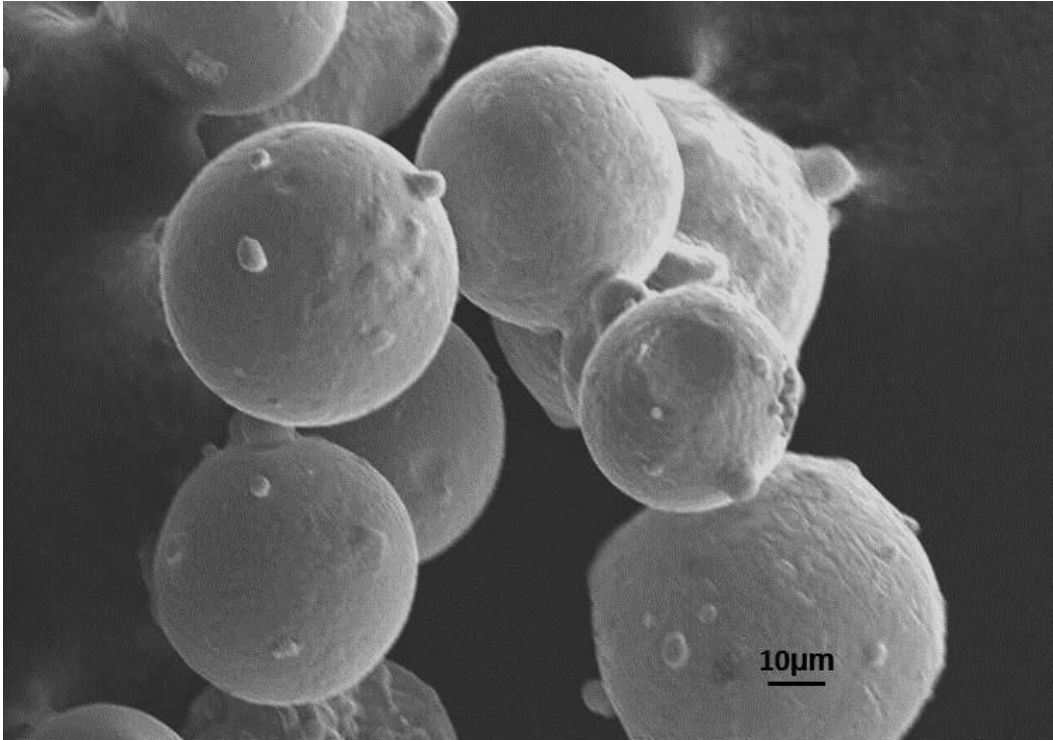
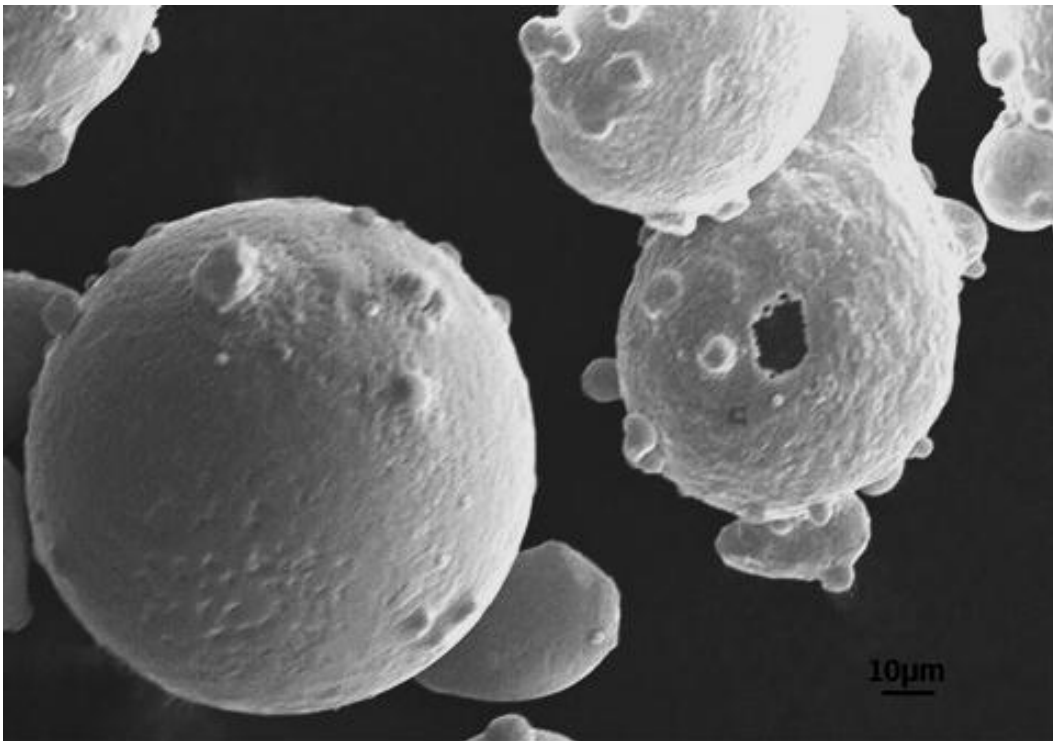


Figure 2.4.1.2 Powder particles histogram



**Figure 2.4.1.3 Higher magnification SEM image of smaller powder particles attached to big particles**



**Figure 2.4.1.4 Defect in powder particle obtained from the gas atomization process**

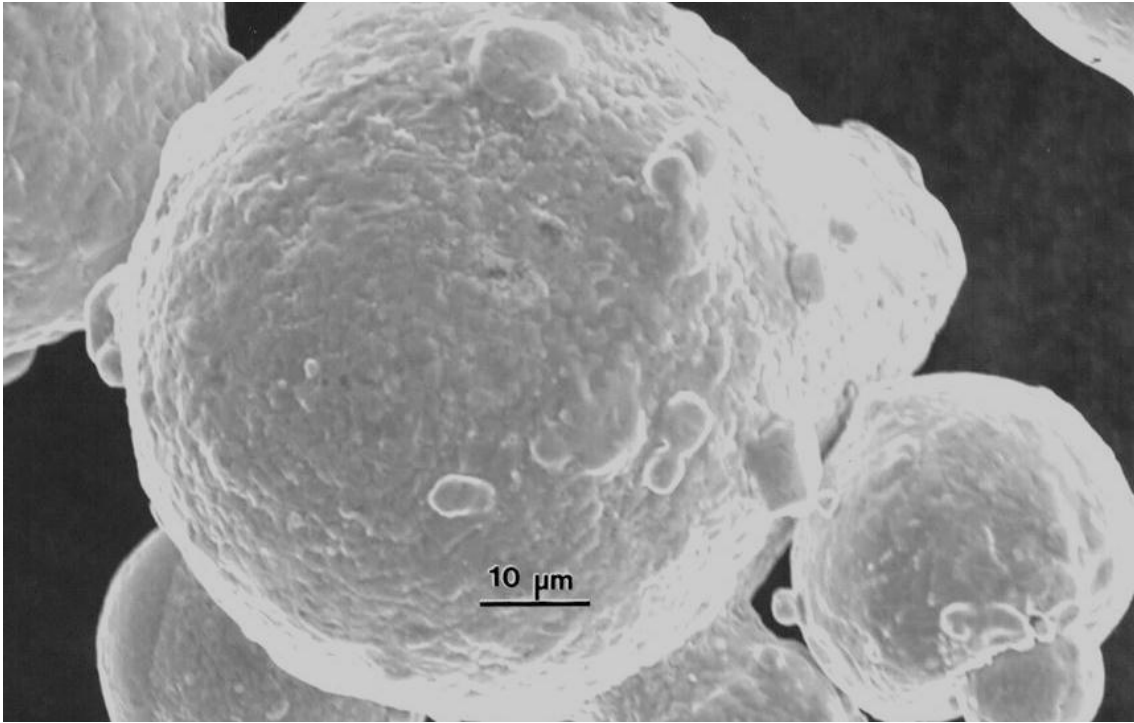


**Figure 2.4.1.5 High magnification of SEM micrograph showing powder particle tomography features**

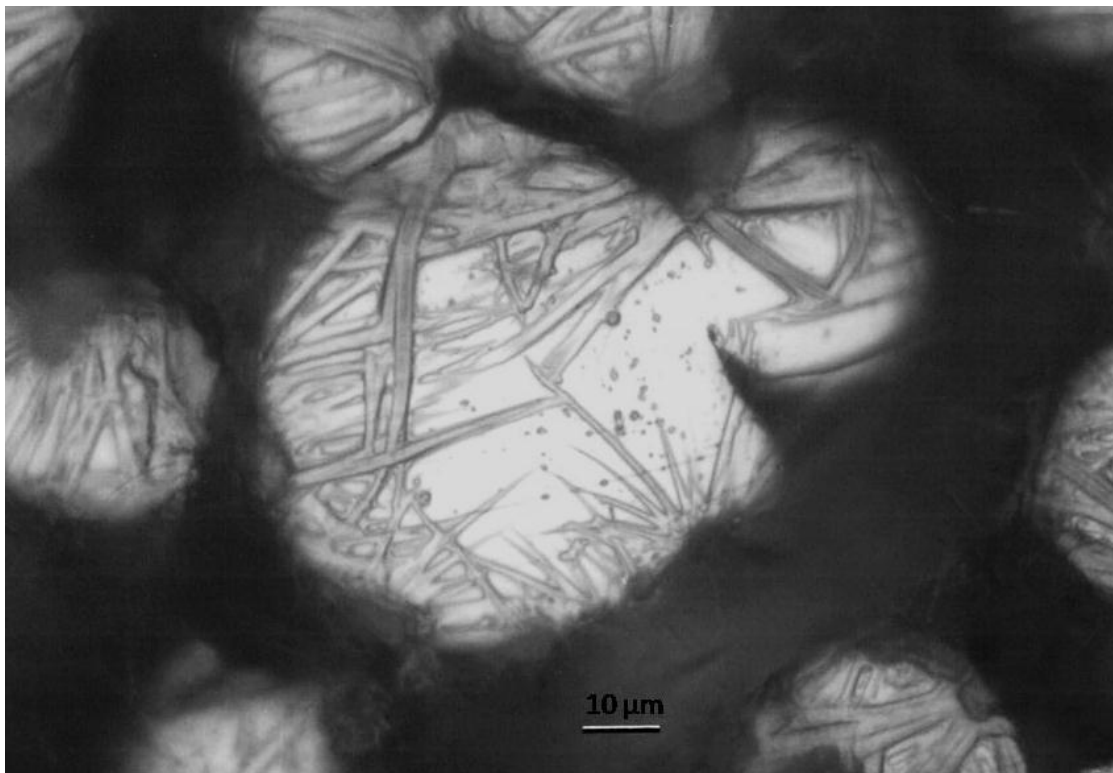


**Figure 2.4.1.6 Microstructural features of powder particles cross section**

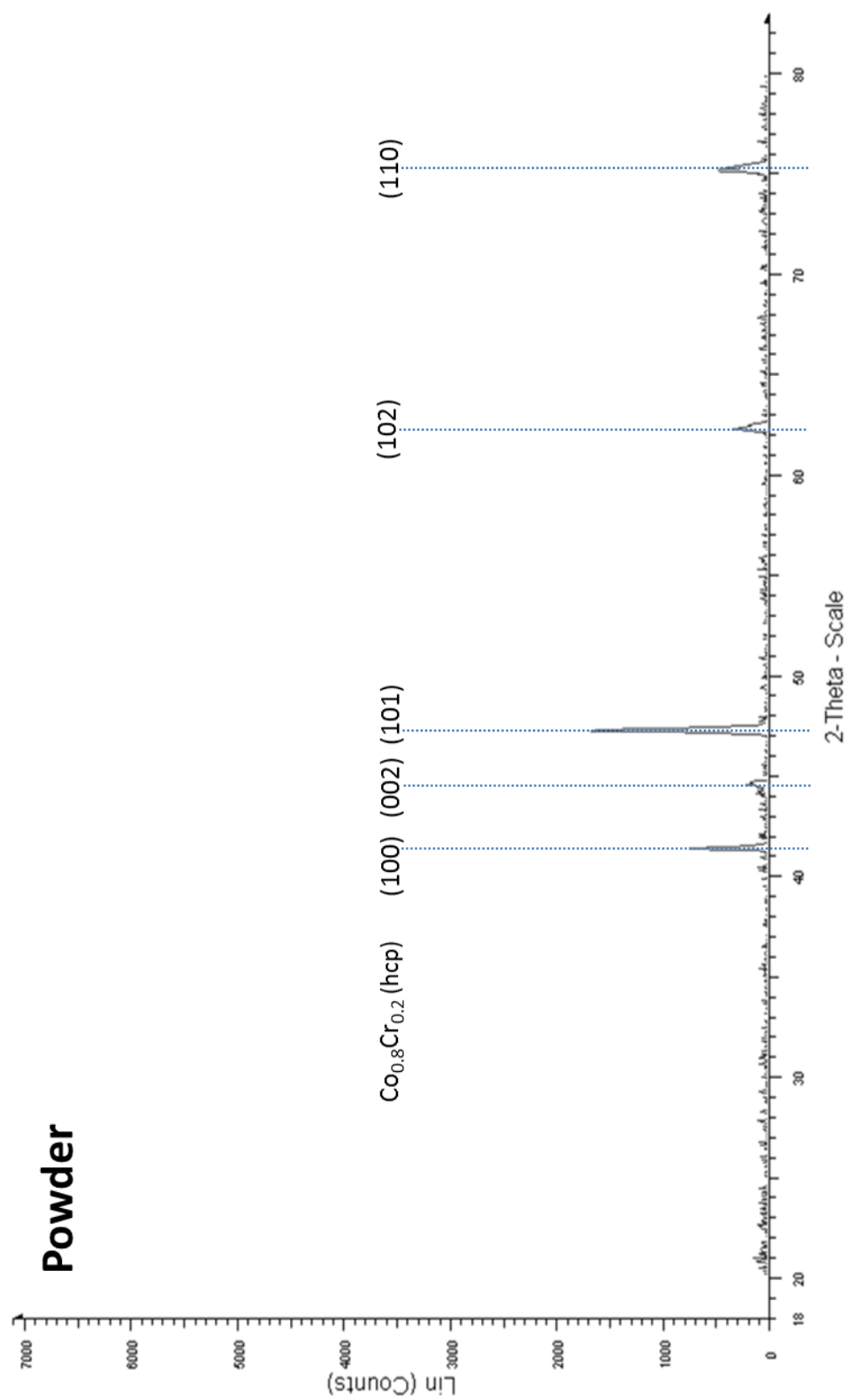


Figure 2.4.1.7 X-ray Diffraction of powder particles

## 4.2 AS-FABRICATED COMPONENTS

As-fabricated components refer to any shape fabricated by EBM that has not been treated after removal from the powder bed in the ARCAM system. By treated it is meant that they have not been under any type of heat treatment such as annealed, they have neither been HIPped, or even polished. These components have been analyzed this way in both vertical and horizontal directions for comparison purposes and they are divided into two different categories. The first one implies fully dense components referred to as “solid component” having an average density of  $\sim 8.4 \text{ g/cm}^3$ . The second category is for the mesh components which consist of lower density shapes due to the addition of open pores to create strong lightweight materials.

For this project, solid components consist of three different shapes as can be observed from Figure 4.2.1, where a) and b) show a block and cylindrical component and the arrow in between the two shapes represents the building direction, as stated previously. Figure 4.2.1 c) and d) show the same femoral knee component viewed from two different angles, the rectangle in figure d) shows the support material (enclosed in a rectangle) that is needed for certain shapes to avoid the sample from collapsing down when the melting process is occurring in the subsequent layers, the arrow indicates the building direction of the component, image on the left shows a radiograph illustrating knee implant. Support material, besides being used to obtain an optimum component shape, is designed so that it can be easily removed and minimum powder material is used for its building. In addition, minimum energy and beam scans are utilized in this support material that is also fabricated out of the Co-Cr-Mo powder.

Figure 4.2.2 shows a rectangular mesh component fabricated by the EBM system. It can be seen how the design of this prototype allows a porous inside where unmelted powder particles can be easily removed from the interior. Measured density for this component was  $\sim 1.5 \text{ g/cm}^3$ , in comparison with fully dense component ( $\sim 8.4 \text{ g/cm}^3$ ). It



should be mentioned that different pore sizes can be achieved by the EBM system allowing a wide range in densities for the components fabricated.

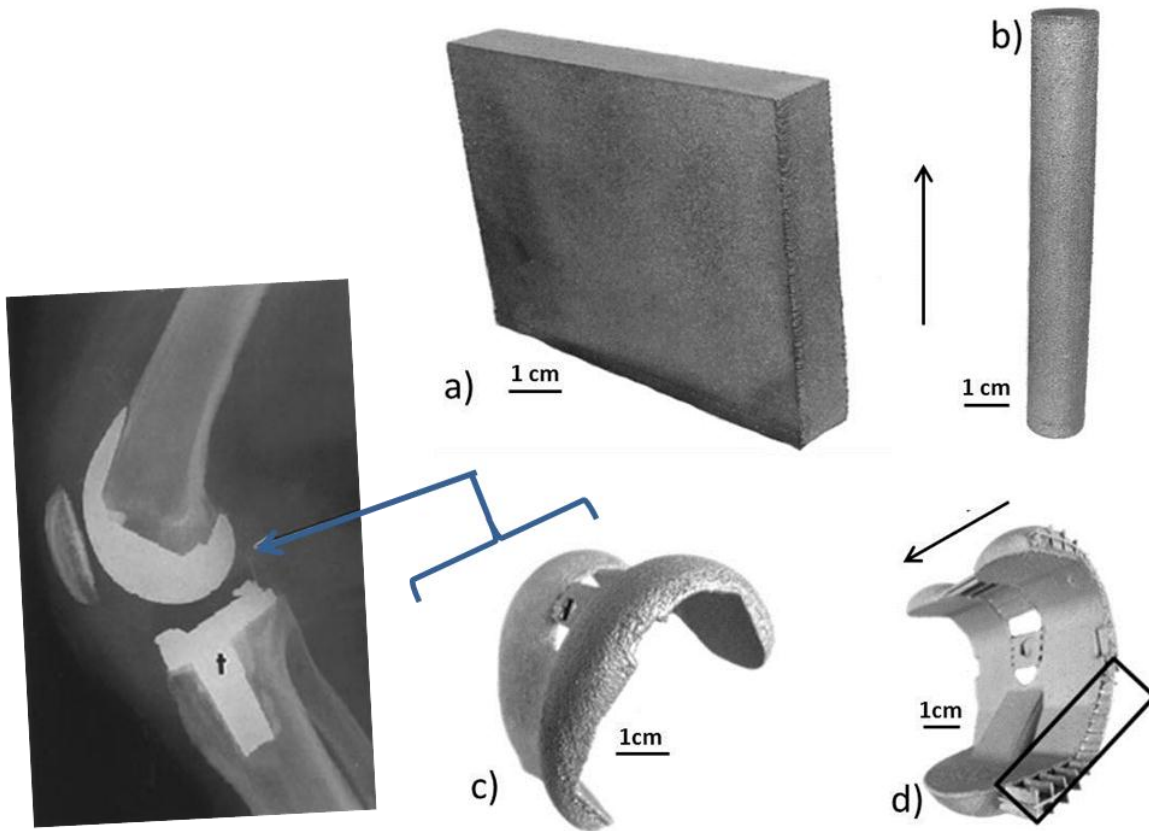


**Figure 2.4.1 Co-Cr-Mo as-fabricated solid components**

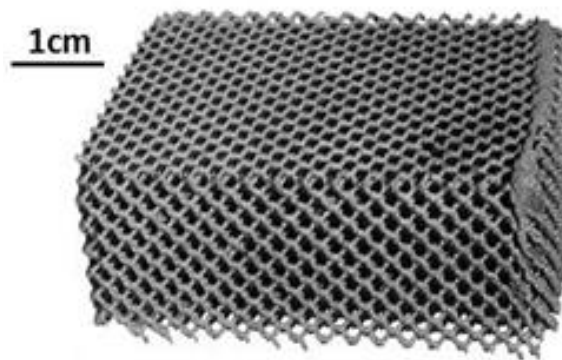


**Figure 4.2.1 Mesh component**

#### 4.2.1 SOLID COMPONENTS

Figure 4.2.1.1 shows the microstructure obtained from the block component. It is a three-dimensional representation of the component geometry illustrating two vertical planes and one horizontal. It can be observed how precipitates are arranged in a columnar fashion in the vertical plane and they have a unique arrangement in the horizontal plane. It can be stated that the beam heat is responsible for the precipitation obtained for this alloy since it is continually created throughout the whole sample and always in a columnar fashion for the vertical plane. This represents a unique, directional solidification microstructural architecture not obtained in any processing regime before.

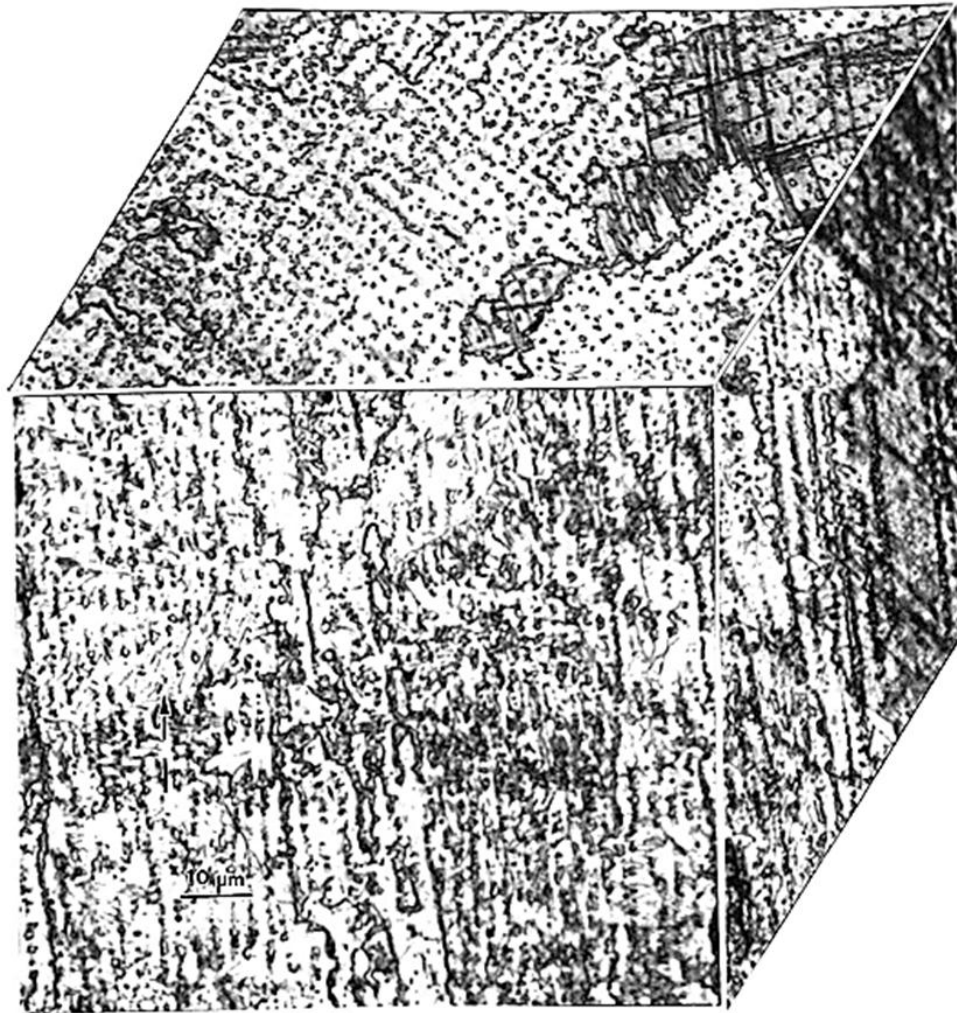


**Figure 4.2.1.1 Columnar architecture from block component**

Samples in both vertical and horizontal directions were prepared for transmission electron microscopy and the shape of the carbide precipitates can be observed from Figure 4.2.1.2 a) and b). Figure 4.2.1.2 a) shows a low TEM magnification while Figure 4.2.1.2 b) shows a higher magnification image. From both images it can be observed how precipitates are interacting with dislocations and stacking faults providing a higher hardness for the material. Again, the arrow in the figure indicates the building direction of the component.

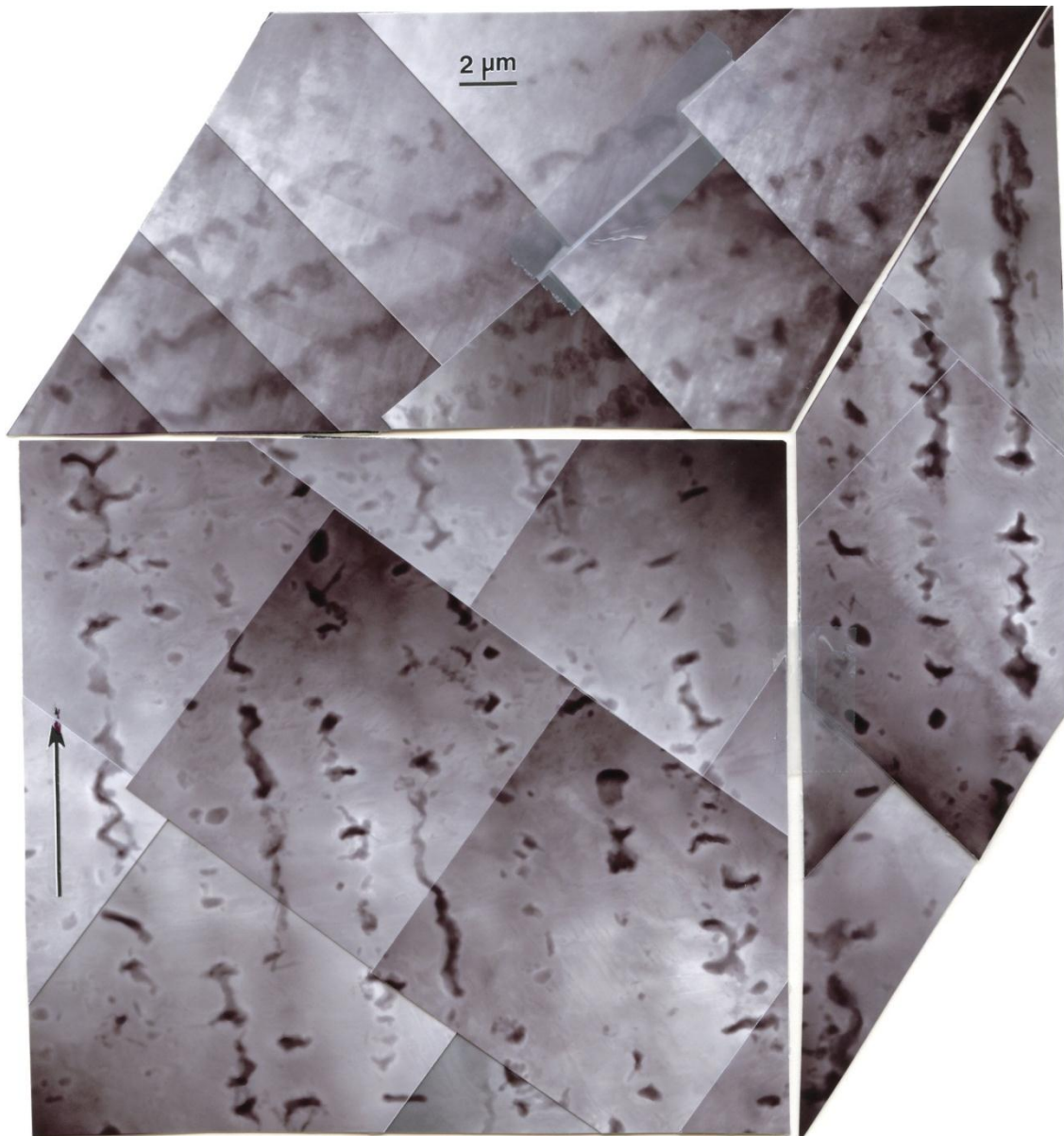
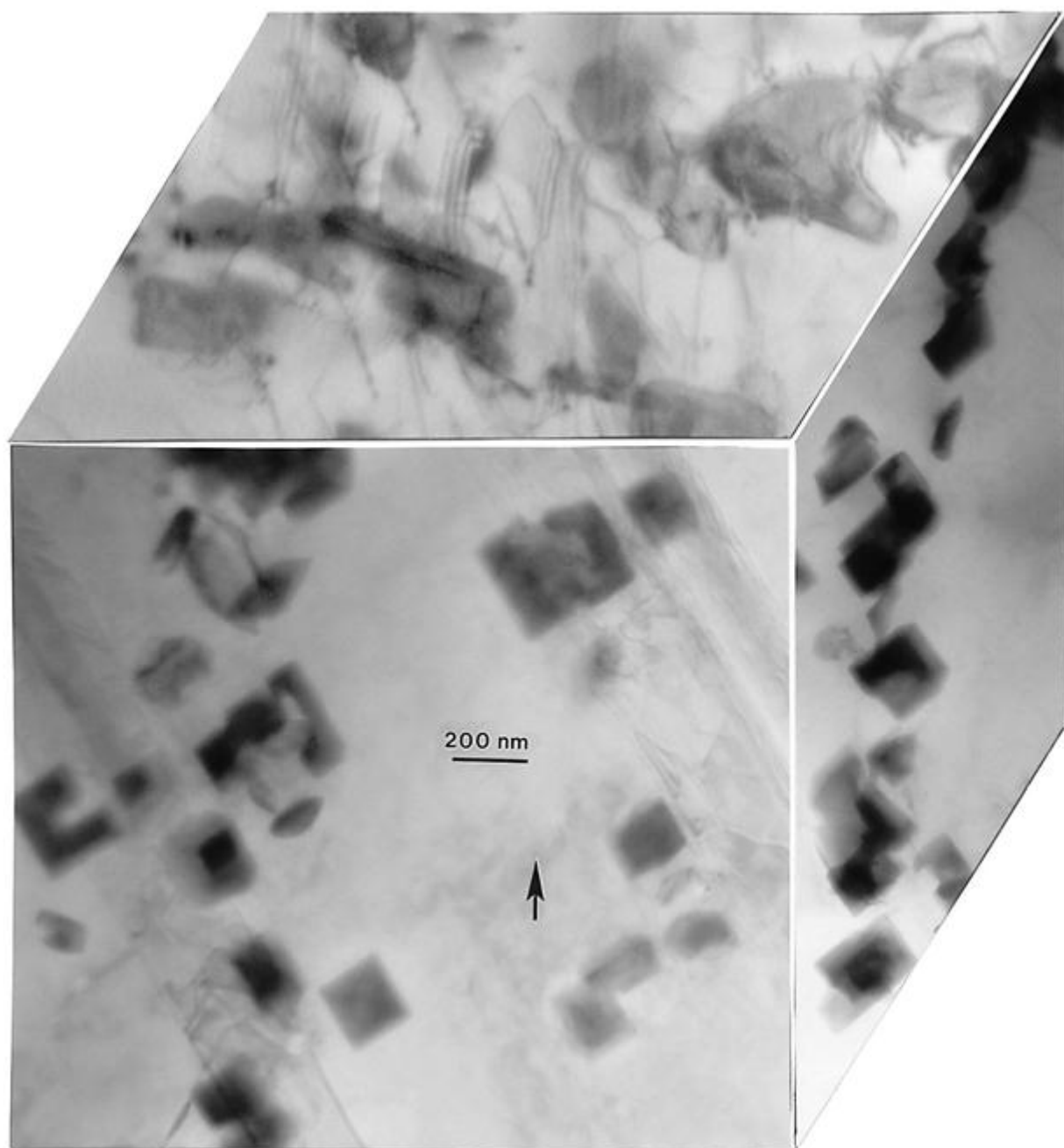
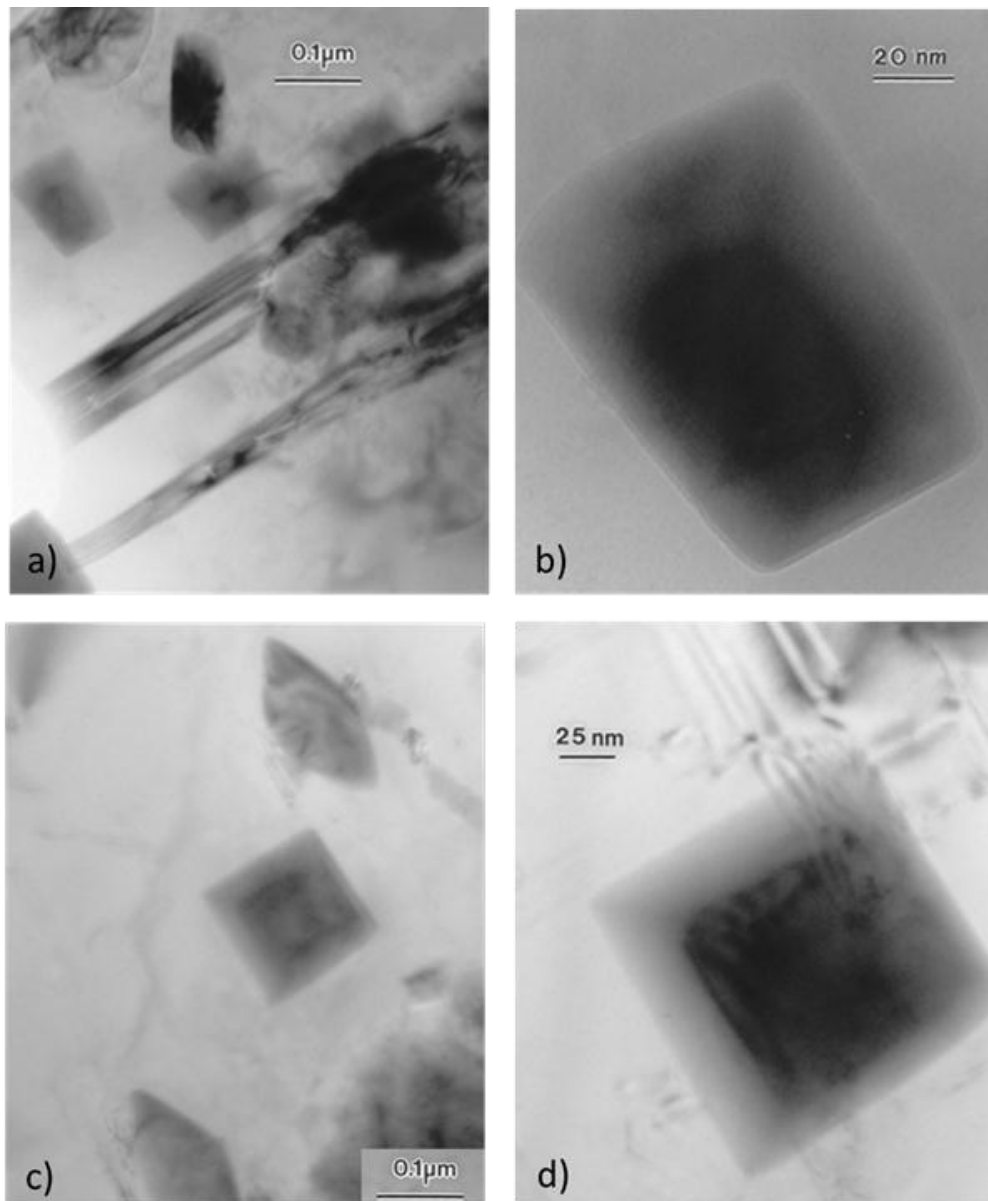


Figure 4.2.1.2 a). TEM image of block component.



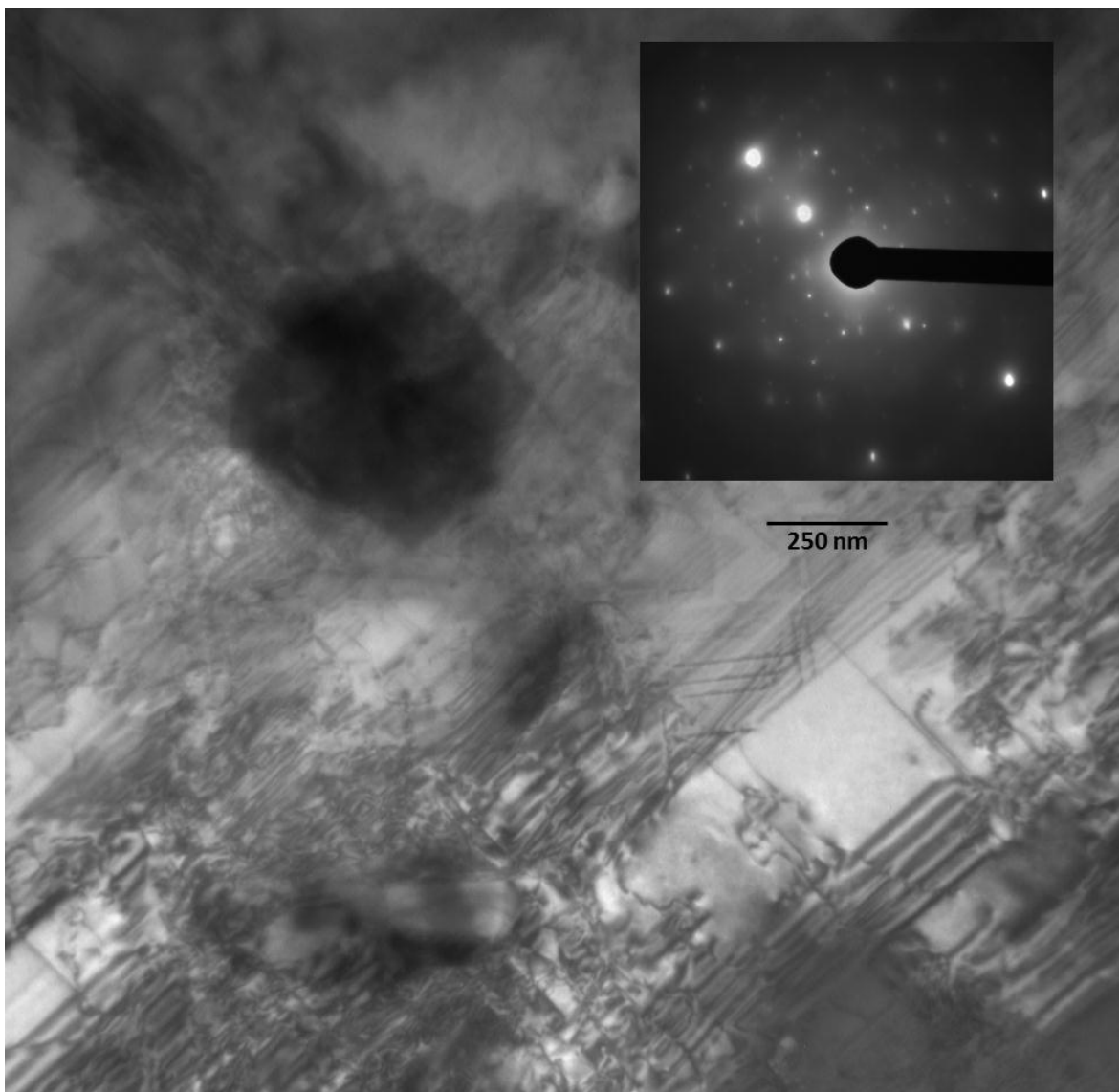
**Figure 4.2.1.2 b). TEM image of block component.**

Figure 4.2.1.3 shows TEM images of the precipitates as observed in the block component can be observed how individual precipitates show a cubic shape measuring about 100 to 200 nm on the side. Figure 4.2.1.3 b) and d) are the higher magnification of figures a) and c) respectively. In order to obtain the precipitate shape sample had to be tilted and consequently dislocations and stacking faults were no longer diffracting and visualization of the same was almost impossible.



**Figure 4.2.1.3  $\text{Cr}_{23}\text{C}_6$  precipitates observed in block component**

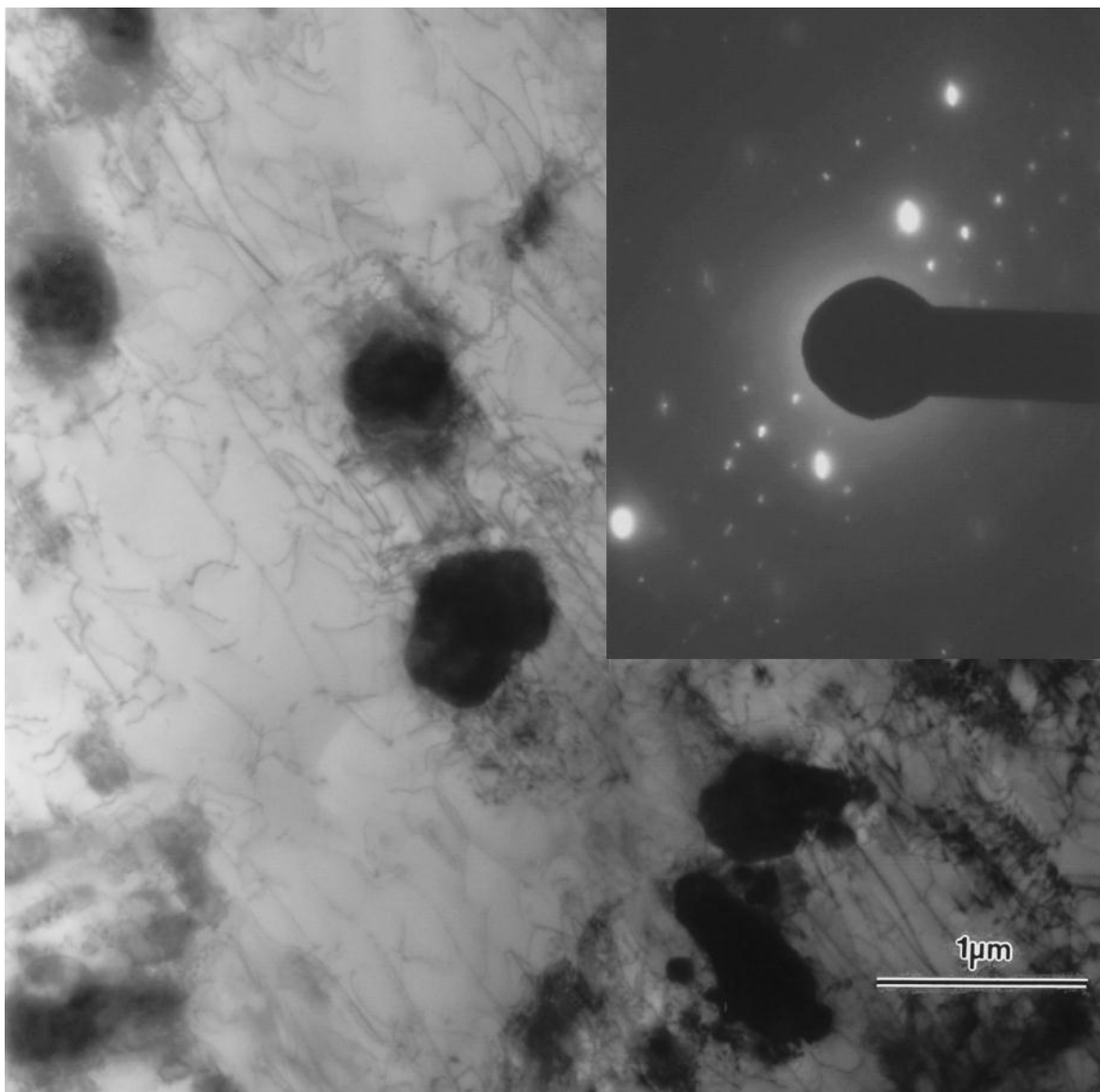
Even when we know that  $\text{Cr}_{23}\text{C}_6$  carbides are face centered cubic in structure and we already observed cubic precipitates present, that was not always the case. Images such as the one shown in figure 4.2.1.4 shows the selected area electron diffraction (SAED) pattern shows microtwins and double diffraction spots representing both the matrix and the precipitates along with some extra reflections characteristic of twin faults created by the EBM process. This SAED pattern is indicative of regions of overlapping intrinsic stacking faults on every  $\{111\}$  plane in the Co-rich fcc matrix ( $a=0.355\text{nm}$ ).



**Figure 4.2.1.4 Stacking faults in block component at 10kx.**

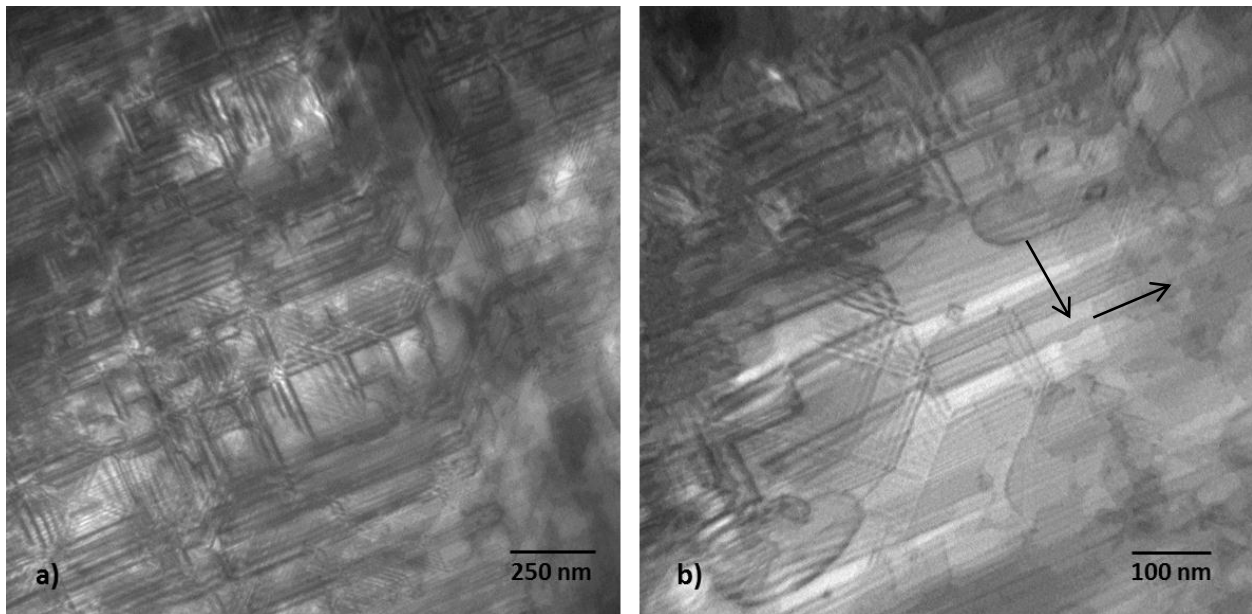


Figure 4.2.1.5 shows  $\text{Cr}_{23}\text{C}_6$  particles interacting with or generating dislocations. In addition, the SAED pattern insert shows  $[100]$   $\text{Cr}_{23}\text{C}_6$  zone axis superimposed on  $[112]$  fcc Co-rich matrix zone axis. Since  $\text{Cr}_{23}\text{C}_6$  lattice parameter  $a=10.66\text{\AA}$  and Co (fcc) has a lattice parameter of  $a=3.55\text{\AA}$ , from the diffraction pattern insert it can be observed how this corresponds to the two components mentioned before. The diffraction spot spacings for the matrix and carbide are therefore a factor of 3 different as noted in the SAED pattern insert in Fig. 4.2.1.5.



**Figure 4.2.1.5 Precipitates and dislocations interaction in as-fabricated EBM component.**

Figure 4.2.1.6 show two different areas obtained from the same sample from the horizontal plane in the block component, where figure 4.2.1.6 b) is at a higher magnification than figure a). Both images show examples of the dense intrinsic stacking-fault arrangements. From the SAED pattern of similar images it can be stated that dense stacking faults intersecting at  $90^\circ$  for faults on  $\{111\}$  planes inclined  $\sim 55^\circ$  to the  $(100)$  surface plane, and in the  $\langle 022 \rangle$  trace directions as shown by the arrows.



**Figure 4.2.1.6 Intersecting intrinsic stacking faults.**

An as-fabricated cylindrical component, shown in figure 4.2.1.7 was also analyzed in both vertical and horizontal directions. Microstructure similar to the block component was also found on the as-fabricated cylindrical component. A columnar array of precipitates was obtained in the vertical plane while a unique array of carbides was obtained in the horizontal plane as shown in the three-dimensional representation in Figure 4.2.1.7. It can be stated that grain boundaries of the component in any direction are the thick wavy lines as shown by the small arrows, while the vertical arrow represents the building direction. It



must be emphasized how this type of architectural microstructure (columnar rows of carbides) is new and not observed by any other processing or manufacturing technology.

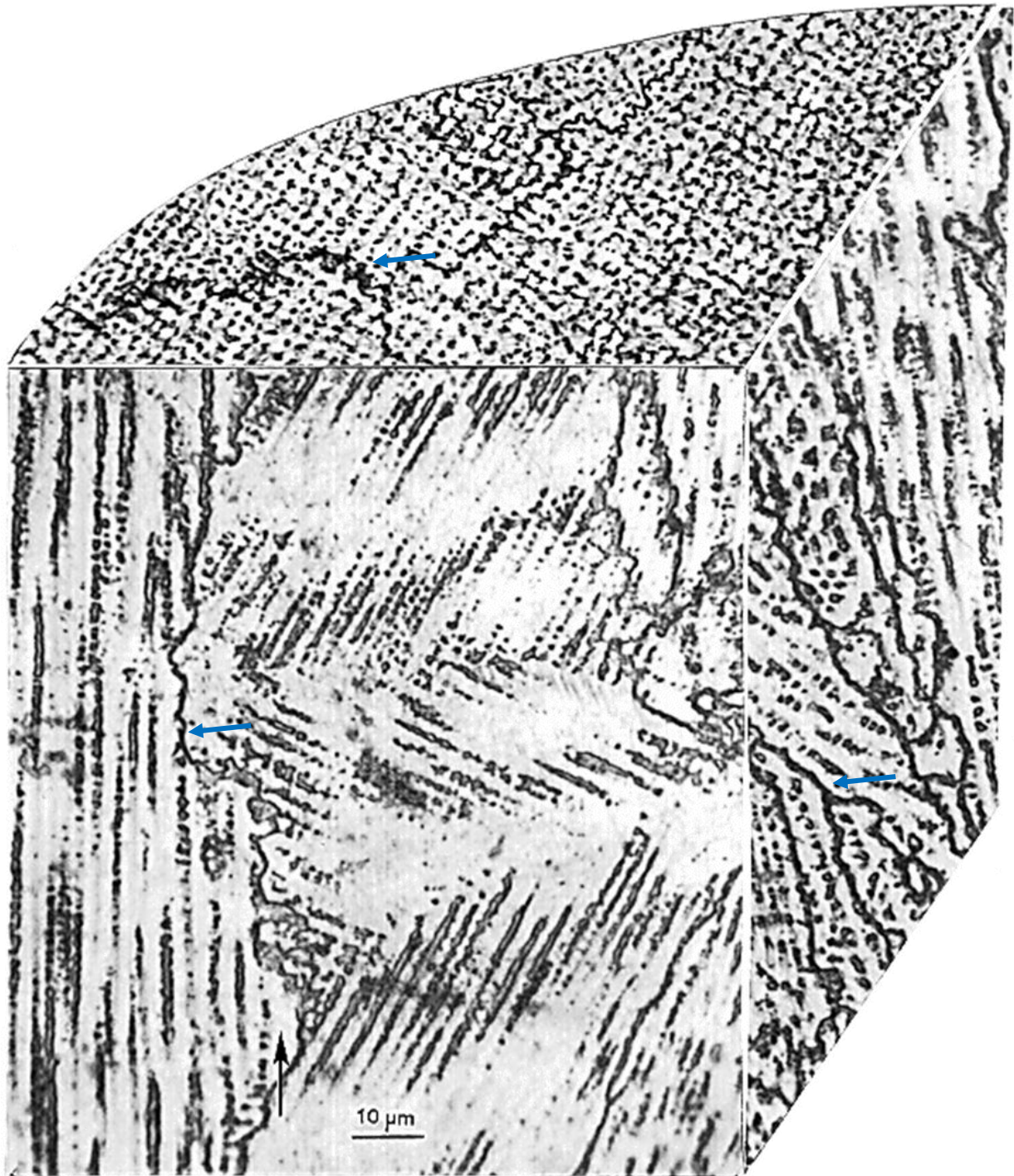


Figure 4.2.1.7 Microstructure obtained from cylindrical component

Figure 4.2.1.8 (bright field TEM image) shows irregular  $\text{Cr}_{23}\text{C}_6$  carbides, dislocations and stacking faults present in the horizontal plane of the cylindrical component. It can be observed from the SAED inserted at the right bottom of the image shows the fcc Co diffraction spots as the matrix including the (100) fcc  $\text{Cr}_{23}\text{C}_6$  diffraction spots. From images like Figure 4.2.1.8 can be stated that the  $\text{Cr}_{23}\text{C}_6$  carbides exhibit a variety of irregular microstructures.

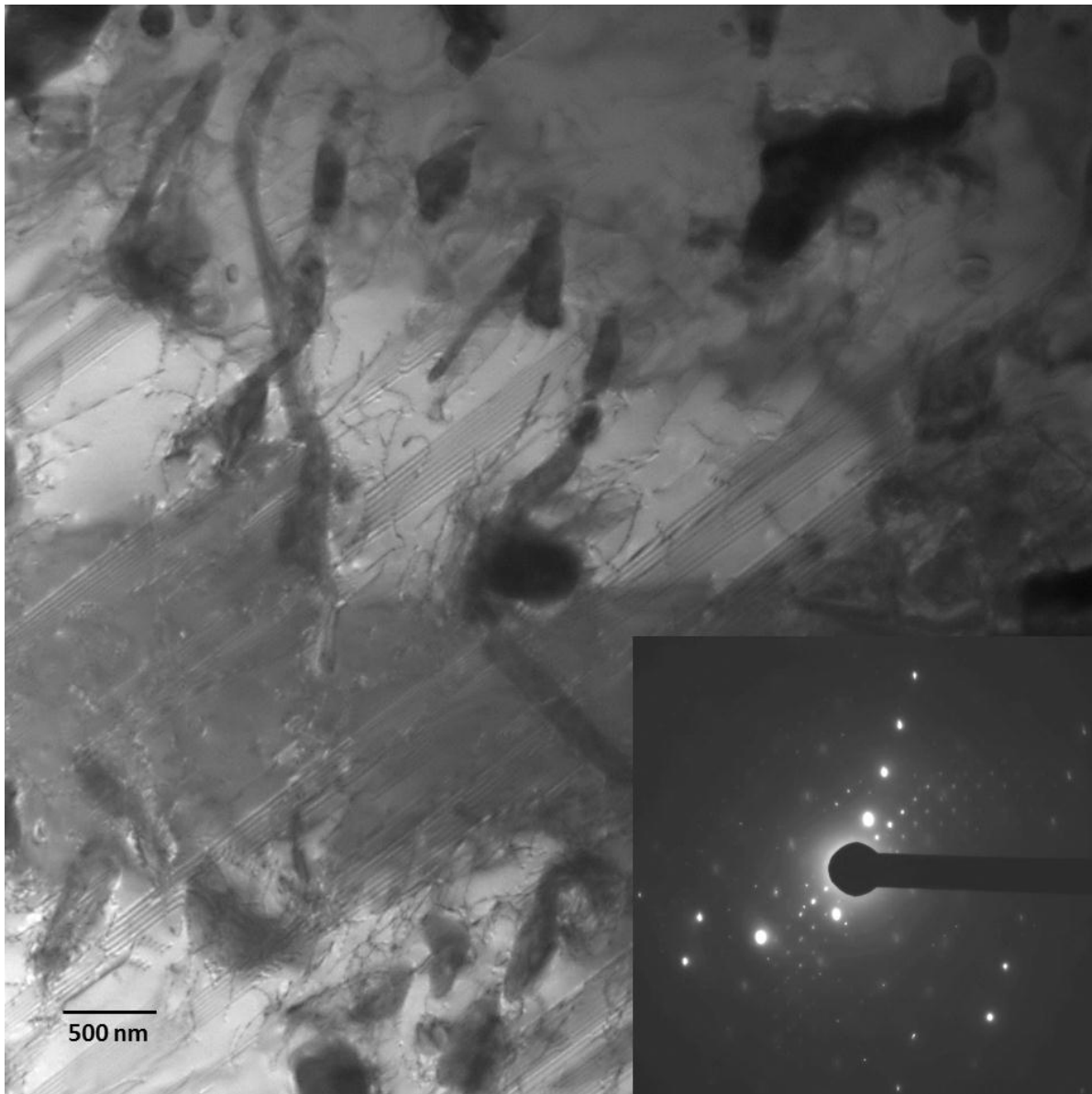
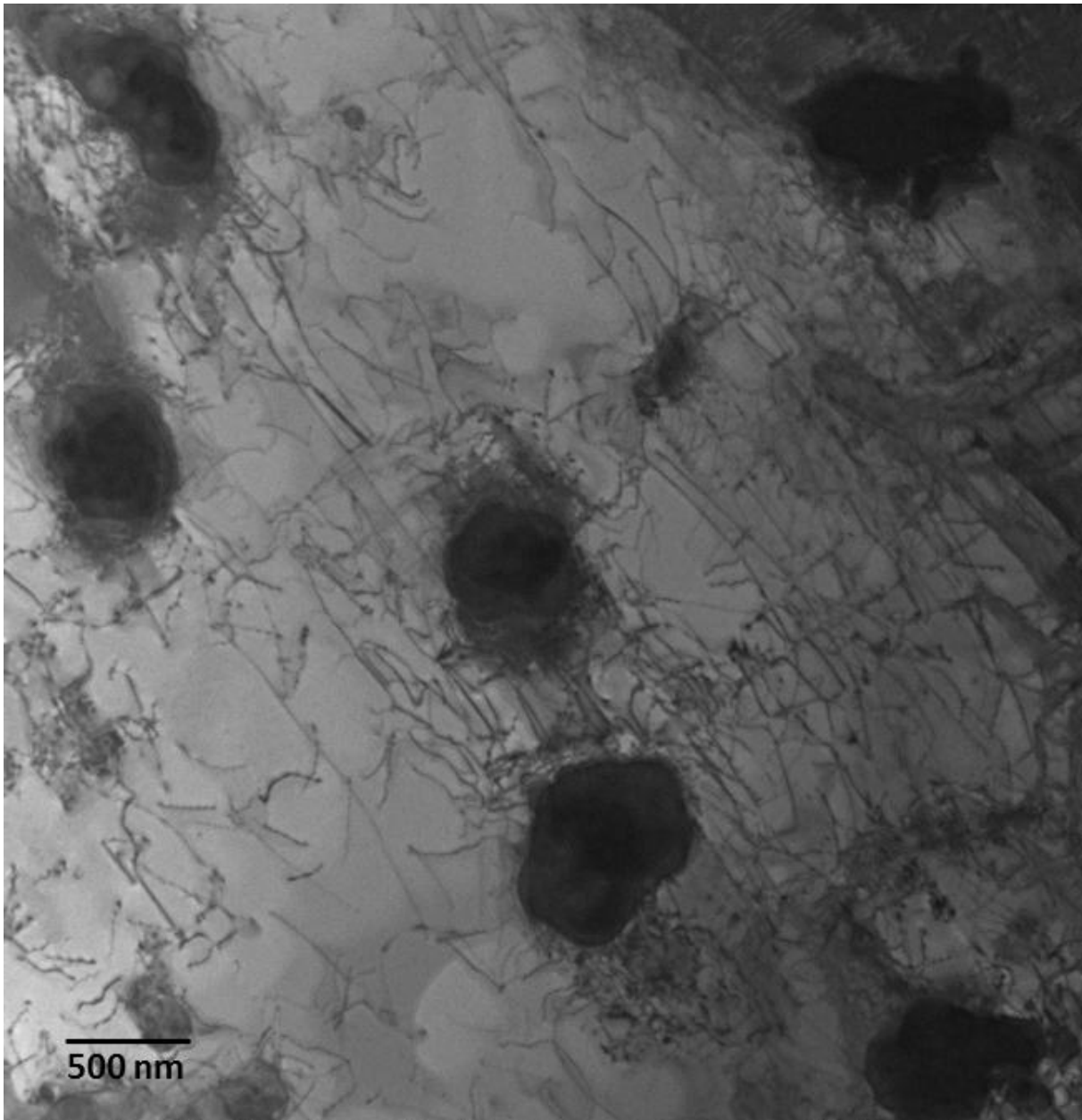


Figure 4.2.1.8 TEM image of cylindrical component at 4000x

Image 4.2.1.9 is an example of how dislocations are interacting with the matrix and precipitates in the as-fabricated cylindrical component. It can also be observed that precipitates are irregular in shape and interaction with the dislocations takes place. A dislocation density of  $3.6 \times 10^9/\text{cm}^2$  was obtained from this image.



**Figure 4.2.1.9 TEM image of as-fabricated cylinder showing a dislocation density of  $3.6 \times 10^9/\text{cm}^2$**

Figure 4.2.1.10 shows the same image at two different tilt angles to show how stacking faults and dislocations become visible at the right inclination. The difference in tilt for these two images is less than 20°. While figure a) only shows irregular precipitates in the presence of contour lines distributed throughout the matrix, figure b) shows dislocation interaction and stacking faults present in the same matrix once the sample was tilted.

Hardness testing in both the Vickers and Rockwell C scale were performed on the available EBM as-fabricated components. For the block component a Vickers hardness average value of 440 HV (4.4 GPa) was obtained for the horizontal plane while the cylindrical component average value for the horizontal plane was 455 HV (4.6 GPa). Vickers hardness for the vertical plane in the as-fabricated femoral knee component was measured to be 585 HV (5.9 GPa). Rockwell hardness measurements in the C-scale were measured to be 44 HRC for the horizontal plane in the block component while a value of 46 HRC was obtained for the vertical plane. The cylindrical component provided an average value of 47 HRC for the horizontal plane while the vertical plane provided an average value of 48 HRC. These represent relatively high hardness values and are consistent with some of the hardest commercially fabricated (wrought) products.

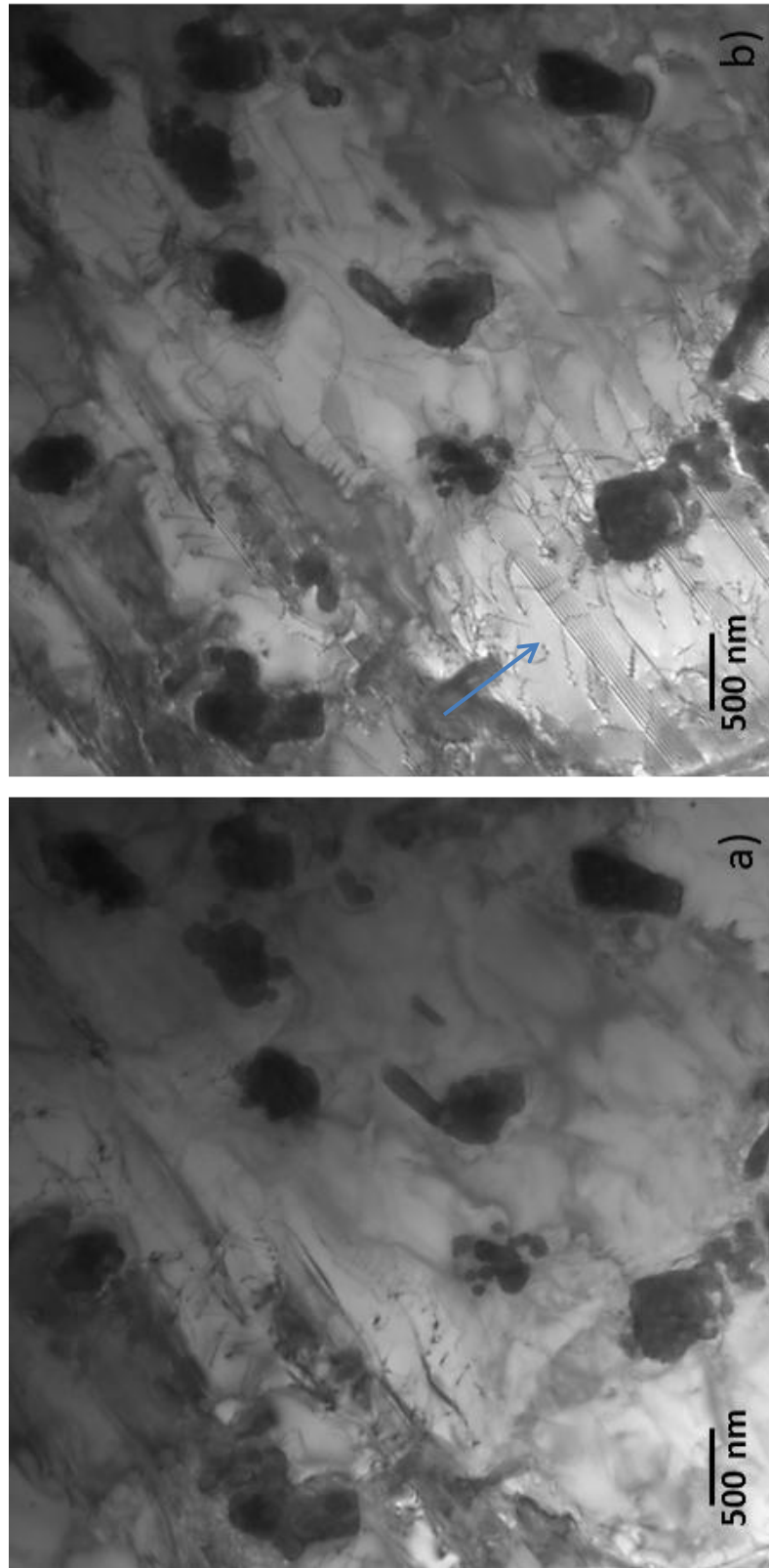


Figure 4.2.1.10 TEM images obtained from cylindrical component. a) and b) show same area with different tilt angle.



Tensile testing was possible by machining the cylindrical components into tensile specimens that were pulled in the direction parallel to the building direction. Tensile specimens were also obtained from the bottom part of the block component so that tensile specimens were pulled in a direction perpendicular to the building direction. The average yield stress obtained for the specimens pulled in the parallel direction was 0.51GPa, while the UTS obtained was 1.45GPa, with an average elongation of 3.6%. Specimens pulled in the direction perpendicular to the building direction provided an average of 0.77GPa for the yield stress, 0.84GPa for the UTS and a 2.7% elongation. The values for the perpendicular direction were higher as might be expected since the columnar array of precipitates is providing a higher strength to the alloy..

Figure 4.2.1.11 a) shows intergranular fracture representative of brittle fracture and from c) to d) a sequence of SEM images increasing in magnification obtained from the fracture surface of a cylindrical component pulled in a direction parallel to the building direction that showed an elongation of 5%. As magnification is increasing it can be observed how the dimple array is cubic in shape simulating the fcc  $\text{Cr}_{23}\text{C}_6$  precipitates and having sizes corresponding to the arrays of carbides ( $\sim 2\text{ }\mu\text{m}$ ). It is important to remember that percent elongation for these samples ranged from 1 to less than 5%, and no necking was observed in the sample. Even when dimple arrays were observed in the sample it can be stated that Co-Cr-Mo alloy as-fabricated by EBM with no post-treatments can be considered a strong and brittle material. Figure 4.2.1.12 shows intergranular fracture from the same as-fabricated tensile specimen sample representative of brittle fracture.

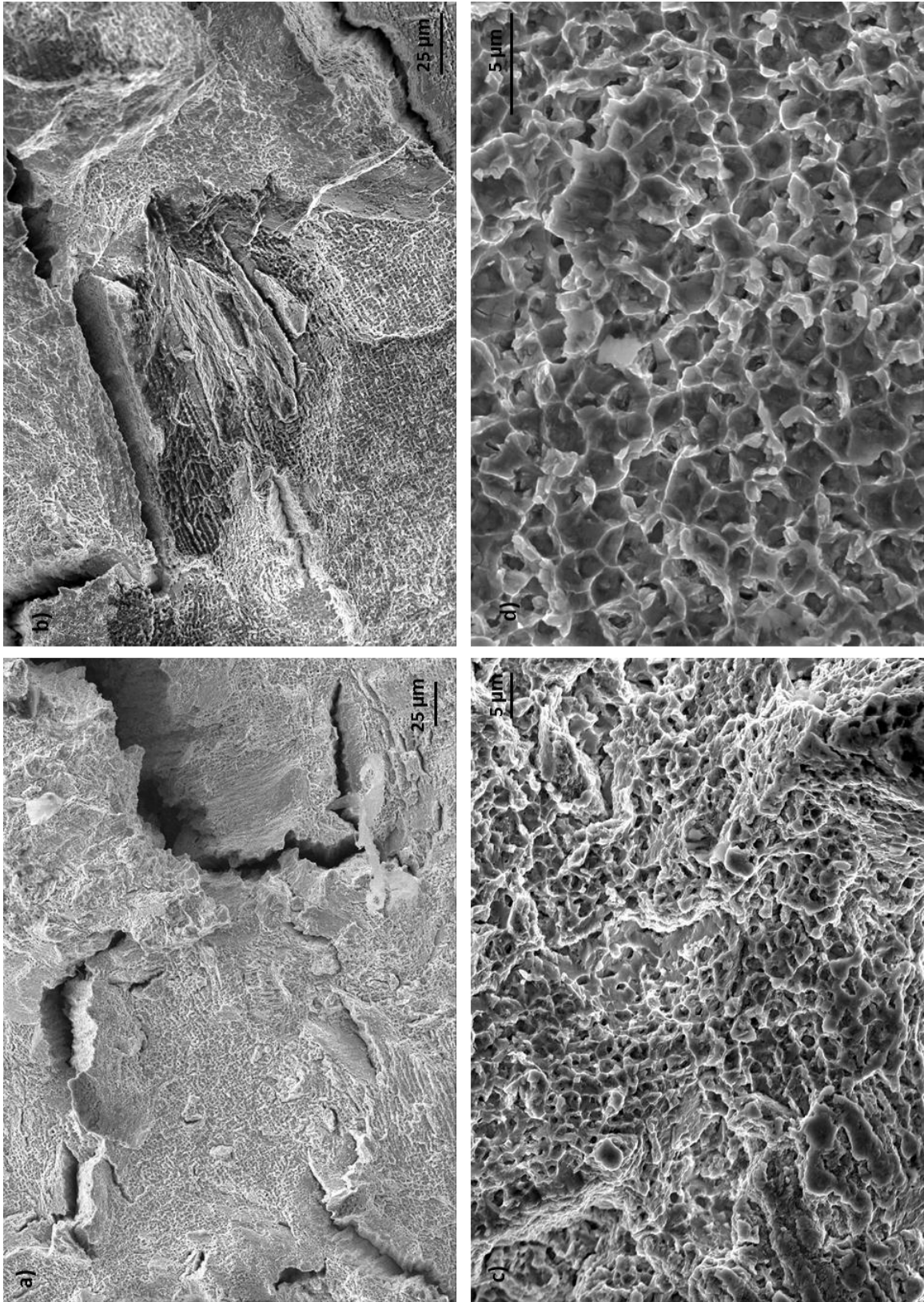
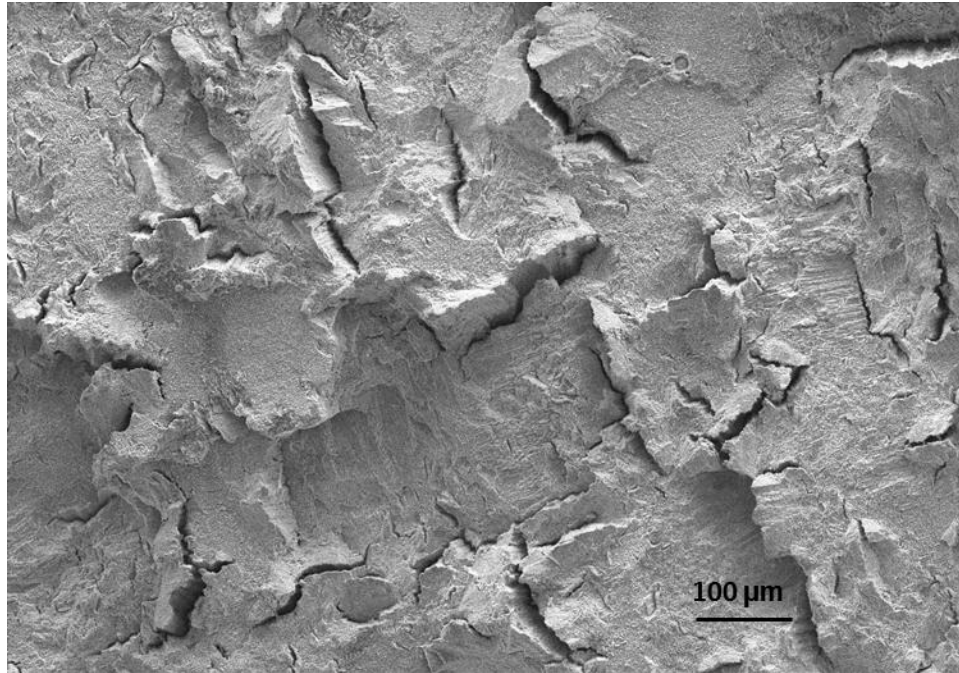


Figure 4.2.1.11 SEM images obtained from fractured end of tensile specimen failed at 5% elongation



**Figure 4.2.1.12 Intergranular fracture from sample elongated 5%**

Figure 4.2.1.13 shows a similar microstructure obtained from the as-fabricated femoral knee component shown in figure 4.2.1 c) and d). The arrow illustrates the building direction of the component. It can be appreciated how grain boundaries are enclosing different directions of the precipitate arrays in a somewhat elongated fashion. The difference in columnar structures can be due to the difference in thickness of the block and cylindrical components, providing a faster cooling rate for thicker components. Figure 4.2.1.14 shows an image from the as-fabricated femoral knee component in the horizontal plane. Both images were etched with a solution consisting of 100 ml H<sub>2</sub>O, 50 ml HCl, 10 ml HNO<sub>3</sub> and 10 gr FeCl<sub>3</sub>, using 8V for 8 s.

Tensile testing was not possible to perform on the as-fabricated femoral knee component since the shape of the same does not make it possible to obtain proper tensile specimens. Even though, it can be stated that thinner EBM components are harder than thicker components since the cooling rate is higher.



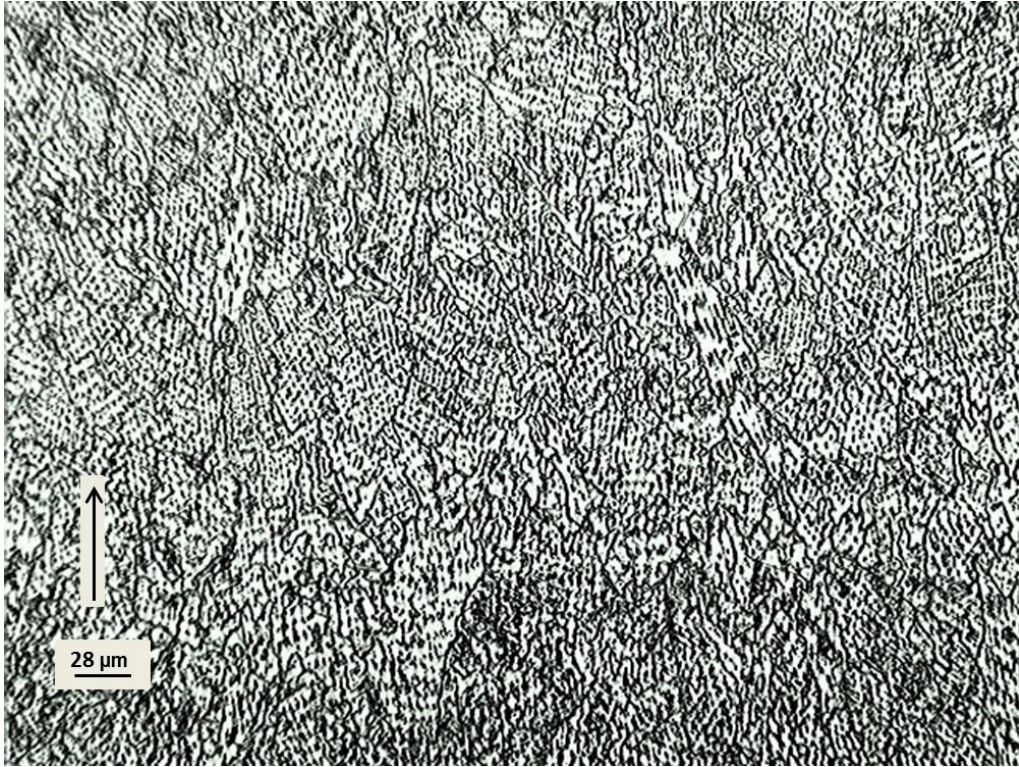


**Figure 4.2.1.13 Microstructure from as-fabricated femoral knee component**

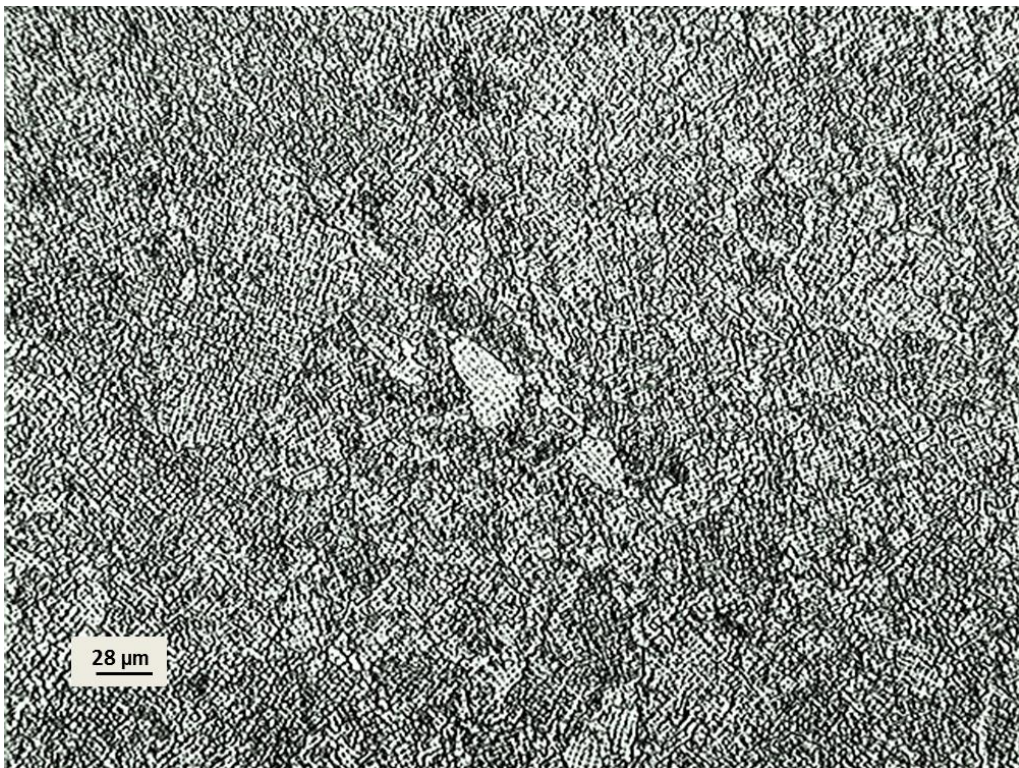


**Figure 4.2.1.14 Microstructure of femoral knee component**

Hardness values obtained for this component were higher than the other solid components. While block and solid components provided an average hardness of 4.4 and 4.6 GPa respectively, the as-fabricated femoral knee component provided an average hardness of 5.9 GPa, this value was obtained from performing microhardness in the Vickers scale (HV) and following the known equivalence of  $1\text{VHN} = 0.01\text{ GPa}$ .

Rockwell hardness C scale was also performed on this component providing an average value of 46 for the as-fabricated Co-Cr-Mo femoral knee component. Even though this a high value, the highest average value was obtained for the vertical plane of a solid cylinder with a hardness value of 48. Nonetheless, hardness values are higher than expected for EBM as-fabricated components and this is maybe due to the unique carbide array achieved by the system.

Corresponding XRD spectra for as-fabricated cylinder and block components in both vertical and horizontal directions as well as the vertical plane of the femoral knee component are shown in Figure 4.2.1.15. In contrast to the XRD powder spectrum, a variety of crystallographic and compositional phase mixtures, mostly hcp with a Co or  $\text{Co}_x\text{Mo}_y$  matrix. XRD data provided information to accurately state that the precipitates created by the EBM process belong to the  $\text{M}_{23}\text{C}_6$  family, more specifically  $\text{Cr}_{23}\text{C}_6$  which is fcc with a lattice of  $a=10.66\text{\AA}$  confirming SAED pattern identification. Other phases present in this spectra are Co (fcc:  $a=3.55$ ), Co (hcp:  $a=8.29$ ,  $c=10.54$ ),  $\text{Co}_{0.82}\text{Mo}_{0.18}$  ( $a=2.6$ ,  $c=4.21$ ),  $\text{Co}_{0.9}\text{Mo}_{0.1}$  (hcp:  $a=2.54$ ,  $c=4.11$ ) and  $\text{Co}_3\text{Mo}_1$  (hcp:  $a=5.12$ ,  $c=4.11$ ). It can be observed how different phases overlap providing insecurity as to which is the right component or how it is integrated into the overall structural composition and therefore each component has been added with the corresponding diffracting planes.



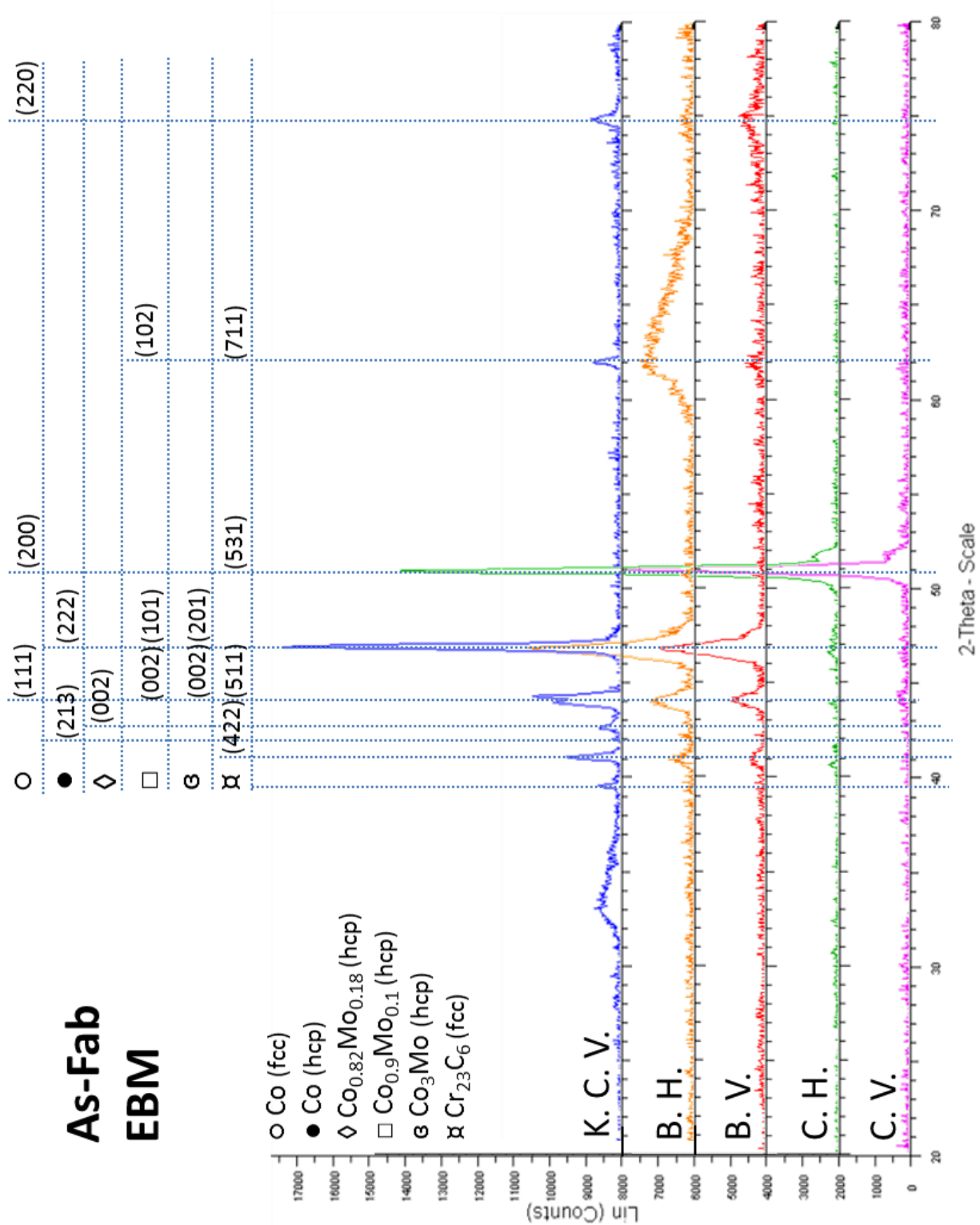


Figure 4.2.1.15 XRD spectra of as-fabricated components.

#### 4.2.2 MESH COMPONENT

Figure 4.2.2.1 is a low magnification SEM image obtained from a surface side from the mesh component shown in figure 4.2.2. It can be observed how each powder layer was melted in a layer by layer sequence as the building table went down approximately one millimeter each time. It can also be observed how powder particles are completely melted to create a strong lightweight component. The arrow shows an example of how partially melted powder particles get solidified and therefore attached to the component. In addition, it can be observed how pores are clean and free of unmelted powder particles, powder remaining inside the pores was removed by utilizing the powder recovery system.

Figure 4.2.2.2 was obtained from the cross section of the mesh component. A similar microstructure to the as-fabricated EBM components is obtained with the difference that precipitate columns and arrays are finer and smaller.

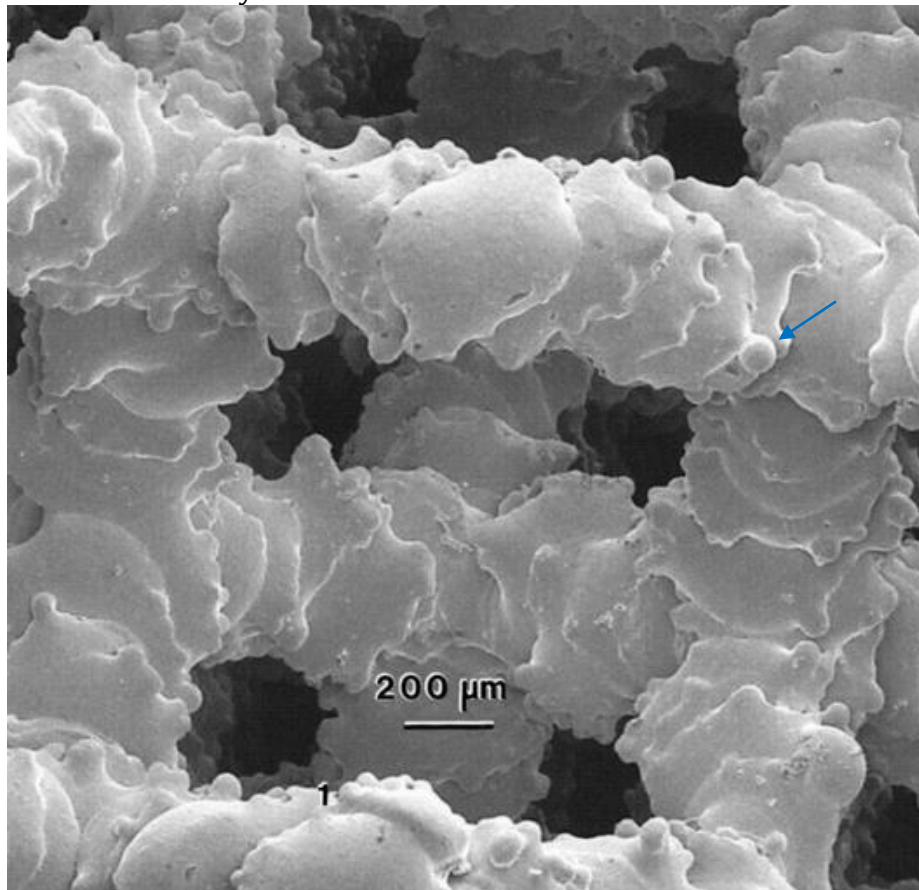
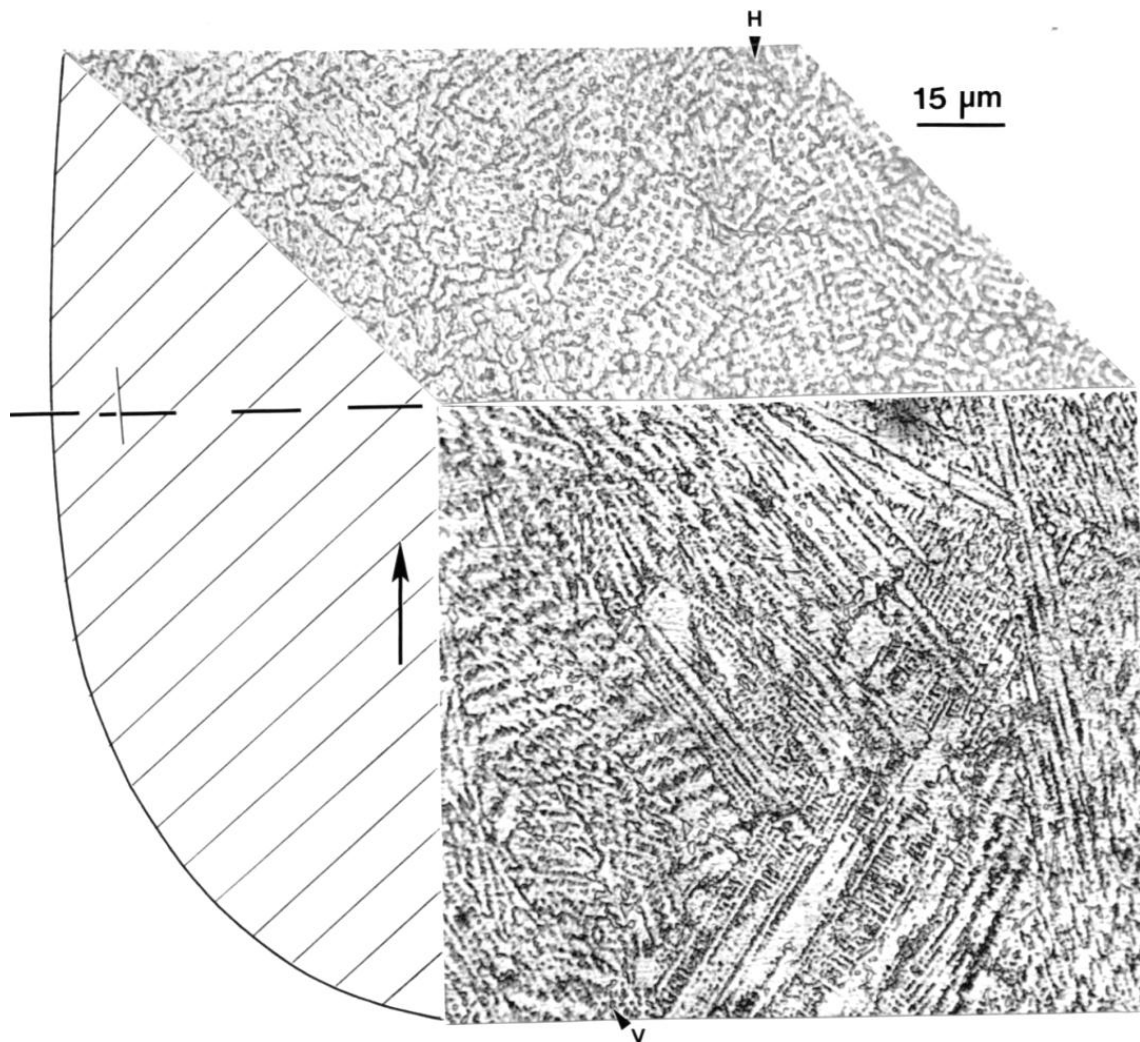


Figure 4.2.2.1. SEM image of mesh component surface

This can be due to the difference in solidification rate since the cooling for mesh components is faster than for thick solid components. Since mesh component wall thicknesses are less than  $\sim 1\text{mm}$  it was not possible to obtain 3mm in diameter specimens for TEM analysis. The same situation applies for Rockwell C scale hardness since it was not possible to perform these measurements because of the large indenter size and load. Therefore, only microhardness was tested in the mesh component, obtaining an average value of 6.8GPa for the horizontal plane and 5.6GPa for the vertical plane. These can be compared as and average of  $\sim 6.2\text{ GPa}$  in contrast to an average microindentation hardness of  $\sim 4.6\text{ GPa}$  for the solid components (block and cylinder)



**Figure 4.2.2.2. Microstructure obtained from Co-Cr-Mo mesh component**

### 4.3 HIPED AND ANNEALED COMPONENTS

The next type of components to be introduced have gone through post-treatment after EBM fabrication. Block and cylindrical samples were built in a single run in April 2008, from an R41 machine (inside series) which belongs to the S12 system and sent to UTEP in 2010 for analysis from Sweden. As mentioned before, the S12 system corresponds to the previous model of the Arcam A1 system, and the same quality of material is expected. Annealed and polished femoral knee component comes also from Sweden but no specifications were provided. Annealing and HIPing procedure was performed under ARCAM's specifications which consists in (as stated by ARCAM website), which also corresponds to ASTM F-75 standards:

- Hot Isostatic Pressing (HIP) in a shared cycle, with the following parameters: 1200°C at 1000 bar argon for 240 minutes.

- Homogenization (HOM) heat treatment, with the following parameters: 1220°C at 0.7-0.9 mbar argon for 240 minutes.

- As rapid quench rate as possible, from 1220°C to 760°C in 8 minutes maximum.

The purpose of this treatment is to dissolve carbides and improve the isotropy of the microstructure, reducing the brittleness of the as-built EBM material [ARCAM]. Annealing is performed to increase ductility of the material, and in the same way hardness will be reduced as well, facilitating forming or machining, and welding, it is also performed to relieve stresses after welding, to produce specific microstructures or to soften age-hardened structures by re-solution of second phases [Bradley et al.]

Samples with a post-treatment available for this project are blocks and cylinders of the same dimensions as the as-fabricated components. Analysis of the samples was performed at similar heights to avoid any data misrepresentation. Figure 4.3.1 shows a similar femoral knee component as the one analyzed as-fabricated by EBM. It has been

assumed that the building direction is the same for figure 4.2.1 c) and d). Figure 4.3.1 a) and b) shows the same component viewed from two different angles, this component has gone under ARCAM's specifications mentioned above and it can be observed that as a final step the sample has been rough polish as compared to the dull-powder-like appearance obtained from the EBM system as observed from figure 4.1.2 . From figure 4.3.1 b) it can be appreciated how mesh structure has been added to the inside of the component. The purpose of this addition is to allow for bone ingrowth into the mesh and therefore provide a better fixation. Figure 4.3.2 shows a magnified view of the section utilized for analysis. It can better be appreciated how the mesh structure only goes into the implant to a depth of  $\sim 0.3$  cm. From the same image it can also be appreciated how powder was melted to form the mesh.

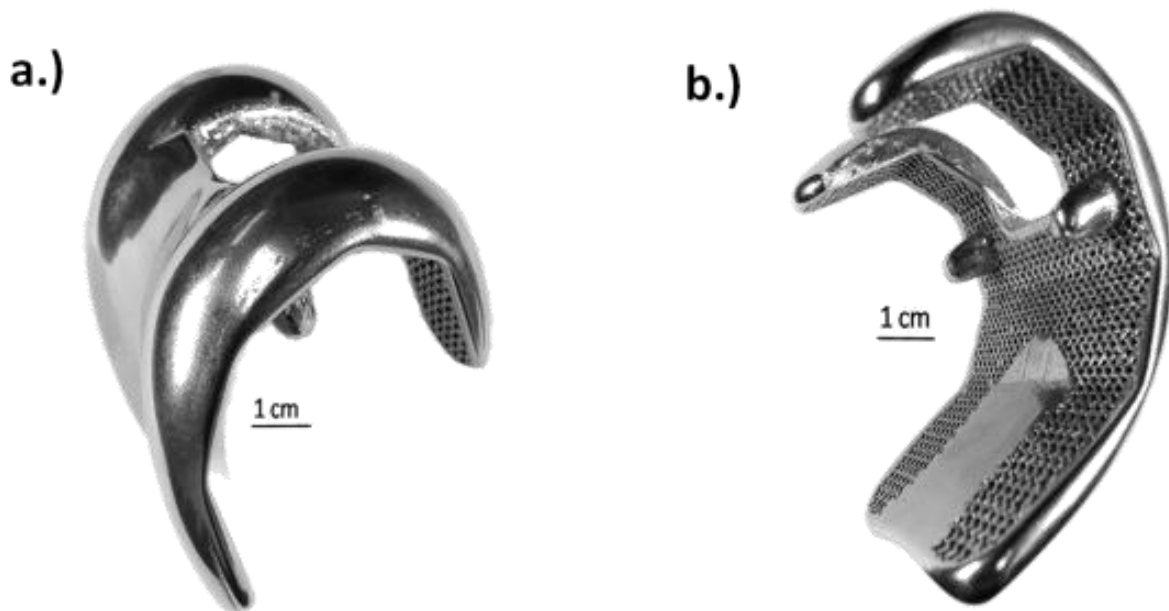


**Figure 4.3.1. Post-treated femoral knee component with mesh inclusion fabricated by EBM.**

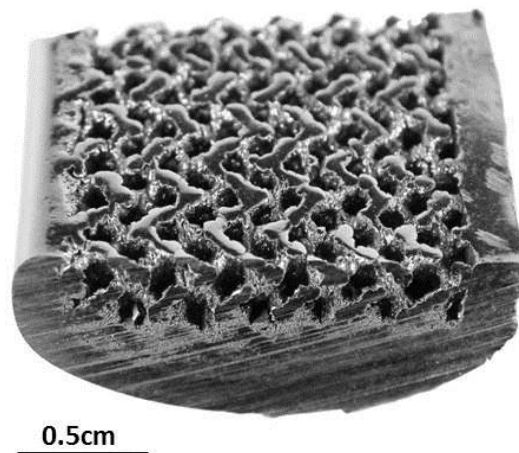


**Figure 4.3.2. Section used for analysis obtained from femoral knee component.**

As already mentioned, etchant solutions were hard to obtain and therefore, the most significant metallography images will be shown below for comparison purposes. Figure 4.3.3 shows the microstructure obtained from the horizontal plane in the block component. An etchant solution consisting of 70 ml of  $H_2O$ , 30 ml of  $HCl$  and a voltage variation from 15 to 20 for 30 seconds was used. It can be observed how precipitates were diluted back into the matrix and grain boundaries were left with a minimum visualization of twin boundaries. It can be observed how grains differ in size as observed in as-fabricated components. Figure 4.3.4 shows the vertical plane of a block component but a different etchant solution was utilized. A solution consisting of 100 ml of  $H_2O$ , 5 ml of  $HCl$  and 10 gr of  $FeCl_3$ , 8V and 20s etched only the grain boundaries and no twin boundaries. Small dots in the image belong to the sample reacting to the etchant and arrow indicates building direction. Notice how precipitates are not observed anymore.

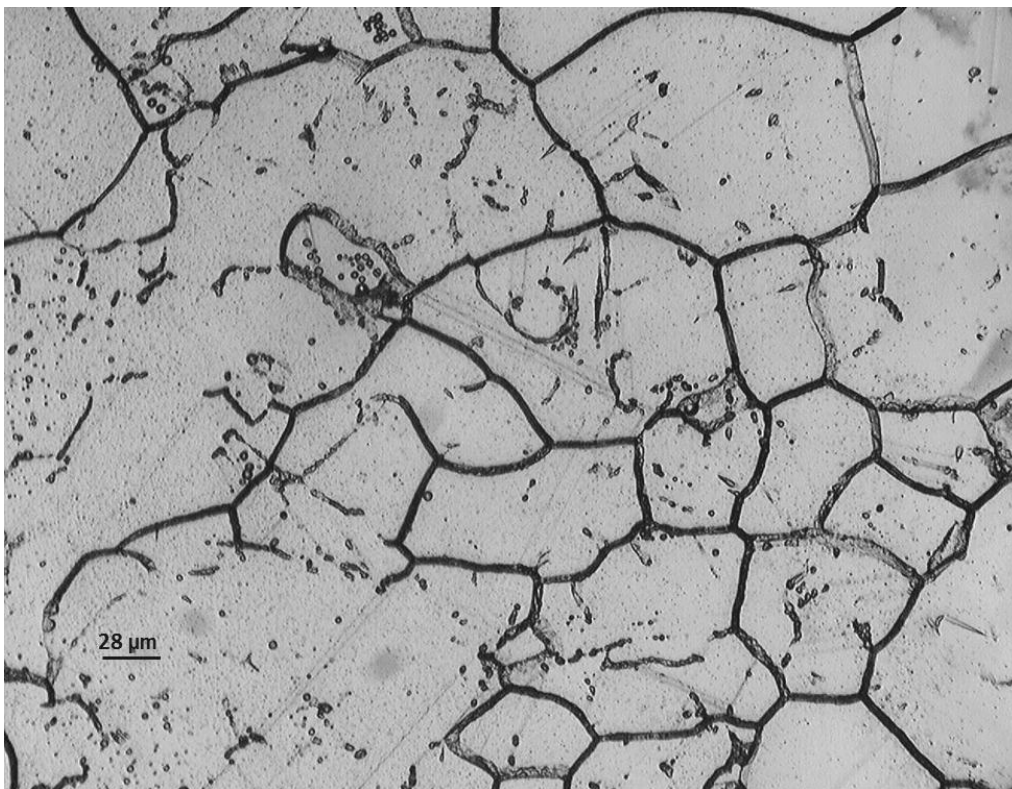
Figure 4.3.5 shows the horizontal plane of the cylindrical component etched with a solution consisting of 60 ml of  $HCl$  and 10 ml of  $H_2O_2$ . It can be observed how twinning is more visible in the over etched grain while small sections throughout the sample were being burned. Figure 4.3.6 shows the vertical plane of the cylindrical component etched with the solution used for the vertical plane of the block component. Grain boundary can



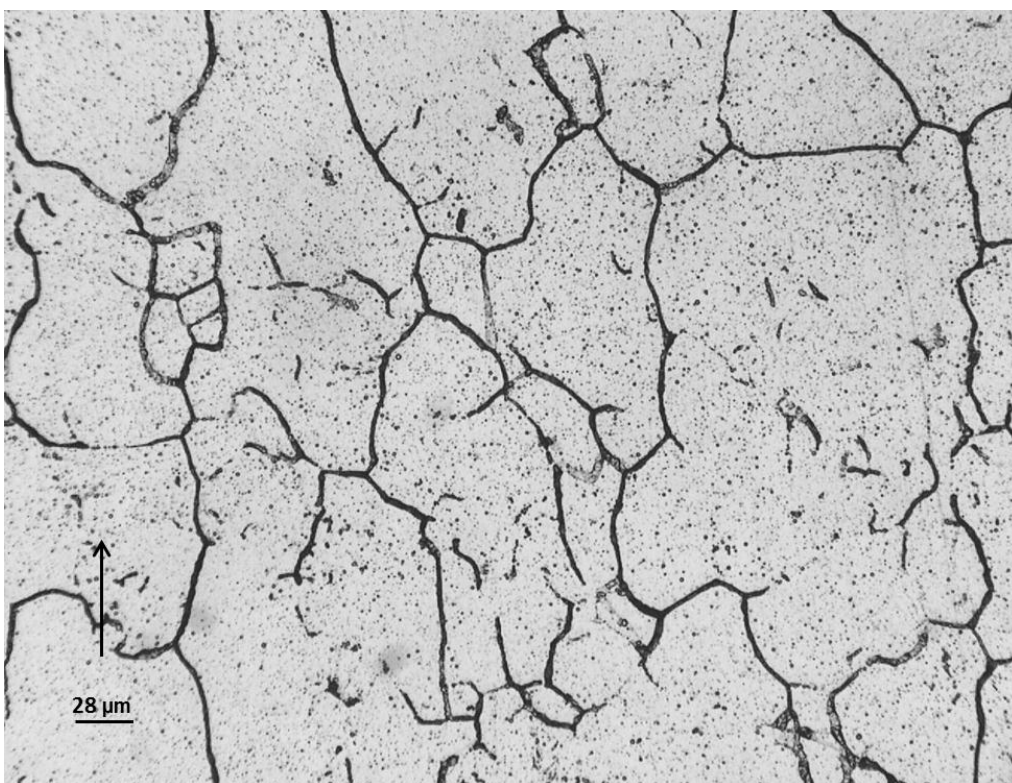
be appreciated, arrow indicates building direction. Grain boundaries in the fcc Co-matrix have an interfacial energy roughly  $\sim 15$  times the coherent twin boundary interfacial energy. Consequently, there is no carbide precipitation on the twin boundaries because the energy is too low for nucleation to occur.

Figure 4.3.7 and 4.3.8 show the vertical plane of the HIPed and annealed femoral knee component. Etchant solutions consists of 60 ml of HCl and 10 ml H<sub>2</sub>O<sub>2</sub> for image 4.3.7 and 100 ml H<sub>2</sub>O, 10 ml HNO<sub>3</sub>, 10 ml HCl and 3 g FeCl<sub>3</sub> for image 4.3.8. It can be appreciated how figure 4.3.7 illustrates the already familiar equiaxed fcc grain structure as depicted by the previous images. It can also be observed how annealing twins are located at preferential grain boundary locations. Preferential carbide etch at high energy grain boundary segments can be observed from figure 4.3.8. The arrows in both figures indicate the building direction of the component, which is a direction parallel to the EBM layer addition.

TEM images representative of the EBM fabricated components that have gone under HIPing and annealing treatments are shown in figures 4.3.9 to 4.3.14.



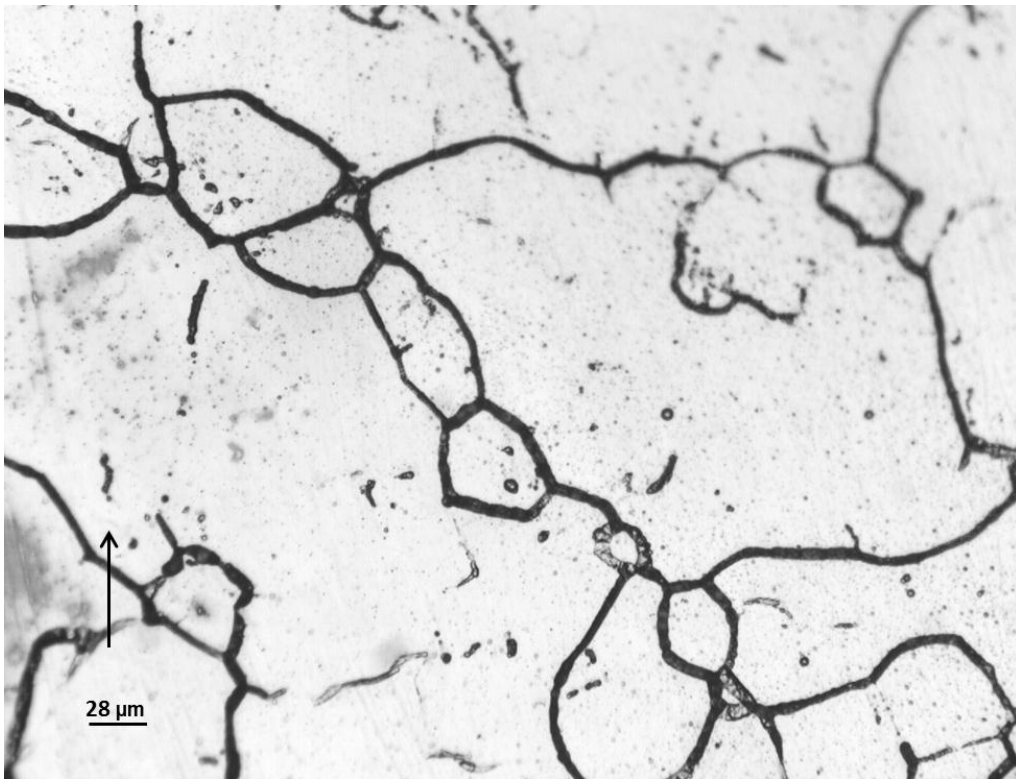
**Figure 4.3.3. Horizontal plane of block component**



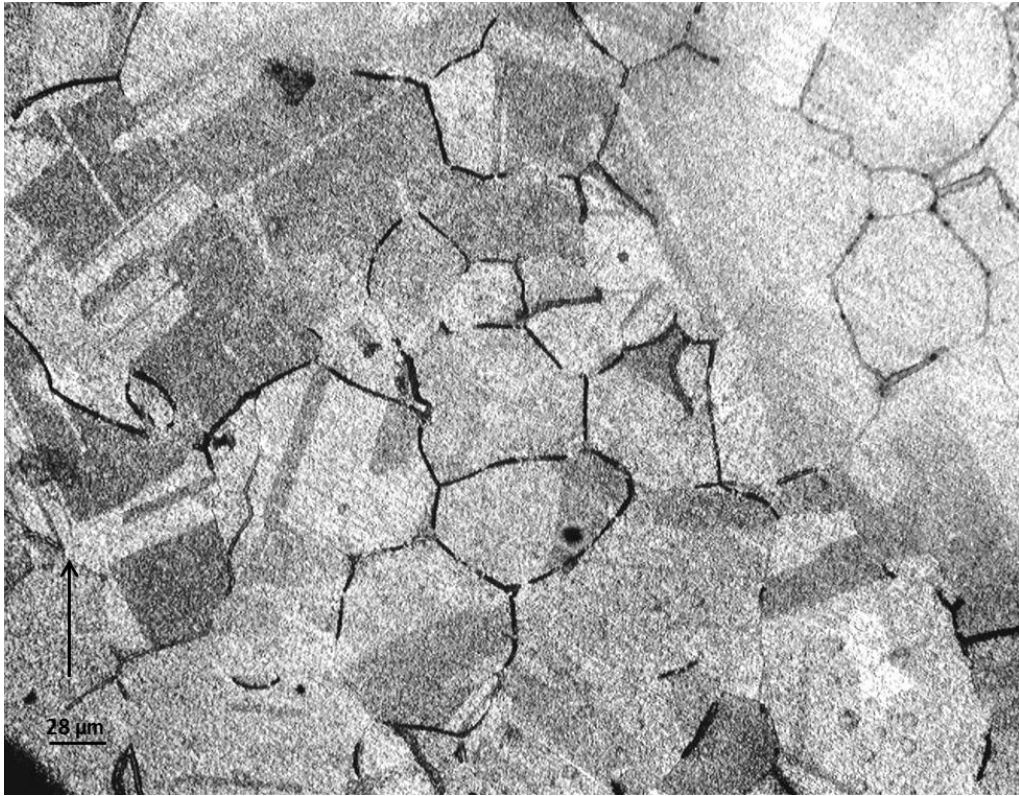
**Figure 4.3.4. Vertical plane of block component.**



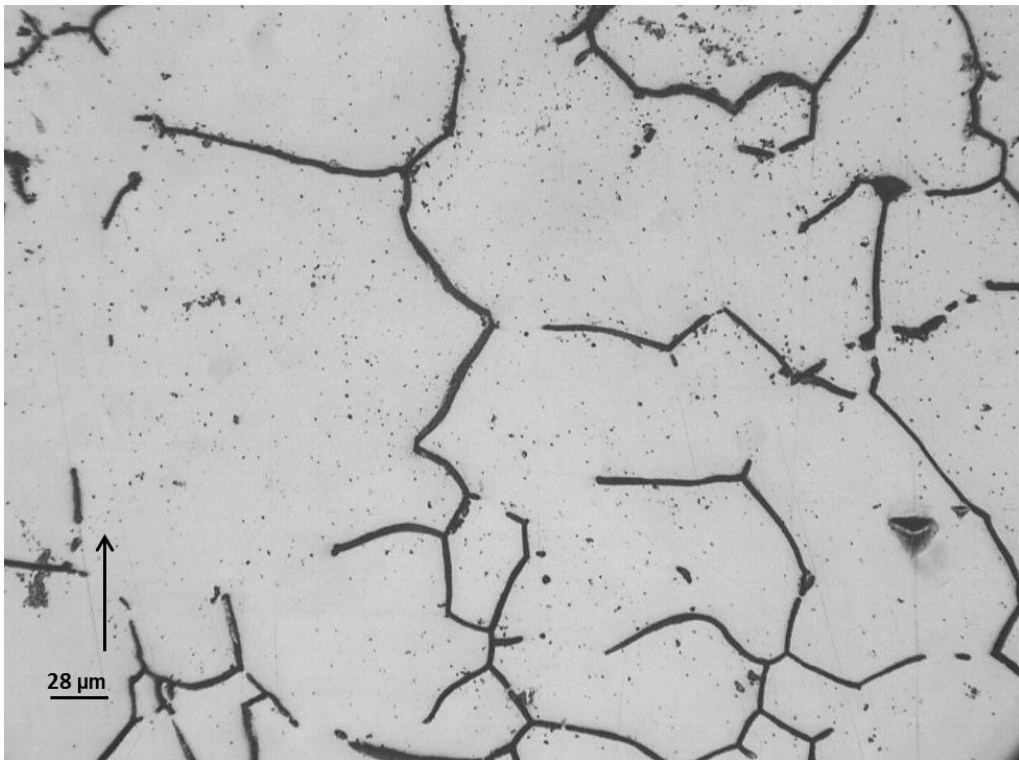
**Figure 4.3.5. Horizontal plane of cylindrical component**



**Figure 4.3.6. Vertical plane of cylindrical component.**

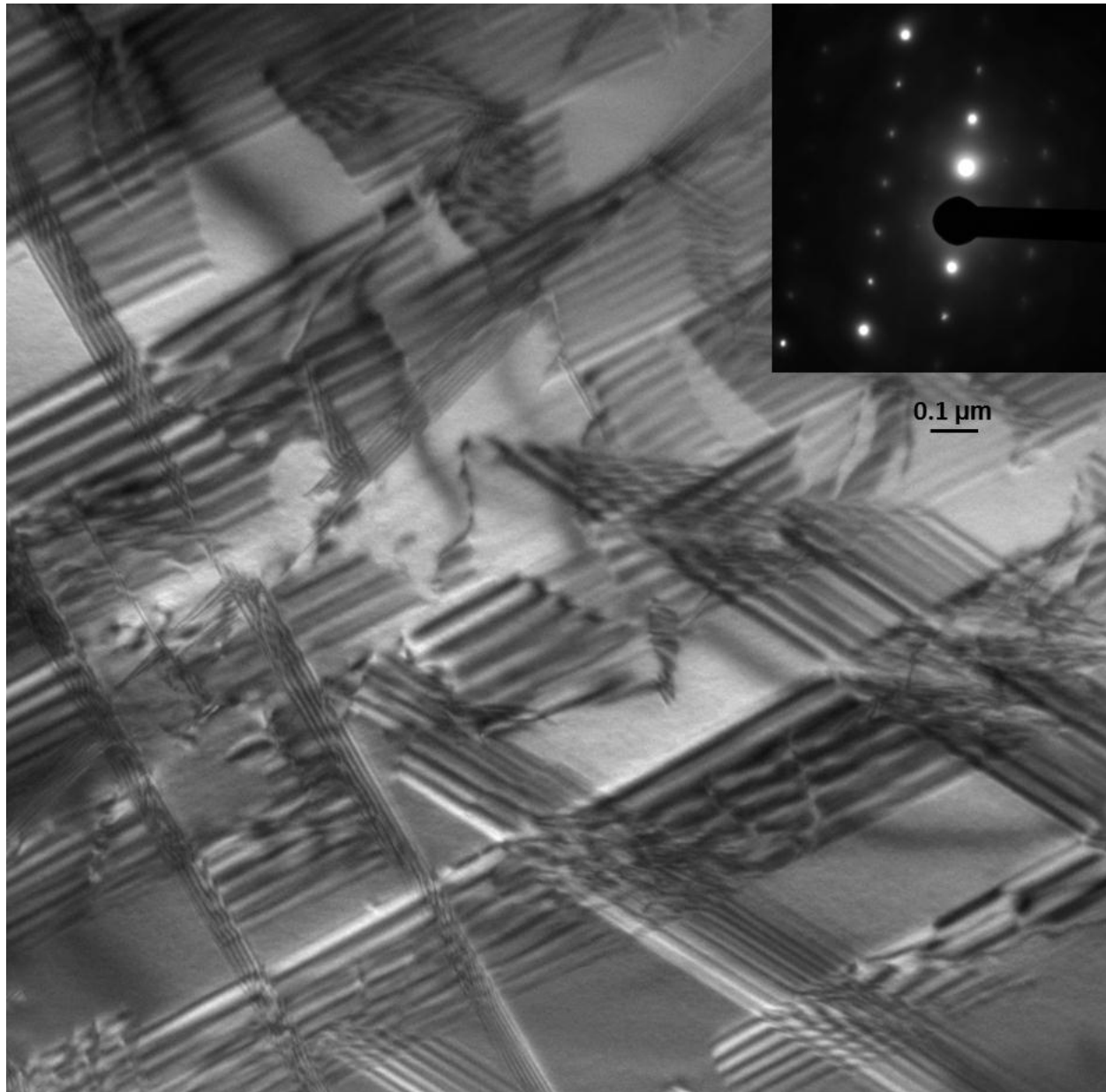


**Figure 4.3.7. Vertical plane of femoral knee component**



**Figure 4.3.8. Vertical plane of femoral knee component**

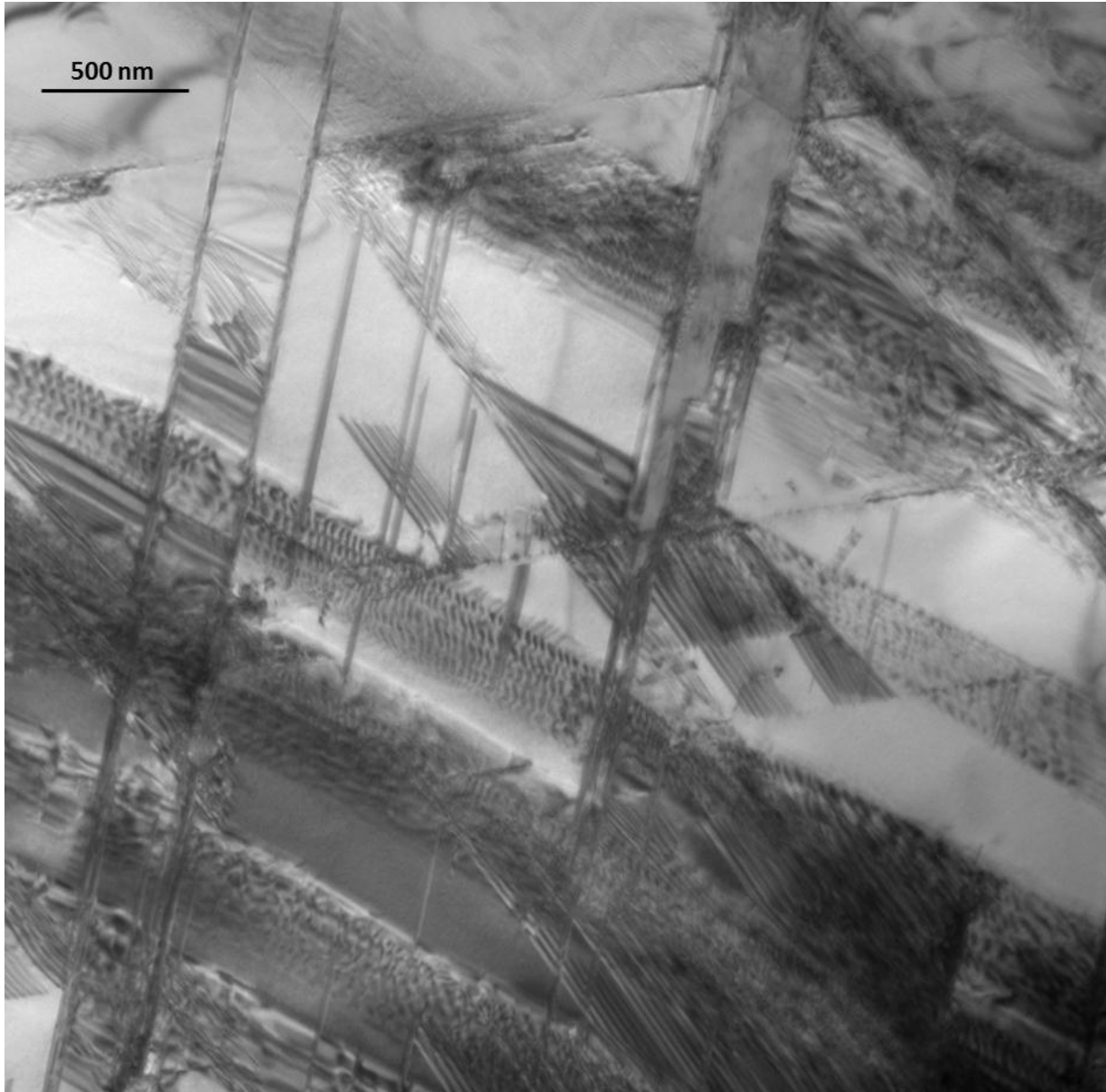
Figure 4.3.9 shows an image corresponding to the horizontal plane in the block component with a high density of stacking faults interaction, from the electron diffraction pattern the lack of precipitates can be observed as compared to the SAED patterns obtained for the as-fabricated EBM components.



**Figure 4.3.9. Block horizontal no precipitates in diffraction**

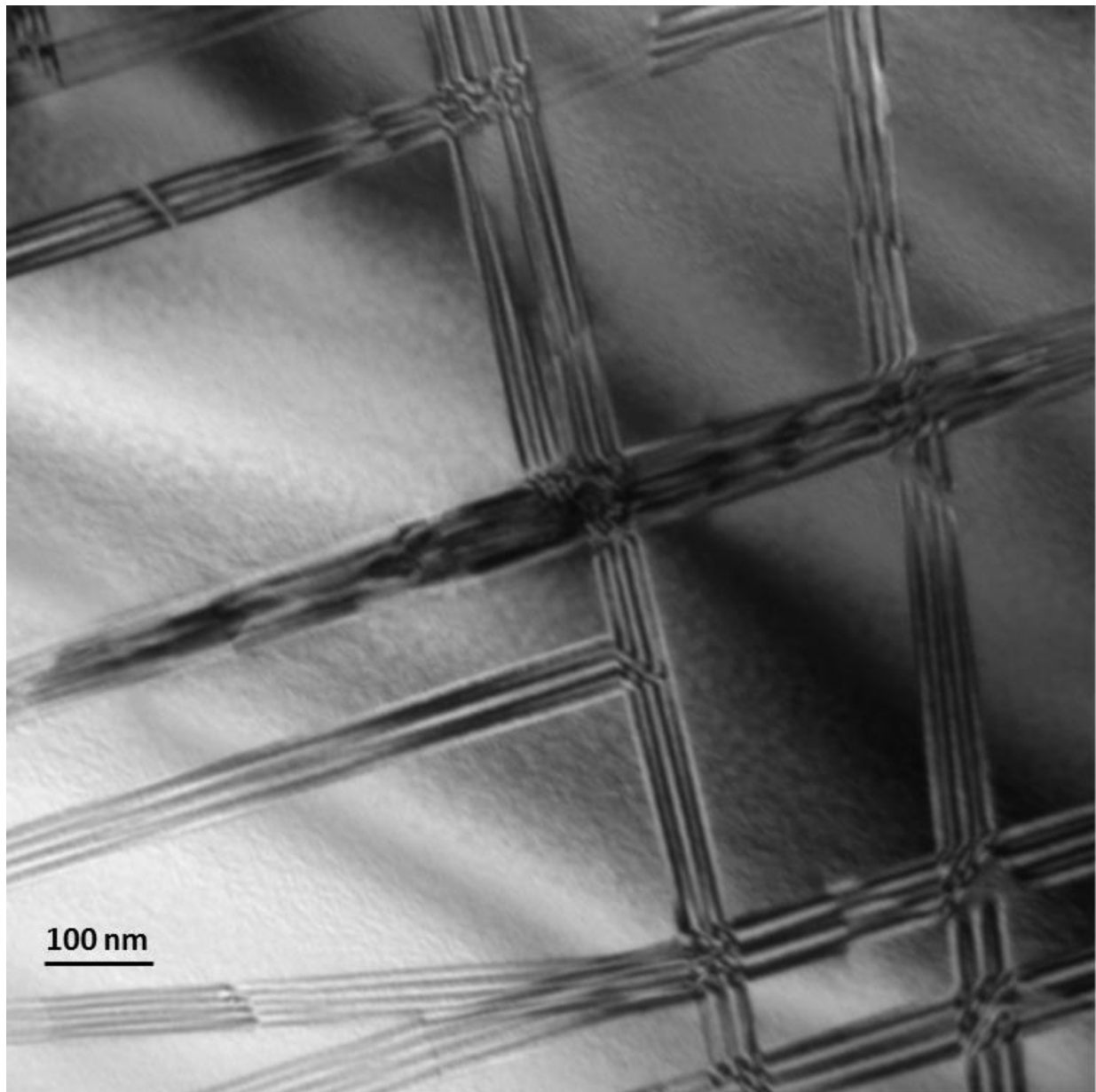


Figure 4.3.10 shows another example of high density of intrinsic stacking faults; this image belongs to the horizontal plane of an annealed cylindrical component.



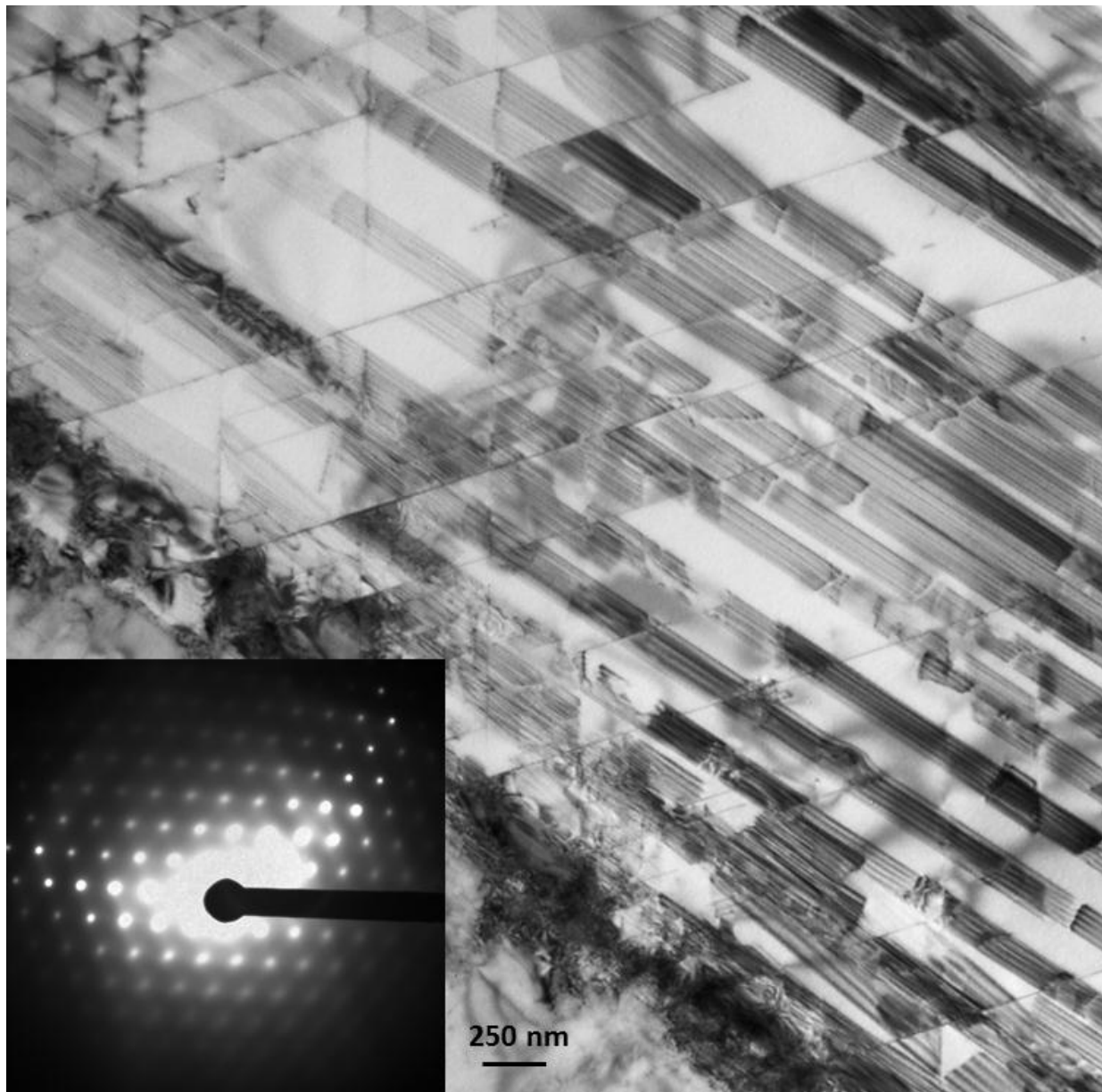
**Figure 4.3.10. Horizontal plane of annealed and HIPed cylindrical component fabricated by EBM**

Figure 4.3.11 shows a high magnification TEM image from the vertical plane from the annealed and HIPed femoral knee component. It can be observed how stacking faults are intersecting at  $\sim 90^\circ$  in a (100) grain orientation. Slight curvature of the thin foil surface can cause a notable geometry projection variance as shown at the bottom of Figure 4.3.11.



**Figure 4.3.11. Vertical plane of annealed femoral knee component**

Figure 4.3.12 shows a low magnification TEM image belonging to the vertical plane of the HIPped and annealed femoral knee component. High density of intrinsic stacking faults on (111) planes coincident with the  $[2\bar{2}0]$  crystal direction shown in the SAED (110) pattern insert.



**Figure 4.3.12. High density of stacking faults in annealed EBM fabricated femoral knee component**



Figure 4.3.13 besides showing the expected stacking faults, also shows a twin boundary visible in the top part of the image as well as in the SAED pattern insert. Stacking faults in the  $[2\bar{2}4]$  direction are being twinned in the  $[002]$  direction while the ones in the  $[\bar{1}1\bar{5}]$  direction are twinned in the  $[\bar{2}24]$  direction obtained from the  $(110)$  diffraction pattern for fcc materials.

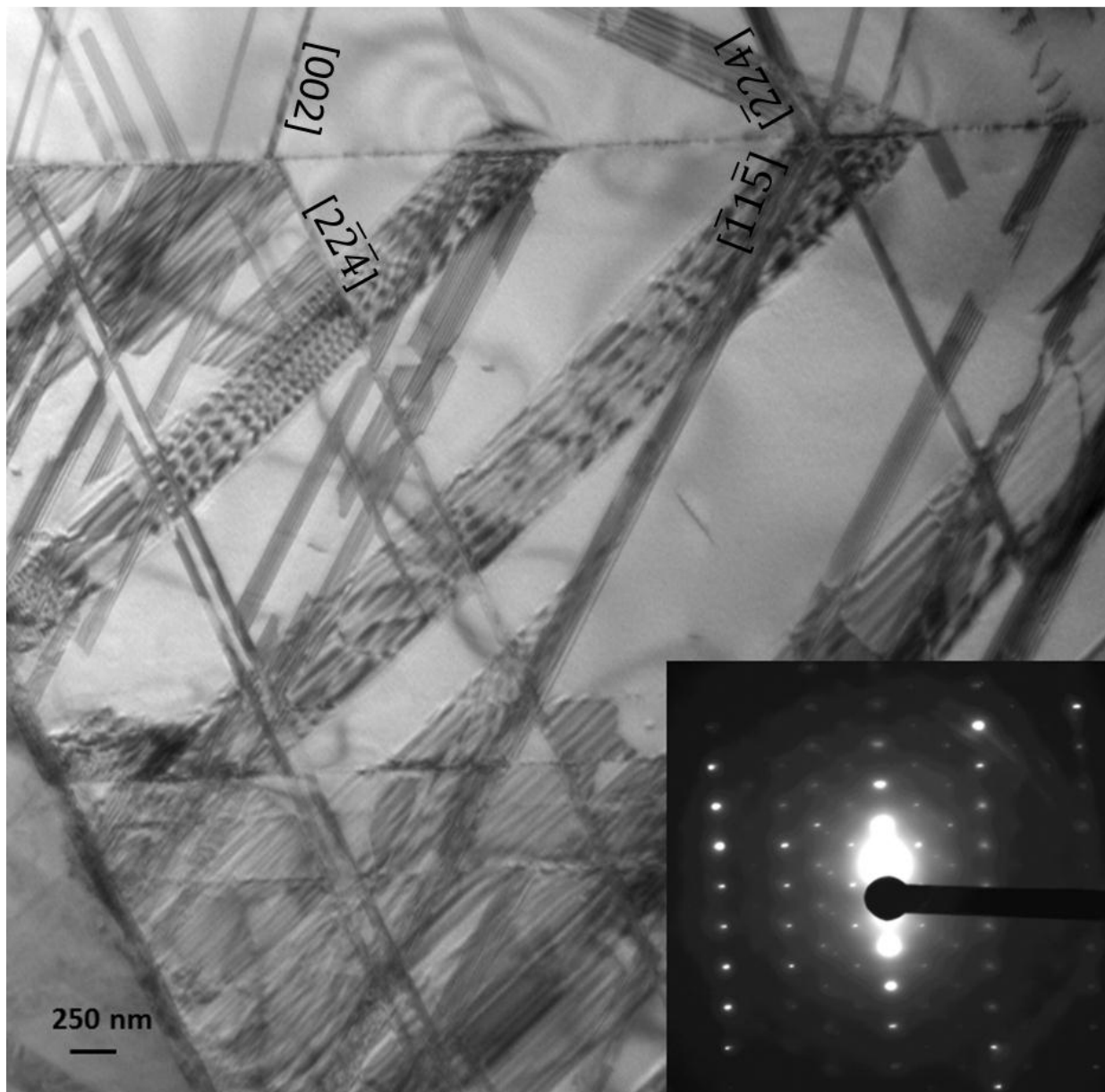


Figure 4.3.13. Vertical plane from annealed femoral knee component

Figure 4.3.14 is another example of high density of stacking faults where the twinning does not have the right diffracting angle. As observed from the diffraction pattern twinning is also obtained from this image, where the brighter spots are aligned in the  $[002]$  and  $[2\bar{2}0]$  directions as obtained from the  $(110)$  diffraction pattern.

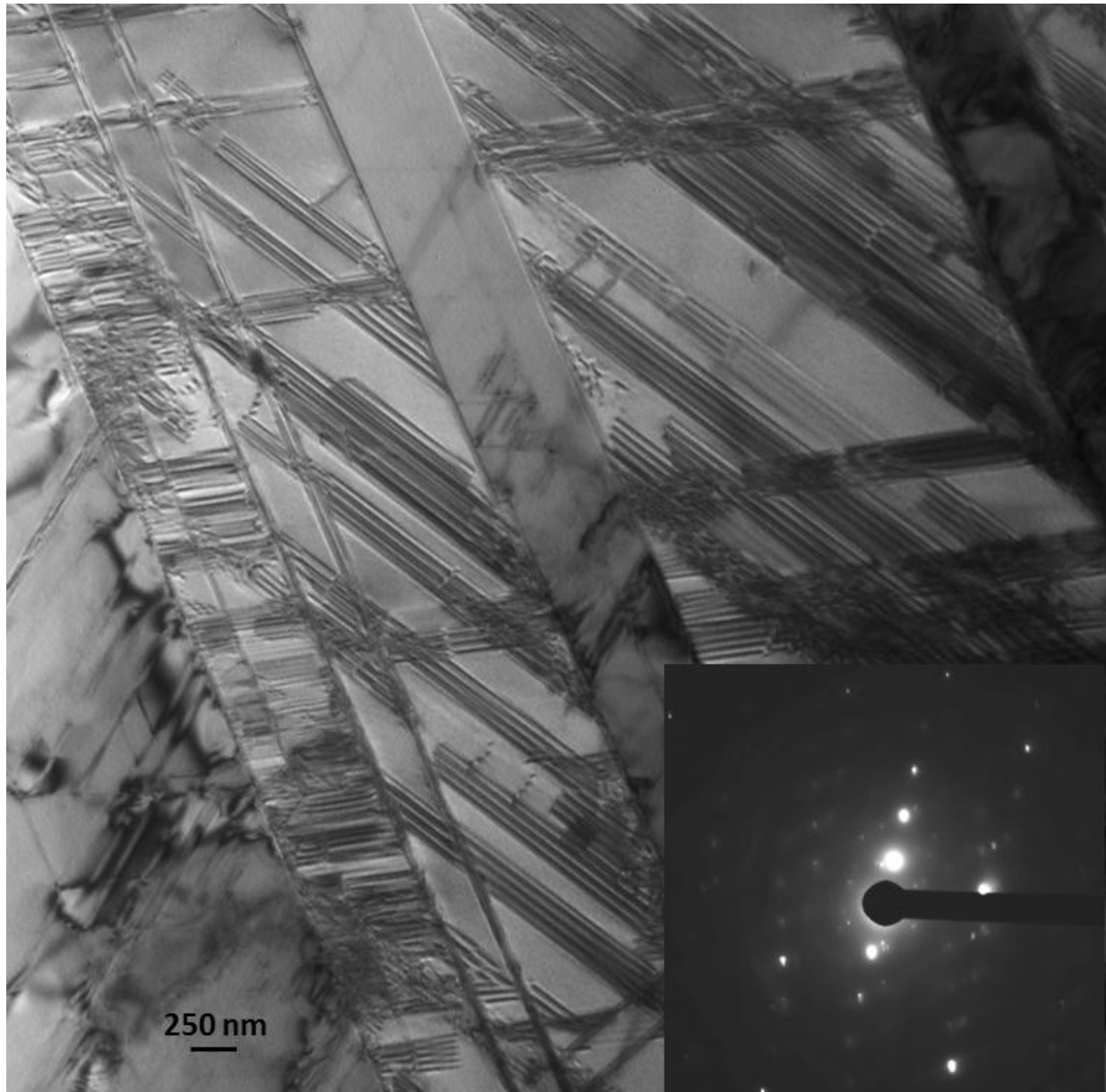


Figure 4.3.14. Vertical plane in annealed knee component

Both microhardness (HV) and hardness (HRC) testing were performed on the annealed and HIPed EBM components. The annealed block component has a hardness of 2.8 GPa in the horizontal plane and 3.3 GPa in the vertical plane obtained from Vickers testing. Rockwell hardness in the C scale provided a hardness of 29 HRC for the horizontal plane and 30 HRC for the vertical plane. Hardness testing for the annealed cylindrical component showed a value of 3.4 GPa for the horizontal plane and 3.7 GPa for the vertical plane while hardness in the Rockwell C scale belongs to a value of 31 HRC for the horizontal plane and 31 HRC for the vertical plane. For the annealed and HIPed femoral knee component a value of 4.7 GPa was obtained for the vertical plane and 40HRC. All the values provided belong to the average of 10 different measurements when the standard deviation was less than 2, and about 15 measurements when the standard deviation was higher.

Tensile testing for the HIPed and annealed components was achieved by machining the cylindrical component and pulling it, this is in the direction parallel to the building direction. From the block component, a tensile testing was machined and pulled from the bottom to perform tensile testing in a direction perpendicular to the building direction. For the specimens pulled in a parallel direction, average yield strength of 0.60 GPa, a UTS of 1.15 GPa and an elongation of 32% was obtained. The specimens pulled in a perpendicular direction showed a yield strength of 0.63 GPa, a UTS of 0.99 GPa and an elongation of 20%. Note these elongations were nearly an order of magnitude higher, on average, than the as-fabricated components

Figure 4.3.15 shows images from the fracture surface that was pulled in a direction perpendicular to the building direction and that showed an elongation of 20%. Figure 4.3.15 a) show intergranular fracture representative of brittle fracture while c) to d) show a sequence of increasing magnification showing dimple structure representative of ductile fracture.

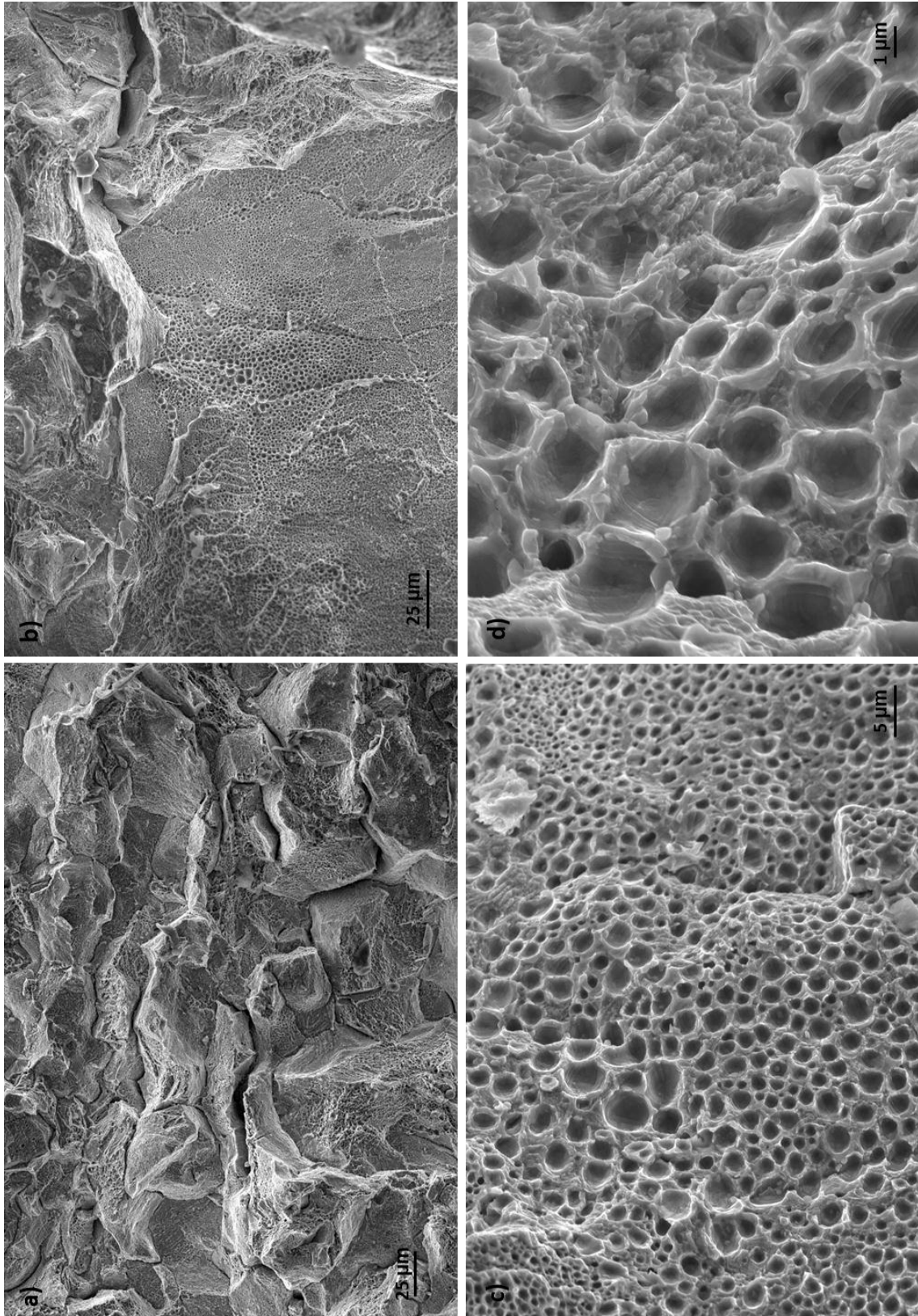
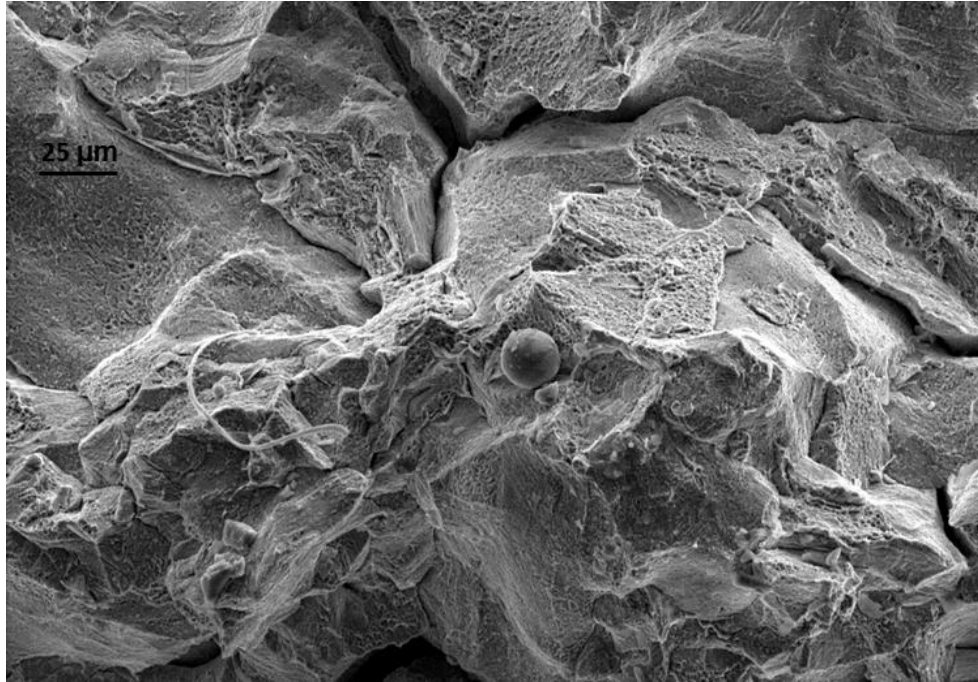


Figure 4.3.15 Fracture surface from tensile testing



**Figure 4.3.16. Fractured surface showing an unmelted powder particle.**

Figure 4.3.16 shows a completely unmelted powder particle were the background shows intergranular fracture found in the fracture surface of the pulled sample having an elongation of 20%, this is an example of what should not be found in solid components.

The HIPed and annealed components were analyzed under the XRD as shown in figure 4.3.17. It can be observed how most of the peaks overlap with at least two different components with the exception of the peak found at  $2\theta=74.9$ , where only Co (hcp) fits. Carbide precipitates for the annealed components correspond to  $\text{Cr}_{23}\text{C}_6$  (fcc) as expected. Other phases present in this spectra are Co (fcc:  $a=3.55$ ), Co (hcp:  $a=8.29$ ,  $c=10.54$ ),  $\text{Co}_{0.8}\text{Cr}_{0.2}$  (hcp:  $a=2.52$ ,  $c=4.06$ ),  $\text{Co}_{0.9}\text{Mo}_{0.1}$  (hcp:  $a=2.54$ ,  $c=4.11$ ) and  $\text{Co}_3\text{Mo}_1$  (hcp:  $a=5.12$ ,  $c=4.11$ ). If we compare this figure to figure 4.2.1.14 the most prominent difference is that instead of having  $\text{Co}_{0.82}\text{Mo}_{0.18}$  we have  $\text{Co}_{0.8}\text{Cr}_{0.2}$  peaks, which were present in the powder. As already stated in the as-fabricated XRD results, all overlapping phases have been included in the results for comparison purposes.

# Annealed

## EBM

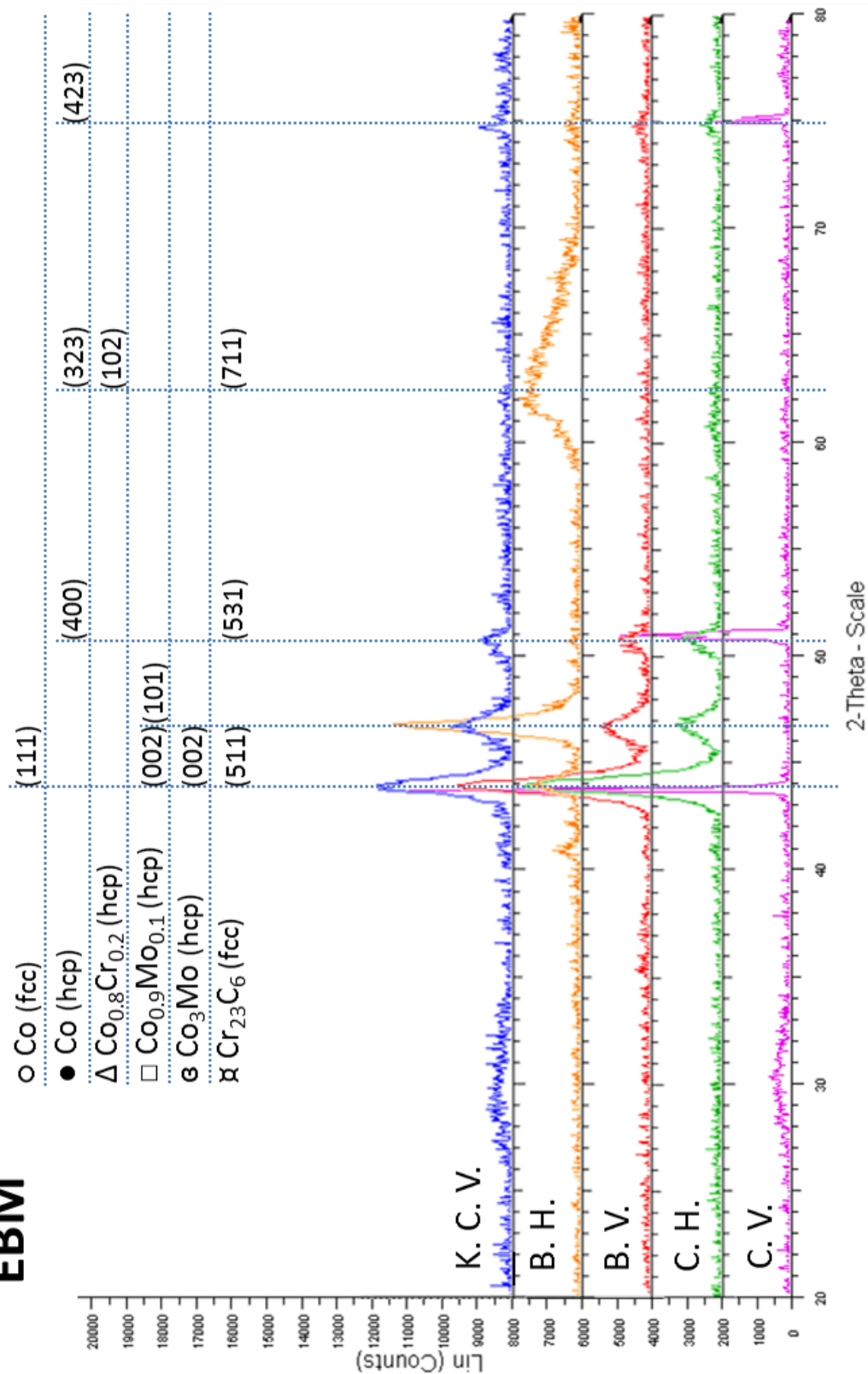


Figure 4.3.17. XRD of annealed and HIPed components.



## 4.4 TRADITIONAL IMPLANT CHARACTERIZATION

The component to compare in this study was a body-removed implant that was manufactured by traditional techniques such as casting, forging, etc. The implant obtained for this project lacks background information. It would have been of use to know how long the implant was inside a body, why it was removed, how old was the person using it, etc. Since no information is available, the analysis will be limited to comparison of microstructure and hardness, since tensile testing is not possible due to insufficient material available to machine tensile specimens. Figure 4.4.1 shows the implant component as received. It can be observed how cement and blood are still attached to the implant, EDAX analysis was performed after cleaning the sample and it can be observed how the knee component is a Co-Cr-Mo alloy comparative to the one utilized for EBM while the rod that goes into the femur to obtain a better fixation is Ti-6Al-4V alloy. Note that this appliance has no porous or open cellular features which would assist bone ingrowth and compatibility.

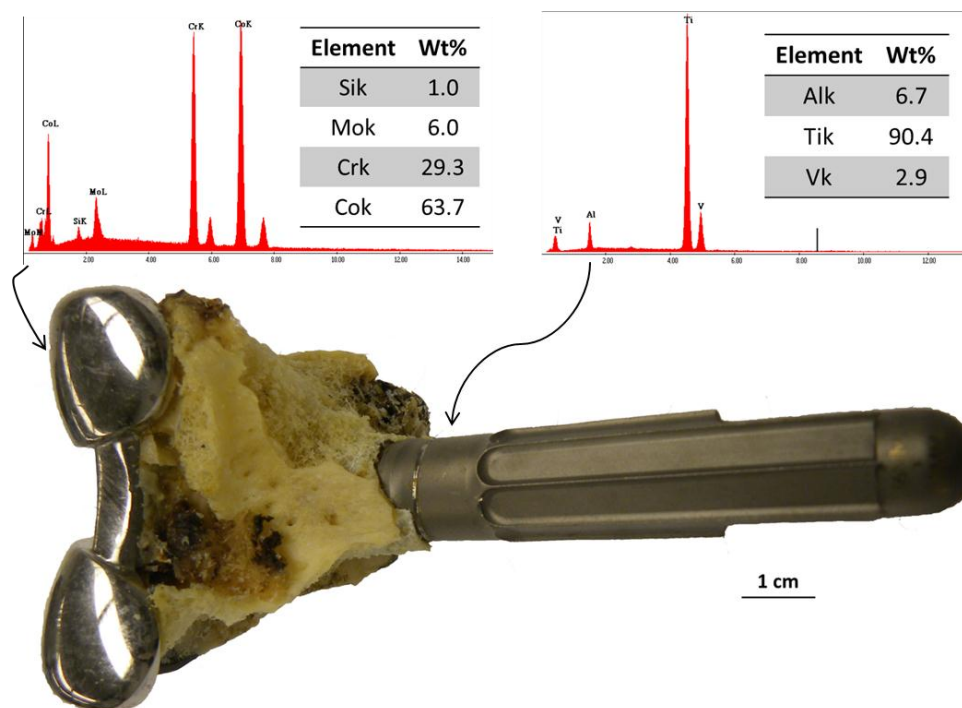
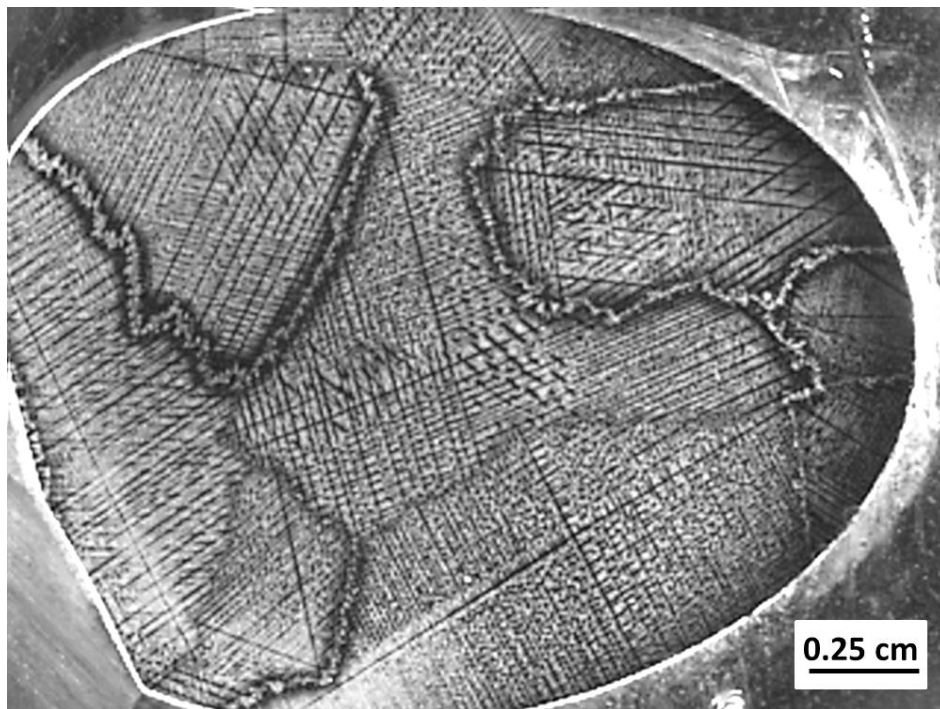


Figure 4.4.1. Traditionally manufactured femoral knee component implant

X-ray fluorescence of this component showed a 28.96% Cr, 6.76% Mo, 0.5% Mn and 63.78% Co. Figure 4.4.2 shows a stereo micrograph image taken after etching the polished Co-Cr-Mo body removed implant. Since the microstructure was visible by the naked eye, an image of this was included for reference. It can be observed how a regular array of precipitates depicts the grain orientation for each section. The same area as for the as-fabricated and the annealed EBM femoral knee components was analyzed even though the fabrication method was different.



**Figure 4.4.2. Co-Cr-Mo low magnification image showing microstructure.**

Figures 4.4.3 and 4.4.4 show two different low magnification images obtained from the same section while figure 4.4.5 shows a higher magnification image of the same. If this component had been built by EBM, the images shown below had been obtained from the vertical plane. It has to be mentioned that this microstructure is different to the microstructure for cast and wrought Co-Cr-Mo alloy as depicted in Volume 9 of ASM handbook (pg. 964). This microstructure resembles a microdendritic array containing a high density of carbide precipitates.





Figure 4.4.3. Low magnification image from traditionally manufactured femoral knee component

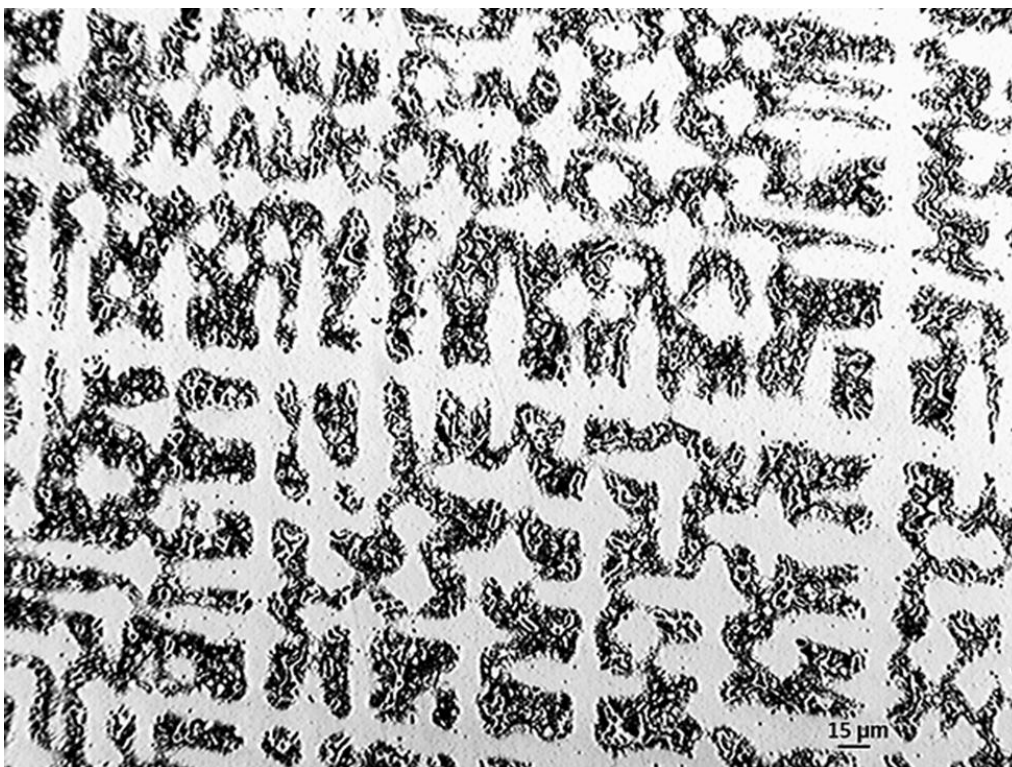
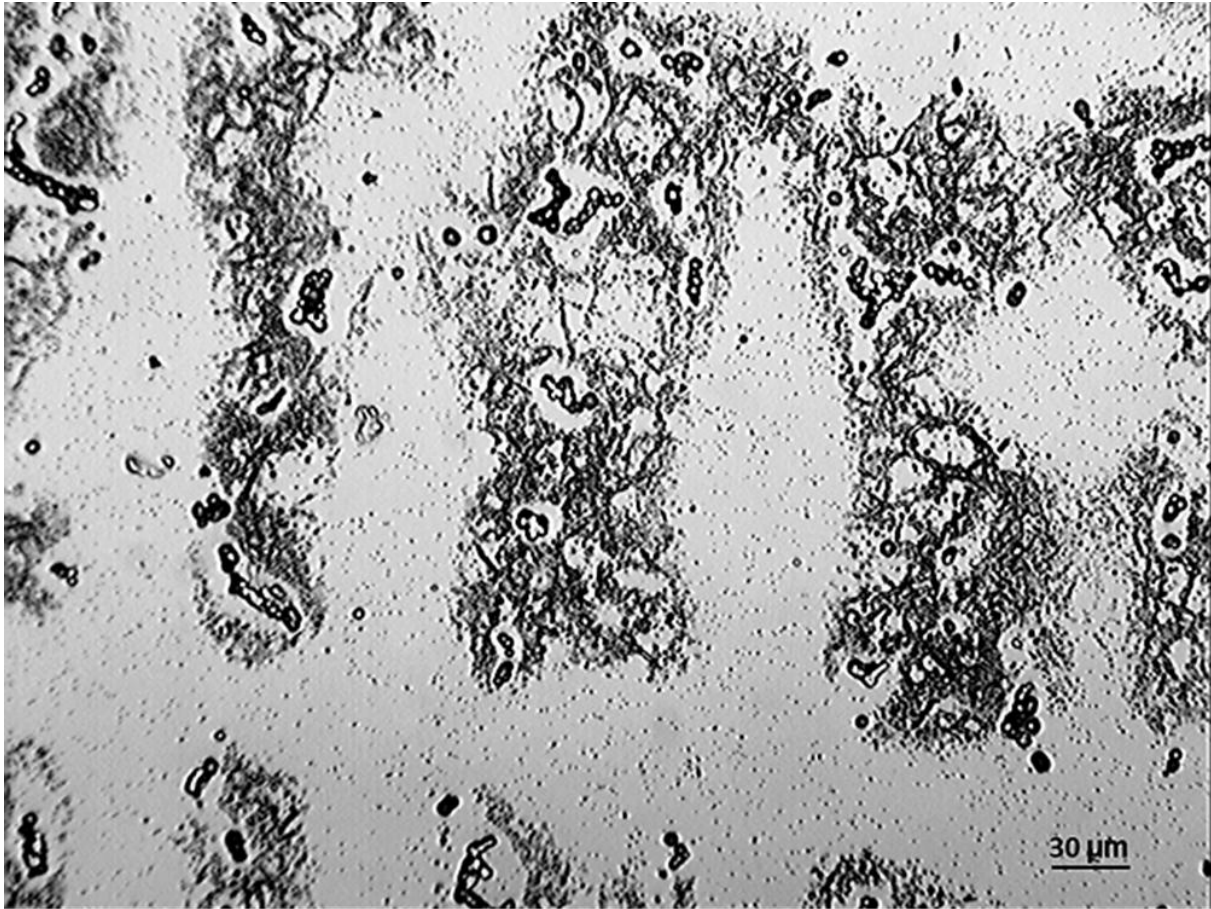


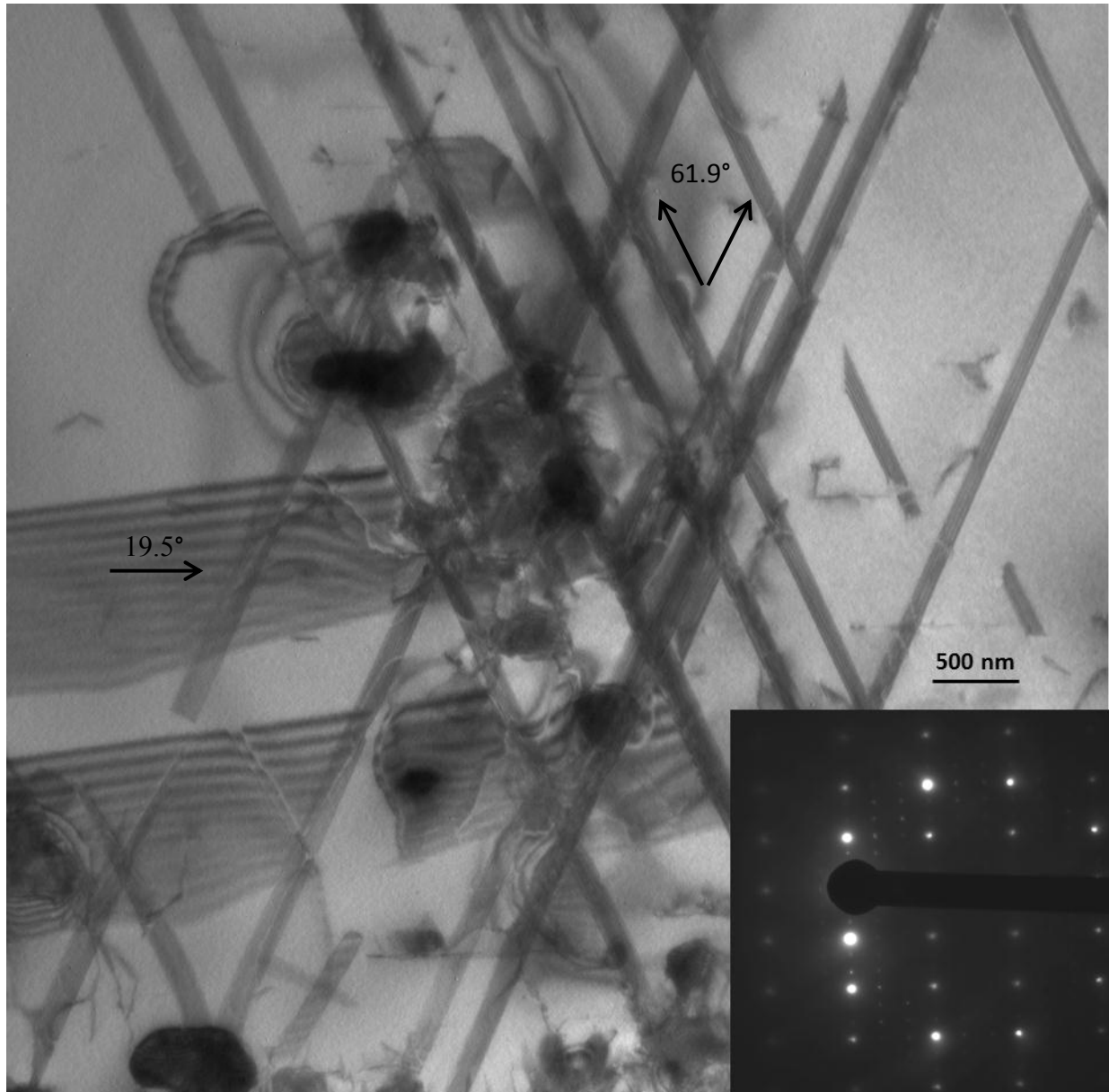
Figure 4.4.4. Low magnification image from traditionally manufactured femoral knee component



**Figure 4.4.5. Traditionally manufactured knee implant**

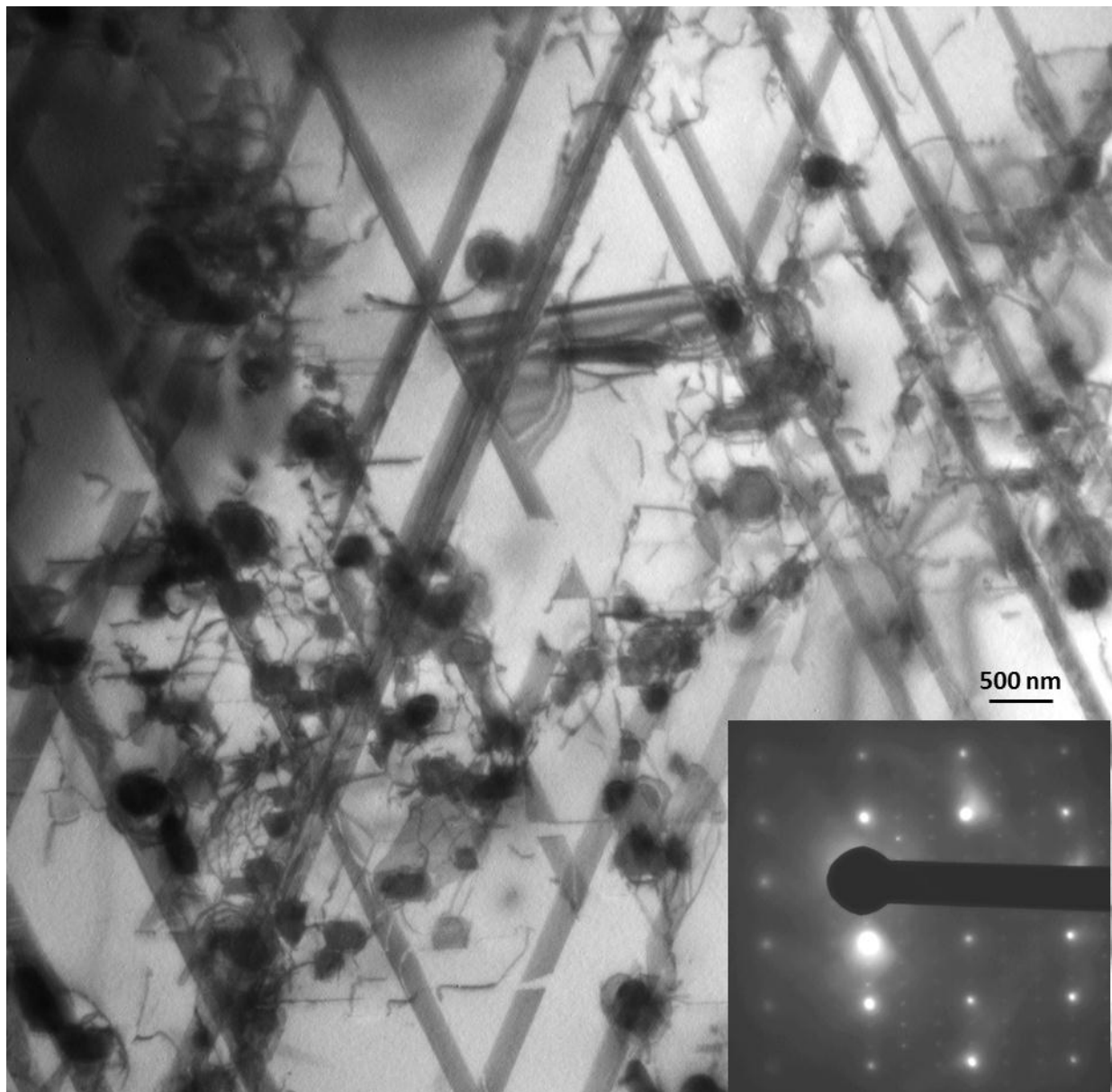
Hardness testing performed on this component shows a HV hardness of 4.6 GPa and for hardness in the Rockwell C scale a value of 26 HRC was obtained. From the microstructure obtained as well as the hardness, it could be assumed that, after casting the implant, a heat treatment was performed that let the microstructure grow in size and at the same time the hardness decreased. It must be stated that tensile testing was not possible to perform from the Co-Cr-Mo implant due to the shape of the same. The presumed anneal would normally follow ASTM F75 standard which was followed for annealing and HIPing of the EBM-fabricated femoral appliance shown in Figure 4.3.1

Figure 4.4.6 shows stacking faults interacting with each other and from the diffraction pattern we can observe the spots array belonging to precipitates. The precipitates can be easily observed in the (112) plane aligned mainly in the  $[1\bar{1}0]$  direction at  $19.5^\circ$ .



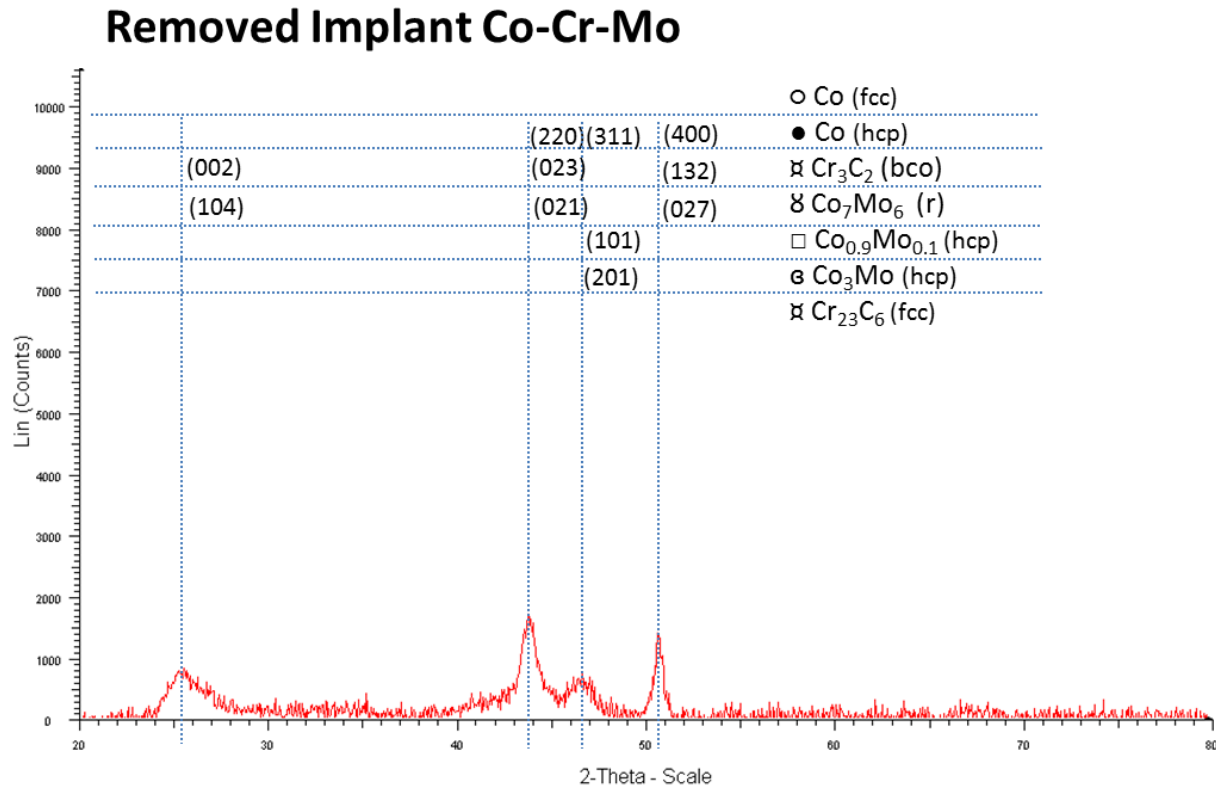
**Figure 4.4.6. TEM image of traditionally manufactured Co-Cr-Mo implant component**

Figure 4.4.7 shows a lower magnification image showing how besides stacking faults interacting with the precipitates, dislocations are also part of the microstructural defects obtained for this sample. Diffraction pattern shows the same as Figure 4.4.6. It is significant to note that in the annealed, EBM-fabricated femoral appliance shown in Figures 4.3.9 to 4.3.14 there are essentially no  $\text{Cr}_{23}\text{C}_6$  precipitates while Figures 4.4.6 and 4.4.7 show a high density of precipitates.



**Figure 4.4.7. Lower magnification TEM image of Co-Cr-Mo traditionally manufactured implant**

XRD results for the body-removed Co-Cr-Mo implant are shown in figure 4.4.8. It can be observed how precipitates unexpectedly correspond to  $\text{Cr}_3\text{C}_2$  (bco:  $a=2.85$ ,  $b=9.25$ ,  $c=6.96$ ) instead of  $\text{Cr}_{23}\text{C}_6$ . Another big difference with EBM fabricated components is that now  $\text{Co}_7\text{Mo}_6$  (r:  $a=4.76$ ,  $c=25.6$ ) fits in all the peaks but the one at  $2\theta=46.5$ .



**Figure 4.4.8. XRD of body removed Co-Cr-Mo knee implant.**

Besides analyzing the microstructure obtained for the Co-Cr-Mo traditionally manufactured component, the Ti-6Al-4V rod component was also analyzed. Figure 4.4.9 and 4.4.10 show low and high magnification optical images showing forged and annealed microstructure of Ti-6Al-4V alloy representing a fine grained alpha-matrix with beta-phase dispersed that can be better appreciated in the higher magnification image. A hardness of 32 HRC and 3.5 GPa was obtained from Rockwell C- scale and Vickers microhardness testing. This is a common hardness for annealed, wrought Ti-6Al-4V.



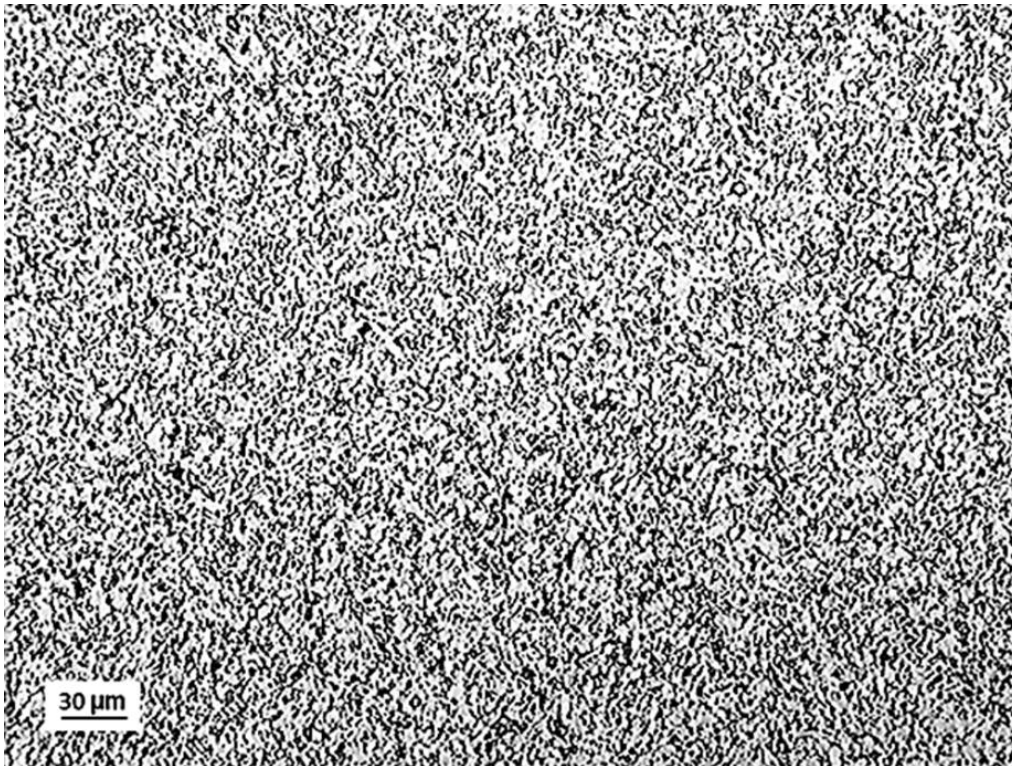


Figure 4.4.9. Low magnification image of Ti-6Al-4V rod component

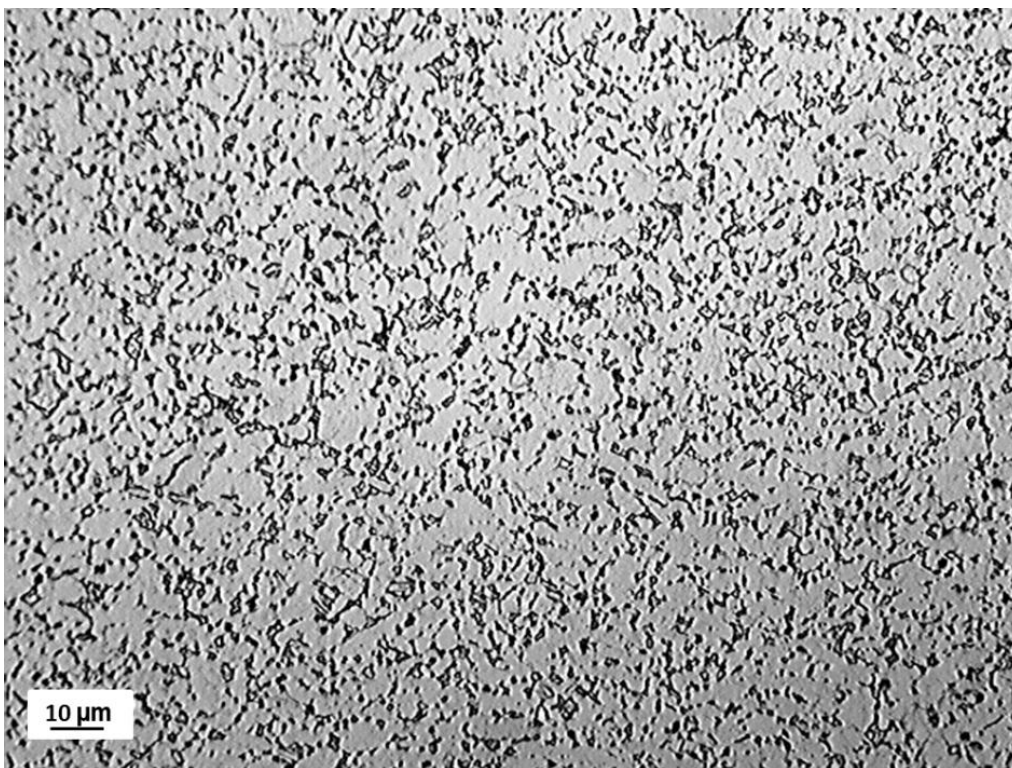
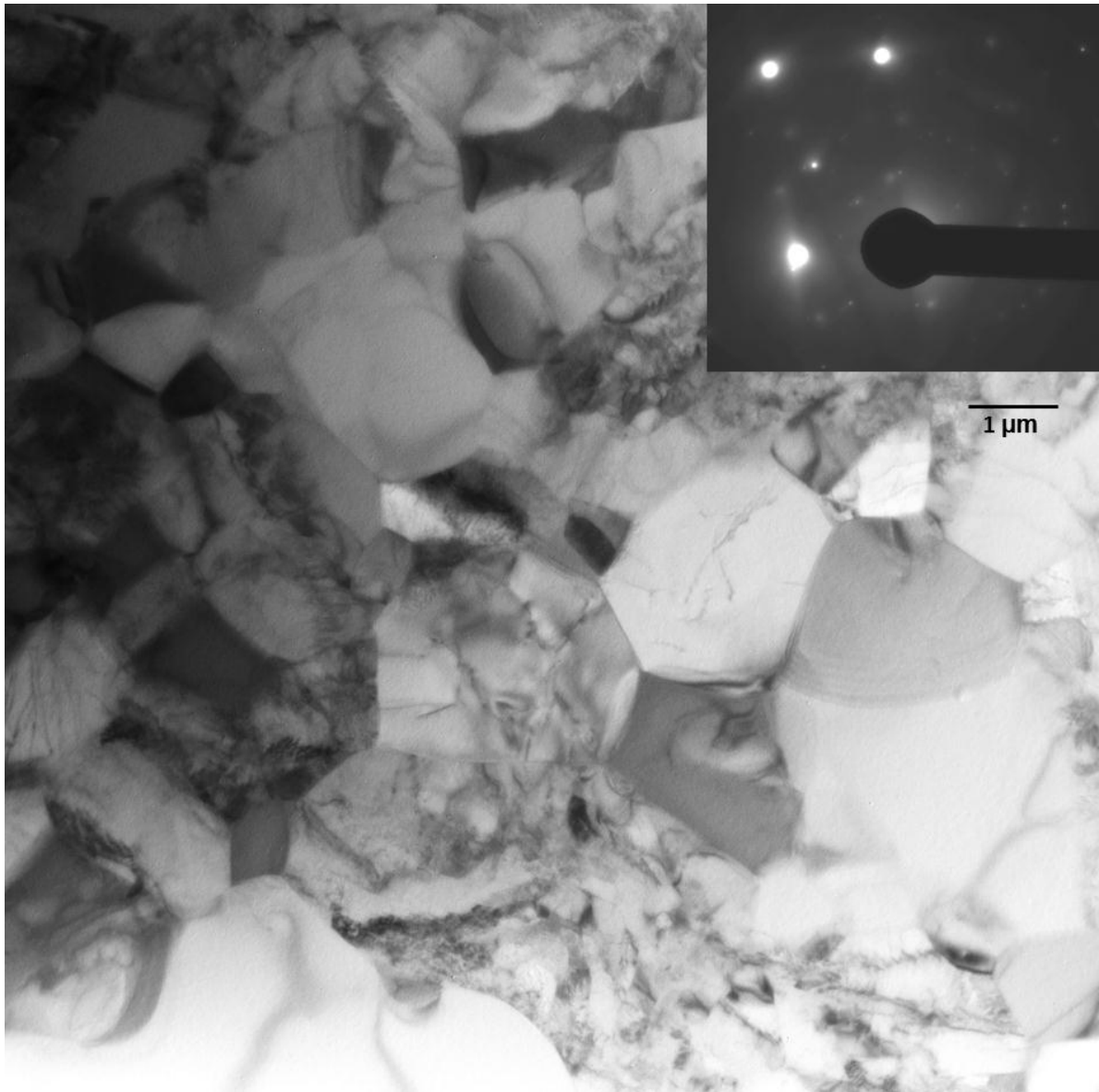


Figure 4.4.10. High magnification image of Ti-6Al-4V rod component

Equiaxed grain structure obtained from Ti-6Al-4V rod component where alpha phase is represented by the white grains and beta phase is present in the dark areas shown in figure 4.4.11. Inserted is the diffraction pattern obtained from the image.



**Figure 4.4.11. TEM image of Ti-6Al-4V rod component**

Higher magnification image of Ti-6Al-4V rod component showing fringe contrast present at the grain boundaries along with dislocations present in the matrix are shown in Figure 4.4.12. The grain boundary fringes indicate that many of the  $\alpha$ -phase grains are separated by a single grain boundary, and no  $\beta$ -phase.

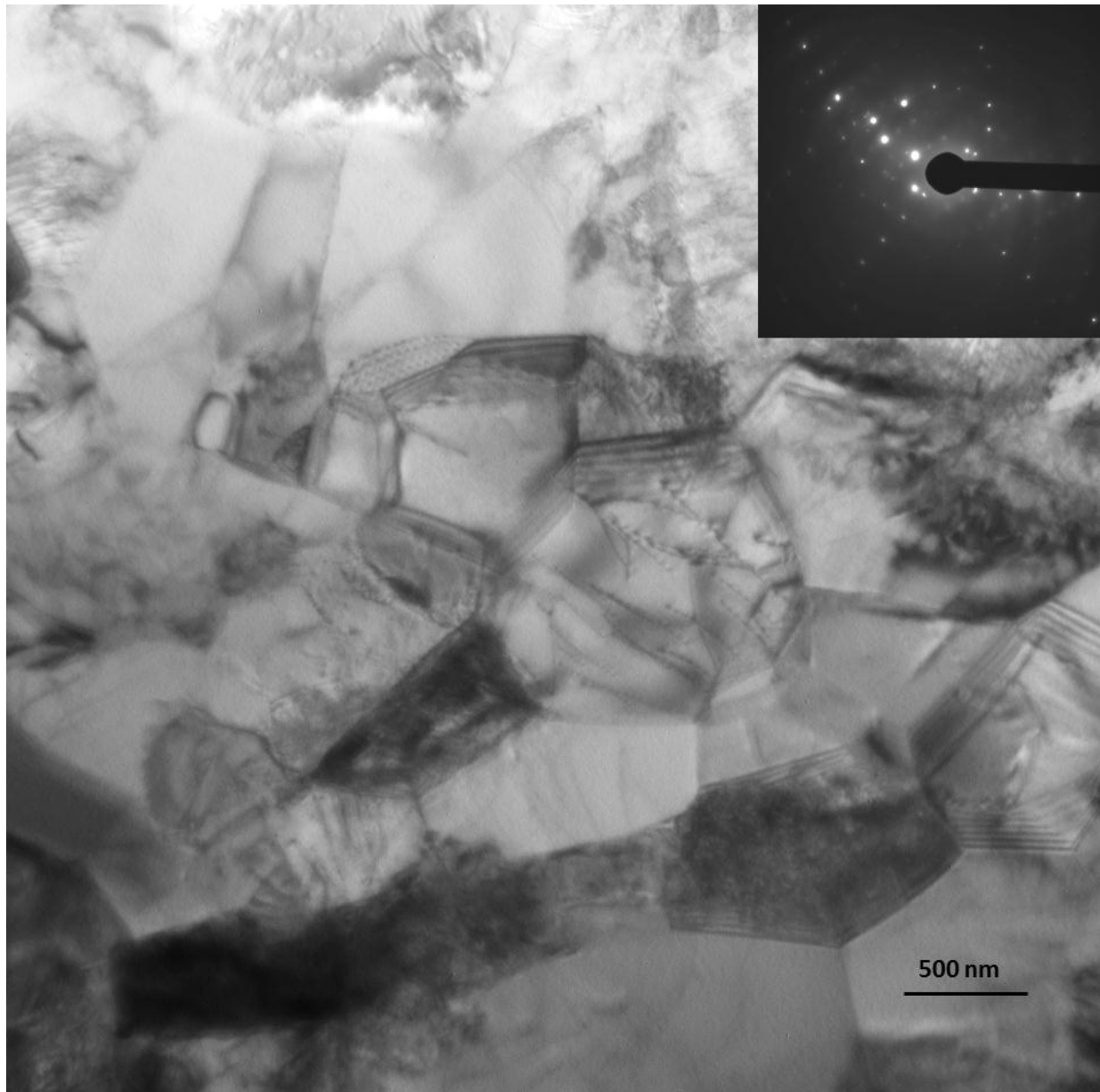


**Figure 4.4.12. Ti-6Al-4V rod component from body-removed implant.**



XRD results for the body removed Ti-6Al-4V implant are shown in figure 4.4.13.  $\text{Ti}_{1.335}\text{Al}_{2.665}$  (hcp:  $a=5.77$ ,  $c=4.64$ ) shows the most peaks match since only  $2\theta=87.5$  does not match. Other components overlapping at different peaks are TiV (bcc:  $a=3.16$ ),  $\text{Ti}_{0.972}\text{V}_{0.028}$  (hcp:  $a=4.6$ ,  $c=2.82$ ),  $\text{Al}_{0.4}\text{Ti}_{0.6}$  (hcp:  $a=2.88$ ,  $c=4.61$ ) and  $\text{Al}_3\text{Ti}$  (bct:  $a=3.85$ ,  $c=8.58$ ).

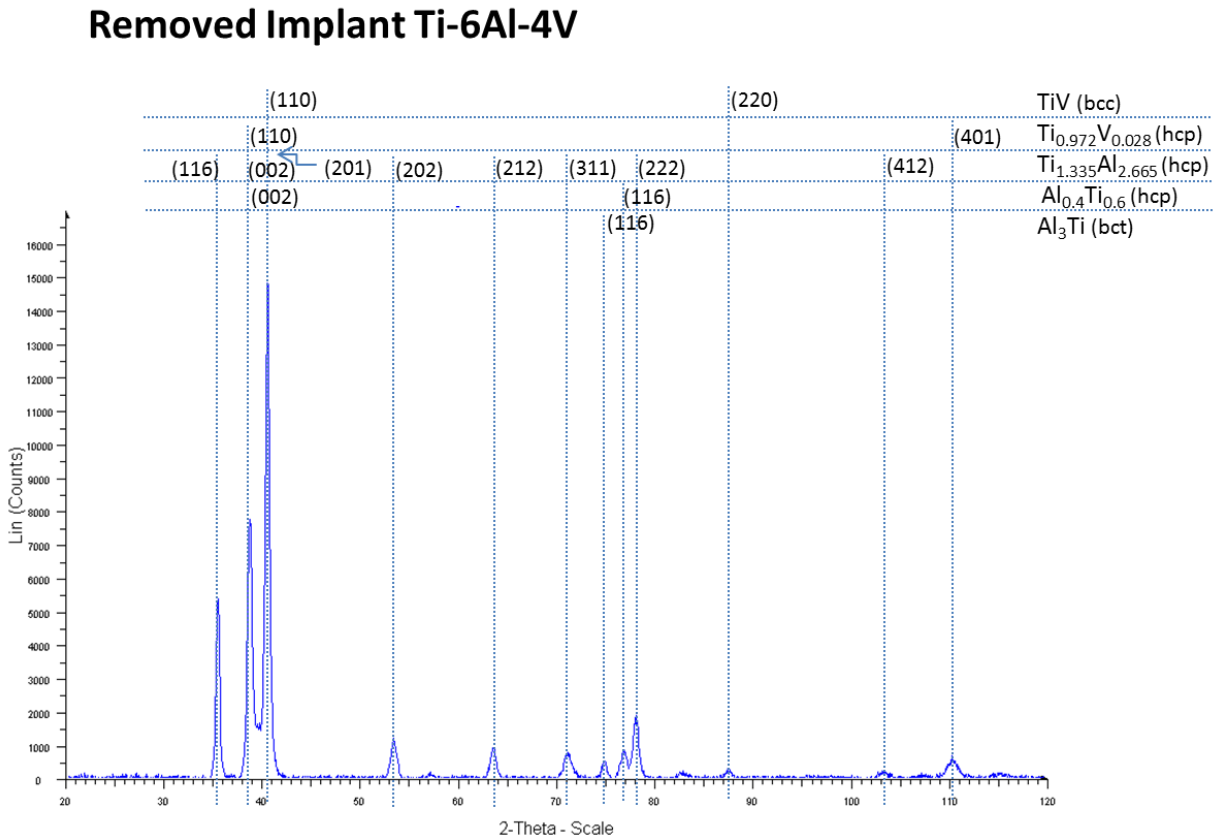


**Figure 4.4.13. XRD of body removed Ti-6Al-4V implant stem.**

Please see appendix figures one to three for Ti-6Al-4V EBM fabricated components for comparison purposes.

## CHAPTER 5

### DISCUSSION

#### 5.1 OPTICAL MICROSCOPY

It can be shown schematically how as-fabricated components have a unique array of carbides representing precipitation in small domains created by the cross scanning of the electron beam during preheating and in successive layer building with dimensions of  $\sim 2\mu\text{m}$  observed in the horizontal plane while similar spacing in between columns is observed in the vertical plane and continuously extending. The schematic shown in figure 5.1.1 shows how precipitates are being created by the successive layer building,  $p(x)$  and  $p(y)$  represent the pre-heat scans while  $m(x)$  and  $m(y)$  are the melt scans, note that beam scan direction reverses each succeeding layer. Carbide spacing is mainly determined by the electron beam focus and scan geometry.

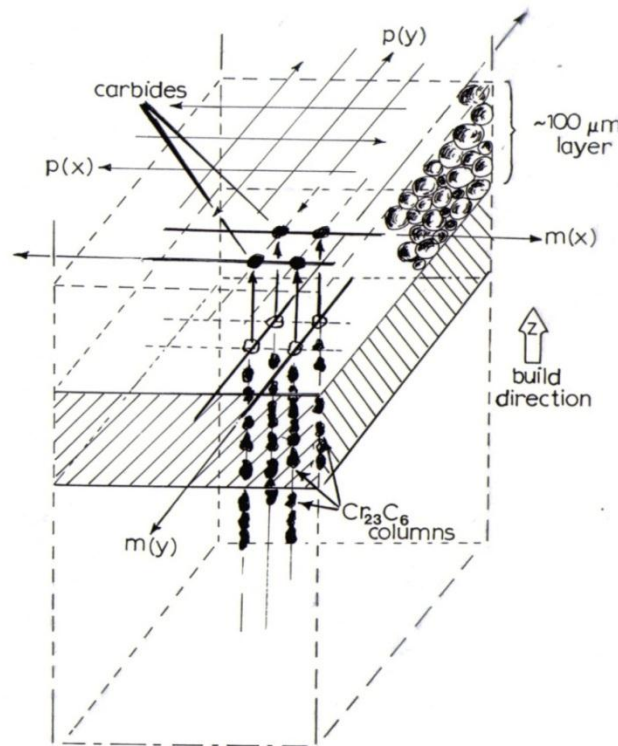
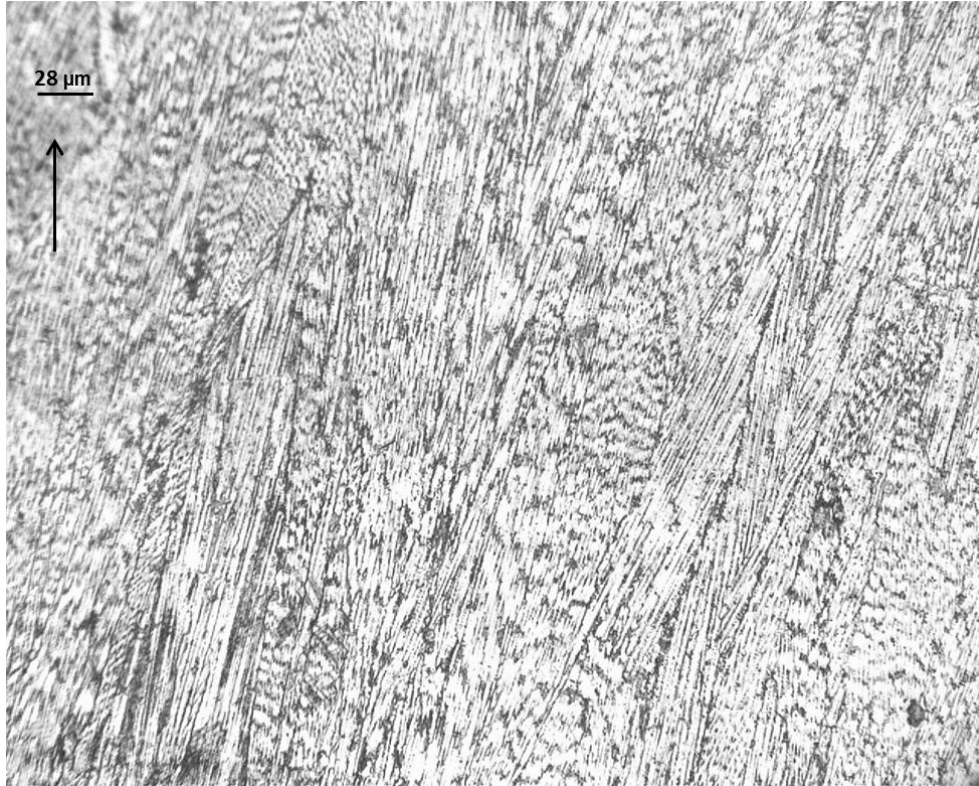


Figure 5.1.1. Carbide precipitates pattern formation.

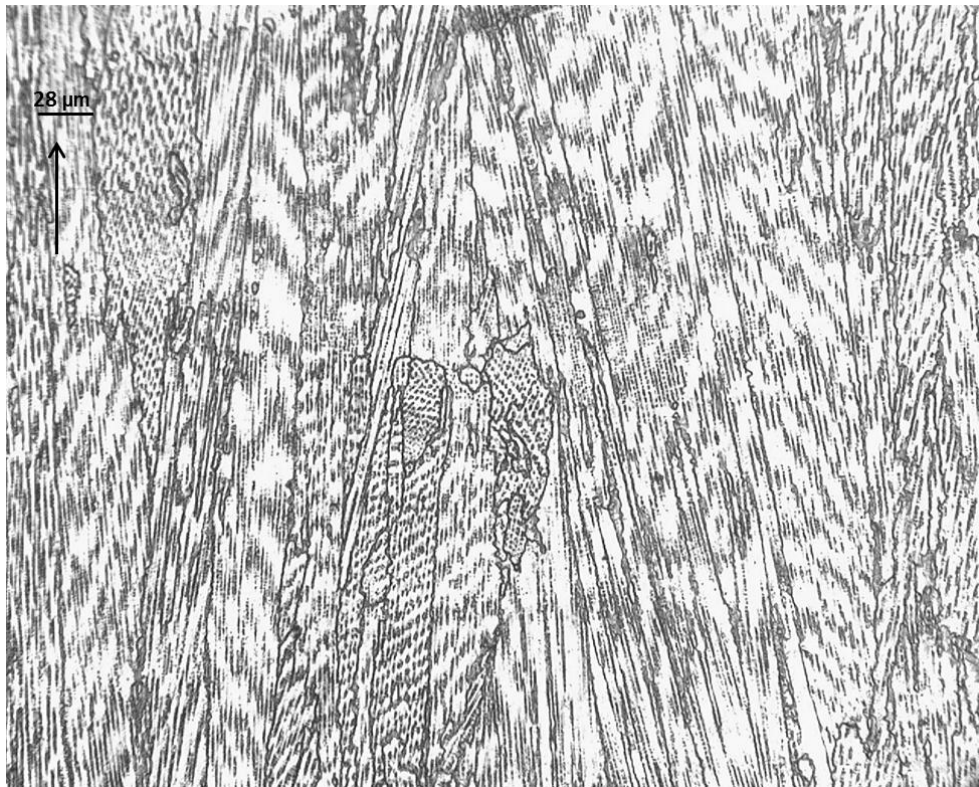
The melt scan forms corresponding arrays of  $\sim 2\mu\text{m}$  melt pools which in effect link across the larger surface, often irregularly as observed from the horizontal images of the EBM fabricated specimens. This irregularity also extends in the vertical plane or in the build direction. If we compare the three different microstructures obtained, it can be seen how different they are. To begin with we have two different views obtained from the as-fabricated EBM components, one would be the vertical plane and the other one belongs to the horizontal plane. Images obtained from a cylindrical component show what has already been demonstrated by L. E. Murr et. al. (Murr, et al. 2009d) where a detailed study of Ti-6Al-4V fabricated by EBM was performed finding that microstructures at the top had an average  $\alpha$ -plate thickness of  $2.1\mu\text{m}$  in contrast to  $1.4\mu\text{m}$  for the bottom. In this project instead of having thicker  $\alpha$ -plate thickness we can observe a wider spacing between each columnar array of precipitates.

Figure 5.1.2 and 5.1.3 compare two different sections obtained from the same as-fabricated cylindrical component. Figure 5.1.2 shows a microstructure obtained from the bottom part of the cylindrical component while figure 5.1.3 shows an image obtained from the top part of the cylindrical component, both images were obtained from the vertical plane. Even though the horizontal plane shows the same situation it is not as easily observed as the vertical plane. Figure 5.1.4 was obtained from bottom section from a cylindrical component while figures 5.1.5 and 5.1.6 were obtained from the top part.

As already mentioned, the EBM system is creating this unique array of  $\text{Cr}_{23}\text{C}_6$  precipitates that enhance hardness as well. Once the as-fabricated components went through annealing the characteristic microstructure was obtained, consisting of equiaxed grains when viewed in a two dimensional array, where the grains form an array of polygons having three or more sides, where only the annealing twin boundaries, which are special low angle boundaries, are straight (Tomer, 1991a). Figure 5.1.7 shows the obtained microstructure for annealed components fabricated by EBM.



**Figure 5.1.2. Vertical plane from the bottom part of as-fabricated cylindrical component**



**Figure 5.1.3. Vertical plane from the top part of as-fabricated cylindrical component**

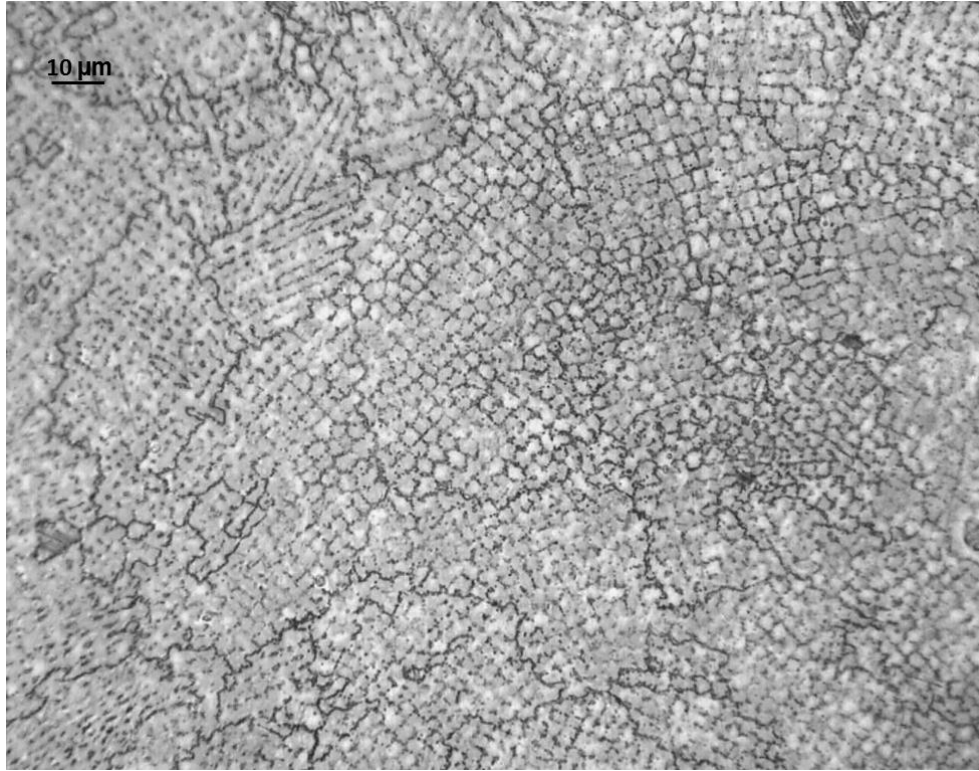


**Figure 5.1.4. Horizontal plane from the bottom part of as-fabricated cylindrical component.**

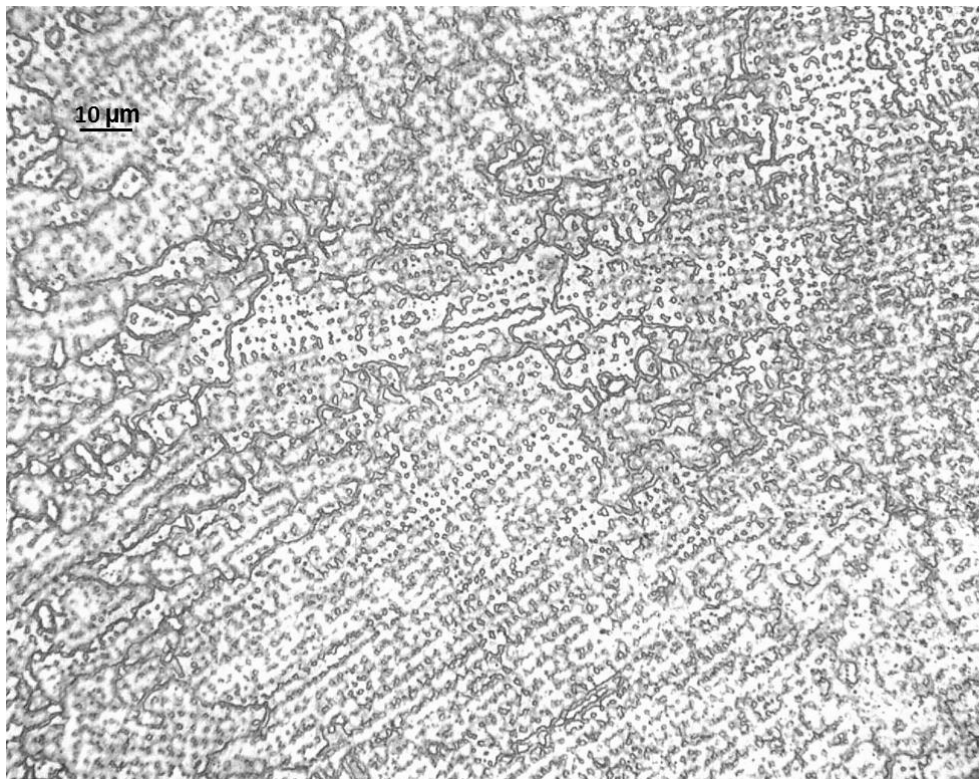


**Figure 5.1.5. Horizontal plane from the top part of as-fabricated cylindrical component.**



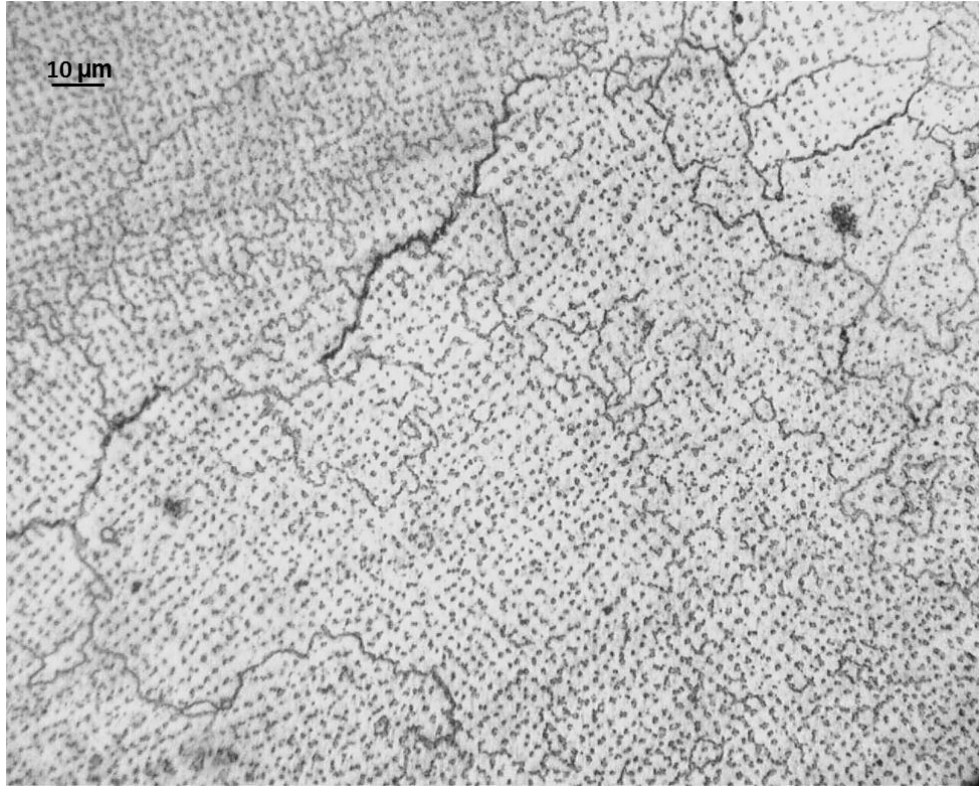


**Figure 5.1.6. Horizontal plane from the top part of as-fabricated cylindrical component.**



**Figure 5.1.7. Horizontal plane from EBM fabricated annealed cylindrical component.**

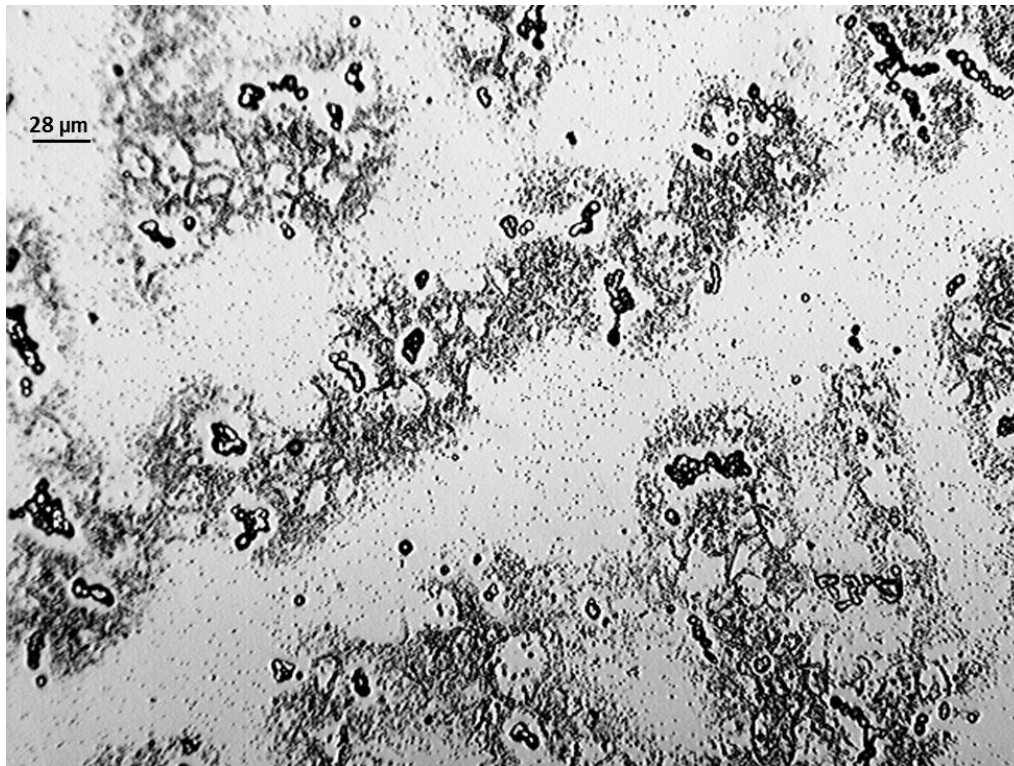


**Figure 5.1.8. Microstructure obtained from body removed Co-Cr-Mo implant**

Finally, the comparison ends with the microstructure obtained for the body removed Co-Cr-Mo femoral knee implant component where microstructure has grown in size probably due to a heat treatment and probably to a somewhat carbon content. According to Tomer, it is generally more common to prefer small grains in your microstructure since each grain has its own orientation providing an anisotropic material (Tomer, 1991), nonetheless, if we consider that by building a component out of EBM and knowing what to expect you can take into consideration the characteristic microstructure obtained by EBM at the time of deciding the building direction of the designed component.

## 5.2 TRANSMISSION ELECTRON MICROSCOPY

Images obtained from the TEM reveal more details than optical imaging. The stacking fault energy of this alloy is  $\sim 15\text{mJ/m}^2$ , and according to Zlateva and Martinova, materials having an SFE less than  $20\text{mJ/m}^2$  have a two-dimensional dislocation distribution, which is more frequent in alloys due to the lowering in SFE. It is energetically more advantageous for dislocations to move by splitting into partials separated by SF, and when the SFE value is low, the SF layer is wider (Zlateva and Martinova, 2008). It is of no surprise that no matter how the alloy was manufactured or what heat treatment was performed, stacking faults were visible in all of them.

Twinning was only observed in the EBM fabricated component after annealing. An important feature of twins is that they do not cross grain boundaries, they can terminate at grain or twin boundaries or inside the grain interior, besides having very low energy due to the perfect fitting of boundary atoms, and they occur during recrystallization of low stacking fault energy materials (Zlateva and Martinova, 2008). For this reason, it can be assumed that the body-removed implant was heat treated since the microstructure grew in size, but no twinning was observed.

TEM imaging for this project revealed characteristic features for each sample. Figure 5.2.1 shows the vertical side of the as-fabricated block component where it can be observed how the precipitates are spread through the sample. Even though figure 5.2.2 doesn't show twinning it can be stated that no precipitates were observed, this image corresponds to the EBM femoral knee component after HIPping and annealing. Figure 5.2.3 corresponds to the body removed femoral knee component showing how precipitates interact with dislocations and stacking faults.



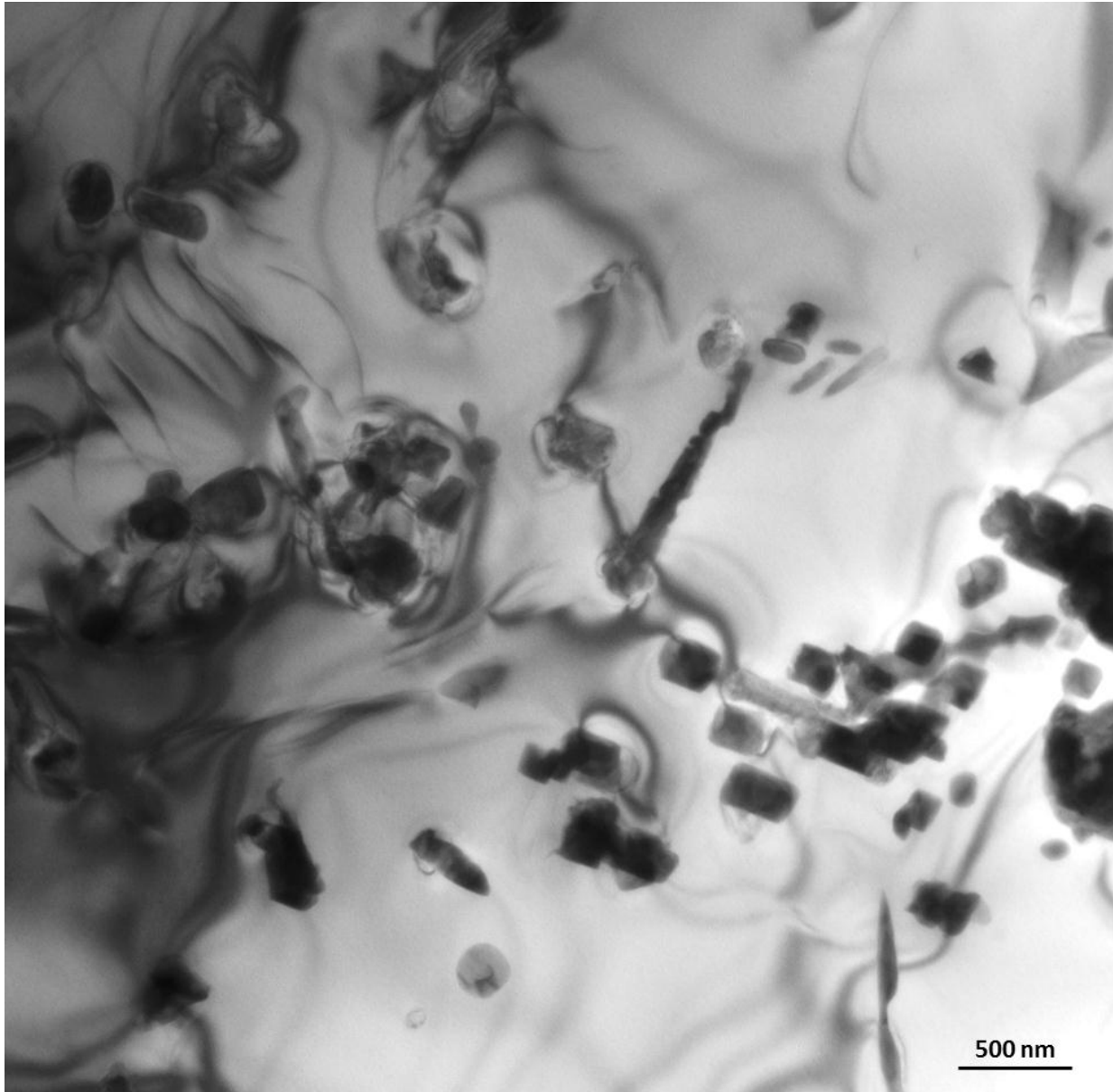


**Figure 5.2.1. a) As fabricated component showing  $\text{Cr}_{23}\text{C}_6$  precipitates.**

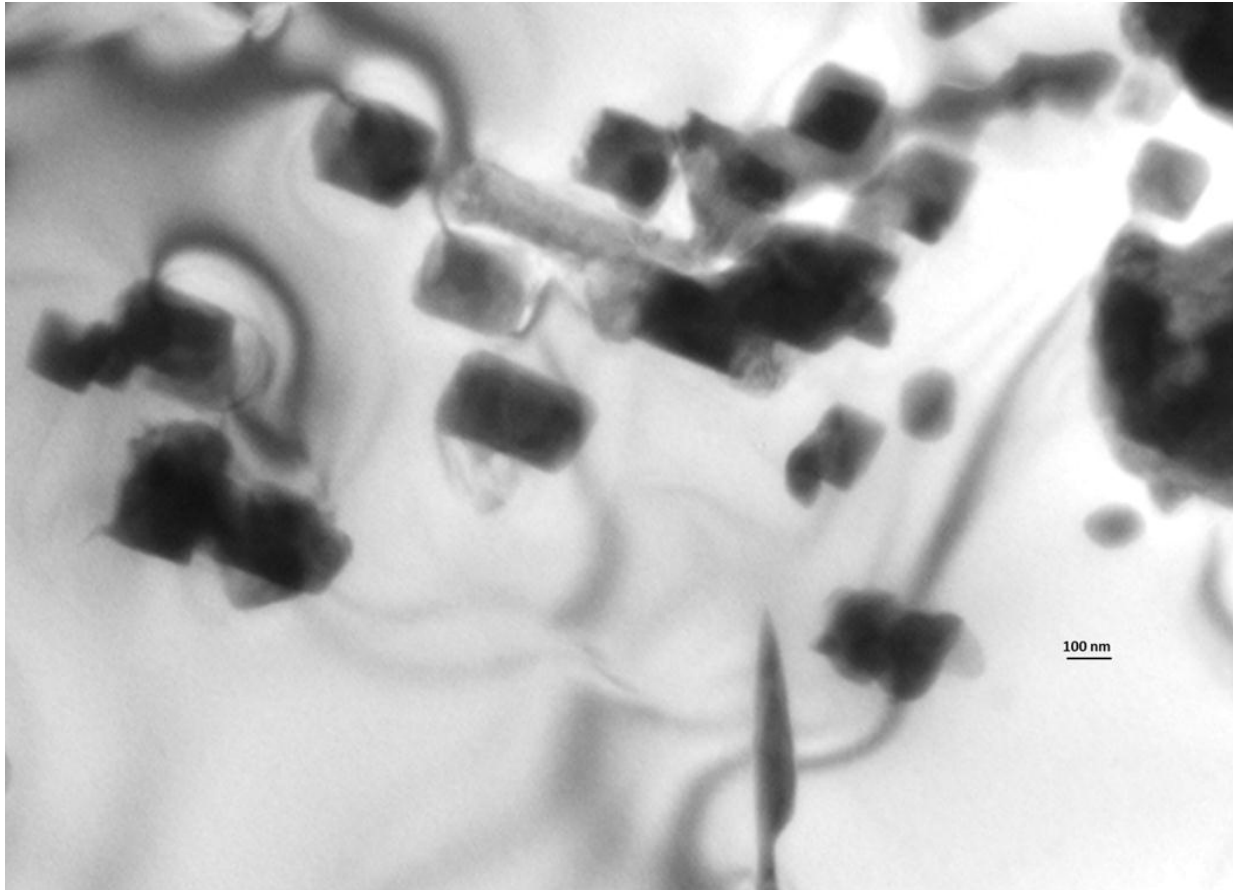


**Figure 5.2.1. b) As fabricated component showing  $\text{Cr}_{23}\text{C}_6$  precipitates magnified.**

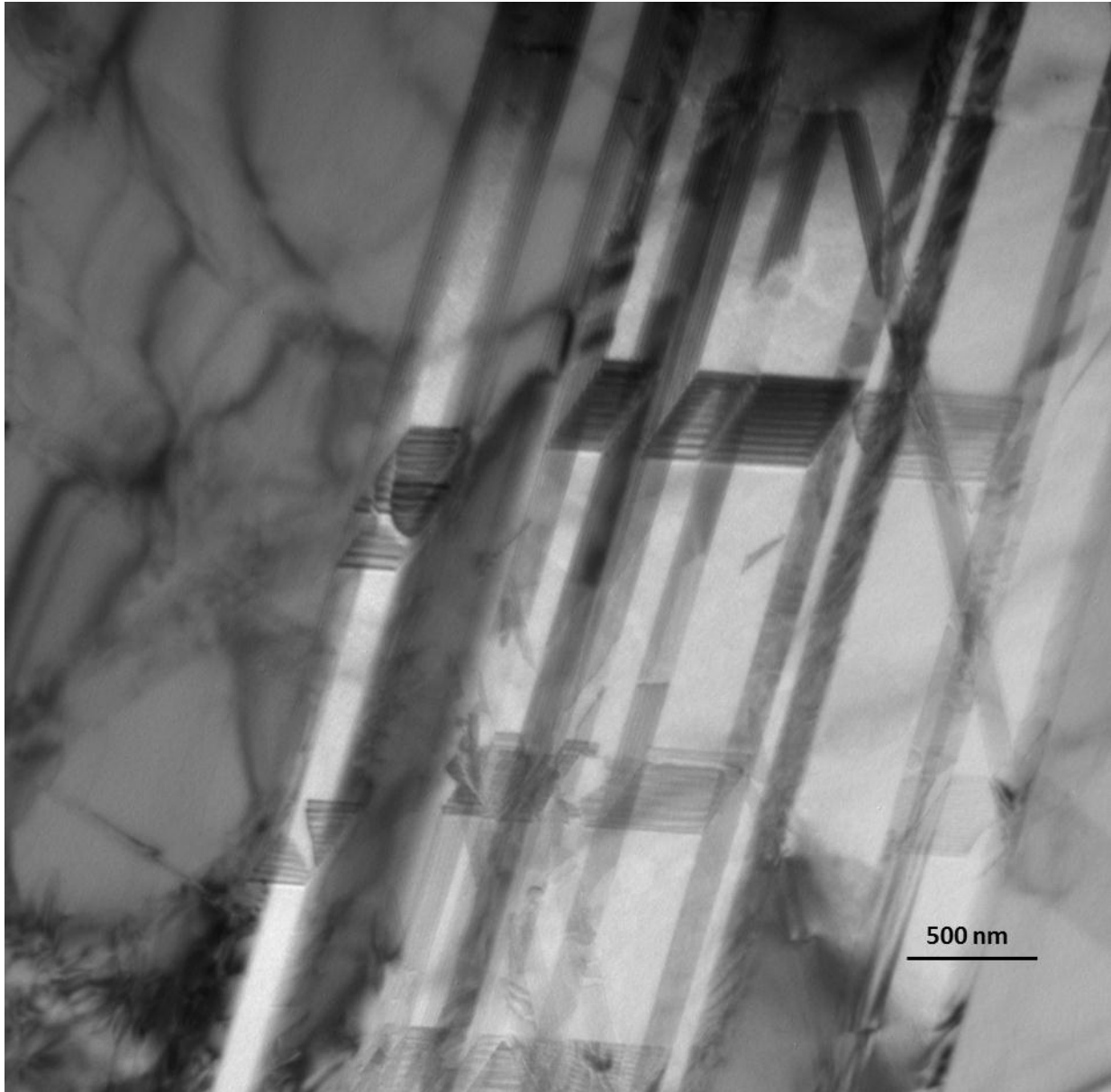


**Figure 5.2.2. EBM fabricated component after annealing.**

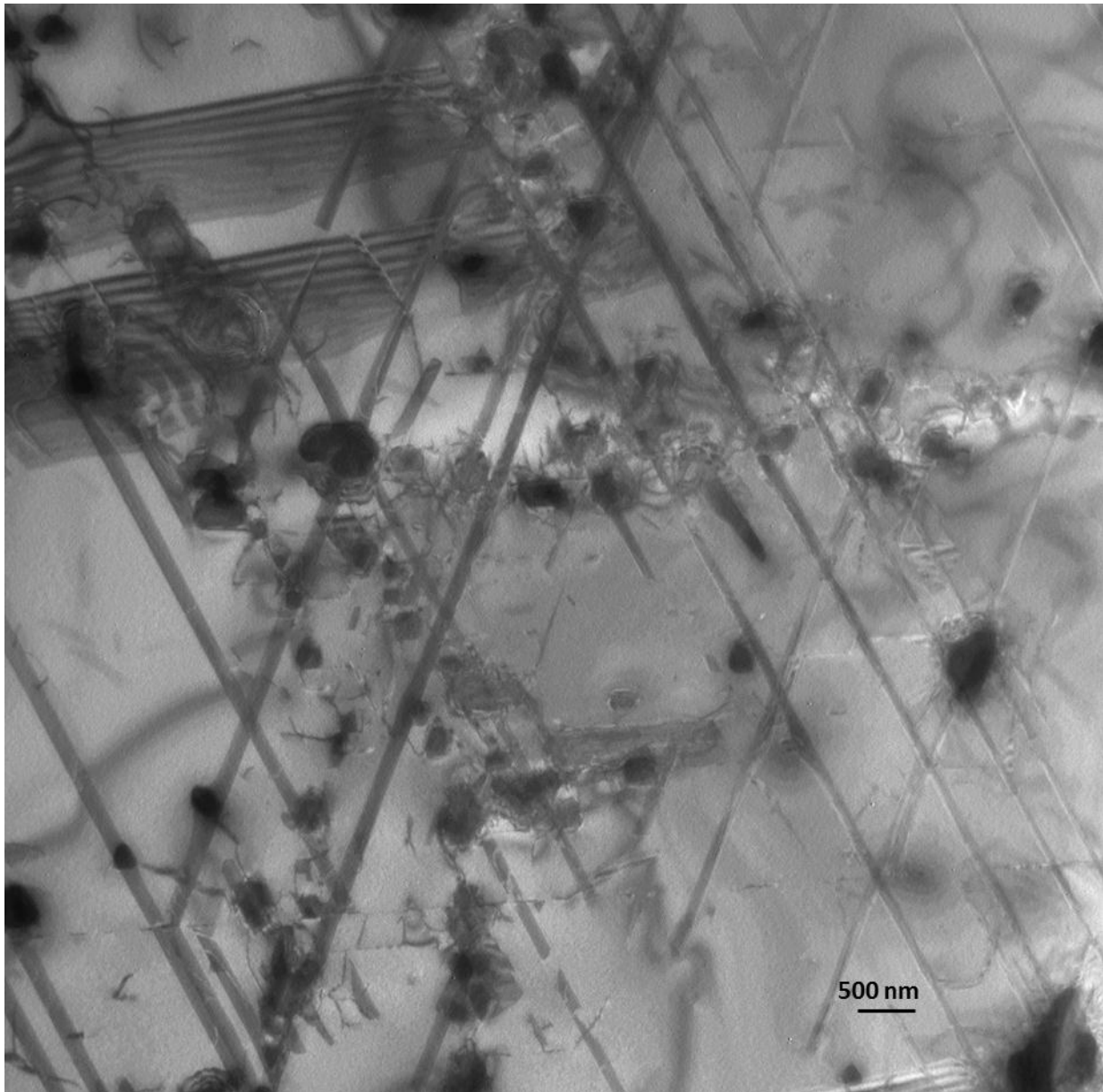


**Figure 5.2.3. Body removed Co-Cr-Mo implant.**

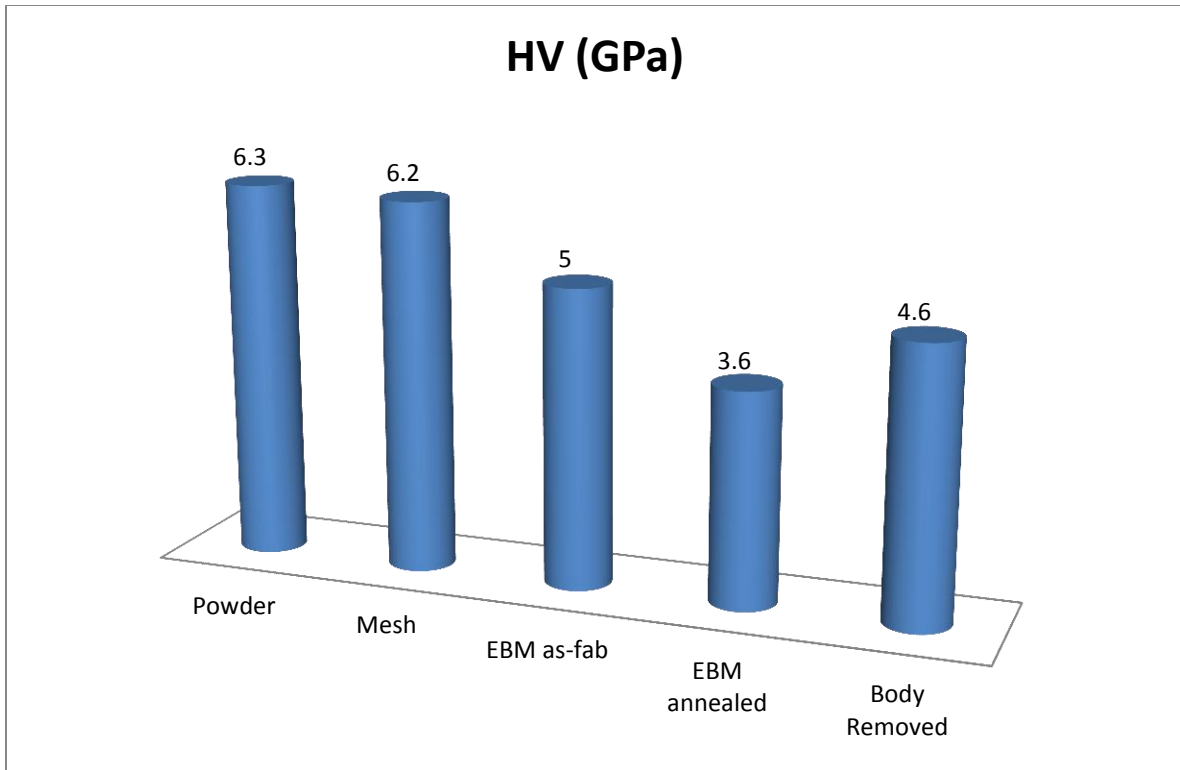
### **5.3 HARDNESS TESTING**

Harness in C scale is different for as-fabricated EBM femoral knee component with an average value of 46 HRC. Once the EBM component was HIPped and annealed, the

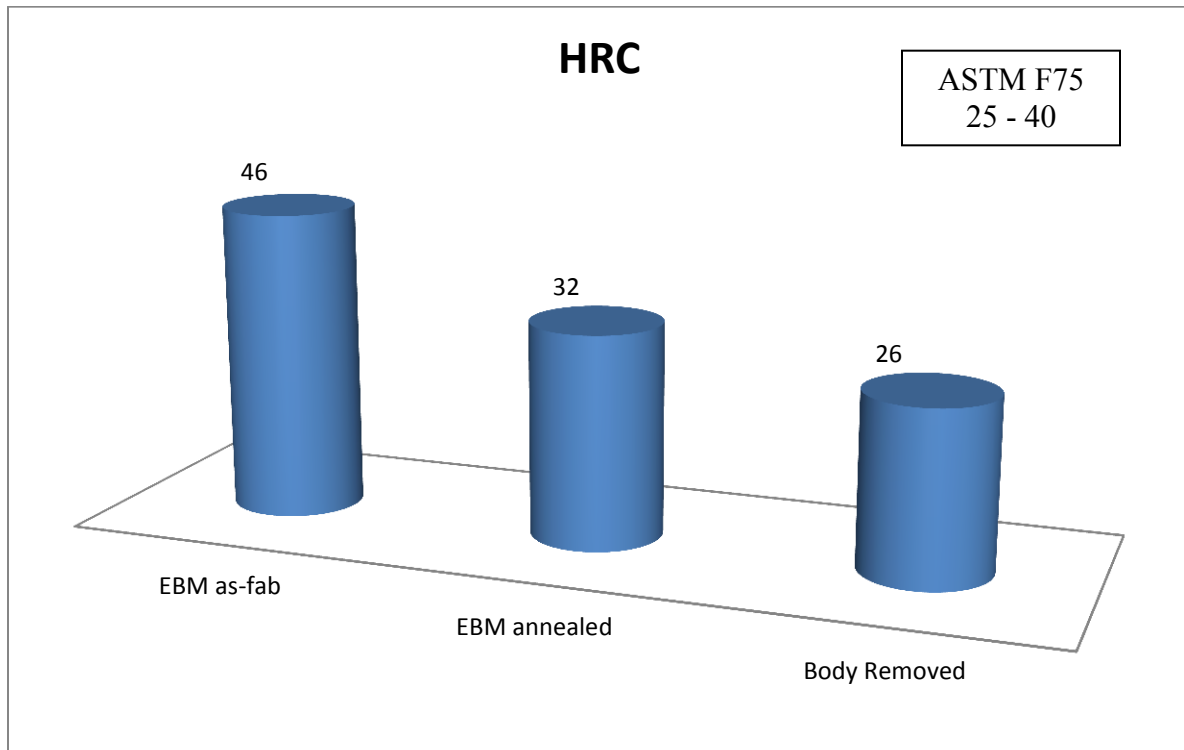
hardness value dropped, as expected, from 46 HRC to an average value of 40 HRC due to the dissolution of precipitates back into the matrix. Even though the hardness value was lower after the heat treatment was performed to the EBM fabricated and treated component it is still a higher value than the body-removed and traditionally manufactured component that provided an average hardness value of 26 HRC. It is important to mention that hardness measurements were taken from the same area in the three components, which is what belongs to the plane parallel to the building direction (vertical plane) in EBM fabricated components.

Figure 5.3.1 shows a better comparison representation where average Vickers hardness has been provided regardless of plane and shape of the component. It can be observed how the highest hardness was obtained for the powder particles and next to it the mesh component. This is due to the cooling rate which is faster for mesh components when compared to solid components, since a finer microstructure is obtained. Having a lower value for the annealed component was not expected since the microstructure obtained for the body-removed implant was bigger. Nonetheless, if we carefully observe Figure 5.3.2, we can see what was expected, that the body-removed implant has the lowest value when compared to EBM components with and without heat treatment. Figure 5.3.2 shows a graphical representation of the Rockwell C-scale hardness averaging components regardless of shape and dimensions and classified only EBM as-fabricated, EBM annealed and body removed.

Many can be the reasons why the HV average value was higher than expected for the body-removed implant, but the more reasonable may be due to the fact that values were only taken from the matrix, and therefore, precipitates were not considered for hardness measurements as compared to Rockwell C-scale hardness testing.



**Figure 5.3.1 HV in GPa comparison.**



**Figure 5.3.2 HRC comparison.**

## 5.4 TENSILE TESTING

Since tensile testing could only be performed from cylindrical and block samples, no comparison could be made with the body-removed femoral knee component. Solid cylinders were used to pull the samples in the direction parallel to the building direction, while block components were machined so that the pulling axis was perpendicular to the building direction. Table II shows the results summarized. The main feature to consider from this table is that the highest elongations obtained were for the HIPped and annealed components regardless of the direction, but specially for the samples pulled parallel to the building direction. If comparing both samples pulled in the same direction, it can be observed how the yield strength was increased for the samples HIPped in the direction parallel to the building direction and how it is lower for the HIPped samples in the direction perpendicular to the building direction. An observation to these results is the fact that no matter what direction the sample was pulled, the ultimate tensile strength was always higher for the HIPped samples. It must be stated that Table II was performed utilizing averages of at least two samples, and (z) corresponds to samples pulled and fabricated in the direction parallel to the pulling axis, while (x,y) corresponds to tensile specimens imitating components fabricated and pulled in the direction perpendicular to the building direction. ASTM F75 standards for wrought and cast Co-base alloys are added for comparison purposes.

**Table 2. Tensile testing results.**

<b>Direction</b>	<b>YS (GPa)</b>	<b>UTS (GPa)</b>	<b>Elongation (%)</b>
<b>EBM (z)</b>	0.51	1.45	3.6
<b>EBM (z) + HIP</b>	0.60	1.15	32
<b>EBM (x,y)</b>	0.77	0.84	2.7
<b>EBM (x,y) + HIP</b>	0.63	0.99	20
<b>ASTM F75</b>	0.5	0.9	<1 to ~5

## 5.5 X-RAY DIFFRACTION

Since carbides provide a huge impact on the materials properties it is important to know how to make better use of them. It is stated that in most superalloys,  $M_{23}C_6$  carbides form at the grain boundaries after a postcasting or postsolution treatment, and this is known to optimize creep-rupture life by preventing grain boundary sliding while providing sufficient ductility in the surrounding grain for stress relaxation to occur without premature failure. On the other side, if carbides precipitate as a continuous grain-boundary film the properties are severely degraded. It has been reported that  $M_{23}C_6$  films reduced impact resistance in different nickel-based alloys and rupture lives and ductility were lowered. Nevertheless, when no grain boundary carbide precipitate is present, premature failure will also occur because grain boundary movement is essentially unrestricted, leading to subsequent cracking at grain boundary triple points (Bradley, 1988).

It can be stated that fabricated components by EBM can generate  $Cr_{23}C_6$  precipitates in a columnar fashion and they can also be dissolved back into the matrix and segregate into the grain boundaries after annealing. Figure 5.5.1 shows the comparison of the powder with the EBM fabricated components before and after annealing as well as the Co-Cr-Mo body removed implant. If we look at this image we can see how peaks seem to be shifting to the left by a few degrees, where different components match, especially the carbides. If we observe Figure 4.1.7 no carbides would match in that spectrum, we only obtained a match after the powder went through the EBM process. For the body-removed implant we can say that the few peaks observed somehow match the peaks for the EBM fabricated and annealed components, but if we go back to Figure 4.4.8 it is easier to see how the peak shift provides a better match with  $Cr_3C_2$  (bco) and  $Co_7Mo_6$  (r) not observed before.



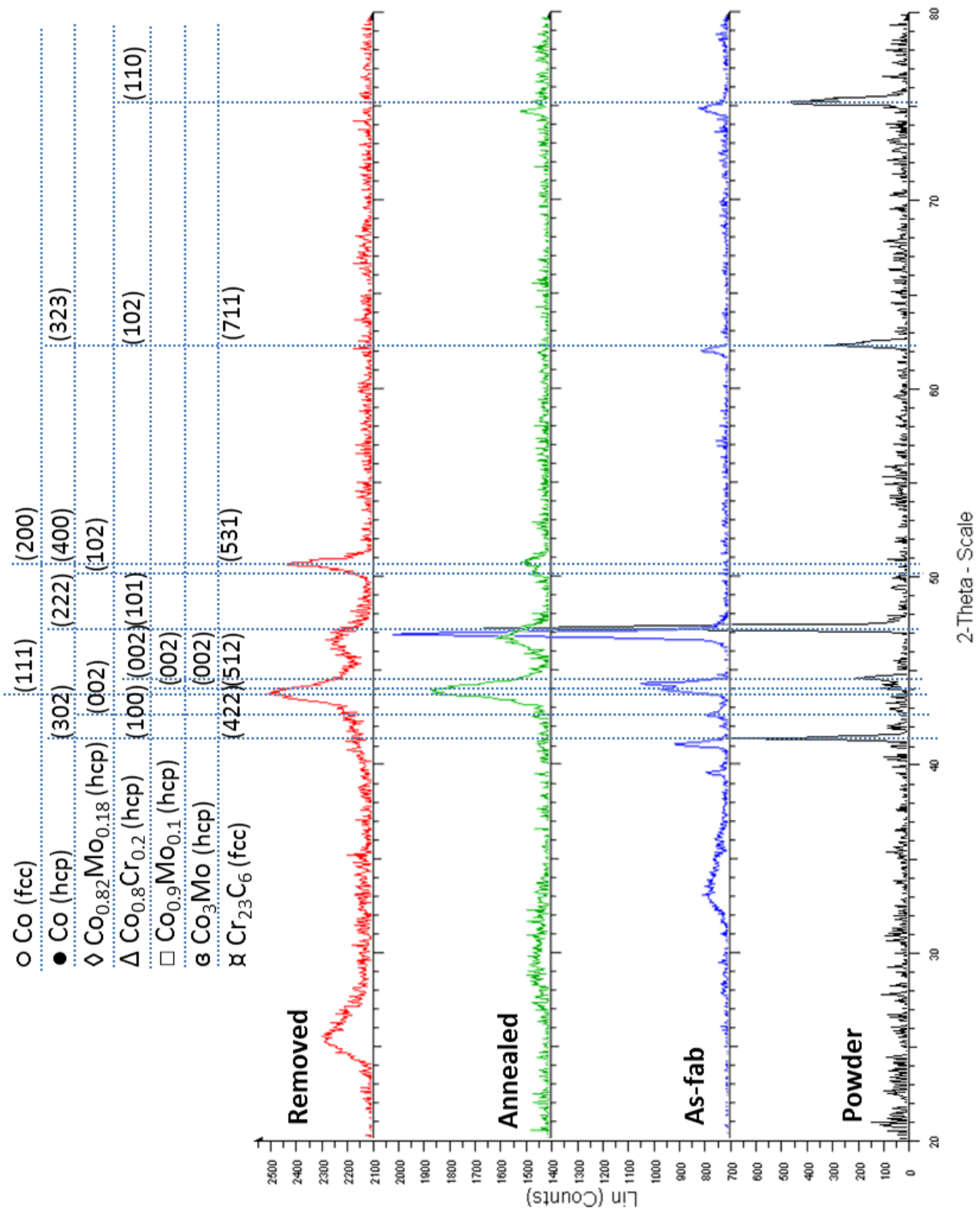


Figure 5.5.1. XRD comparison.

## CHAPTER 6

### CONCLUSIONS

These results demonstrate the concept of materials with controlled microstructural architecture (MCMA) which can be considered a fundamental extension of the traditional material-science and engineering paradigm which relates structure, properties, process, and performance as illustrated in figure 6.1. The ability to control or develop microstructural architectures adds an additional feature for this paradigm where properties, processing and performance may be linked not only by microstructure, but for selective or systematic organization of microstructures into architectures or architectural arrays. The EBM processing, which creates small ( $\sim 2\mu\text{m}$ ) melt pool domains which are linked by scanning across each powder layer, allows  $\text{Cr}_{23}\text{C}_6$  carbides to form within these domain arrays, and they are propagated in columns as each layer is added. Although the beam or other EBM processing parameters have not been selectively altered in this work, it may be possible to change the precipitate size or spacing within the melt column arrays. Adding carbon to the alloy may also contribute to higher carbide precipitate density and thereby alter the residual properties by forming denser or continuously carbide columns.

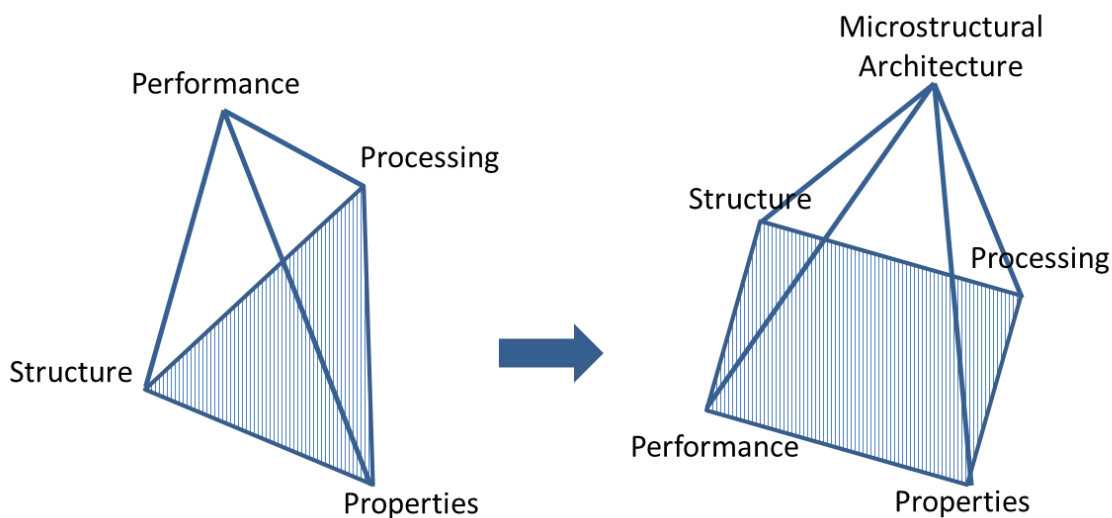


Figure 6.1. Materials science and engineering paradigm extension

Comparison for this project is basically based on EBM fabricated components versus the body removed Co-Cr-Mo knee implant. So far it can be stated that EBM fabricated components show to be more promising basically for two reasons. Implants fabricated by EBM can be customized or in other words they can be patient specific, meaning that the patient in need of an implant can obtain a better fit out of the same. The second reason is that implants, besides showing outstanding mechanical properties, can be fabricated including a mesh portion which will allow for the bone to grow into the implant and therefore obtain a better fixation besides the advantage of having a lighter component due to the porosity included in the implant.

- By comparing microstructures, EBM as-fabricated components provide better properties due to the alignment of the carbides when it is as-fabricated. Once the component is annealed, properties, such as hardness, are less promising since grain growth with precipitates concentrating at the low energy grain boundaries occur. TEM work confirms what stated even though no precipitates or even boundaries could be observed in the annealed components.

- Since there is no background available on the body-removed implant, from the microstructure observed it can be stated that it was probably annealed, and providing a microstructural growth. By looking at the TEM images it can be stated that the body-removed Co-Cr-Mo went under some work hardening treatment after the annealing since dislocations were observed at locations close to the precipitates.

- Hardness testing, especially Rockwell C-scale, shows a nice representation of what would be expected from the microstructure, EBM as-fabricated components show the highest hardness with a value of 46 while the body-removed Co-Cr-Mo component shows the lowest with a value of 26. Again, this was expected after observing the microstructure of each component. It can be observed how EBM-

fabricated components show a higher hardness compared to ASTM F75 Co-base alloy standards, even after performing the annealing treatment.

- Since tensile testing could not be performed on the body-removed implant obtained, comparison could not be made in this section, but it can be concluded that EBM fabricated components can obtain ductility that is visible even to our naked eye, by observing at the necking obtained after pulling the tensile specimens. It can be concluded that EBM Co-Cr-Mo components are capable of increasing their percent elongation from  $\sim 2.7$  for components fabricated in the direction perpendicular to the building direction to  $\sim 20\%$  after annealing the components. In the same way, EBM fabricated component in the direction parallel to the building direction can increase their percent elongation from  $\sim 3.6\%$  to  $32\%$  after annealing.

- From the XRD results the main conclusion is that EBM fabricated components before and after annealing show  $\text{Cr}_{23}\text{C}_6$  precipitates while the body removed implant shows  $\text{Cr}_3\text{C}_2$ . Another big difference is the type of components present, which are responsible for the mechanical properties and microstructure obtained.

More traditional implant fixtures, such as the body-removed fixture, have no features for enhanced biocompatibility by bone cell ingrowth into porous structures. Attempts to coat these fixtures have been made, but this is not an efficient methodology. The huge Ti-6Al-4V stem attached to the body-removed implant can also be eliminated by better attachment design. EBM fabrication can produce complex monoliths with sufficient, efficient open-cellular structures. Furthermore, micro CT can provide patient-specific design strategies for building optimal fixtures for the patient. This research has demonstrated these features and systematically examined their corresponding microstructures and mechanical properties.

## REFERENCES

- Alamert, S., and Bhadeshia, H.K.D.H. 1989. Comparison of the microstructure and abrasive wear properties of Stellite hardfacing alloys deposited by arc welding and laser cladding. *Metals Technol.* 20. 1037-1054.
- Antony, K. C. 1983. Wear-resistant cobalt base alloys. *J. metals* 35 (1983) 52-60.
- ARCAM A2. 2011. Setting the Standards for Additive Manufacturing.  
<<http://www.arcam.com/CommonResources/Files/www.arcam.com/Documents/Products/Arcam-A2.pdf>>
- ARCAM. 2011a. ASTM F75 CoCr Alloy. Arcam EBM system.  
<<http://www.arcam.com/CommonResources/Files/www.arcam.com/Documents/EBM%20Materials/Arcam-ASTM-F75-Cobalt-Chrome.pdf>>
- Askeland, D. R., and Phule, P. P. 2006. *The Science and Engineering of Materials*, Fifth Edition. Nelson, a division of Thomson Canada Limited.
- ASM International. 2004. *Metallography and Microstructures*. ASM Handbook, Volume 9, pg 964.
- Battelle Memorial Institute. 1960. Cobalt Monograph. Centre D'Information Du Cobalt
- Bertol, L. S., et al. 2010. Medical Design: Direct Metal Laser Sintering of Ti-6Al-4V. *Materials and Design*. Doi: 10.1016/j.matdes.2010.02.050.
- Betteridge, W. 1982. Cobalt and its alloys. Printed in Great Britain by R. J. Acford, Chichester.
- Bradley, E. F. 1988. *Superalloys. A technical guide*. ASM International.
- Campbell, F. C. 2008. *Elements of Metallurgy and Engineering Alloys*. ASM International.
- Cawley, J., et al. 2003. A tribological study of cobalt chromium molybdenum alloys used in metal-on-metal resurfacing hip arthroplasty. *Science direct, wear* 255. 999-1006.
- Chua, C. K. et al., 2003. *Rapid Prototyping. Principles and Applications*. 2<sup>nd</sup> Edition. World Scientific Publishing Co. Pte. Ltd.
- Cristofolini, L., et al. 2009. Implant fixation in knee replacement: Preliminary in vitro comparison of ceramic and metal cemented femoral components. *The knee* 16. 101-108.
- Durand-Charre, M. 1997. *The Microstructure of Superalloys*. Overseas Publishers Association.
- Escobedo, J., et al. 1996. Effects of nitrogen on the microstructure and mechanical properties of a Co-Cr-Mo alloy. *Materials Design* 17 (2). 79-83.
- España, F. A., et al. 2010. Design and fabrication of CoCrMo alloy based novel structures for load bearing implants using laser engineered net shaping. *Materials Science and Engineering C* 30. 50-57.
- Gaytan, S. M., et al. 2010. Comparison of Microstructures and Mechanical Properties for Solid and Mesh Cobalt-Base Alloy Prototypes Fabricated by Electron Beam Melting. *Metallurgical and Materials Transactions A*. Vol. 41, No. 12, pp. 3216-3227.

- German, R. M. 2005. A Z of Powder Metallurgy. Metal Powders Technology Series: Bernard Williams.
- Higuchi, F., et al. 1997. Metal-on-metal CoCrMo McKnee-Farrar total hip arthroplasty: characteristics from a long-term follow-up study. Arch Orthop Trauma Surg. 116. 121-124.
- Janaki, G. D. 2008. Microstructure and wear properties of LENS deposited medical grade CoCrMo. J Mater Sci: Mater Med 19. 2105-2111.
- Kilner, T., et al. 1982. Phase identification and incipient melting in a Co-Cr surgical implant alloy. J. Biomed. Mater. Res. 16, 63-79.
- Marti, A. 2000. Cobalt-base alloys used in bone surgery. Injury, Int. J. Care Injured 31. S-D18-21.
- Murr, L. E. and Stein, C. 1976. Frontiers in Materials Science. Distinguished Lectures. Marcel Decker, Inc. Chapter 12. 421-454.
- Murr, L. E. et al. 2009c. Metallographic Characterization of Additive-Layer Manufactured Products by Electron Beam Melting of Ti-6Al-4V Powder. Practical Metallography.
- Murr, L. E., et al. 2009a. Microstructure and mechanical behavior of Ti-6Al-4V produced by rapid-layer manufacturing, for biomedical applications. Journal of the Mechanical Behavior of Biomedical Materials, Vol 2, (1). 20-32.
- Murr, L. E., et al. 2009d. Microstructures and mechanical properties of electron beam-rapid manufactured Ti-6Al-4V biomedical prototypes compared to wrought Ti-6Al-4V. Materials characterization 60, pg 96-105.
- Murr, L.E. et al. 2009b. Advanced Metal Powder Based Manufacturing of Complex Components by Electron Beam Melting. Materials Technology. Vol 24, No. 3. 180-190.
- Ning, Y., et al., 2005. Effects of fabrication process and coating of reinforcements on the microstructure and wear performance of Stellite alloy composites. Materials Science and Engineering A 391. 313-324.
- Noorani, R. 2006. Rapid Prototyping. Principles and Applications. John Wiley & Sons, Inc
- Oshida Y. 2007. Bioscience and Bioengineering of Titanium Materials. Elsevier.
- Pham, D. T., et al. 2002. Rapid manufacturing - the technologies and applications of rapid prototyping and rapid tooling. Book review/Materials and Design (23) 345-350.
- Radu, Iulian., et al. 2004. Tribological behavior of Stellite 21 modified with yttrium. Wear 257. 1154-1166.
- Ramsdale, R. Engineers handbook. 2004-2006.  
<<http://www.engineershandbook.com/RapidPrototyping/ebm.htm>>
- Reed, R. C. 2006. The Superalloys. Fundamentals and Applications. Cambridge University Press.

- Ryan, G., et al. 2006. Fabrication methods of porous metals for use in orthopaedic applications. *Biomaterials* 27. 2651-2670.
- Shetty, R.H. 1995. WI-I Metals in Orthopedic Surgery. *Encyclopedic Handbook of Biomaterials and Bioengineering* (1).
- Shin, J., et al. 2003. Effect of molybdenum on the microstructure and wear resistance of cobalt-base Stellite alloys, *Surf. Coat. Technol.* 166. 117-126.
- Sims, C. T. et. al. 1987. *Superalloys II*. John Wiley & Sons, Inc.
- Society of Manufacturing Engineers. 2009. SEM Honors Rapid Prototyping Practitioners and Researchers at RAPID 2009. <<http://www.sme.org/cgi-bin/get-press.pl?&&20090030&PR&&SME&>>
- Tomer, A.1991. *Structure of Metals Through Optical Microscopy*. ASM International, translated by L and C. E. Robinson.
- Ulf, A. e-mail message to author. May, 5<sup>th</sup>, 2011.
- Vail, N. K., et al. 1999. Materials for biomedical applications. *Materials and Design* 20. 123-132. 22
- Wohlers, T. 2010. *Wohlers Report 2010. Additive Manufacturing State of the Industry. Annual Worldwide Progress Report*. Wohlers Associates, Inc.
- Yan, X. and Gu, P. 1996. Survey: A review of rapid prototyping technologies and systems. *Computer-Aided Design*. Vol 28, No. 4. 307-318.
- Yongnian, Y., et al. 2009. *Rapid Prototyping and Manufacturing Technology: Principle, Representative Technics, Applications, and Development Trends*. Tsinghua Science and Technology, 14 (S1) 1-12.
- Zlateva and Martinova. 2008. *Microstructure of Metals and Alloys. An Atlas of Transmission Electron Microscopy Images*. CRC Press, Taylor and Francis Group.

## APPENDIX

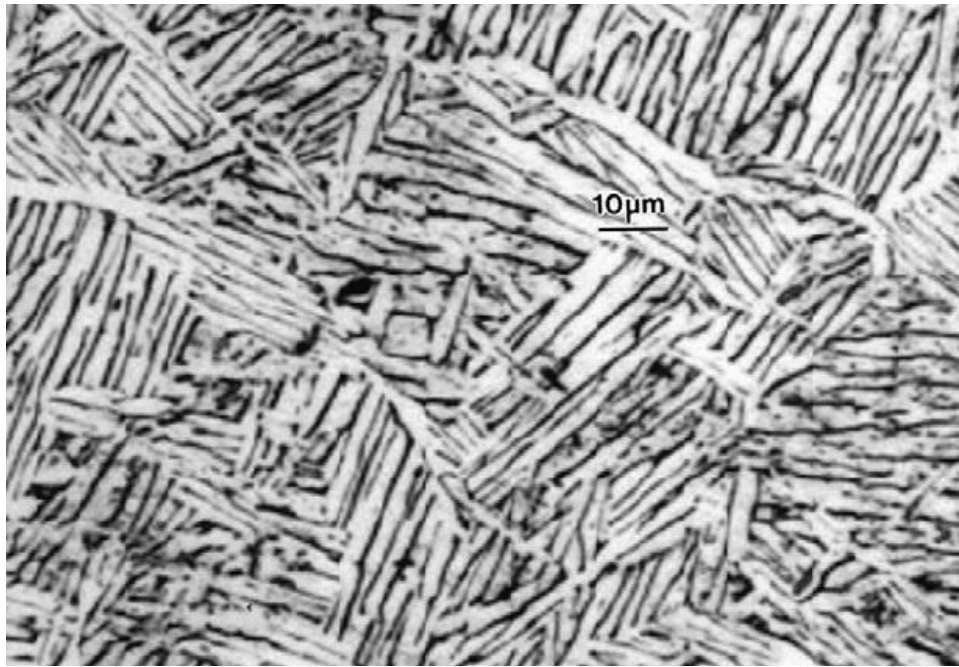


**Figure 1. Optical micrograph showing acicular  $\alpha$  -phase microstructure for a solid EBM cylindrical component. Hardness was 3.5 GPa (Murr, 2010)**

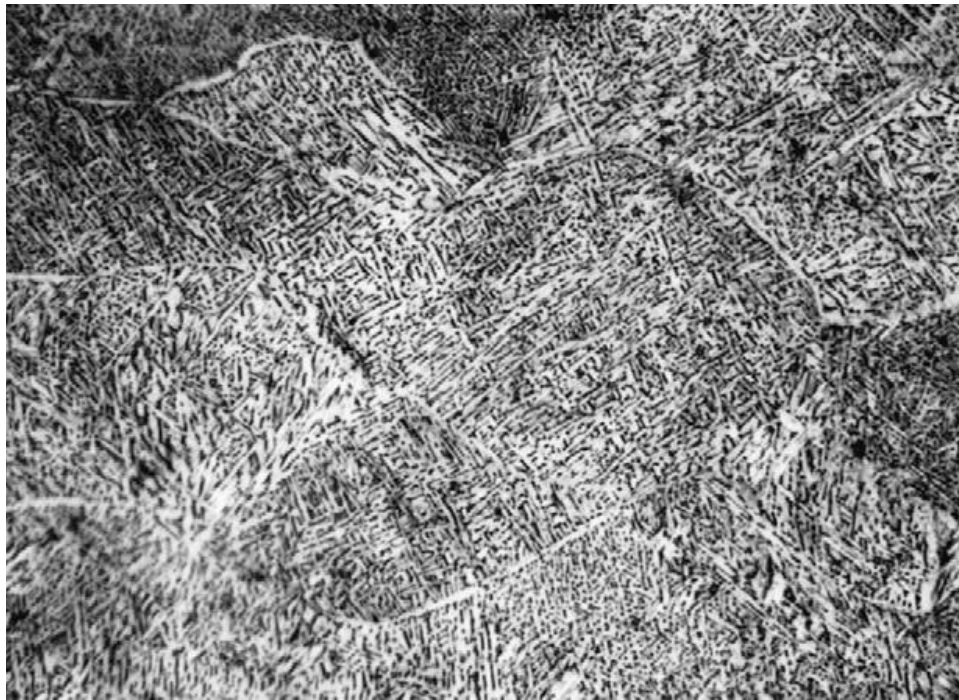


**Figure 2. 1.1mm thick strip in a test element , showing refined  $\alpha'$  and  $\beta'$  phase (dark dots), where the hardness was 4.8 GPa. Same magnification as figure 1 (Murr, 2010).**



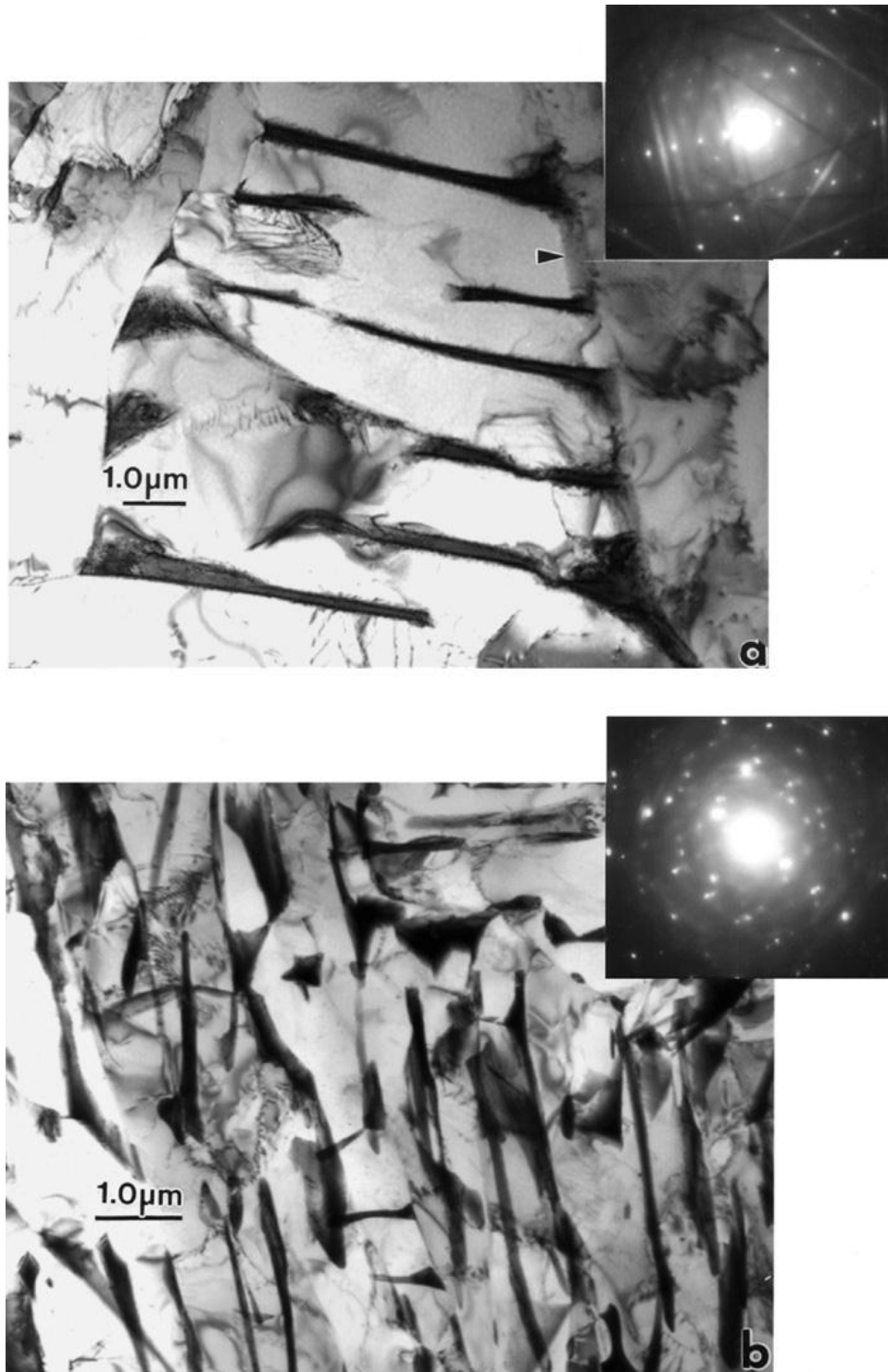


**Figure 3.** TEM bright-field images corresponding to figures 1 and 2. (a) Solid monolith exhibiting 2  $\mu\text{m}$  wide  $\alpha$ -platelets with  $\beta$ -phase boundaries. Arrow denotes an  $\alpha/\alpha$  grain boundary. (b) 1.1 mm test plate TEM image illustrating refined  $\beta$  (dark). The selected area electron diffraction (SAED) pattern insert in (a) shows the  $\alpha$ -phase (hcp) (0 0 1) plane while the SAED pattern insert in (b) shows additional, multiple diffraction spots from the refined  $\beta$ -phase (Murr, 2010).

- Murr, L. E., Gaytan, S. M., et al. 2010 “Characterization of Ti-6Al-4V open cellular foams fabricated by additive manufacturing using electron beam melting” *Materials Science and Engineering A*, 527, pp. 1861-1868.
- Gaytan, S. M., et al. 2010. Comparison of Microstructures and Mechanical Properties for Solid and Mesh Cobalt-Base Alloy Prototypes Fabricated by Electron Beam Melting. *Metallurgical and Materials Transactions A*. Vol. 41, No. 12, pp. 3216-3227.
- Gaytan, S. M., et al. 2011. A TEM Study of Cobalt-Base Alloy Prototypes Fabricated by EBM. *Materials Sciences and Applications*, 2011, Vol. 2, pp. 355-363. Published Online May 2011 (<http://www.SciRP.org/journal/msa>)

# Comparison of Microstructures and Mechanical Properties for Solid and Mesh Cobalt-Base Alloy Prototypes Fabricated by Electron Beam Melting

S.M. GAYTAN, L.E. MURR, E. MARTINEZ, J.L. MARTINEZ, B.I. MACHADO, D.A. RAMIREZ, F. MEDINA, S. COLLINS, and R.B. WICKER

The microstructures and mechanical behavior of simple, as-fabricated, solid geometries (with a density of 8.4 g/cm<sup>3</sup>), as-fabricated and fabricated and annealed femoral (knee) prototypes, and reticulated mesh components (with a density of 1.5 g/cm<sup>3</sup>) all produced by additive manufacturing (AM) using electron beam melting (EBM) of Co-26Cr-6Mo-0.2C powder are examined and compared in this study. Microstructures and microstructural issues are examined by optical metallography (OM), scanning electron microscopy (SEM), transmission electron microscopy (TEM), energy-dispersive X-ray spectrometry (EDS), and X-ray diffraction (XRD), while mechanical properties included selective specimen tensile testing and Vickers microindentation hardness (HV) and Rockwell C-scale hardness (HRC) measurements. Orthogonal (X-Y) melt scanning of the electron beam during AM produced unique, orthogonal and related Cr<sub>23</sub>C<sub>6</sub> carbide (precipitate) arrays (a controlled microstructural architecture) with dimensions of ~2  $\mu$ m in the build plane perpendicular to the build direction, while connected carbide columns were formed in the vertical plane, parallel to the build direction, with microindentation hardnesses ranging from 4.4 to 5.9 GPa, corresponding to a yield stress and ultimate tensile strength (UTS) of 0.51 and 1.45 GPa with elongations ranging from 1.9 to 5.3 pct. Annealing produced an equiaxed fcc grain structure with some grain boundary carbides, frequent annealing twins, and often a high density of intrinsic {111} stacking faults within the grains. The reticulated mesh strut microstructure consisted of dense carbide arrays producing an average microindentation hardness of 6.2 GPa or roughly 25 pct higher than the fully dense components.

DOI: 10.1007/s11661-010-0388-y

© The Minerals, Metals & Materials Society and ASM International 2010

## I. INTRODUCTION

COBALT-BASE alloys or cobalt-base superalloys (most commonly known as Deloro Stellite\* alloys)

---

\*Deloro Stellite is a registered trademark of Deloro Stellite, St. Louis, MO.

---

have been used extensively in cast and hardfacing forms over the past 2 decades.<sup>[2-4]</sup> Typical applications have involved a variety of bearing materials or high temperature and high wear resistance applications such as valve seats in nuclear power plants, automobile engines, aerospace fuel nozzles, and engine vanes and components, as well as biomedical implants.<sup>[5-7]</sup> Common Stellite compositions include the standard Co-base alloy, Stellite 21 (with a nominal composition of

27 pct Cr, 5.5 pct Mo, 3 pct Fe, 2 pct Ni, 1 pct each Si and Mn, and 0.25 pct C; balance Co, in weight percent). A popular variance includes the Co-27Cr-5Mo-0.05 C alloy or stoichiometric ranges encumbered under ASTM F75 standards: 27 to 30 pct Cr, 5 to 7 pct Mo, <0.35 pct C, <1 pct Si, Mn, <0.25 Fe, <0.5 Ni, balance Co in weight pct, which apply to the preferred cobalt-base alloy for biomedical (implant) applications. While pure cobalt is characterized by an  $\epsilon$  (hcp) low-temperature phase and an fcc,  $\gamma$  phase at higher temperature, the addition of Cr improves the corrosion and oxidation resistance as well as the hardness, ductility, and wear resistance through carbide formation: Cr<sub>23</sub>C<sub>6</sub> (also Cr<sub>17</sub>Co<sub>4</sub>Mo<sub>2</sub> C<sub>6</sub>), M<sub>6</sub>C, and M<sub>7</sub>C<sub>3</sub>, depending upon the carbon content and kinetics. Molybdenum acts as a solid-solution strengthener by forming the intermetallic Co<sub>3</sub>Mo (hcp phase) as well as improving the corrosion resistance of the alloy.<sup>[5]</sup>

The  $\epsilon$  (hcp)  $\rightarrow$   $\gamma$  (fcc) transformation in pure Co takes place at 703 K (430 °C) ( $A_s$ ), while the reversible  $\gamma \rightarrow \epsilon$  transformation occurs on cooling at 663 K (390 °C) ( $M_s$ ). However, upon alloying with Cr and other elements as noted,  $A_s$  is increased significantly. For example,  $A_s$  is 1243 K (970 °C) for the Co-27Cr-5Mo-0.05C alloy.<sup>[8]</sup> The  $\gamma \rightarrow \epsilon$  transformation is also induced by plastic deformation or quenching from the temperature range of the stable  $\gamma$  phase.<sup>[9]</sup> Cooling from the

---

S.M. GAYTAN, B.I. MACHADO, and D.A. RAMIREZ, Graduate Students, L.E. MURR, Murchison Professor and Chairman, and E. MARTINEZ and J.L. MARTINEZ, Undergraduate Students, Department of Metallurgical and Materials Engineering, and F. MEDINA, Graduate Student, and R.B. WICKER, Professor, Keck Center for 3D Innovation, are with The University of Texas at El Paso, El Paso, TX 79968. Contact e-mail: lemurr@utep.edu S. COLLINS, Consultant, is with Additive Manufacturing Processes, Camarillo, CA 93012.

Manuscript submitted February 22, 2010.

Article published online August 21, 2010



melt produces primarily  $\gamma$  (fcc), while rapid solidification can produce mixed phase systems as noted previously, including carbides.<sup>[2]</sup>

Traditional surgical implant Co-base alloys over the past several decades have been produced in cast or wrought forms<sup>[10,11]</sup> and heat treated to develop requisite properties under ASTM F75 or similar standards. These standards are characterized by residual hardnesses ranging from Rockwell C-scale hardness (HRC) 25 to 40, ultimate tensile strength (UTS)/yield stress of 0.9 GPa/0.5 GPa and <1 to ~5 pct elongations for cast and wrought products, respectively. Recent experimental production of Co-Cr-Mo alloy by laser powder microdeposition<sup>[12]</sup> has been shown to have microstructures similar to Co-based (Stellite) hardfacing alloys deposited by arc welding and laser cladding<sup>[6]</sup> to develop abrasive wear features.

We have recently conducted extensive studies and evaluations of a number of Ti-6Al-4V prototype products fabricated by additive manufacturing (AM) using electron beam melting (EBM).<sup>[13–18]</sup> These have included various simple, solid geometries as well as reticulated mesh arrays,<sup>[17]</sup> open cellular foams,<sup>[17,18]</sup> and complex, multifunctional components having varying densities and geometries for innovative applications in biomedical, aeronautical, and automotive areas.<sup>[17–19]</sup> EBM fabrication is a relatively new manufacturing concept involving solid freeform fabrication, which can create complex products from precursor powders by selectively melting individual powder layers using a computer-aided design (CAD) system to direct the electron beam. This layer building is particularly compatible with digital layer data such as that which characterizes CT scans, and these allow for the development of CAD programs.

This article describes fundamental and applied research involving the fabrication of Co-26Cr-6Mo-0.2C (cobalt-base alloy) components by EBM. The components included several simple/solid (fully dense) geometries, specialized biomedical prototypes, and reticulated mesh arrays. These components were examined by optical metallography (OM), scanning electron microscopy (SEM, including energy-dispersive X-ray spectrometry (EDS)), transmission electron microscopy (TEM), and X-ray diffraction (XRD). Structural and microstructural observations were composed and correlated with mechanical property measurements, which included, where feasible, tensile testing and microindentation hardness measurements. Fracture surface microstructures were also examined using SEM.

## II. EXPERIMENTAL DETAILS

### A. Component Fabrication by EBM

Figure 1(a) shows a schematic view of the Arcam A2 EBM system (Arcam AB, Mölndal, Sweden) used in this research program for the fabrication of a number of component geometries from Co-Cr-Mo precursor powder illustrated in Figure 1(b). The schematic of Figure 1(a) illustrates an electron beam forming system similar to a SEM or an electron beam welding facility

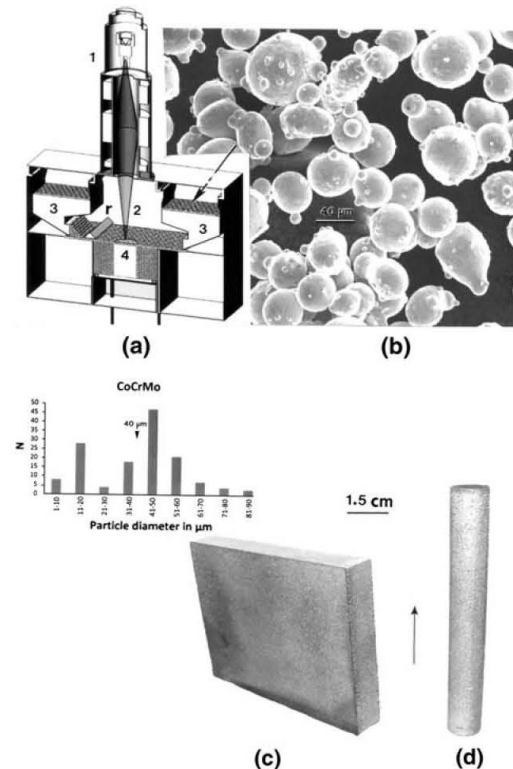


Fig. 1—(a) EBM system schematic showing key features (text). (b) Precursor powder in the SEM. (c) Powder particle size distribution (histogram). (d) Rectangular and cylindrical Co-Cr-Mo components built in the EBM system illustrated in (a).

that consists generally of an electron gun (1) and an electron beam focusing (electromagnetic) lens system with included beam scan coils (2). The electron beam accelerating potential of 60 kV along with an optimized beam current and focus during layer melting produces an energy density of  $\sim 10^2$  kW/cm<sup>2</sup>. Co-Cr-Mo powder (Figure 1(b)) having a nominal composition shown in Table I was gravity fed from cassettes (3) onto a build table (4) where it was raked (*r*) into a layer thickness of  $\sim 100$   $\mu$ m. The nominal powder size ( $\sim 40$   $\mu$ m) and size distribution (which illustrates a bimodal feature as a consequence of satellite particles attached to larger particles) are shown in Figure 1(c). Each newly raked powder layer is initially rastered by the electron beam at high beam current in alternating (X-Y), multiple passes to preheat the layer to  $\sim 1103$  K (830 °C). The melt scan is rastered at  $1$  to  $2 \times 10^3$  mm/s at a reduced beam current of  $\sim 10$  mA. The melt scan is driven by a 3-D CAD program, which melts only prescribed layer portions for the building component. The beam scan direction is alternated to 90 deg (perpendicular) every other layer build. The build chamber in the EBM system (Figure 1(a)) has a nominal vacuum of  $10^{-4}$  torr where a

**Table I. Chemical Composition for Precursor Co-Cr-Mo Powder and EBM Fabricated Components**

Material Component	Element (Wt Pct)								
	Cr	Mo	C	Fe	Ni	Si	N	Mn	Co
ASTM F75*	27 to 30	5 to 7	<0.35	<0.75	<0.50	<1.0	<0.25	<1.0	bal
Powder <sup>†</sup>	29	6	0.22	—	0.25	0.7	0.15	0.5	bal
As-fabricated knee <sup>‡</sup>	26	4.4	—	—	—	—	—	1	bal
Mesh <sup>‡</sup>	28	5.2	—	—	—	—	—	—	bal

\*ASTM F75 standard chemical composition/composition ranges.  
<sup>†</sup>Chemical analysis by mass spectrometry.  
<sup>‡</sup>Chemical analysis by EDS.

helium gas bleed at the build zone reduced the vacuum to  $\sim 10^{-2}$  torr to facilitate build cooling and thermal stability.

A range of EBM built Co-Cr-Mo component geometries were fabricated for analysis in this study. These included simple, fully dense ( $8.4 \text{ g/cm}^3$ ) cylindrical and orthogonal (block) structures (Figure 1(c) and (d)); femoral, knee implant components; and orthogonal, open-cellular mesh components similar to those described in detail in previous EBM fabrication of Ti-6Al-4V mesh components.<sup>[17–19]</sup> The implant and mesh structures were created using selective space structures (3S) software, a product of Fruth Innovative Technologien GmbH (FIT), Nürnberg Area, Germany ([www.pro-fit.de](http://www.pro-fit.de)). The specific mesh (3S) structure generator or unit cell was 3S diamond. These structure generators build CAD models, as described previously.<sup>[17]</sup>

An as-fabricated, femoral knee component was annealed and rough polished. Annealing (heat treatment) followed ASTM F75 CoCr alloy standard and consisted of initial, hot isostatic pressing at  $\sim 1473 \text{ K}$  ( $1200^\circ\text{C}$ ) for 4 hours in Ar at  $10^3$  bar, followed by a quench from a homogenizing treatment at  $1493 \text{ K}$  ( $1220^\circ\text{C}$ ) for 4 hours in Ar, at  $248 \text{ K/min}$  ( $75^\circ\text{C/min}$ ). This homogenizing temperature was  $\sim 0.8 T_M$ , where  $T_M$  (the melting temperature) is  $\sim 1703 \text{ K}$  ( $1430^\circ\text{C}$ ). This homogenizing temperature allowed for significant grain growth and carbide dissolution.

#### B. Microstructural and Microchemical Characterization

Microstructures for the various EBM-built components were observed and examined initially by OM and XRD, followed by SEM and TEM, both using EDS. TEM analysis also used selected-area electron diffraction (SAED) coupled with, and facilitating, dark-field imaging of selected microstructures. The OM was performed using a digital imaging Reichert MEF4 A/M system (Reichert, Inc., Depew, New York) after specimens/sample coupons were variously cut from each component, polished, and etched. The precursor Co-Cr-Mo powder illustrated in Figure 1(b) was also mounted, polished, and etched to reveal the initial microstructures. Etching protocols varied for specific samples. The cylindrical and orthogonal, rectangular components were etched with a solution consisting of 6:1 HCl:H<sub>2</sub>O<sub>2</sub> (3 pct) for 16 hours at room temperature, while the

as-fabricated and annealed knee and mesh components were etched for 1 to 2 minutes. In contrast, the annealed and polished knee component along with the mounted and polished precursor powder were etched with a solution consisting of 100 mL H<sub>2</sub>O, 50 mL HCl, 10 mL HNO<sub>3</sub>, and 10 g FeCl<sub>2</sub> for short times (ranging from 1 to 2 minutes). The as-fabricated knee component was etched in a 12:1 HCl:H<sub>2</sub>O<sub>2</sub> (3 pct) solution for 16 hours.

XRD spectra were obtained for the precursor powder (Figure 1(b)) and from representative samples extracted from several of the EBM fabricated components. The XRD system was a Bruker AXS-D8 Discover system (Bruker AXS, Madison, WI) using a Cu target.

SEM analysis used a Hitachi S-4800 field-emission (FE)-SEM (Pleasanton, CA) fitted with an EDAX EDS system and operated primarily at 20 kV accelerating potential in the secondary electron emission mode. An example of these images is shown in Figure 1(b). The TEM analyses were performed in either a Hitachi H-8000 analytical TEM fitted with a goniometer-tilt stage and operated at 200 kV or a Hitachi H-9500 high-resolution TEM fitted with a goniometer-tilt stage and an EDAX-EDS system, and operated at 300 kV accelerating potential. Samples were prepared for TEM analysis by cutting and carefully grinding coupons from the cylindrical and orthogonal, rectangular block components along with the as-fabricated knee component and the annealed and polished knee component. These coupons were ground and polished to a thickness of  $\sim 200 \mu\text{m}$ , and 3-mm discs were punched from these samples. The discs were mechanically dimpled and electropolished in a Tenupol-5 (Struers, Inc., Cleveland, OH), dual jet unit at temperatures ranging from 303 K to 313 K ( $30^\circ\text{C}$  to  $40^\circ\text{C}$ ) using an electropolishing solution consisting of 15 pct perchloric acid and 85 pct acetic acid, at 20 V and 3 to 30 mA.

#### C. Mechanical Testing

Tensile specimens were machined from cylindrical build components, as illustrated in Figure 1(d), and tested in an INSTRON\*\* 500 R tensile machine at a

\*\*INSTRON is a trademark of Instron, Canton, MA.

strain rate of  $3 \times 10^{-3} \text{ s}^{-1}$ , at room temperature



( $\sim 293$  K (20 °C)). Fracture surfaces for failed tensile specimens were also examined using FE-SEM.

Microindentation hardness and macroindentation hardness measurements were made using a Vickers microindentation hardness (HV) indenter (25 to 100 gf (0.25 to 1N) load at  $\sim 10$  seconds load time) in a Shimadzu HMV-2000 system (Shimadzu Scientific Instruments, Inc., Columbus, MD) and a HRC tester (1.5 kN load), respectively. HV measurements on mounted, polished, and etched mesh samples used the lightest load (25 gf: 0.25N). All microindentation (HV) and macroindentation (HRC) measurements were averaged for a minimum of 10 indentations.

### III. RESULTS AND DISCUSSION

#### A. Powder Characterization

Figure 2(a) illustrates a magnified SEM view for the Co-Cr-Mo atomized, precursor powder shown in Figure 1(b). Correspondingly, Figure 2(b) shows a section of powder placed in mounting material, which was ground, polished, and etched to reveal a unique solidification microstructure. Figure 3(a) illustrates the characteristic XRD spectrum for the Co-Cr-Mo powder in Figure 1(b) to represent  $\text{Co}_{0.8}\text{Cr}_{0.2}$  hcp/hexagonal

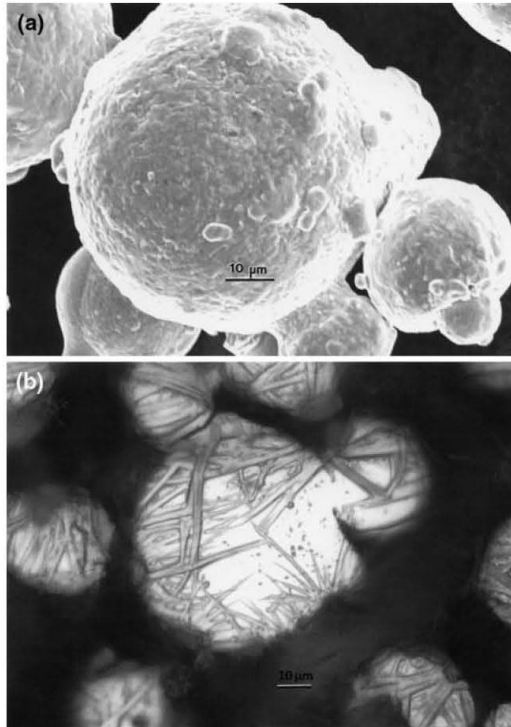


Fig. 2—(a) Enlarged SEM view of precursor Co-Cr-Mo powder in Fig. 1(b). (b) Mounted, polished, and etched powder sections observed by OM.

crystal structure with a  $P63/mmc$  space group and lattice parameters  $a = 2.52$  Å and  $c = 4.06$  Å. There was no evidence of carbides or intermetallic ordered compounds such as  $\text{Co}_3\text{Mo}$  (hcp) as might be expected for incipient melting or slower solidification processes.<sup>[20]</sup> The precursor Co-Cr-Mo powder microindentation hardness measured on polished and etched sections similar to Figure 2(b) averaged 6.3 GPa (630 HV) (Table II).

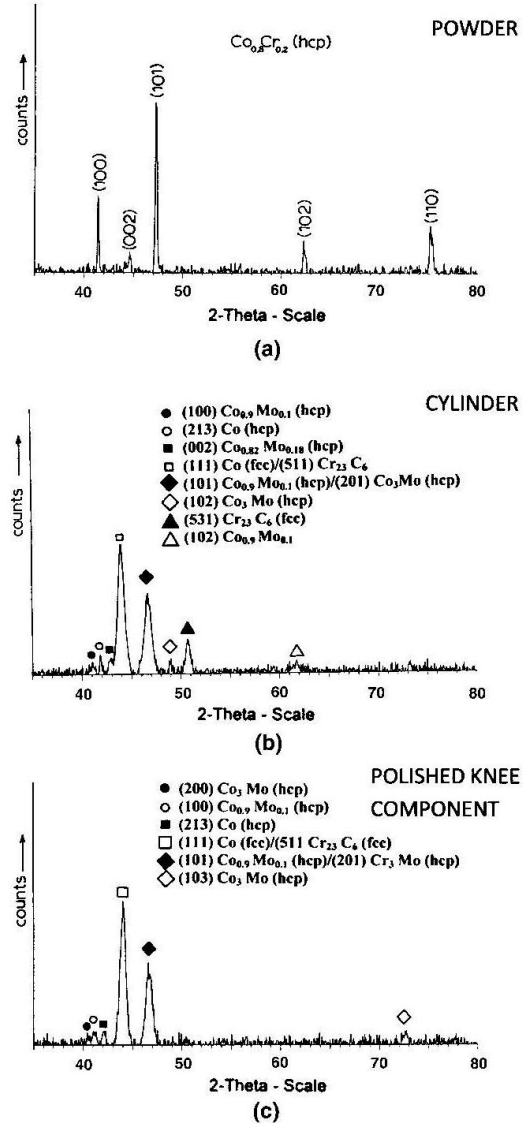


Fig. 3—(a) XRD  $\text{Co}_{0.8}\text{Cr}_{0.2}$  (hcp) spectrum for precursor powder in Fig. 1(b). Indexed ( $hkl$ ) diffracting planes are indicated. (b) XRD pattern corresponding to the horizontal plane view for the cylindrical component shown in Fig. 1(d). (c) XRD pattern corresponding to the section cut from the annealed and polished femoral (knee) component in Fig. 8. Indexed peaks are noted by keys.

Table II. Mechanical Properties for EBM Fabricated Co-Cr-Mo Components

Component	Hardness		Tensile <sup>†</sup>		
	HV* (GPa)	HRC**	Yield Stress (GPa) <sup>†*†</sup>	UTS (GPa)	Elongation (Pct)
Precursor powder	6.3	—	—	—	—
Solid block	4.4* <sup>†</sup>	44/46 <sup>‡</sup>	—	—	—
Solid cylinder	4.6* <sup>†</sup>	47/48 <sup>‡</sup>	0.51	1.45	3.6
As fabricated knee (femoral)	5.9	46	—	—	—
Annealed/polished knee (femoral)	4.7	40	—	—	—
Mesh array	6.8/5.6 <sup>‡</sup>	—	—	—	—

\*Vickers microindentation hardness (VHN or HV): 1 VHN = 0.01 GPa.

\*\*Rockwell C-scale hardness.

\*<sup>†</sup>Horizontal plane (Figs. 4(a) and (c)).

<sup>†</sup>Average for two tests.

<sup>‡</sup>Horizontal plane hardness/vertical plane hardness (Figs. 4(a), (c), and 12).

<sup>†\*</sup>0.2 pct engineering offset yield stress.

Figure 3(b) illustrates the corresponding XRD spectrum for a horizontal section cut from the cylindrical specimen represented by Figure 4(a). In contrast to the powder XRD pattern (spectrum) shown in Figure 3(a), Figure 3(b) shows a variety of crystallographic and compositional phase mixtures, mostly hcp with a Co or CoCr fcc matrix.

The only major carbide represented is  $M_{23}C_6$  or  $Cr_{23}C_6$  (fcc:  $a = 10.66$  Å), where M can also be  $Cr_{17}Co_4Mo_2$ .<sup>[2,4]</sup> Note the overlap of (511)  $Cr_{23}C_6$  with the (111) Co (fcc:  $a = 3.55$  Å) peak as well as the CoMo component overlap at  $2\theta = 46.5$  deg. A small  $\epsilon$ -Co (hcp:  $a = 2.51$  Å,  $c = 4.08$  Å) peak occurs at  $2\theta = 41.8$  deg, and this hcp structure space group ( $P63/mmc$ ) also characterized the other hexagonal components shown in Figure 3(b):  $Co_{0.9}Mo_{0.1}$  ( $a = 2.52$  Å,  $c = 4.11$  Å);  $Co_{0.80}Mo_{0.18}$  ( $a = 2.60$  Å,  $c = 4.21$  Å); and CoMo ( $a = 5.12$  Å,  $c = 4.11$  Å).

#### B. Characterization of As-Fabricated, Fully Dense Cylinders and Blocks

In contrast to the initial powder solidification microstructure shown in Figure 2(b), the EBM fabricated cylindrical and rectangular block components (Figure 1(d)) are characterized by unique arrays of carbide microstructures illustrated typically in the optical metallographic images and image compositions shown in Figure 4. In Figure 4, the EBM build direction is indicated by the arrows. In Figures 4(a) and (c), regular carbide arrays representing precipitation in small domains created by the cross scanning of the electron beam during preheating and in successive layer building, with dimensions of  $\sim 2$   $\mu$ m, are observed in the horizontal (or build) plane, while similarly spaced columns of carbides are shown extending along the build direction (arrows), along with other regular and irregular columnar carbide features observed in the vertical planes parallel to the build direction (arrows). These unique microstructural features are highlighted in the vertical plane metallographic view shown for the cylindrical component in Figure 4(b), which provides the appearance of zigzag-like carbide features along with columnar-like grains and regular precipitate patterns, with

dimensions similar to those shown in the horizontal plane views in Figures 4(a) and (c) (and having dimensions of  $\sim 2$   $\mu$ m). It can be noted in Figures 4(a) through (c) that the grain boundaries are also concentrated with carbides and are difficult in some cases to distinguish. Their sizes range from  $\sim 10$  to  $\sim 50$   $\mu$ m and are more prominent as columnar grains in Figure 4(b). The zigzag-like carbide patterns arise by systematic beam scan shifts either in the preheat scans or in successive melt scans. Figure 4(d) illustrates these carbide precipitation features schematically.

The arrays of carbides shown in Figures 4(a) through (c) represent a controlled microstructural architecture, which results from electron beam parameters, scan rates, and scan geometries that may be altered to produce a range of microstructural architectures resulting in predictable property and performance characteristics as a consequence of the architectural geometry and size scale. In addition, functionally graded microstructural architectures and associated property variations can also be achieved by electron beam build variations.

HV in the horizontal plane for the rectangular block sample (Figure 4(c)) and the cylindrical sample (Figure 4(a)) averaged 4.4 and 4.6 GPa, respectively (Table II). Corresponding HRC measurements were also made in both the horizontal and vertical planes for the block (Figure 4(c)) and cylindrical (Figure 4(a)) samples, as shown in Table II. These values are consistent with the nearly 0.1:1 conversion for HV:HRC values (Table II). The microindentation hardness values for the EBM fabricated cylindrical and rectangular block components are nearly 30 pct softer than the precursor Co-Cr-Mo powder in spite of the high carbide density or fraction, which averages  $\sim 0.2$  to  $0.3$ , and is similar to cast ASTM F75 Co-Cr-Mo alloy, which is also dominated by  $M_{23}C_6$  carbides.<sup>[21]</sup> The measured hardnesses are also consistent with Stellite alloys, which range from HV 4.1 to 5.5 GPa and HRC 42 to 53.

Figure 5 shows bright-field TEM images for horizontal plane specimens from the (a) and (b) rectangular block and (c) cylindrical components. Figure 5(c) shows carbide ( $M_{23}C_6$ ) precipitates along with their corresponding and superimposed SAED pattern in the SAED pattern insert. These images also show a high dislocation



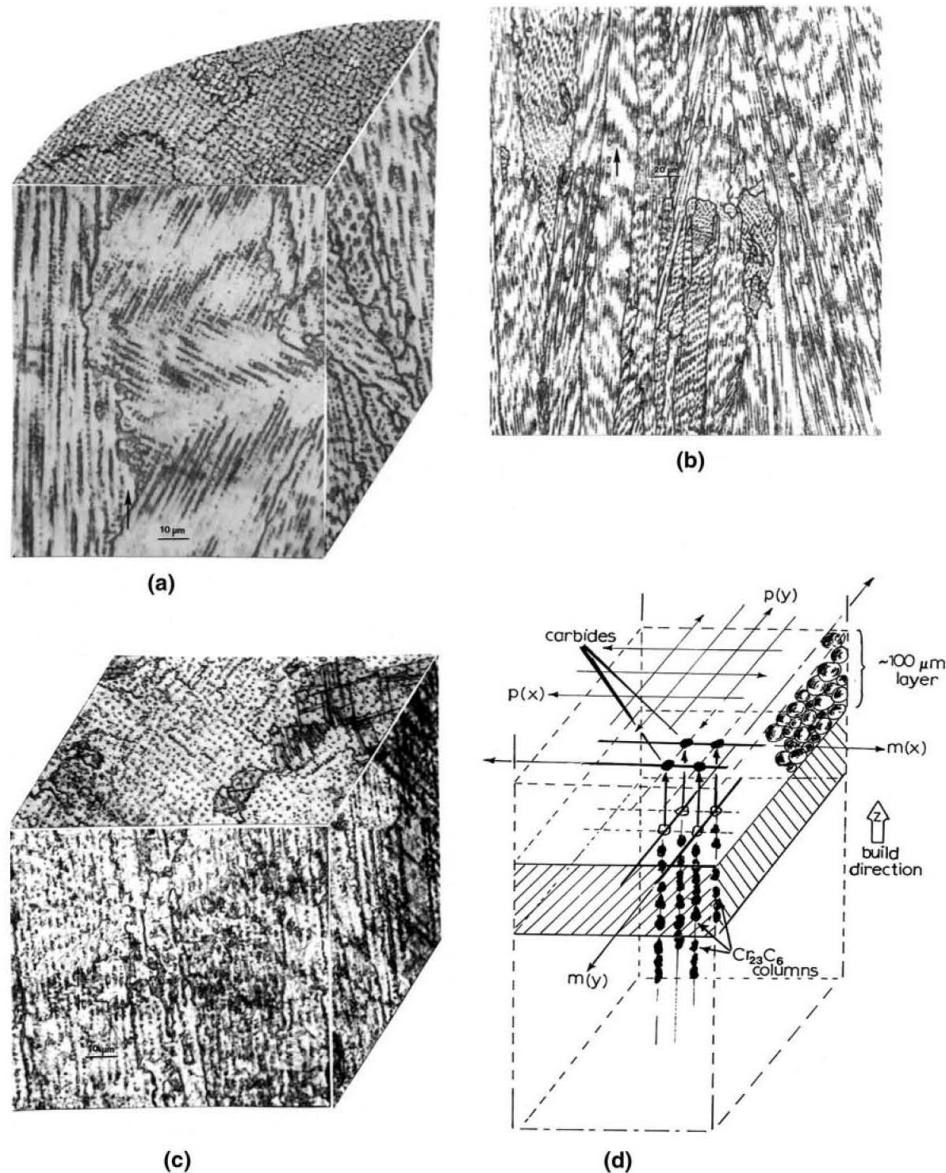


Fig. 4—(a) 3-D OM composite/section view for a mounted and etched cylindrical component, as in Fig. 1(d). Arrow indicates the EBM build direction in the vertical plane. Note orthogonal carbide arrays in the horizontal plane and connected carbide columns in the vertical plane (parallel to the build direction). (b) Cylindrical component vertical plane optical metallographic view showing complex carbide columns and related carbide arrays in the build direction (arrow). (c) 3-D OM composite/section view for a mounted and etched rectangular block specimen cut from the EBM built component shown in Fig. 1(d). The arrow to the left illustrates the build direction in the vertical plane. (d) Schematic view of carbide precipitate pattern formation in (a) and (c). Note beam scan direction reverses each succeeding layer.  $P(x)$  and  $P(y)$  indicate pre-heat scans, while  $m(x)$  and  $m(y)$  denote melt scans in successive layer building.

density and numerous stacking faults, which attest to the fcc Co structure. Similar features are noted in Figures 5(a) and (b) for a horizontal section from the rectangular block component (Figure 1(d)). Especially prominent in both Figures 5(a) and (b) is the relatively

high stacking fault density, with numerous overlapping faults, which are characteristic of the very low stacking fault free energy ( $\sim 15 \text{ mJ/m}^2$ ) for fcc Co.<sup>[21]</sup> Figure 5(b) shows dense  $\text{Cr}_{23}\text{C}_6$  precipitates within or associated with a grain boundary marked by small arrows. It can



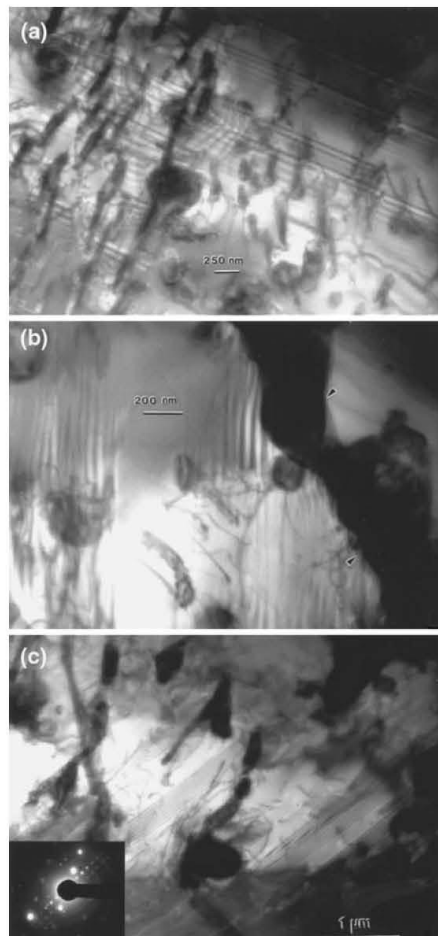


Fig. 5—TEM bright-field image examples in the horizontal plane for the block component (Fig. 4(c)) showing (a) irregular  $\text{Cr}_{23}\text{C}_6$  carbides in the fcc Co matrix and (b) similar carbide concentrations in a grain boundary (arrows). Note overlapping stacking faults in both (a) and (b). (c) TEM bright-field image showing horizontal plane thin section microstructure for a cylindrical component, as shown in Fig. 4(a). Prominent microstructure features include  $\text{Cr}_{23}\text{C}_6$  precipitates, dislocations, and stacking faults. The SAED pattern insert shows fcc Co (matrix) diffraction spots and (100) fcc  $\text{Cr}_{23}\text{C}_6$  diffraction spots (arrow).

be noted in Figure 5 that the  $\text{Cr}_{23}\text{C}_6$  carbides exhibit a variety of irregular microstructures.

### C. Knee Component/Prototype Characterization

Figure 6 shows an as-fabricated (EBM) femoral (knee) component prototype (Figures 6(a) and (b)). The larger arrow in Figure 6(b) shows the corresponding build direction from left to right, while the small arrow near the bottom of the image illustrates where test samples were cut for mounting, polishing, and etching for OM and hardness testing. Figure 7(a) shows a

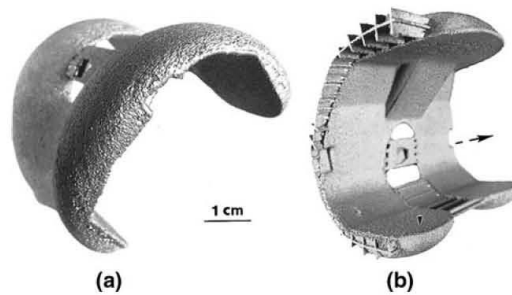


Fig. 6—(a) and (b) As-fabricated (EBM) femoral (knee) prototype. (a) and (b) Outer and inner views. The larger arrow (right) in (b) indicates the build direction, while the small arrow to the left indicates the sectioning of the component for examination.

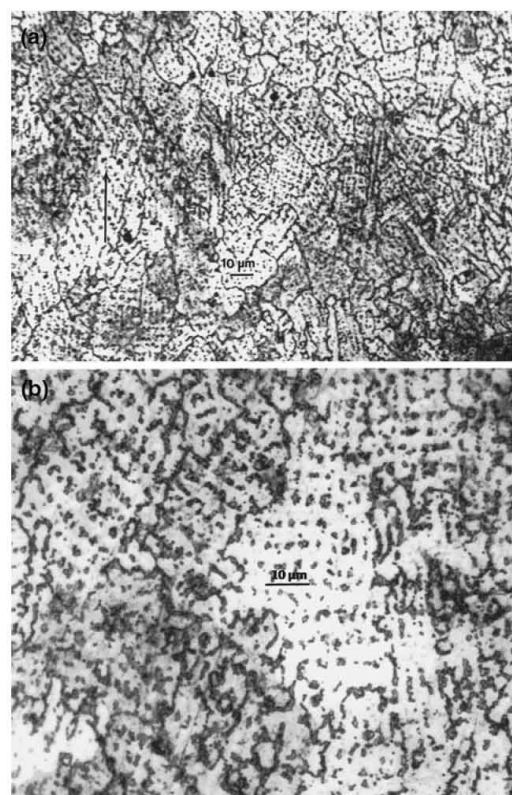


Fig. 7—OM views for the cut section for the as-fabricated femoral (knee) component in Fig. 6(b). (a) A lower magnification image with the build direction (at arrow) corresponding to that shown in Fig. 6(b). (b) A magnified view showing variations of carbide ( $\text{Cr}_{23}\text{C}_6$ ) arrays and columnar strings.

typical view of the microstructure in this cut plane, which, because of the build direction, would roughly correspond to the vertical plane for the cylindrical and block specimens illustrated in Figure 4. However, the

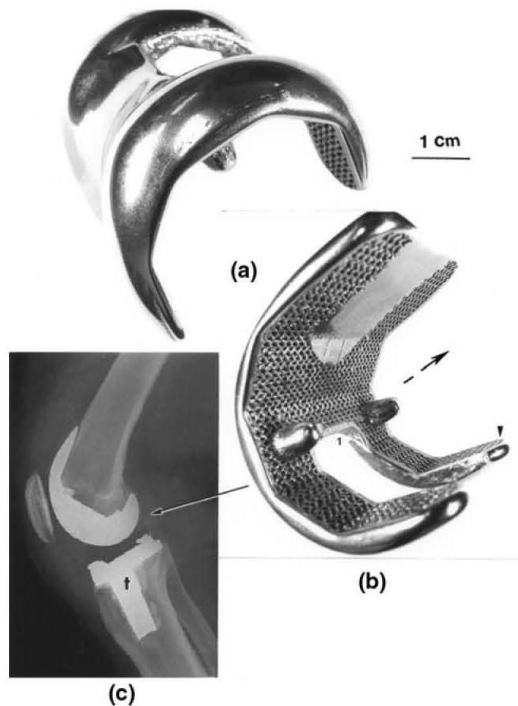


Fig. 8—(a) and (b) Annealed and polished femoral (knee) prototype built with porous mesh features for bone tissue ingrowth at femoral attachment shown in corresponding views. In (b), the larger arrow indicates the build direction, as in Fig. 6(b), while the smaller arrow to the right indicates the sectioning of the component for examination. (c) A commercially implanted Co-Cr-Mo femoral (knee) component (arrow) and a Ti-6Al-4 V tibial (knee) component (at *t*).

microstructure in Figure 7(a) and in a magnified view in Figure 7(b) shows mixtures of columnar carbides and carbide arrays measuring roughly 2 to 3  $\mu\text{m}$ , as noted previously in the horizontal plane views for Figure 4. Figures 8(a) and (b) show views for the annealed and polished femoral (knee) component similar to Figures 6(a) and (b), while Figure 8(c) illustrates the placement of a commercial knee component in a total knee replacement, which also includes the tibial insert illustrated at *t* in Figure 8(c). In many commercial applications, the tibial knee fixture is Ti-6Al-4V with a highly cross-linked polyethylene block inserted on the upper table of this implant (not visible in the X-ray image of Figure 8(c)). As in Figure 6(b), Figure 8(b) illustrates the build direction by the larger arrow and the section from which a section was removed for analysis indicated by the smaller arrow. Figure 9(a) shows a typical etched specimen from the plane section removed, as illustrated at the small arrow in Figure 8(b), which shows a generally equiaxed fcc grain structure, containing numerous, coherent annealing twins, as well as concentrated, grain boundary carbides ( $\text{Cr}_{23}\text{C}_6$ ) (Figure 9(b)). The average grain dimension, not including annealing twin boundaries, was measured to be  $\sim 42 \mu\text{m}$ . These

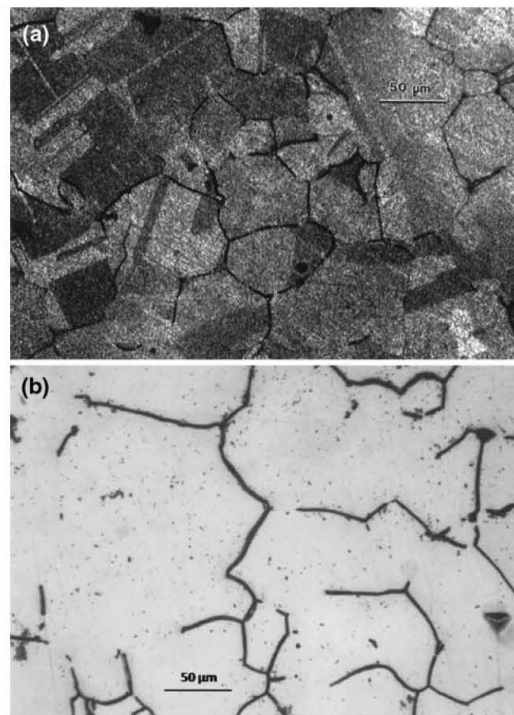


Fig. 9—OM views for the cut section for the annealed and polished femoral (knee) component in Fig. 8(b). (a) An equiaxed, fcc grain structure containing annealing twins with fine carbides ( $\text{Cr}_{23}\text{C}_6$ ) at some grain boundaries. (b) A preferential carbide etch at high energy grain boundary segments.

carbides, which can be preferentially etched at higher energy grain boundary segments, are illustrated in Figure 9(b).<sup>[21]</sup> However, the high carbide fraction noted in Figures 4 and 8 is significantly reduced in the annealed knee component (Figure 9). This is most apparent on comparing the XRD pattern for the as-fabricated cylinder in Figure 3(b) with the annealed knee component pattern in Figure 3(c), where the prominent (531)  $\text{Cr}_{23}\text{C}_6$  carbide peak (in Figure 3(b)) is missing.

While annealing at high temperature has dissolved a large fraction of the CoCr fcc matrix carbides (and cellular arrays of carbides), as shown on comparing Figure 7 with Figure 9, the characteristic fcc stacking fault microstructures have not been altered, as indicated in the comparative TEM images in Figure 10. Figure 10(a) shows stacking faults in an annealed knee component sample, while Figure 10(b) illustrates a corresponding TEM bright-field image for a cylindrical component horizontal plane sample, as shown in Figure 5(c). The stacking faults exhibit similar features in Figures 10(a) and (b), while the as-fabricated and unannealed cylindrical specimen in Figure 10(b) containing prominent  $\text{Cr}_{23}\text{C}_6$  precipitates also contains a



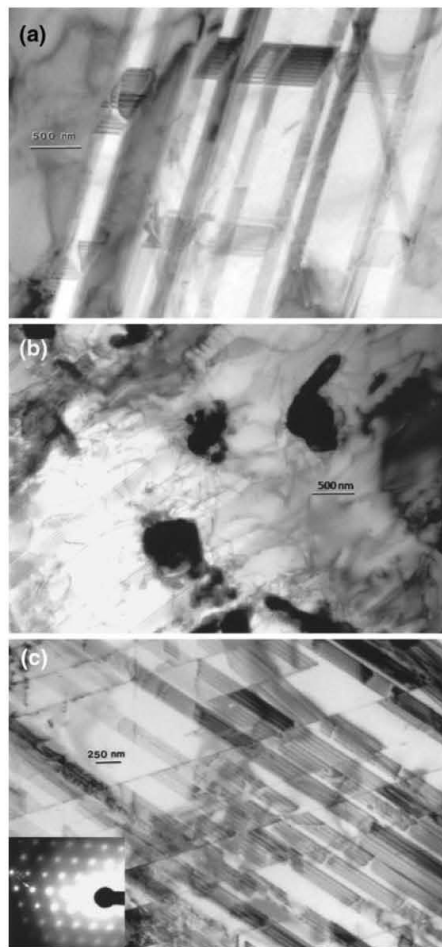


Fig. 10—(a) TEM bright-field image comparison for the annealed and polished femoral knee component and (b) the horizontal plane for the as-fabricated cylindrical component. (a) Stacking faults on nonconcurrent {111} planes. (b) Irregular  $\text{Cr}_{23}\text{C}_6$  carbides and stacking faults. (c) High density of intrinsic stacking faults on (111) planes coincident with the [220] crystal direction shown in the SAED (110) pattern insert. Representative (110) grain in an annealed and polished femoral (knee) component shown in Fig. 8(b).

significantly higher dislocation density. Correspondingly, there was a generally greater density of stacking faults in the annealed knee component, as illustrated in Figure 10(c). In contrast to Figure 5(c), the SAED pattern insert in Figure 10(c) shows no evidence of  $\text{Cr}_{23}\text{C}_6$  carbides, and the (110) fcc SAED pattern exhibits a calculated lattice parameter of 3.55 Å, consistent with fcc Co.

In this context of microstructure variations for the as-fabricated (knee) component vs the annealed (knee) component (Figures 7 and 9), the corresponding hardness results supported the expected variation in mechanical properties. The HV and corresponding HRC values are shown for comparison in Table II, which shows a

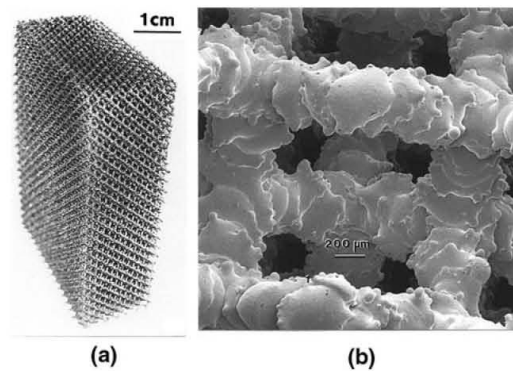


Fig. 11—Reticulated Co-Cr-Mo mesh prototype fabricated by EBM. (a) Rectangular mesh component. (b) SEM image for a side section in (a) showing mesh strut structure.

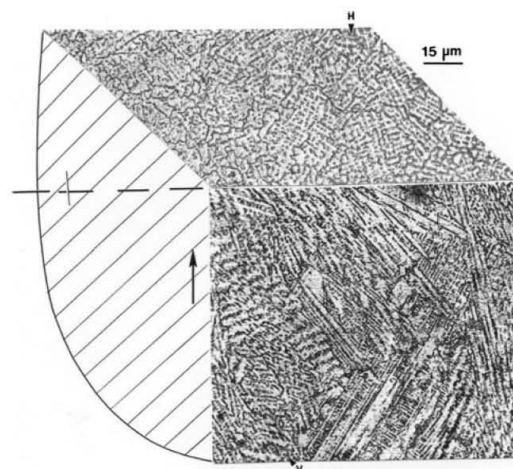


Fig. 12—OM composite views for a mounted, polished, and etched mesh strut section from Figs. 11(a) and (b). (H) and (V) denote the horizontal and vertical planes relative to the cylindrical strut section and the build direction indicated by the large arrow.

25 pct reduction in HV and 15 pct reduction in HRC after annealing.

#### D. Mesh Component Characterization

Figure 11(a) illustrates the as-fabricated Co-Cr-Mo mesh component, while the microstructural features are shown in the SEM view of Figure 11(b). Quantitative comparisons for the Co-Cr-Mo components are also shown in Table I. This EBM fabricated mesh (Figure 11(a)) had a density of 1.5 g/cm<sup>3</sup> in contrast to the fully dense cylindrical and rectangular block components with a density of 8.4 g/cm<sup>3</sup>.

The mesh sample shown in Figure 11(b) was processed similar to extracted coupons, which were mounted, ground, polished, and etched for OM, as described earlier. Figure 12 illustrates the typical

microstructures observed, which are similar to the carbide arrays observed in the composite horizontal and vertical plane views for the cylindrical and block components in Figures 4(a) and (c), respectively. However, unlike the cubelike carbide array in Figure 4, the carbides in Figure 12 are often concentrated in slightly more concentrated and circular, cell-like arrays resembling subgrain structures with dimensions of  $\sim 2\text{ }\mu\text{m}$ , similar to the more open, geometrical, cubelike (orthogonal) arrays in Figures 4(a) and (c). These arrays occur, in part, because of the circular element involved in building the cylindrical struts composing the mesh. The vertical plane component view shown in Figure 12 is similar to, but more irregular than, the cylindrical section illustrated in Figure 4(b). As noted, the cylindrical geometry and the rapid solidification contribute to these more irregular carbide columns. As noted for comparison in Table II, the average HV measured for these mesh struts was 6.8 GPa in the horizontal plane and 5.6 in the vertical plane, or roughly 25 pct harder than the as-fabricated, fully dense cylindrical and rectangular block components (Figures 4(a) and (c), respectively). This hardness difference for the Co-Cr-Mo mesh array (strut lengths, in particular), in contrast to solid, fully dense components, is similar to Ti-6Al-4V mesh arrays in contrast to fully dense Ti-6Al-4V components, where the microindentation hardness difference varied from 31 to 75 pct.<sup>[17]</sup> The hardness and corresponding microstructure variations for mesh strut components is due, in part, to the rapid cooling rate during EBM fabrication in contrast to much slower cooling for larger EBM fabricated components (Figures 4(a) and (c), for example). These features have been observed for Ti-6Al-4V reticulated mesh structures<sup>[17]</sup> as well as cellular foams.<sup>[18]</sup> Moreover, there is an increase in the carbide precipitate fraction, which contributes significantly to the hardness increase. In contrast to Figures 4(a) through (c), this microstructural architecture illustrates the degree of control or variation implicit in electron beam scan rate variations and related beam induced solidification phenomena.

Co-Cr-Mo mesh prototypes represented by Figure 11 are a testament to the prospects for creating multifunctional, next generation biomedical components, as previously demonstrated for Ti-6Al-4V mesh structures.<sup>[17]</sup> These porous surface structures can allow for effective bone cell ingrowth. A similar but more shallow mesh structure has been fabricated as a monolithic component, as shown for the annealed and polished femoral (knee) prototype in Figure 8(b).

#### E. Mechanical Testing and Fractography

The tensile testing of two specimens prepared from as-fabricated cylindrical components produced average yield stress, UTS, and elongation measurements as noted for comparison in Table II. In contrast to the HV, the yield stress of 0.51 GPa is roughly half of that expected for many metals where yield stress  $\approx$  HV/3. However, while the yield stress is consistent with wrought and cast products, the UTS is considerably higher than as-cast or wrought ASTM F75 Co-Cr-Mo

alloy, where nominally the yield stress and UTS are 0.5 and 0.9 GPa, respectively. Correspondingly, as-cast Co-Cr-Mo (ASTM F75) alloy has an elongation  $<1$  pct, while wrought Co-Cr-Mo alloy has an elongation  $\sim 5$  pct. These elongations compare to an average elongation of 3.6 pct for two tensile tests (Table II), where the elongation ranged from 1.9 pct for one sample to 5.3 pct for the other.

Figure 13 illustrates the horizontal plane optical metallographic microstructure (carbide arrays) in contrast to a similarly magnified and typical portion of the fracture surface for failed tensile specimens. Note that small ductile dimple arrays (arrows in Figure 13(b)) essentially match the orthogonal carbide arrays in Figure 13(a). This fracture feature is even more prominently illustrated in the magnified SEM fractography images shown in Figures 13(c) and (d).

## IV. SUMMARY AND CONCLUSIONS

The EBM fabrication of components and prototypes from Co-26Cr-6Mo-0.2C powder having a  $\text{Co}_{0.8}\text{Cr}_{0.2}$  (hcp) crystal structure creates Co-26Cr-6Mo-0.2C monoliths having an fcc CoCr matrix with CrMo phase components and unique, electron beam, scan-produced  $\text{Cr}_{23}\text{C}_6$  fcc orthogonal carbide arrays when viewed perpendicular to the build direction and carbide columns connected to these arrays when viewed in a plane parallel to the build direction. This is an example of a controlled microstructural architecture that can be altered with appropriate electron beam parameter and scanning variations. Correspondingly, when these EBM fabricated prototypes are annealed, an equiaxed, fcc CoCr grain structure containing  $\{111\}$  coincident annealing twins forms with  $\text{Cr}_{23}\text{C}_6$  carbides in predominantly high energy grain boundary portions. TEM bright-field observations of these annealed grains show a high density of intrinsic stacking faults on  $\{111\}$  planes, and essentially no matrix carbides.

The EBM fabrication of a reticulated mesh structure having a density of  $1.5\text{ g/cm}^3$  is characterized by cell-like  $\text{Cr}_{23}\text{C}_6$  carbide arrays with a higher carbide content than the solid monoliths with a density of  $8.4\text{ g/cm}^3$ . The corresponding HV for the mesh struts varied from 5.6 to 6.8 GPa in contrast to the solid monolithic components (including the femoral knee prototype, which varied from 4.4 to 5.9 GPa). While a slight increase in carbide content for the reticulated mesh structures accounts in large part for this hardness increase, the more rapid cooling rate for the reticulated mesh was also a contributing factor.

The tensile testing of specimens, machined from cylindrical components fabricated by EBM, produced an average UTS of 1.45 GPa, a 0.2 pct engineering yield stress of 0.51 GPa, and an elongation of 3.6 pct. These values are somewhat better than wrought or cast Co-26Cr-0.6Mo alloys such as ASTM F75.

The fracture surface microstructure for failed tensile specimens exhibited a unique, orthogonal ductile dimple cell structure that exactly matched the  $\text{Cr}_{23}\text{C}_6$  carbide arrays observed in the as-fabricated cylinders from



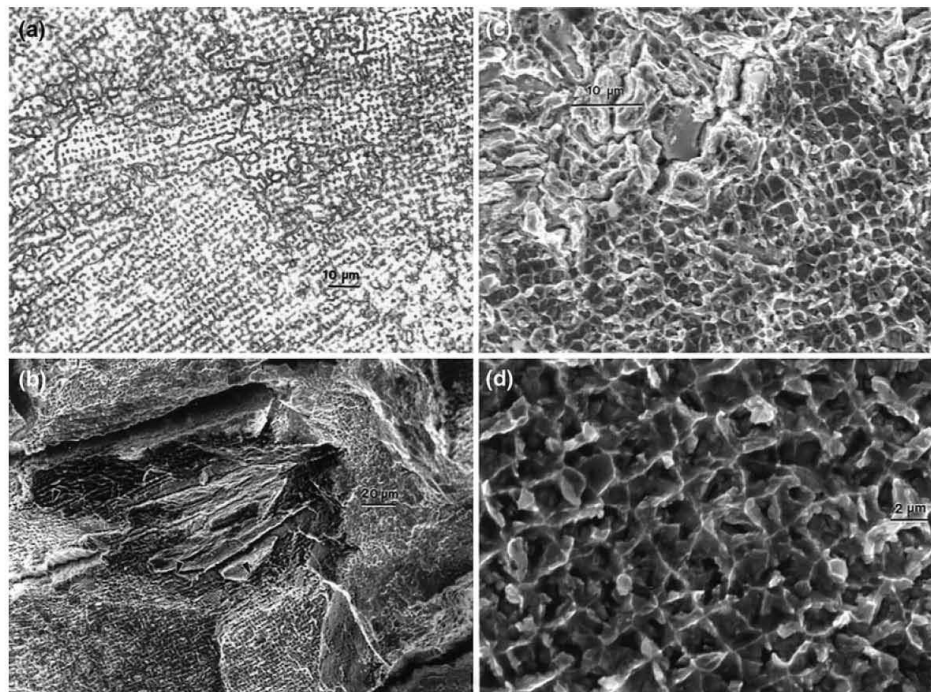


Fig. 13—OM and SEM fractography comparison for cylindrical Co-Cr-Mo components represented in Fig. 1(d). (a) Carbide arrays in the horizontal plane (perpendicular to the cylinder axis and EBM build direction). (b) Corresponding fracture surface. Arrows show fracture surface features corresponding to carbide arrays in (a). (c) Detailed and (d) magnified SEM fracture surface views for the dimple arrays shown in (b). (d) Orthogonal-like dimple arrays, which match the carbide (cellular) arrays in the horizontal tensile specimen plane.

which the tensile specimens were machined. These microstructural features illustrate the unique nature of EBM fabrication of cobalt-base alloy products containing significant carbon and the prospects for structure-property manipulation similar to commercial, cast Co-base alloys.

The ability to fabricate solid, fully dense, and complex Co-26Cr-6Mo-0.2C monoliths as well as high-strength, low-density reticulated mesh structures by EBM-AM suggests that, like EBM-fabricated Ti-6Al-4V products,<sup>[17,18]</sup> multifunctional, complex monoliths having a wide range of mechanical properties can be produced with Co-base alloys. These monolithic components can include mesh or open cellular foam-coated biomedical devices for efficient bone cell ingrowth, impact energy absorbing arrays for aerospace or automotive applications, and a variety of thermal energy management systems.

#### ACKNOWLEDGMENTS

This research was supported by Mr. and Mrs. MacIntosh Murchison, Endowed Chairs at the University of Texas at El Paso. A Graduate Assistantship through the Materials Science and Engineering Ph.D.

Program at the University of Texas at El Paso also supported part of this research. We are grateful to Mylin Cumberland of DePuy (a Johnson & Johnson Company) for providing the Arcam, as-built femoral knee component used in this research as well Arcam built rectangular block and cylinder components from Ryan Kircher of Medical Modeling, Inc. (Golden, CO). We are also grateful to ARCAM-AB, Sweden for their support and the provision of the reticulated mesh sample.

#### REFERENCES

1. *Superalloys II*, T.C. Sims, N.S. Stoloff, and W.C. Hagel, eds., Wiley, New York, NY, 1987, pp. 230–52.
2. P. Crook: *ASM Metals Handbook*, ASM INTERNATIONAL, Materials Park, OH, 1993, pp. 446–56.
3. *Nickel, Cobalt and Their Alloys*, ASM INTERNATIONAL, Materials Park, OH, 2000.
4. K.C. Antony: *J. Met.*, 1983, vol. 35, pp. 52–60.
5. S. Alamert and H.K.D.H. Bhadeshia: *Met. Technol.*, 1989, vol. 20, pp. 1037–54.
6. J. Shin, J.M. Doh, J.K. Yoon, D.Y. Lee, and J.S. Kim: *Surf. Coat. Technol.*, 2003, vol. 166, pp. 117–26.
7. J.S. Garcia, M.A. Medrano, and A.S. Rodriguez: *Metall. Mater. Trans. A*, 1999, vol. 30A, pp. 1177–84.
8. P. Huang and H.F. Lopez: *Mater. Lett.*, 1999, vol. 39, pp. 244–48.
9. T.M. Devine and J. Wulff: *J. Biomed. Mater. Res.*, 2004, vol. 9 (2), pp. 151–67.

10. D.G. Poitout: *Biomechanics and Biomaterials in Orthopaedics*, Springer, New York, NY, 2004.
11. C.G. Meacock and R. Vilar: *J. Laser Appl.*, 2009, vol. 21 (2), pp. 88–95.
12. L.E. Murr, E.V. Esquivel, S.A. Quinones, S.M. Gaytan, M.I. Lopez, E.Y. Martinez, F. Medina, D.H. Hernandez, E. Martinez, J.L. Martinez, S.W. Stafford, D.K. Brown, T. Hoppe, W. Meyers, R.B. Wicker, and U. Lindhe: *Mater. Characterization*, 2009, vol. 60, pp. 96–105.
13. L.E. Murr, S.A. Quinones, S.M. Gaytan, M.I. Lopez, A. Rodela, E.Y. Martinez, D.H. Hernandez, E. Martinez, F. Medina, and R.B. Wicker: *J. Mech. Behavior Biomed. Mater.*, 2009, vol. 2, pp. 20–32.
14. L.E. Murr, S.M. Gaytan, M.I. Lopez, E. Martinez, F. Medina, and R.B. Wicker: *Practical Metall.*, 2009, vol. XLVI, pp. 442–53.
15. S.M. Gaytan, L.E. Murr, F. Medina, E. Martinez, M.I. Lopez, and R.B. Wicker: *Mater. Technol.: Adv. Perform. Mater.*, 2009, vol. 24 (3), pp. 180–90.
16. L.E. Murr, S.M. Gaytan, F. Medina, H. Lopez, E. Martinez, D.H. Hernandez, L. Martinez, M.I. Lopez, R.B. Wicker, and J. Bracke: *Phil. Trans. R. Soc. A*, 2010, vol. 368, pp. 1999–2032.
17. L.E. Murr, S.M. Gaytan, F. Medina, E. Martinez, J.L. Martinez, D.H. Hernandez, B.I. Machado, D.A. Ramirez, and R.B. Wicker: *Mater. Sci. Eng. A*, 2010, vol. 527, pp. 1861–68.
18. S.M. Gaytan, L.E. Murr, F. Medina, E. Martinez, J.L. Martinez, and R.B. Wicker: *Global Innovations in Manufacturing of Aerospace Materials*, Proc. 11th MPMD (TMS) Global Innovations Symp., 2010, in press.
19. T. Kilner, R.M. Pilliar, G.C. Weatherly, and C. Allibert: *J. Biomed. Mater. Res.*, 1982, vol. 16, pp. 63–79.
20. M. Caudillo, M. Herrera-Trejo, M.R. Castro, E. Ramirez, C.R. Gonzalez, and J.I. Juarez: *J. Biomed. Mater. Res.*, 2001, vol. 59 (2), pp. 378–85.
21. L.E. Murr: *Interfacial Phenomena in Metals and Alloys*, Addison-Wesley, New York, NY, 1975; reprinted by Tech Books, Herndon, VA, 1990, pp. 87–164, and available from CBLIS.com.

# A TEM Study of Cobalt-Base Alloy Prototypes Fabricated by EBM

Sara M. Gaytan, Larry E. Murr, Diana A. Ramirez, Brenda I. Machado, Edwin Martinez, Daniel H. Hernandez, Jose L. Martinez, Francisco Medina, Ryan B. Wicker

University of Texas at El Paso, El Paso, TX 79968 USA.  
Email: [smgaytan@miners.utep.edu](mailto:smgaytan@miners.utep.edu)

Received February 1<sup>st</sup>, 2011; revised March 15<sup>th</sup>, 2011; accepted April 1<sup>st</sup>, 2011.

## ABSTRACT

*A novel microstructural architecture consisting of  $\text{Cr}_{23}\text{C}_6$  carbide spatial columns was created in solid components of Co-26Cr-6Mo-0.2C fabricated from powder by additive manufacturing using electron beam melting. These columns of carbides extended in the build direction and are formed by the x-y rastering of the electron beam to pre-heat and melt powder layers using CAD models. These microstructural architectures are similar to rapidly solidified/unidirectionally solidified structures created by heat extraction in the direction perpendicular to the build plane. These columnar carbide architectures were observed by optical metallography and transmission electron microscopy (TEM) and compared with intrinsic stacking fault microstructures observed in annealed components. The TEM analysis allowed the details of the carbide crystal structure and corresponding cubic morphology to be observed.*

**Keywords:** Electron Beam Melting, Stacking Faults, Precipitates

## 1. Introduction

There have been significant developments in the creation and applications of metals and alloys over the past decades (since about 1960) when the discipline of materials science and engineering emerged, embodying the structure-properties-processing-performance paradigm [1,2]. Despite the discoveries and associated improvements in the properties and performance of metals and alloys, there remain limitations in structural/(microstructural) control inherent in conventional (bulk) processing and processing routes. These are consistent with the corresponding materials science and engineering paradigm limitations in the range of achievable properties and performance. While it is common to modify material microstructures to achieve predictable property variations such as hardness, strength (and elastic modulus), toughness, thermal and electrical conductivity and the like, the controlled development of spatial arrangements of microstructural features (or architectures) such as directional solidification has produced columnar arrays of fibers, especially eutectic fibers, which provide directional properties [3-5]. Similar processing routes have recently been demonstrated by additive manufacturing (AM) using electron beam melting (EBM) for the fabrication of

Co-base alloy (Co-26Cr-6Mo-0.2C) components [6], and a Ni-base superalloy where columnar  $\text{Ni}_3\text{Nb}$  precipitates were formed [7]. In this prior Co-base alloy study [6]  $\text{Cr}_{23}\text{C}_6$  precipitates were observed to form spatial arrays of carbide columns generally in the EBM build direction as a consequence of unique thermodynamic zone arrays characteristic of the electron beam preheat and melt-raster geometry which was conducive to carbide precipitate formation. It has been stated by Stoloff and others that cobalt-base alloys are hardened by precipitation of either carbides or intermetallic compounds [8].

This paper examines the microstructural architecture characterized mainly by spatial columns of  $\text{Cr}_{23}\text{C}_6$  carbides and dislocations which occur in solid Co-base alloy prototypes fabricated by EBM. CoCrMo has a high corrosion resistance due to the high chromium content that forms a thin passive oxide layer, which makes it an ideal candidate for metal-on-metal bearing surfaces in orthopaedic implants. This alloy also provides a high wear resistance depending on the size, shape and distribution of carbide precipitates [9]. A study conducted by Cawley *et al.*, basically consisted in comparing the microstructures of the same Co-Cr-Mo alloy as cast, wrought and with different heat treatments, finding that the carbides obtained from all the thermally processed samples were



richer in chromium than molybdenum and no difference in hardness was obtained from the as-cast and the thermally treated materials [10]. We demonstrate these architectures by constructing and comparing 3D image composites from optical microscopy and transmission electron microscopy (TEM). Intrinsic stacking faults characteristic of the Co-rich fcc, low stacking fault energy crystal structure are also observed in the background of these microstructures, and become the dominant microstructure upon appropriate annealing to cause carbide dissolution and dislocation annihilation.

## 2. Experimental Methods and Procedures

Although we have described the EBM-AM process in detail elsewhere [6,11], it will provide a necessary context if we outline the process briefly herein. We begin by providing an overview of the Arcam A2-EBM system as illustrated in **Figure 1**. The major components illustrated in **Figure 1** are the electron-optical column (1) which focuses and scans the electron beam (in vacuum) over the building component (3) as powder is supplied by gravity feed from the cassettes shown at (2), and raked into a layer roughly 100  $\mu\text{m}$  thick. **Figure 2(a)** illustrates the Co-26Cr-6Mo-0.2C powder (with nominal size of 40  $\mu\text{m}$ ) used in this study while **Figure 2(b)** shows some simple component geometries fabricated.

**Figure 2(a)** shows Co-26Cr-6Mo-0.2C powder observed in the SEM. As implicit in **Figure 1**, the electron beam is rastered orthogonally ( $x$ - $y$ ) in multiple passes to preheat each powder layer to roughly 830°C. This is followed by a melt scan ( $x$ , $y$ ) at reduced beam current and scan rate which builds component geometries layer-by-

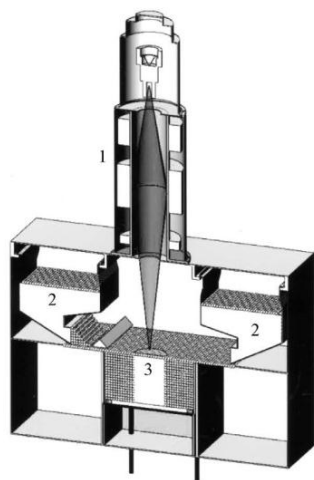


**Figure 1.** Arcam A2 EBM system.

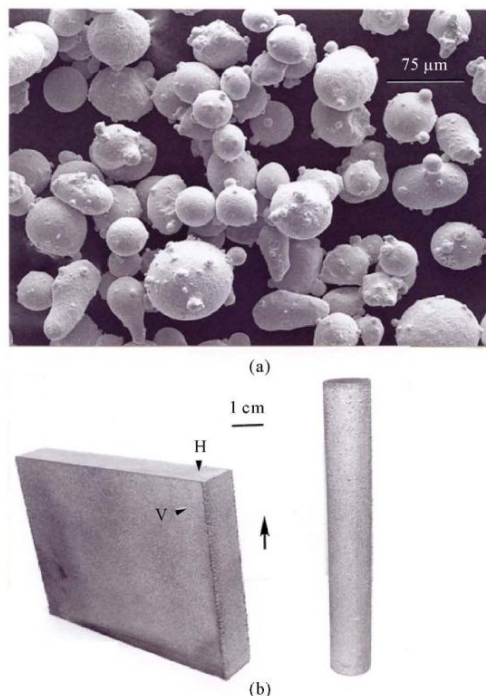


**Figure 2.** (a) Precursor powder; (b) Components fabricated by EBM.

layer in a direction shown by the arrow in **Figure 2(b)**. Horizontal and vertical planes (perpendicular to and parallel to the build direction) are noted by H and V, respectively in **Figure 2(b)**. The rectangular block and cylindrical components fabricated as illustrated in **Figure 2(b)** were observed to be essentially fully dense, with a density of 8.4 g/cm<sup>3</sup>.

Optical metallography (OM) on extracted sections from rectangular block and cylindrical builds illustrated in **Figure 2(b)** was a precursor characterization prior to developing TEM thin foils.

We employed a Reichert MEF4 A/M metallographic system for extracted specimens which were ground, polished, and etched with a 6:1 HCl: H<sub>2</sub>O<sub>2</sub> (3%) etchant for 16 h at room temperature (~22°C). Annealed samples were etched in much less time (~2 min.). The annealing conditions involved HIP at ~1200°C for 4 h in Ar followed by a quench from a homogenizing treatment at 1220°C for 4 h in Ar at a quench rate of ~7.5°C/min. As illustrated in **Figures 3 (a)** and **(b)**, OM was conducted for both the horizontal (H) and vertical (V) planes.

As illustrated in **Figure 3(c)**, specimens extracted from the EBM-fabricated components as in **Figure 3(a)** and **3(b)**



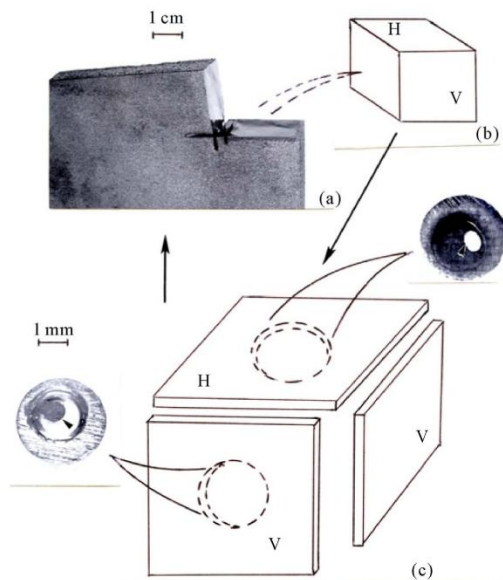


**Figure 3.** TEM samples obtained from block component in vertical and horizontal plane.

were also sliced using a diamond saw along the H and V planes and smaller coupons cut from these slices, ground to  $\sim 0.2$  mm thickness, and 3 mm discs punched from these ground coupons. These discs were mechanically dimpled and electropolished in a Tenupol-5 dual jet unit at temperatures ranging from 30 - 40°C using an electropolishing solution consisting of 15% perchloric acid and 85% acetic acid, at 20 V and 3 - 30 mA. Punched and electropolished 3 mm discs are shown in the inserts in **Figure 3(c)**.

### 3. Results and Discussion

#### 3.1. Block Component Fabricated by Electron Beam Melting

**Figure 4** shows an OM 3D composite for an extracted, polished, and etched specimen as illustrated in **Figures 3(a)** and **(b)** forming  $\text{Cr}_{23}\text{C}_6$  carbide columns with spacings determined largely by the electron beam focus and scan geometry, including the spatial dimensions of the X-Y scans. **Figure 5** illustrates this processing feature in the EBM. The columns are generally parallel to the build direction marked by the arrows in **Figures 4** and **5**.

The microstructure (microstructural architecture or carbide columns in **Figure 4**) is similar to structures developed by rapid solidification or directional solidification [3-5], by heat extraction in the build direction. As the electron beam scans and melts the powder the spatial,



**Figure 4.** OM 3D composite for a block component.

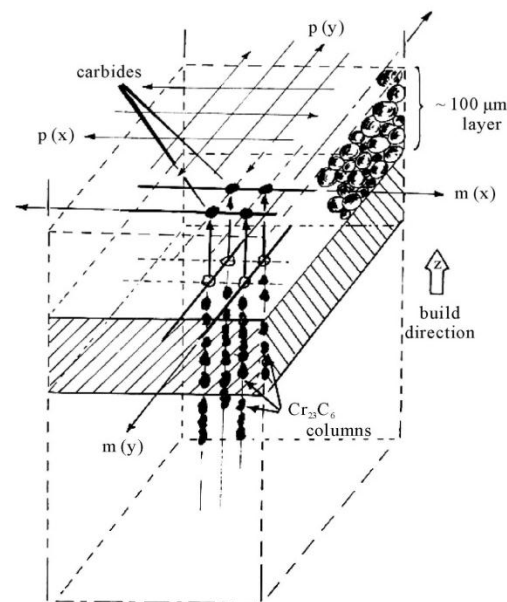


**Figure 5.** Carbide precipitate architecture as fabricated by EBM.

small liquid volume rapidly cools, solidifying with a plane front or cellular liquid/solid interface (**Figure 5**). The carbon within these zone segregates to the boundaries of the cellular interface, resulting in the columnar of aligned  $\text{Cr}_{23}\text{C}_6$  precipitates. These features can be varied somewhat as described for precipitate columns formed by EBM in a Ni-base (Inconel 718)) alloy [7], and in the

production of  $\alpha$ -phase columnar grains in the selective laser melting (SLM) of Ti-6Al-4V [9]. In the SLM study [12], energy density, scanning velocity, and hatch spacing (shown schematically in **Figure 5**) were referred to as a scanning strategy which can be used to manipulate associated microstructures and microstructural architecture.

**Figures 6 and 7** show 3D section views observed in the TEM at low and high magnification, respectively. The TEM views show the carbide columns in **Figure 4** to be spaced  $\text{Cr}_{23}\text{C}_6$ , incoherent carbide precipitates. **Figure 7** in particular shows clearly the incoherent cubic (fcc:  $a = 1.07 \text{ nm}$ )  $\text{Cr}_{23}\text{C}_6$  particles spaced roughly 100 to 200 nm in the EBM fabricated columns which are correspondingly spaced  $\sim 2 - 3 \mu\text{m}$  as illustrated in both **Figures 4 and 6**. Contrast fringes indicating linear stacking-fault features are apparent in both the horizontal (H) and vertical (V) plane views in **Figure 7** along with dense dislocation arrangements intermingled with the carbide precipitates. These features are also observed at higher magnifications as shown in **Figure 8** which illustrates individual precipitate cubes and related crystal geometries measuring  $\sim 100$  to  $200 \text{ nm}$  on a side.

**Figures 9 to 11** show several examples of the dense intrinsic stacking-fault arrangements intercalated with dense dislocation structures. The selected-area electron diffraction (SAED) pattern insert in **Figure 9** shows micro-twin and double-diffraction spots indicative of regions of overlapping intrinsic stacking faults on every  $\{111\}$  plane in the Co-rich fcc matrix ( $a = 0.355 \text{ nm}$ ). The magnified views for dense stacking-fault arrays for stacking-faults on  $(111)$  and  $(\bar{1}\bar{1}1)$  planes intersecting at  $90^\circ$  in the  $(100)$  surface orientation are illustrated by the SAED pattern insert in **Figure 10**. The magnified view of these intersecting stacking faults is shown in **Figure 11** where dense stacking faults intersecting at  $90^\circ$  for faults on  $\{111\}$  planes inclined  $\sim 55^\circ$  to the  $(100)$  surface plane, and in the  $\langle 022 \rangle$  trace directions are shown. Similar but far less dense intrinsic stacking-fault arrays were demonstrated in the prior work of Atamert and Bhadeshia [13] for nominal compositions of Co-28Cr-4.8W-1.3C (Stellite 6). In addition, the observations in **Figures 8 to 11** illustrate stacking faults on all  $\{111\}$  variant planes in contrast to observations of the favoring of a particular variant by Atamert and Bhadeshia [13]. The corresponding Rockwell C-scale hardness (HRC) values for the horizontal/vertical planes as in **Figure 4** were observed to be 44/46.

### 3.2. Cylindrical Component Fabricated by Electron Beam Melting

**Figure 12** shows similar  $\text{Cr}_{23}\text{C}_6$  carbide column architectures in a representative cylindrical specimen as arrays

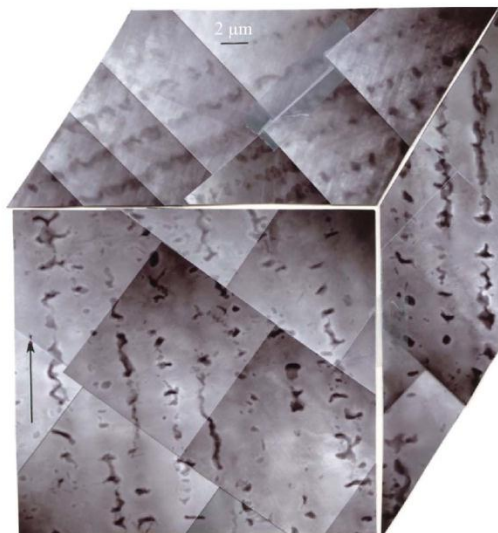


**Figure 6.** 3D TEM representation of carbide columns.

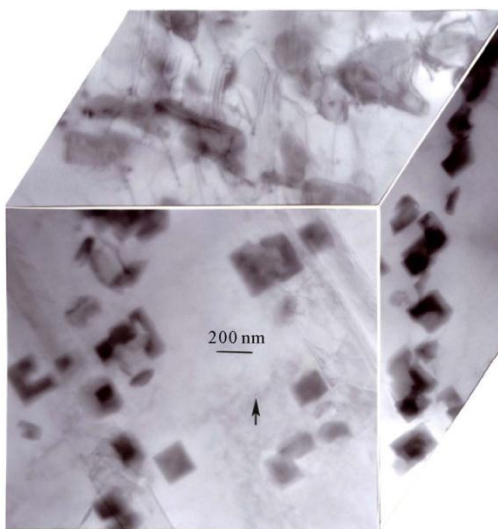


**Figure 7.** 3D TEM representation at higher magnification.

observed in both the horizontal and vertical planes are essentially the same as shown for the fabricated block in **Figure 4**. The associated HRC values are correspondingly 47/48. In **Figure 13**, the horizontal (OM) carbide array in **Figure 13(a)** is compared with corresponding TEM images for the same horizontal orientation. The SAED pattern insert in **Figure 13(c)** shows a  $(100)$  plane orientation with superimposed  $\text{Cr}_{23}\text{C}_6$  carbide reflections, and these features are shown for aggregated carbide precipitates in



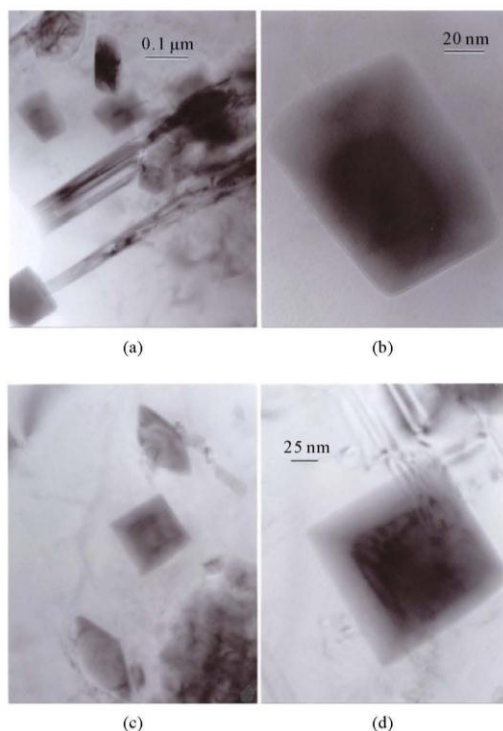
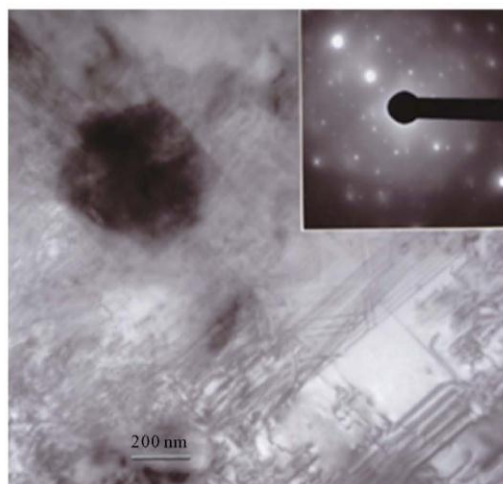
Figure 8.  $\text{Cr}_{23}\text{C}_6$  precipitates.

Figure 9. Stacking faults and double-diffraction spots.

**Figure 14** which range in particle size from ~50 to 500 nm, with their (100)-fcc diffraction pattern superimposed on the Co-rich matrix SAED pattern insert in **Figure 14**.

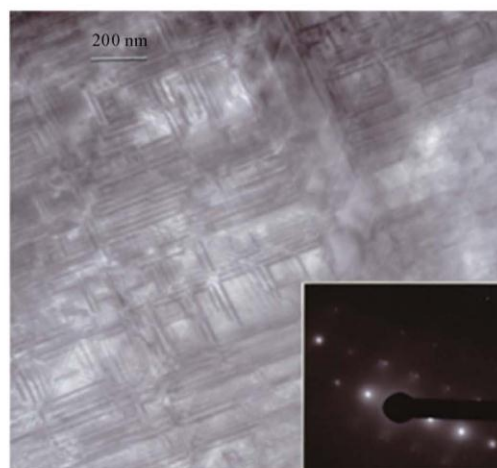


Figure 10. Intersecting intrinsic stacking faults.

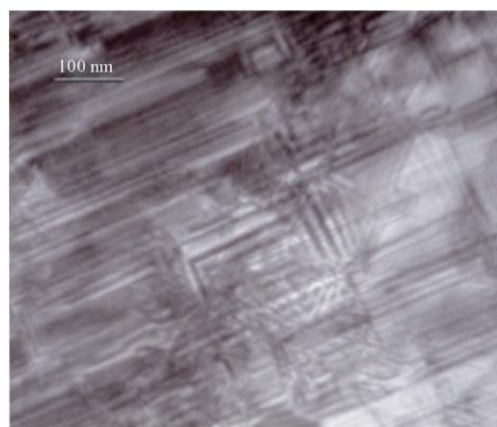


Figure 11. Magnified image of stacking faults.

**Figure 14** also shows a high density of dislocations especially associated with the carbide precipitates, the SAED pattern insert shows [100]  $\text{Cr}_{23}\text{C}_6$  zone axis superimposed on [112] fcc Co-rich matrix zone axis. **Figure 15** shows dense stacking-fault arrays similar to those shown in **Figures 9-11** for a block specimen (**Figure 3**). Here again, the intersections of faults on {111} planes which intersect at  $90^\circ$  produce diffraction contrast features for these intersecting {111} planes at  $45^\circ$ . The SAED pattern insert in **Figure 15** also shows the same (100) orientation as observed in **Figures 9-11**, along with some extra reflections characteristic of twin faults created by the systematic, overlapping intrinsic stacking faults.

As shown previously by Gaytan, *et al.* [6], the fracture surface for failed cylindrical samples illustrated a spatial

array of ductile dimples matching the cubic-shape carbide precipitate array illustrated typically in **Figures 12** and **13** in the horizontal plane, coincident with the fracture surface; this feature is illustrated in **Figure 16**. Corresponding UTS and elongation were 1.45 GPa and 3.6%, respectively, as previously determined by Gaytan, *et al.* [6].

Grain boundaries and regular grain structures were difficult to differentiate in the carbide arrays but more regular  $\text{Cr}_{23}\text{C}_6$  precipitation and corresponding etching made them somewhat apparent as noted in the etching patterns of **Figure 4**. Here the average grain sizes are observed to be about 20  $\mu\text{m}$ , or an order of magnitude larger than the carbide column arrays. There seems to be a preference for [100] orientations parallel to the build direction, which is also characteristic of orientation preference in commercial processed copper billets and plate.

### 3.3. Components Fabricated by Electron Beam Melting after Annealing

In the annealed condition, the carbide column architectures disappear, leaving an fcc grain structure containing a propensity of annealing twin boundaries. While  $\text{Cr}_{23}\text{C}_6$  carbides generally dissolve in the grain matrix, there are residual carbides in the grain boundaries, and these promote exaggerated etching, especially at high angle or high energy grain boundaries. In this regard, note that there is no carbide-associated etching along the straight coherent twin boundaries where the energy is roughly the same as the stacking faults ( $\sim 15 \text{ mJ/m}^2$ ), and about 0.03 times the grain boundary free energy [14]. These features are illustrated typically in **Figure 17** where the average grain size, including twinned grains (light grains) was  $\sim 35 \mu\text{m}$ . This is roughly a 75% increase over the as-fabricated Co-26Cr-6Mo-0.2C components (**Figure 2(b)**). Correspondingly, the residual hardness (HRC) was 40 in contrast to  $\sim 47$  for the as-fabricated components; a decrease of  $\sim 15\%$ . The high density of stacking faults and twin-faults declined measurably as illustrated in comparative views of stacking faults shown in **Figures 18-20**, where **Figure 18** represents a surface orientation of (112) with  $[1\bar{1}0]$  direction shown by the arrow. **Figure 19** is a magnified view of stacking faults in the (100) surface orientation with their traces in the  $\langle 022 \rangle$  directions. **Figure 20**, like **Figures 18** and **19**, illustrates intrinsic stacking faults on essentially all  $\{111\}$  plane variants in contrast to the prior Co-base alloy TEM observations by Atamert and Bhadeshia [13].

It is of interest to compare, retrospectively, the annealed, equiaxed grain structure (**Figure 17**) and the associated stacking fault microstructure (**Figures 18-20**) with the more dense stacking fault microstructure and unique carbide microstructural architectures created by EBM fabrication as illustrated in **Figures 9-11** and **15**, and **Figures 4**, **6-8**, and **12-14**. **Figure 18** shows a TEM bright-field im-

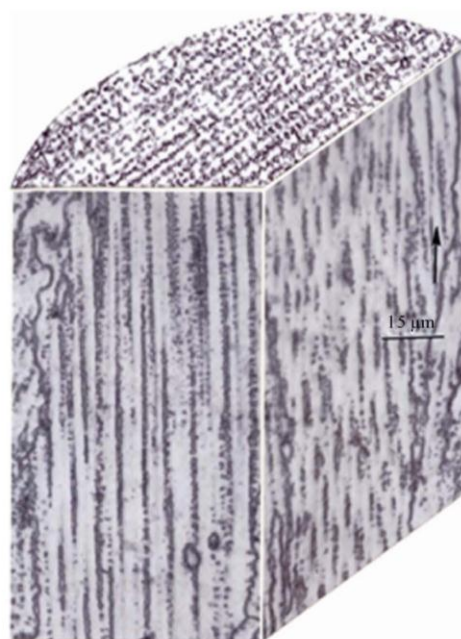


Figure 12. Columnar architecture in cylindrical component.

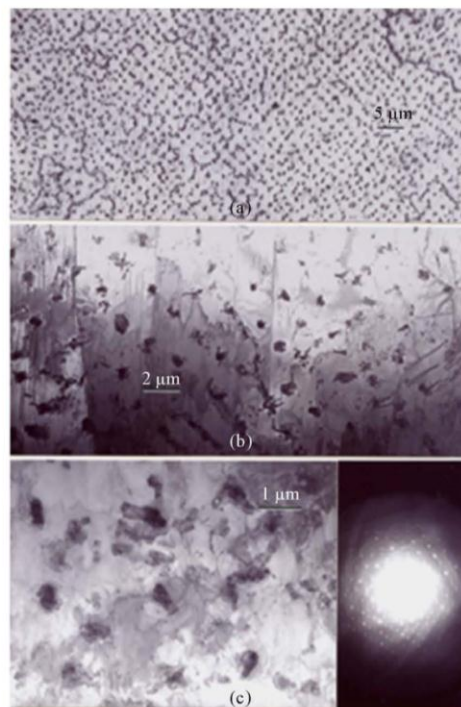


Figure 13. OM and TEM images of carbides.



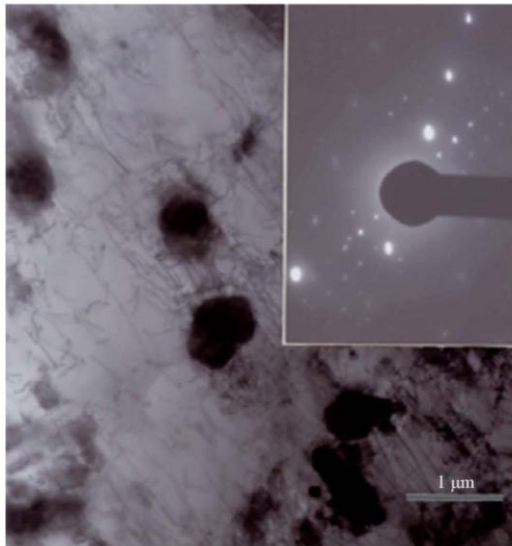


Figure 14.  $\text{Cr}_{23}\text{C}_6$  particles interacting with or generating dislocations.

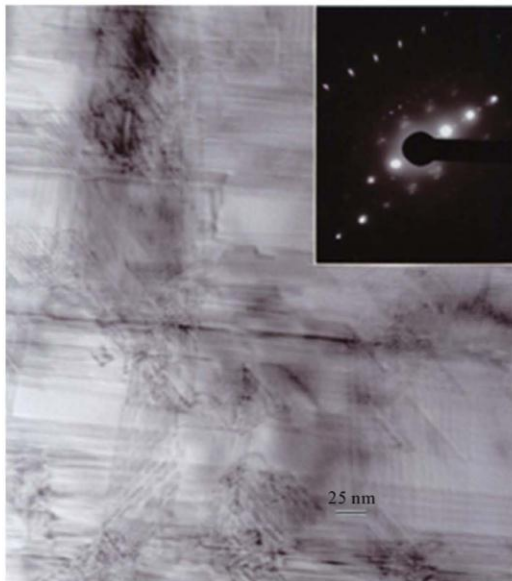
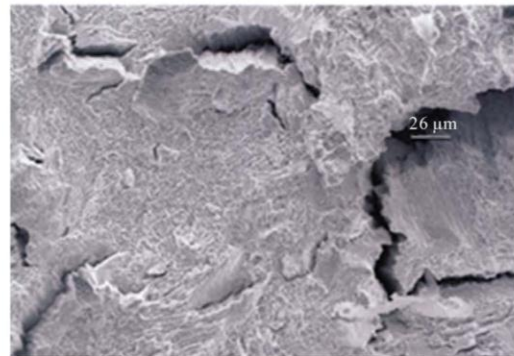
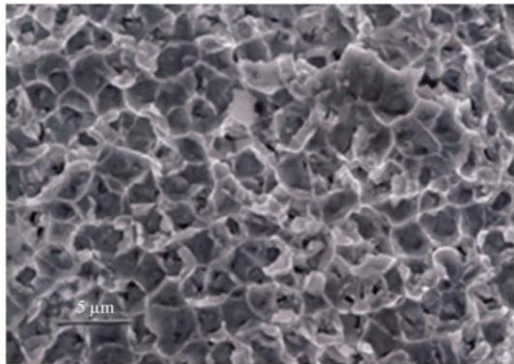


Figure 15. Dense, intersecting stacking faults.

age of intrinsic stacking faults in the (112) orientation for the annealed Co-base alloy in **Figure 17**. The arrow indicates the trace of the  $[1\bar{1}0]$  direction, while **Figure 19** is a TEM image of stacking faults intersecting at  $\sim 90^\circ$  in a (100) grain orientation and **Figure 20** shows multi-variant  $\{111\}$  stacking faults in the annealed Co-base



(a)



(b)

Figure 16. Fractured surface from a cylindrical component fabricated by EBM, a) Low magnification and b) High magnification image.

alloy. These comparisons provide a compelling example of a controlled microstructural architecture in contrast to the conventional (carbide) microstructural regime. Although the  $\text{Cr}_{23}\text{C}_6$  column architectures are not continuous or even proximate carbide particles, the concept as it can be created through systematic, additive manufacturing using EBM, suggests a revolutionary extension of the conventional microstructure-property-processing-performance materials science an engineering paradigm. Indeed, in the same way compositions (in this case especially carbon content) or chemistries of alloy systems can influence the microstructure-property relationships in particular, the prospects for microstructural architecture manipulation and the attendant property-processing-performance variations, attest to the novelty and potential features of the concept. Increasing the carbon content in the Co-26Cr-6Mo-C alloy, especially to more contemporary levels for aerospace superalloy applications ( $\geq 0.5\text{C}$ ) should have a controlling effect on the carbide particle

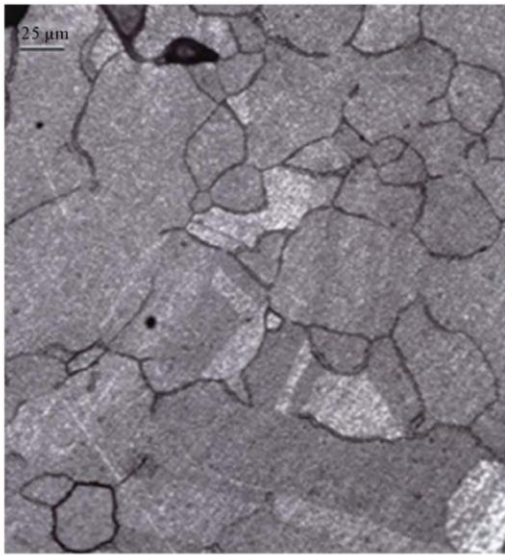


Figure 17. EBM fabricated components after annealing treatment.

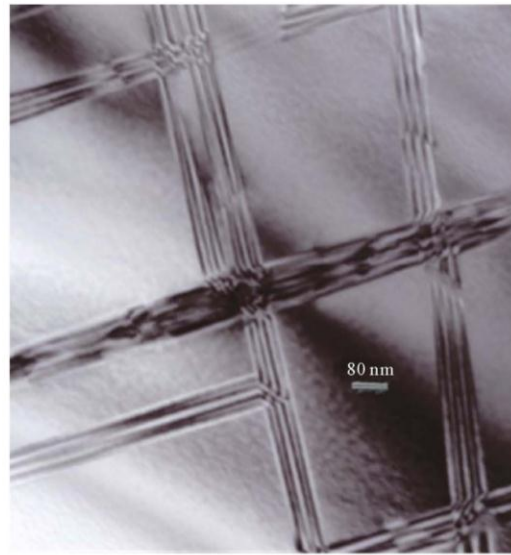


Figure 19. Stacking faults intersecting at  $\sim 90^\circ$  in a (100) grain orientation.

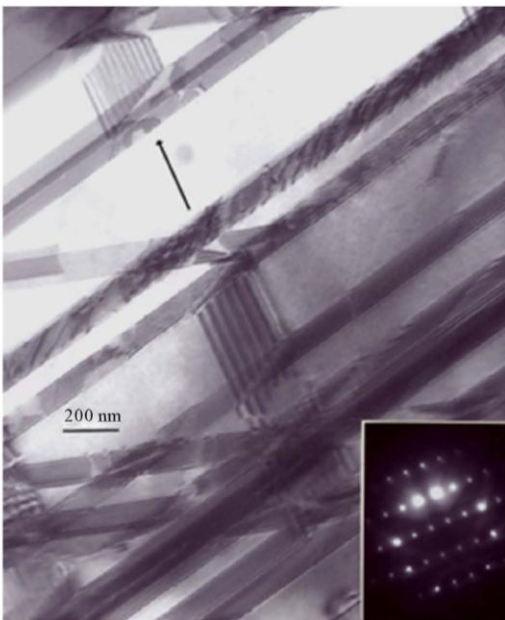


Figure 18. Intrinsic stacking faults in the (112) orientation.

densities (or spacings) in the EBM-produced columns (Figures 4, 6 and 7). This in turn should influence simple mechanical properties such as residual hardness (even directionally), strength, elongation, and even the elastic

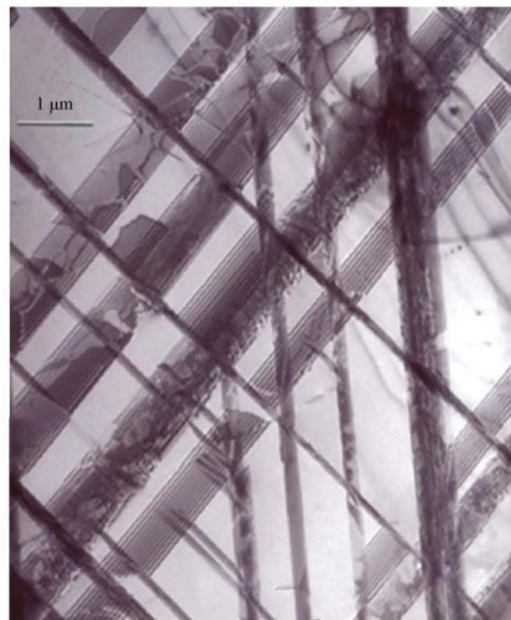


Figure 20. Multivariant {111} stacking faults in the annealed Co-base alloy.

(Young's) modulus. The latter would be especially notable if the carbide particle columns began to act somewhat like fiber-arrays in a matrix where the volumetric addition



of such reinforcing features alter the elastic modulus in relation to their spatial relationship as it influences the so-called rule of mixtures for the ideal isostrain condition where the stress is applied in the direction of the fibers. Of course these features are only speculative at this point.

#### 4. Conclusions

Using TEM, we have illustrated the details of  $\text{Cr}_{23}\text{C}_6$  carbide columns created by the systematic, spatial scans of an electron beam in the additive manufacturing of Co-26Cr-6Mo-0.2C prototypes using EBM. These columns represent an example of a controlled microstructural architecture. In this study, we have in principle compared these uniquely fabricated architectures with more conventional, stacking fault microstructures by annealing the carbides and their attendant architectures. These architectures represent length scales ranging from microns-to-nanometers which may be extended systematically to the macroscale represented by millimeters-to-meters. The TEM analyses have demonstrated  $\text{Cr}_{23}\text{C}_6$  carbides to be exclusive in the formation of column architectures with spacings of 1 - 3  $\mu\text{m}$  for carbide particles ranging nominally from < 100 nm to > 200 nm.

#### 5. Acknowledgements

This work was supported in part by Mr. & Mrs. MacIntosh Murchison endowments at The University of Texas at El Paso.

#### REFERENCES

- [1] R. Roy, "Materials Science and Engineering in the United States," The Pennsylvania State University Press, State College, 1970.
- [2] Materials Science and Engineering for the 1990s, "Maintaining Competitiveness in the Age of Materials," National Academy Press, Washington, 1989.
- [3] G. A. Chadwick, "Eutectic Solidification," In: T. J. Hughel, Ed., Liquids: Structure, Properties, *Solid Interactions*, Elsevier, New York, 1965, pp. 238-255.
- [4] H. W. Weart and J. D. Mack, "Eutectic Solidification Structures," *Transactions of the Metallurgical Society of AIME*, Vol. 212, 1958, pp. 664-671.
- [5] R. W. Kraft, "Eutectic Solidification," *Journal of Metals*, Vol. 8, No. 2, 1966, pp. 192-198.
- [6] S. M. Gaytan, L. E. Murr, E. Martinez, J. L. Martinez, B. I. Machado, D. A. Ramirez, F. Medina, S. Collins and R. B. Wicker, "Comparisons of Microstructures and Mechanical Properties for Solid and Mesh Cobalt-Base Alloy Prototypes Fabricated by Electron Beam Melting," *Metallurgical and Materials Transactions A*, Vol. 41, No. 12, 2010, pp. 3216-3227. doi:10.1007/s11661-010-0388-y
- [7] A. Strondl, R. Fischer, G. Frommeyer and A. Schneider, "Investigations of MX and  $\gamma'/\gamma$  precipitates in the Nickel-based Superalloy 718 Produced by Electron Beam Melting," *Materials Science and Engineering A*, Vol. 480, No. 1-2, 2008, pp. 138-147. doi:10.1016/j.msea.2007.07.012
- [8] C. T. Sims, N. S. Stoloff and W. C. Hagel, "Superalloys II," John Wiley & Sons, New York, 1987.
- [9] G. D. Janaki, "Microstructure and Wear Properties of LENS® Deposited Medical Grade CoCrMo," *Journal of Materials Science: Materials in Medicine*, Vol. 19, No. 5, 2008, pp. 2105-2111. doi:10.1007/s10856-007-3078-6
- [10] J. Cawley, J. E. P. Metcalf, A. H. Jones, T. J. Band and D. S. Skupien, "A Tribological Study of Cobalt Chromium Molybdenum Alloys Used in Metal-on-Metal Resurfacing Hip Arthroplasty," *Wear*, Vol. 255, No. 7-12, 2003, pp. 999-1006. doi:10.1016/S0043-1648(03)00046-2
- [11] L. E. Murr, E. V. Esquivel, S. A. Quinones, S. M. Gaytan, M. I. Lopez, E. Y. Martinez, F. Medina, D. H. Hernandez, E. Martinez, J. L. Martinez, S. W. Stafford, D. K. Brown, T. Hoppe, W. Meyers, U. Lindhe and R. B. Wicker, "Microstructures and Mechanical Properties of Electron Beam-Rapid Manufactured Ti-6Al-4V Biomedical Prototypes Compared to Wrought Ti-6Al-4V," *Materials Characterization*, Vol. 60, No. 2, 2009, pp. 96-105. doi:10.1016/j.matchar.2008.07.006
- [12] L. Thijs, F. Verhaeghe, T. Craeghs, J. van Humbeeck and J.-P. Kruth, "A Study of the Microstructural Evolution during Selective Laser Melting of Ti-6Al-4V," *Acta Materialia*, Vol. 58, No. 9, 2010, pp. 3303-3312. doi:10.1016/j.actamat.2010.02.004
- [13] S. Atamert and H. K. D. H. Bhadeshia, "Comparison of the Microstructures and Abrasive Wear Properties of Stellite Hardfacing Alloys Deposited by Arc Welding and Laser Cladding," *Metallurgical and Materials Transactions*, Vol. 20, No. 6, 1989, pp. 1037-1054. doi:10.1007/BF02650140
- [14] L. E. Murr, "Interfacial Phenomena in Metals, and Alloys," Addison-Wesley, Reading, 1975.

## VITA

Sara M. Gaytan was born in Chihuahua Mexico in 1985. Daughter of Rosa Guillen and Martin Gaytan, and older sister of Oscar and Omar Gaytan. Her bachelors and masters degrees were obtained from The University of Texas at El Paso in Metallurgical and Materials Engineering in May 2008 and December 2009 respectively.

Publications/Projects assisted/ co-authored by Gaytan, S. M.:

\* Gaytan, S. M., Murr, L. E. et al. 2011. "A TEM Study of Cobalt-Base Alloy Prototypes Fabricated by EBM". Materials Sciences and Applications, 2011, Vol. 2, pp. 355-363. Published Online May 2011 (<http://www.SciRP.org/journal/msa>)

\*Ramirez, D. A.; Gaytan, S. M. et al. "Open-Cellular Copper Structures Fabricated by Additive Manufacturing Using Electron Beam Melting" Materials Science and Engineering A, 2011, Vol. 528A. pp. 5379-5386.

\*Murr, L.E.; Gaytan, S. M. et al "Microstructural Architecture, Microstructures, and Mechanical Properties for a Nickel-Base Superalloy Fabricated by Electron Beam Melting", Metallurgical and Materials Transactions A, 2011,

\*Murr, L. E.; Gaytan, S. M. et al "Next Generation Orthopaedic Implants by Additive Manufacturing Using Electron Beam Melting", Frontiers in Bioscience, Encyclopedia of Bioscience, to be published, 2011.

\*Murr, L. E.; Gaytan, S. M. et al "Microstructure and Mechanical Properties of Open-Cellular Biomaterials Prototypes for Total Knee Replacement Implants Fabricated by Electron Beam Melting" Journal of the Mechanical Behavior of Biomedical Materials, 2011, vol. 4, pp. 1396-1411.

\*Murr, L. E.; Gaytan, S. M. et al "Contributions of Light Microscopy to Contemporary Materials Characterization: The New Directional Solidification", Visual Light Microscopy (G. VanDerVoort ed.) Elsevier, 2011.

\*Machado, B.I.; Gaytan, S. M. et al "Materials Characterization of Railgun Erosion Phenomena", Materials Science and Engineering A, 2011

\*Puebla, K., Gaytan, S. M. et al "Advanced Metallic Materials: Technological Exploitation of Mechanical Properties" Advanced Materials and Processes, 2011 pp. 29-31.

- \*Gaytan, S. M.; Murr, L. E., et al. "Comparison of Microstructures and Mechanical Properties for Solid and Mesh Cobalt-Base Alloy Prototypes Fabricated by Electron Beam Melting" *Metallurgical and Materials Transactions A*. 2010, Vol. 41A pp. 3216-3227. Published online: 21, August 2010.
- \*Murr, L. E.; Gaytan, S. M. et al "Next Generation Biomedical Implants Using Additive Layered Manufacturing of Complex, Cellular and Functional Mesh Arrays" *Philosophical Transactions (Royal Society, London) A*, 2010. Vol 368, pp. 1999-2032.
- \*Murr, L. E.; Gaytan, S. M. et al "Characterization of Ti-6Al-4V open cellular foams fabricated by additive manufacturing using electron beam melting" *Materials Science and Engineering: A*, Vol. A527, Issues 7-8, March 25, 2010, pp. 1861-1868.
- \*Murr, L. E.; Gaytan, S. M. et al "Characterization of Titanium Aluminide Alloy Components Fabricated by Additive Manufacturing Using Electron Beam Melting" *Acta Materialia*, 2010, vol 58, pp. 1861-1868.
- \*Murr, L. E.; Gaytan, S. M. et al "Fabrication and Characterization of Reticulated, Porous Mesh Arrays and Foams for Aerospace Applications by Additive Manufacturing using Electron Beam Melting", *Global Innovations in Manufacturing of Aerospace Materials, Proceedings of 11<sup>th</sup> MPMD (TMS) Global Innovations Symposium, Supplemental Proceedings: Volume 1: Materials Processing and Properties, TMS (The Minerals, Metals and Materials Society)*, 2010, pp. 283-290.
- \*Tackett, R. J., Gaytan, S. M. et al "Evidence of Low-Temperature Superparamagnetism in Mn<sub>3</sub>O<sub>4</sub> Nanoparticle Ensembles", *Nanotechnology*, 2010, vol 21. 365703 (1-8).
- \*Puebla, K. Gaytan, S. M. et al "Analysis of the Characterization and Quality Control of Build Orientation and Building Parameters of Ti-6Al-4V Specimens Manufactured by Electron Beam Melting (EBM)" *Adv: Metallic Materials: Technological Exploitation of Mechanical Properties, Proceedings, MS&T 2010: Materials Performance (2010)*, CD.
- \*Murr, L. E. Gaytan, S. M. et al "Characterization and Cytotoxicity Assessment of Ballistic Aerosol Particulates for Tungsten Alloy Penetrators into Steel Target Plates" *International Journal of Environmental Research and Public Health*, 2010, vol. 7 (9) pp. 3313-3331.
- \*Murr, L. E.; Gaytan, S. M. et al "Metallographic Characterization of Additive-Layer manufactured Products by Electron Beam Melting of Ti-6Al-4V Powder" *Practical Metallography*, Vol. 46, Number 9, 2009, pp. 442-453.
- \* Gaytan, S. M.; Murr, L. E., et al "Advanced Metal Powder-Based Manufacturing of Complex Components by Electron Beam Melting" *Materials Technology: Advanced Performance Materials*, Vol. 24, Number 3, September 2009, pp. 180-190.

\* Gaytan, S. M.; Murr, L. E., et al “Structure-Property-Process Optimization in the Rapid-Layer Manufacturing of Ti-6Al-4V Components by Electron Beam Melting” TMS publication, Supplemental Proceedings: Volume 1, 2009.

\*Murr, L. E.; Gaytan, S. M. et al “Microstructures and Mechanical Properties of Electron Beam-Rapid Manufactured Ti-6Al-4V Biomedical Prototypes Compared to Wrought Ti-6Al-4V” Materials Characterization, 2009, pp. 96-105.

\*Murr, L. E.; Gaytan, S. M., et al “Microstructure and mechanical behavior of Ti-6Al-4V produced by rapid-layer-based manufacturing, for biomedical applications” Journal of Mechanical Behavior of Biomedical Materials 2, 2009, pp. 20-32.

\*Murr, L. E.; Gaytan, S. M. et al “Microstructures and mechanical properties of electron beam-rapid manufactured Ti-6Al-4V biomedical prototypes compared to wrought Ti-6Al-4V” Materials Characterization, Volume 60, Issue 2, Feb. 2009, pp. 96-105.

\*Murr, L.E.; Gaytan, S. M., et al “Properties and Microstructures of Electron Beam Rapid Manufactured Ti-6Al-4V Biomedical Prototypes Compared to Wrought Ti-6Al-4V” Medical and Engineering Publishers, Inc., 2008

\*Munoz, V.B.; Gaytan, S. M. et al “Characterization of 3-phase (ternary-like) n-type and p-type thermoelectric materials fabricated by explosive (shock-wave) consolidation” Materials Characterization, 2008, vol. 59, pp. 1258-1272.

\*Murr, L. E.; Gaytan, S. M. et al “Metallurgical and Acoustical Characterization of a Hydroformed, 304 Stainless Steel, Caribbean-style Musical Pan” Materials Characterization, 2008, vol. 59, pp. 321-328.

\*Martinez, F.; Gaytan, S. M., et al “Dynamic Deformation and Adiabatic Shear Microstructures Associated with Ballistic Plug Formation and Fracture in Ti-6Al-4V Targets” Materials Science and Engineering A, 2007, vol. 454A, pp. 581-589.

\*Murr, L. E.; Gaytan, S. M., et al “Metallurgical and Acoustical Characterization of an Aluminum Alloy (6061) Caribbean Pan” Materials Characterization, 2006, vol. 57, pp. 232-243.

\*Martinez, F.; Gaytan, S. M., et al “Adiabatic Shear Bands Associated with Plug Formation and Penetration in Ti-6Al-4V Targets: Formation, Structure, and Performance: A Preliminary Study” TMS publication, 2006, pp. 137-142.

#### Presentations:

\*“Materials with Controlled Microstructural Architecture (MCMA) Fabricated by Electron Beam Melting (EBM)” Oral presentation at the 2011 TMS Annual Meeting

\*“Comparison of Microstructures and Mechanical Properties for Solid and Mesh Cobalt-Base Alloy Components and Biomedical Implant Prototypes Fabricated by Electron Beam Melting” Oral presentation and “A TEM Study of Cobalt-Base Alloy Prototypes with Controlled Microstructural Architecture Fabricated By EBM” poster presentation at the 21st International SFF Symposium – An Additive Manufacturing Conference, and at the MS&T 2010 Conference

\*“Fabrication and Characterization of Reticulated, Porous Mesh Arrays and Foams for Aerospace Applications by Additive Manufacturing Using Electron Beam Melting” Oral presentation at the 2010 TMS Annual Meeting

\*“Additive Layered Manufacturing of Reticulated Ti-6Al-4V Biomedical Mesh Structures by Electron Beam

Melting” Oral presentation at the 25th Southern Biomedical Engineering Conference, 2009

\*“Structure-Property Process Optimization in the Rapid-Layer Manufacturing of Ti-6Al-4V Components by Electron Beam Melting” Oral presentation at the 2009 TMS Annual Meeting

\*“Microstructures and Mechanical Properties of Electron Beam Rapid Manufactured Ti-6Al-4V Biomedical Prototypes Compared to Wrought Ti-6Al-4V” Oral presentation at the 24th Southern Biomedical Engineering Conference, 2008 and Poster presentation at the 2008 TMS Annual Meeting

\*“Metallurgical Aluminum Burst?” Poster presentation at the summer school: “Analysis in Art with Radiation” at Mühlhausen, Germany, 2007 and Poster presentation at the 2007 TMS Annual Meeting

\*“Fabrication of an Aluminum, Caribbean-Style, Musical Pan: Metallurgical and Acoustical Characterization” Poster presentation at the 2006 TMS Annual Meeting

Permanent address: Paseo 4, # 508, Fracc. Paseo del Rio

Cd. Juarez, Chih. Mexico 32414

This dissertation was typed by Sara M. Gaytan.